Conference Proceedings of the Society for Experimental Mechanics Series

Julie Harvie *Editor*

Dynamic Environments Testing, Volume 7

Proceedings of the 41st IMAC, A Conference and Exposition on Structural Dynamics 2023

SEM

Springer

Conference Proceedings of the Society for Experimental Mechanics Series

Series Editor

Kristin B. Zimmerman
Society for Experimental Mechanics, Inc.,
Bethel, CT, USA

The Conference Proceedings of the Society for Experimental Mechanics Series presents early findings and case studies from a wide range of fundamental and applied work across the broad range of fields that comprise Experimental Mechanics. Series volumes follow the principle tracks or focus topics featured in each of the Society's two annual conferences: IMAC, A Conference and Exposition on Structural Dynamics, and the Society's Annual Conference & Exposition and will address critical areas of interest to researchers and design engineers working in all areas of Structural Dynamics, Solid Mechanics and Materials Research.

Julie Harvie
Editor

Dynamic Environments Testing, Volume 7

Proceedings of the 41st IMAC, A Conference and Exposition on Structural Dynamics 2023

Springer

Editor
Julie Harvie
Albuquerque, NM, USA

ISSN 2191-5644 ISSN 2191-5652 (electronic)
Conference Proceedings of the Society for Experimental Mechanics Series
ISBN 978-3-031-34929-4 ISBN 978-3-031-34930-0 (eBook)
https://doi.org/10.1007/978-3-031-34930-0

This Springer imprint is published by the registered company Springer Nature Switzerland AG
The registered company address is: Gewerbestrasse 11, 6330 Cham, Switzerland

Paper in this product is recyclable.

Preface

Dynamic Environments Testing represents one of ten volumes of technical papers presented at the 41st IMAC, a Conference and Exposition on Structural Dynamics, organized by the Society for Experimental Mechanics, held February 13–16, 2023. The full proceedings also include volumes on *Nonlinear Structures and Systems*; *Dynamic Substructures*; *Model Validation and Uncertainty Quantification*; *Dynamic Substructures*; *Special Topics in Structural Dynamics and Experimental Techniques*; *Computer Vision and Laser Vibrometry*; *Sensors and Instrumentation and Aircraft/Aerospace Testing Techniques*; *Topics in Modal Analysis and Parameter Identification*; and *Data Science in Engineering*.

Each collection presents early findings from experimental and computational investigations on an important area within dynamic environments testing and other structural dynamics areas.

The organizers would like to thank the authors, presenters, session organizers, and session chairs for their participation in this track.

Albuquerque, NM, USA — Julie Harvie

Contents

Chapter 1
Designing Accelerated Vibration Tests Using Model-Based Equivalent Damage Prediction

Taylor Kinnard, Davis McMullan, Katherine Pane, Garrison S. Flynn, Thomas Thompson, and Keegan Moore

Abstract The use of vibration testing to complete qualification of critical components is important for a wide variety of industries to understand the life cycles of their products in operational environments. A common problem with testing components to failure is the time and cost associated with mimicking the full life of a part, creating a need for shorter-duration testing that provides comparable life cycle information. The most common methods that accelerate damage tests use Miner's Rule, an equation that sums damage percentages caused by varying stress amplitudes. The aim of using Miner's Rule in damage analysis is to find a shorter-duration test cycle that will provide equivalent damage to the part's real-world environment. This method has demonstrated accuracy under constant amplitude loading but loses reliability under variable amplitude loadings due to its lack of regard toward the loading sequence. Furthermore, translating from a stress-cycle (SN) curve to design amplitudes for testing requires system knowledge. Finally, the entire process of damage equivalence for additively manufactured (AM) parts is minimally explored in current research. This study seeks to improve the quality of test acceleration by utilizing models of the system under test to not only provide a method for faster, more accurate equivalent damage analysis but also to fill a void of a lack of information regarding test compression of AM parts. To do this, AM specimens designed with a failure point under a complex stress history are evaluated. First, parts are vibration tested on a shaker to achieve experimental failure time. Next, the base inputs used for experimentation are modeled in simulation to evaluate theoretical failure time. Finally, test results of the experimental setup and simulated environment were compared to evaluate the accuracy of Miner's rule in equivalent damage analysis, as well as test accuracy of SN curves for designing tests of AM parts.

Keywords Fatigue testing · Finite element analysis · Miner's rule · Shock and vibration

1.1 Introduction

In any field of engineering, fatigue testing is an essential step in the qualification of a part in order to evaluate its life cycle. The term "life cycle" is in reference to not only how long the part lasts in the field, but in what ways and how much it gets damaged during predicted use. These fatigue tests often take over one-third of project development time and can accumulate high labor and material costs for the manufacturer. However, this testing is necessary to ensure that a product is not used past its life expectancy, due to the harm or damage that could occur from doing so. If done efficiently, fatigue testing undoubtedly

T. Kinnard
Department of Aerospace and Mechanical Engineering, University of Notre Dame, Notre Dame, IN, USA

D. McMullan
Department of Mechanical Engineering, Texas A&M University, College Station, TX, USA

K. Pane
Department of Materials Science and Mechanical Engineering, Harvard University, Cambridge, MA, USA
e-mail: kpane@college.harvard.edu

G. S. Flynn (✉) · T. Thompson
Los Alamos National Laboratory, Los Alamos, NM, USA
e-mail: garrison@lanl.gov; tnthompson@lanl.gov

K. Moore
Department of Mechanical and Materials Engineering, University of Nebraska, Lincoln, NE, USA
e-mail: kmoore@unl.edu

J. Harvie (ed.), *Dynamic Environments Testing, Volume 7*, Conference Proceedings of the Society for Experimental Mechanics Series, https://doi.org/10.1007/978-3-031-34930-0_1

saves both time and money in the long run because engineers will know how long a part can last in its field of use, in order to maximize the part's duration of functionality without leaving it in use too long. This means no lost material and engineering cost from taking it out too early and, more importantly, no serious safety concerns that arise from not removing it soon enough. An efficient method of fatigue testing is accomplished through accelerated testing, a process in which a higher stress loading environment can be applied to a part in order to more rapidly evaluate its fatigue life to total failure. This is done using a method known as Miner's Rule, a decades old theory whose inaccuracies sometimes outweigh its benefit.

The Palmgren-Miner Rule (Miner's Rule) is a linear damage summation rule in which each term is the ratio of the number of cycles endured at a specific stress cycle amplitude (n_i) to the number of cycles the part would require for failure at that amplitude (Ni) [1]. Miner's Rule defines these N_i values from an empirical stress-cycle (SN) curve dependent on the part's material and failure method [1, 2]. Miner's Rule remains a popular method of damage quantification due to its simplicity and ease of application to a variety of test environments. Unfortunately, Miner's Rule has some critical inaccuracies due to its assumption of linearity. When stresses of different magnitudes are applied to a part, Miner's Rule sums all stresses without regard to the order of loading. With non-constant loadings being unavoidable in testing in order to accurately recreate a real-use environment, it's important to know how accurate Miner's Rule really is under these unideal conditions. The results from an experiment by Head and Hooke completed within a decade of the creation of Miner's Rule showed that the actual lifespan of a part subject to random loading was shorter than Miner's Rule's prediction by a factor of between 2 and 3.5 [3]. This finding suggests Miner's Rule may dangerously overestimate the time it takes for an object to fail. Later, other tests confirmed inaccuracies in damage prediction due to the linearity of Miner's Rule. The equation gives overly conservative estimates when stresses go from low to high amplitude, and dangerously weak estimates when stress starts at a high magnitude and moves to a low magnitude [4, 5].

The other critical inaccuracy of Miner's Rule is the reliance on an empirical SN curve. This causes the damage estimation using Miner's Rule to only be as good as the quality of the SN curve available. A core exploration of this study is in relation to this SN curve inaccuracy, particularly regarding the wide differences in data collected for a single material depending on the part geometry and failure method [2]. If a part under test has a complex stress history, enduring multiple methods of failure at once in more than one location, it is almost guaranteed the part will need its own destructive fatigue testing to create a unique SN curve prior to evaluating damage or creating equivalent test environments. With these complex stress histories also comes a challenge in evaluating the maximum stress in the part at the place that causes failure and what to do with these values in terms of continuing and altering testing. The utilization of simulated models to inform and predict experimental test results saves overall test time and allows for a wider range of tests to be performed in the virtual domain that may not be possible in a physical environment.

1.1.1 Background

There are many existing methods of accelerated testing that intend to mitigate the errors of Miner's Rule. However, many of these methods either still utilize Miner's Rule as a base calculation or rely on a complex definition of damage and failure that are not applicable to all systems. For example, the Fatigue Damage Spectrum method, based on Henderson and Piersol's Damage Potential Spectrum, utilizes signal processing to find the amount of energy or stress applied per frequency of a given signal [6–8]. This is done by first converting the signal into a power density spectrum, and then Miner's Rule is used to normalize the power density spectrum into a Fatigue Damage Spectrum. The result is more accurate than using Miner's Rule on its own, but still carries with it an unreliable amount of uncertainty. The same issue is inherent in the mission synthesis method, where the test environment is decomposed into a power spectral density (PSD) plot to be imitated in a test environment [9]. The PSD is then decomposed into a summation of sinusoidal loadings to be added using Miner's rule. In addition to all previously described methods, there are several other less commonly used methods for damage equivalence that are described in detail by Fatemi and Yang [10].

Other methods avoid Miner's Rule attempting to maintain higher accuracy when accelerating test duration in nonconstant environments. A similar method to mission synthesis has been proposed for sine-on-random (SoR) loadings by synthesizing the SoR waveform rather than the PSD to gain greater accuracy in test shortening [11]. There are also many studies that have attempted to evaluate equivalent damage from a statistical standpoint, namely by using the Weibull distribution to influence data analysis rather than the Gaussian distribution Miner's Rule assumes [12].

The most basic model for damage equivalence in test acceleration is the one investigated in this study, which is simply moving up and down the material's SN curve. As mentioned, this is an inherently flawed method despite its ease of use. Not only are SN curves slightly unreliable due to under-sampled data or inconsistent test environments, but the method relies on a correct assumption that total damage is equivalent to 1 regardless of load endured [4, 12]. It is widely known that the worse

the accuracy, the more complex the system under test becomes; hence, the parts tested to failure in this study are additively manufactured (AM) and designed to have a complex stress history with multiple methods of failure occurring simultaneously [2].

The use of AM parts adds more of a challenge to this study due to the limited knowledge on the fatigue life and failure of various AM materials. The parts used in this study are printed from ABS plastic using the PolyJet technology from Stratasys, which introduces even more unknowns in fatigue life due to the newness and uniqueness of the process. From limited literature, it can be said that PolyJet 3D printed ABS experiences a more brittle fracture than other methods of printing on similar materials due to its impressive fill density and material strength [13]. The expected failure method of the parts used in this study is a combination of bending and torsion at a specific notch point. This complicated stress history paired with the inherently variant behavior of AM plastic causes the behavior of the part as it undergoes fatigue and "total failure" to be somewhat unpredictable.

1.1.2 Motivation

It is critical that the flaws of Miner's Rule be evaluated in the context of non-constant loading and complex stress histories in order to provide a foundation for application to more accurate and informed accelerated fatigue testing. By allowing tests to use Miner's Rule to over- or under-predict failure of a part in use, money and resources can be wasted and user safety is at risk. These restrictions in accuracy also prevent the use of such a simple damage model in more complex systems. For example, multiaxial fatigue introduces significantly more uncertainties in the physical environment that are only worsened by the mathematical shortcomings of Miner's Rule [14]. In shock testing, Miner's Rule is hardly even considered due to its dependence on a cyclical loading [15]. The analysis in this study is intended to open discussion of applications for altered damage quantification and accelerated testing techniques in these more complicated testing regimes, specifically shock and other types of variable input. In addition to the evaluation of Miner's Rule in damage quantification, it is also critical for this study to test the limits of simulated modeling to predict and inform physical test environments. Integrating modeling into fatigue testing opens opportunities for more accurate testing of complex parts by eliminating uncertainties in the system and allowing for a type of nondestructive testing to be performed on a geometry before moving to a physical experiment.

1.2 Methodology

With the long-term goal of evaluating the accuracy of Miner's Rule, a primary focus of this study is exploring the ways in which simulated models can be used to design experimentation and supplement analysis of real environments. Accelerated testing is critical for being able to collect fatigue data quickly and accurately for a part before it is put into use, and advancements in simulated fatigue testing could greatly assist this process for more complex geometries. The stress histories of these complex parts can be visualized through validated simulations in order to better evaluate the entire fatigue life rather than just quantify total failure. Assumptions in use throughout this study are as follows: (1) the AM parts used in testing can be accurately represented in simulation by entering the correct material properties into the program and (2) anisotropy need not be considered in detail because all parts are printed at the same orientation using the same method with high density fill.

1.2.1 Part Design

The parts used in testing are designed to fail with a complex stress history. Fatigue testing quickly increases in complexity when multiple failure modes are present in a single part. By creating a part that will fail in both bending and torsion at one specific stress concentration, it is possible to collect consistent failure data while also presenting the challenge of being unable to apply many of the assumptions used in more simple fatigue environments. Such complex stress histories present opportunity for numerical simulations to gather cumulative stress data at various points on the part.

The most important location to study the fatigue of the part in Fig. 1.1 is the notch; a carefully placed stress concentration ensures failure at the same point with the same method every time. At this point, the larger spherical mass creates a bending stress due to the torque caused by the part only being attached to the vertical shaker at the connection point on the end of the part. The smaller spherical mass on the opposite end creates a torsional stress on that same point as it follows the vertical

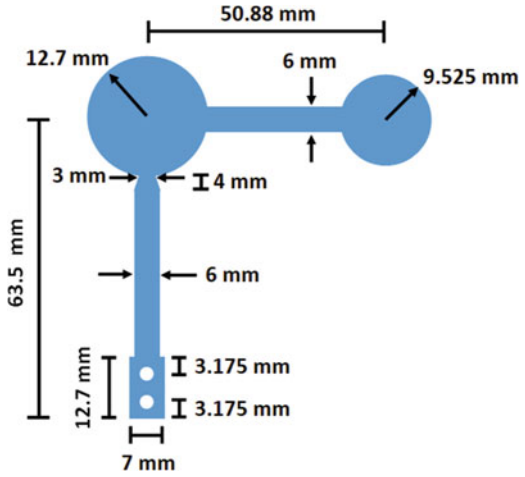

Fig. 1.1 2D digital drawing of part with dimensions in millimeters

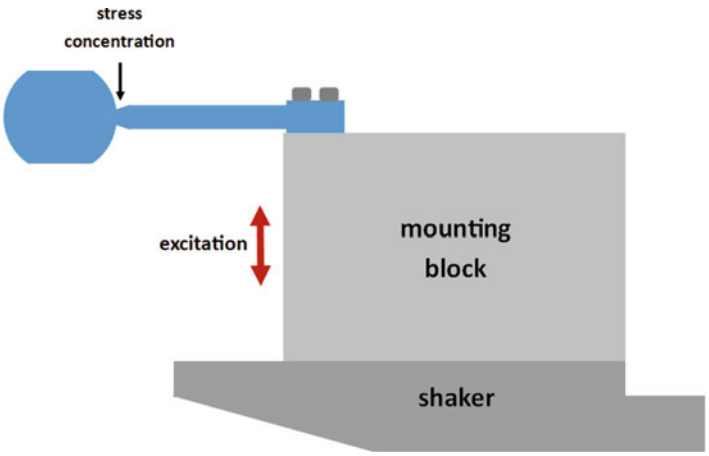

Fig. 1.2 Identification of stress concentration point and direction of motion under excitation

motion of the shaker. Figure 1.2 illustrates this motion relative to the shaker. This consistent failure method allows for a collection of data that can be more accurately analyzed as representing the same environment every time.

As a qualification of the need for simulated stress data in a complex part, it is important to illustrate the time and effort required to evaluate stress at the failure point if a simulated model was not accessible. First, the maximum bending and torsional stresses in the part, $\sigma_{\max}$ and $\tau_{\max}$ respectively, would need to be calculated.

$$\sigma_{\max} = k_{\text{notch}}\sigma_o \quad \text{where} \quad \sigma_o = \frac{Mc}{I} \tag{1.1}$$

$$\tau_{\max} = k_{\text{notch}}\tau_o \quad \text{where} \quad \tau_o = \frac{Tc}{J} \tag{1.2}$$

Equations 1.1 and 1.2 can be mostly solved using properties obtained from part geometry, and k_{notch} is obtained from published diagrams based on notch diameter and radius. A complication arises, however, with the moment and torque calculations, which would require a knowledge of the force applied on the part as it moves on the shaker. It is now necessary to deal with relative accelerations of the masses, which introduces an entirely separate analysis to the already demanding fatigue analysis. Another calculation involving the input acceleration to the shaker is the need for a stress input in order to compare input to output stress and confirm a one-to-one relationship. This would be done using a Von Mises stress element analysis.

$$\sigma_V^2 = \frac{1}{2}\left[(\sigma_1 - \sigma_2)^2 + (\sigma_2 - \sigma_3)^2 + (\sigma_3 - \sigma_1)^2 + 6\left(\tau_{2,3}^2 + \tau_{1,3}^2 + \tau_{1,2}^2\right)\right] \tag{1.3}$$

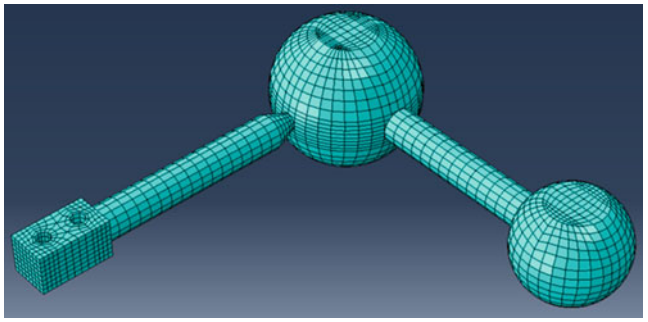

Fig. 1.3 ABAQUS model of previously described test geometry

Equation 1.3 above can be simplified by considering only the applicable directions of motion for the part on the vertical shaker.

$$\sigma_V = \sqrt{\sigma_1^2 + 3\left(\tau_{2,3}^2 + \tau_{1,3}^2\right)} \tag{1.4}$$

The stress calculated with Eq. 1.4 requires further assumptions and calculations of individual stress and torsion components. At this point, it would be possible to compare input stress to output stress at the failure point and derive relationships from there. Simulated models provide the opportunity to confirm or deny these common assumptions as well as analyze the constantly changing stress at the failure point in seconds.

As for the use of AM in manufacturing the parts used in testing, this decision was made purely as a simple method for manufacturing this somewhat complex geometry and avoid complications in traditional manufacturing of such a small, detailed part, as well as to be able to produce a large amount in less time. Despite the relative lack of literature regarding the fatigue life and damage quantification of AM parts, the behavior of the AM material used as opposed to its traditionally manufactured counterpart is outside the scope of this study. It is, however, important to note that the variability in composition of the parts being both plastic and additively manufactured did create complications in data collection in this study, as will be explored in later sections.

1.2.2 Simulation

The use of simulated modeling provides a simple and efficient way to input acceleration data and extract the resulting stress information without enduring the computational difficulties of drawing those relationships analytically in a complex part. The simulation software used for this study is ABAQUS, a vast software suite used for finite element modeling. Before any simulations could be run, the test specimen needed to be accurately modeled and validated.

The model, shown in Fig. 1.3, was built in multiple parts, each given the same material properties and individually meshed, and then assembled altogether. To make the assembly one coherent structure, tie constraints bonding one surface to another were placed on all the connection points. In order to give the model the same dynamic behavior of the test specimen, it was necessary to create boundary conditions that replicated those that were present in the actual test setup. This experimental setup is described in detail in a later section.

I. Modal Analysis

As previously stated, an ABAQUS model must first be validated to ensure the modeled part looks and behaves in a way consistent with the physical part before it can be used for analysis. The validation for this study was done using a type of experimental modal analysis. Parts were put on the same vertical shaker used for experimentation and subject to a random loading, while accelerometers on the connection point of the part as well as on both spherical masses collected response data. Tap tests were also performed on some parts to confirm results from the random loading frequency response. This data was used to build a frequency response function (FRF) using MATLAB, which then indicated the natural frequencies of the part. To validate the model, the natural frequencies of the model's modes needed to be calculated and then must align with those found by the experimental FRF.

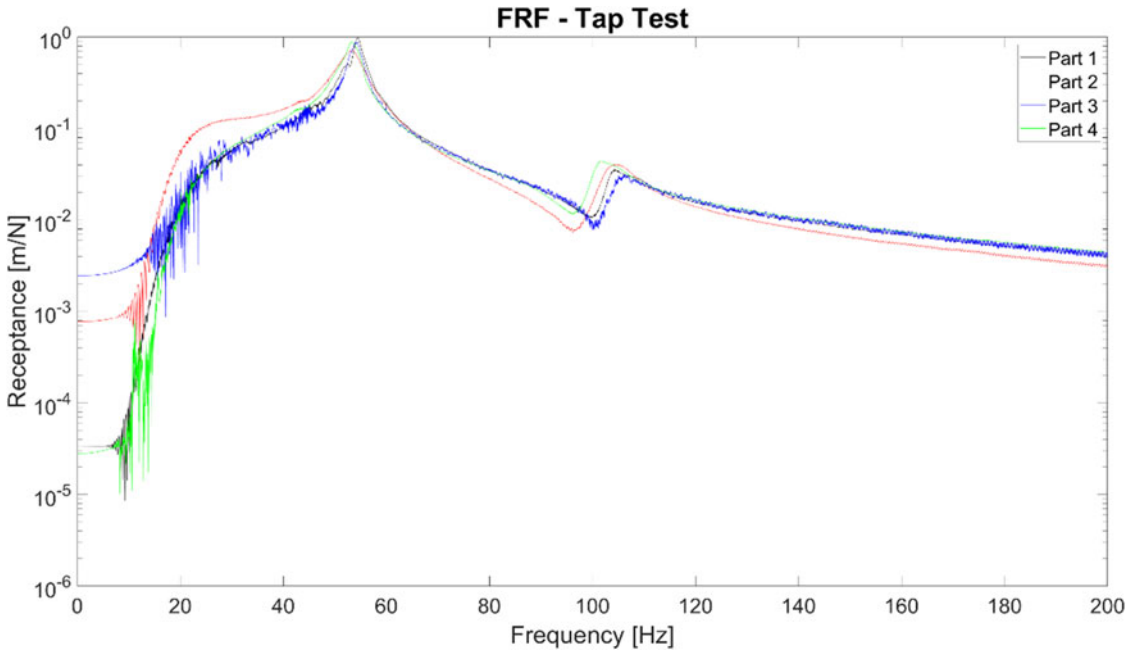

Fig. 1.4 FRF of parts as a result of performing tap tests on four specimens

To find the natural frequencies of the model, a simulated modal analysis was done. To start the ABAQUS modal analysis test, a frequency step was created that would test the modeled part at its first ten natural frequencies. Running the step required the creation and submission of a job. The database output results were the first ten mode shapes of the part, along with the natural frequencies of those modes.

Properly fitting the model to output the same natural frequencies as the FRFs required inputting accurate material properties. The density was calculated by experimentally measuring the mass of the physical part and dividing that by the volume provided by the model. The damping coefficients were calculated using the widths of the peaks of the FRFs. Finally, the elastic modulus of the part was determined by doing an optimization. Modal analysis simulations were run using a range of values as the elastic modulus. The error values between the experimental mode frequencies and those of the model were then plotted, and the modulus that minimized error was found and plugged into the material properties. Based on the closeness of natural frequencies experienced by the model and physical part (shown by the FRF above in Fig. 1.4), it was determined that the stiffness, mass, density, geometry, and other related properties of the model are accurate in their representation of the dynamics of the physical part. As seen in Fig. 1.4 above, the first natural frequency occurred around 54 Hz and the model provided a very near result of 54.7 Hz. This is the frequency the parts were tested at using the controls for the shaker table, intended to create maximum damage and avoid long testing times.

II. Base Excitation

After validating the modal analysis, the model could be used for a variety of ABAQUS testing capabilities. For this study, the primary function of the model was to replicate the experimental shaker tests and calculate the maximum stress experienced at the known failure point on the part under a specified loading. During experimentation, the part is vibrated vertically, and accelerations were recorded at multiple points on the specimen. These recorded acceleration histories were treated as a set of acceleration data from a real environment, like a truck traveling down a road or a plane flying through turbulence. The acceleration data collected at the base of the part was converted to displacement data and used as the input excitation in the ABAQUS simulations.

ABAQUS replicated the experimental base excitations through a modal dynamic step. Within that step, the model received a one-second displacement versus time input that was applied to the rectangular base of the modeled part, just as it was during experimentation, where the real part screws onto the shaker. The goal of the simulation was to extract information about the stress experienced by the part. Stress history outputs were requested at the elements that made up the notch, the intended failure point. At each of those elements, ABAQUS outputted Von Mises stress values at every time increment. The stresses at each element, which were constant-amplitude and cyclical, were plotted in order to identify the maximum stress value seen by the notch.

Fig. 1.5 Experimental bench setup with vertical shaker and single part

Gaining stress information from ABAQUS is useful both for the creation of an SN curve and for forming a relationship between acceleration and stress, which is especially useful for non-constant loading. The specific processes for applying the stress information from ABAQUS will be discussed in a later section.

1.2.3 Experimentation

The experimental setup utilizes a Modal Shop Dual Purpose shaker Model 2075E in a vertical orientation. The shaker is then controlled using an LDS USB Dactron controller, and acceleration data at various points on the parts and shaker is collected using IEPE accelerometers. Parts were bolted onto the shaker at 5 in-lb torque prior to every test to ensure consistent boundary conditions.

It has been said earlier that for complex parts with mixed methods of failure it is better to create a unique SN curve for the specific part, thus the first goal of data collection was to get enough information for an SN curve. This required exciting the parts at constant-amplitude acceleration (and therefore constant stress) cycles, recording their cycles to failure, and obtaining the stress value for each run to failure.

After trial-and-error attempting to achieve accurate data collection with a fully loaded shaker containing eight parts per test, it was determined testing one part at a time would provide the most consistent data.

As seen in Fig. 1.5, the accelerometers were specifically placed to measure the base excitation (used as the "environmental input" for the ABAQUS simulations) of the shaker as well as the accelerations of both the large and small spherical masses on the parts. The measurement locations on the parts were used (1) for confirmation of one-to-one stress response throughout the part, meaning the large and small masses experienced one displacement cycle for each shaker displacement cycle and (2) as an indication of failure of the part, since the acceleration of the masses decreased exponentially when approaching failure.

The damage the part accumulated during testing changed the stiffness of the fatigue part. This change in stiffness shifts the natural frequency away from the test frequency, caused plastic failure in the parts, and resulted in the exponential decay seen in the acceleration of the masses toward the end of the test.

Once the part masses reached the steady-state acceleration seen in Fig. 1.6, it was determined that the part had expended its usable fatigue life. At this point, the parts were so fragile that they could not survive a second modal analysis to track how their natural frequencies had shifted.

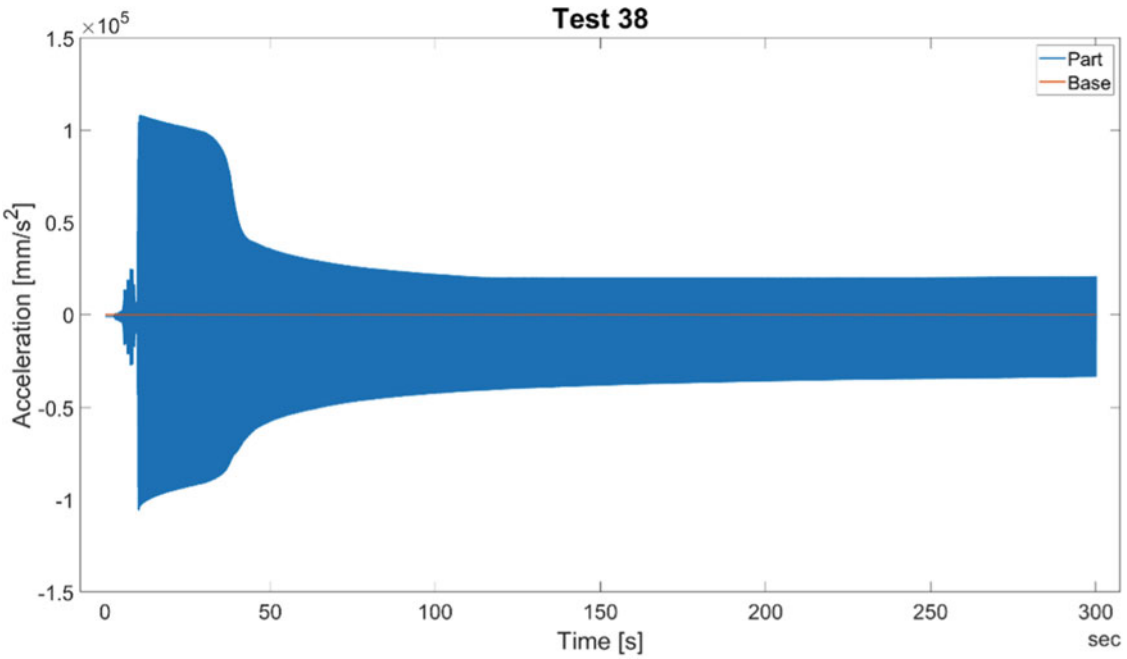

Fig. 1.6 Example of a test where part experienced plastic deformation resulting in acceleration amplitude decay

Because of this unexpected behavior, part failure needed to be defined more specifically than simply waiting for a clean break. For the purposes of this study, full failure (theoretical damage = 1) is reached when the acceleration response of the masses fell within 5% of the steady-state root mean square of the acceleration.

1.2.4 Creating the SN Curve

SN curves are always empirically derived and therefore tend to only account for simple stress histories, such as rotating bending, tensile, or compressive loading. The failure method a part endures greatly impacts its SN curve, and these differences only worsen when looking at AM parts due to anisotropy in printing as seen [2]. Due to the complexity of the part and failure method used in this study, in combination with the previously stated issues, it was deemed impossible to utilize an existing SN curve. This study began with running extensive constant amplitude sine wave inputs on dozens of parts to generate an SN curve for this geometry and loading.

Generating this SN curve will require the number of cycles to failure (N) and stress at failure point (S). The cycles to failure can be calculated using the steady-state failure criteria described in experimentation. The start time of the test is subtracted from the failure time calculated from the failure criteria to find total test time. The time to failure in seconds multiplied by the frequency used (54 Hz) equals N, cycles to failure:

$$N = (t_{\text{fail}} - t_{\text{start}}) * \text{Frequency} \tag{1.5}$$

The stress at the notch is obtained through ABAQUS, as described in the previous section. This combination of experimental and simulated data to create the baseline SN curve is possible due to the model being validated through experimental modal analysis, also previously described.

1.2.5 Utilizing the SN Curve

Variable loading experiments had two experimental procedures: low amplitude to high amplitude, and high amplitude to low amplitude. The low amplitude input was approximately 0.8 g acceleration while the high amplitude was roughly 1.1 g. Note

the use of "approximately" with those values – the shaker control allows for changing an input voltage, which when paired with a manually set gain value on the controller corresponds to a specific acceleration in g the shaker experiences. Because of what was available for testing at the time of this study, open loop control had to be used for experimentation. This resulted in slight variation in what the shaker experienced as tests ran; thus, each test ran had its own base acceleration data evaluated to ensure as accurate of data processing as possible.

Both experimental procedures were set for the first loading amplitude (low or high) to run to 50% of its theoretical fatigue life. These theoretical cycles to damage were taken to be 0.5 N, where N is the number of cycles to total failure according to the SN curve. Then, the test would continue running to a total of 10 min, the same amount of time tested for constant loadings, to allow the second amplitude to bring the part to failure. In theory, the second amplitude, regardless of whether high or low loading came first, should bring the part to failure in 50% of its theoretical cycles to failure also according to the SN curve. In reality, this will likely not be the case.

Once all data were collected, the ABAQUS model was used to find the stress of the part for each base acceleration amplitude using the same method described for constant tests. The base acceleration amplitudes were taken for each section of the experiment, the starting and ending amplitudes, separately in order to accurately evaluate the differences in high to low and low to high loading environments. The way in which damage was calculated and evaluated using this data is explained below.

1.3 Results and Discussion

It became evident at many points during experimentation that the inherent variability in AM parts, especially in plastic parts, would prove to be a challenge for collecting viable data that can be analyzed for the intentions of this study. The data collected, while prone to the variability caused by the AM process, was able to inform evaluation of the usefulness of simulation in predicting and informing subsequent experimentation. Below, the accuracy of Miner's Rule is challenged in the context of variable loading, and future applications of using modeling as a damage prediction method are discussed.

1.3.1 Constant Loading and Creating the SN Curve

With a total of 19 viable data points, the SN curve for the part being used was created and fit to a logarithmic curve shown in Fig. 1.8. As seen in the R^2 value of 0.6148, the variability in the data collected was quite large. This is the best visualization resulting from the experimentation to show the inconsistency in failure of AM parts, specifically plastic parts. It was stated in an earlier explanation of experimental methodology that failure had to be characterized as a specific condition of deformation rather than a brittle fracture. This was because there was no "expected" or "normal" result. Some parts would break immediately just from the minor shock of the shaker table being started up, others at lower amplitudes would never show any signs at all of failure or fatigue after hours of testing, and most experienced the decay in acceleration exhibited by Fig. 1.6. Due to this decay being the most common result noticed in data collection at moderate input acceleration amplitudes, it was decided that parts which experienced that method of failure would be considered the viable data points.

Since the SN curve revealed the extreme variability in testing AM parts to failure, it was determined that creating a mathematical relationship between shaker base input acceleration and the stress experienced by the parts at the specially designed failure point would be helpful for future analysis.

The relationship shown in Fig. 1.8 above was created by inputting all experimental base acceleration amplitudes tested for the SN curve into ABAQUS simulations and retrieving the maximum stresses at the failure point. By having the equation produced by this relationship readily available for further analysis, it became far easier to evaluate variable loading data.

1.3.2 Variable Loading

In order to properly test the limits of using simulated data to qualify failure and damage, the relationships derived in the prior section were used to calculate theoretical cycles to failure for the various tests ran under variable amplitude loadings. The method for deciding experimental cycles to failure, or n, for the first section of the test duration is described in an above section. It is not dependent on anything, but rather chosen by the person testing the parts. The n for the second section of the

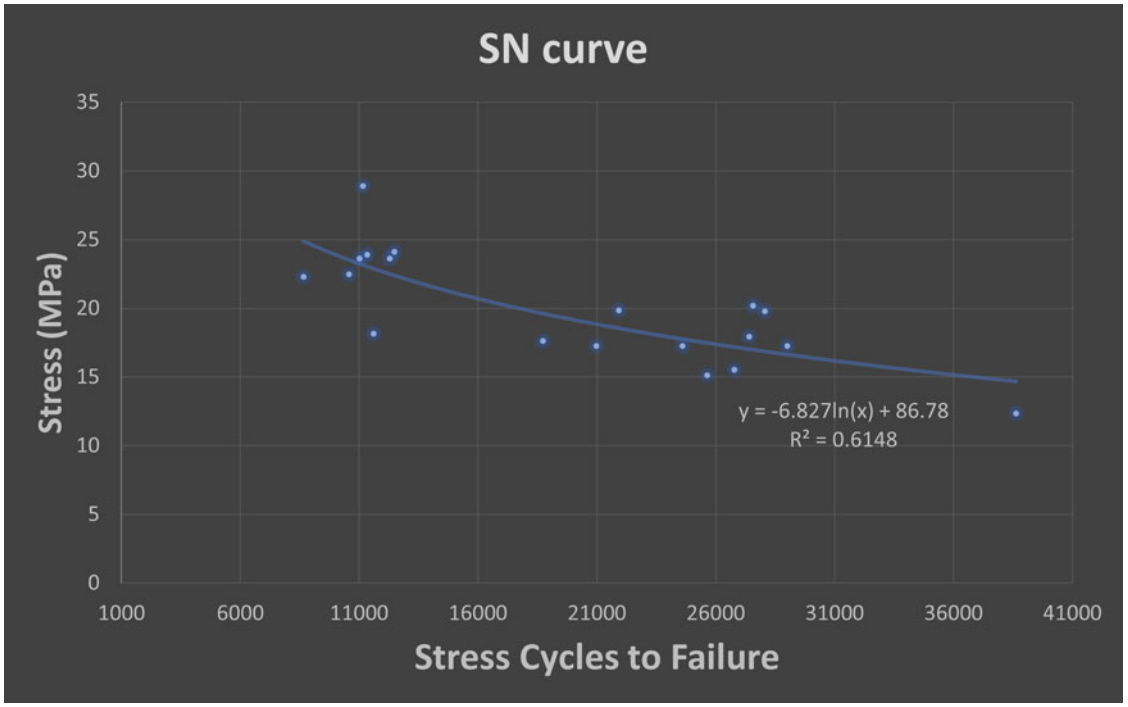

Fig. 1.7 Stress-cycle (SN) curve using simulated stresses garnered from empirical data

test at the other amplitude was calculated by evaluating the total failure time of the test and subtracting the first section's n from that value.

The theoretical N values, however, required far more calculation. For both the starting and ending amplitudes, the base acceleration amplitude was plugged into the equation derived from the acceleration to stress plot in Fig. 1.9:

$$S = 0.0016A - 0.5879 \tag{1.6}$$

In Eq. 1.6 above, S = stress in MPa and A = acceleration in mm/s^2. The acceleration being converted out of g is due to the unit constraints of ABAQUS, as well as to properly achieve stress values in MPa. Once a stress is calculated for each base acceleration amplitude, that stress can be plugged into the mathematical relationship from the SN curve of Fig. 1.8 to achieve theoretical cycles to failure:

$$N = e^{\frac{S-86.78}{-6.827}} \tag{1.7}$$

Note that Eq. 1.7 is in exponential form while the curve of Fig. 1.7 shows a logarithmic relationship. This is because the plot equates to stress, while Eq. 1.7 is shifted to equate for cycles to failure, N. These values of N calculated with this equation are present in the damage table, Table 1.1.

With experimental cycles to failure n and theoretical cycles to failure N available for both amplitudes of the variable tests, Miner's Rule can be used to evaluate damage in these environments.

$$D = \sum_{i=1} \frac{n_i}{N_i} = \frac{n_{\text{start}}}{N_{\text{start}}} + \frac{n_{\text{end}}}{N_{\text{end}}} \tag{1.8}$$

By plugging in all n and N values from Table 1.1 into Eq. 1.8, damage for each test ran can be calculated. As anticipated by the literature regarding variable loading, Miner's Rule underestimates the damage caused by a high to low amplitude loading (seen by $D < 1$) and overestimates damage in low to high loadings ($D > 1$).

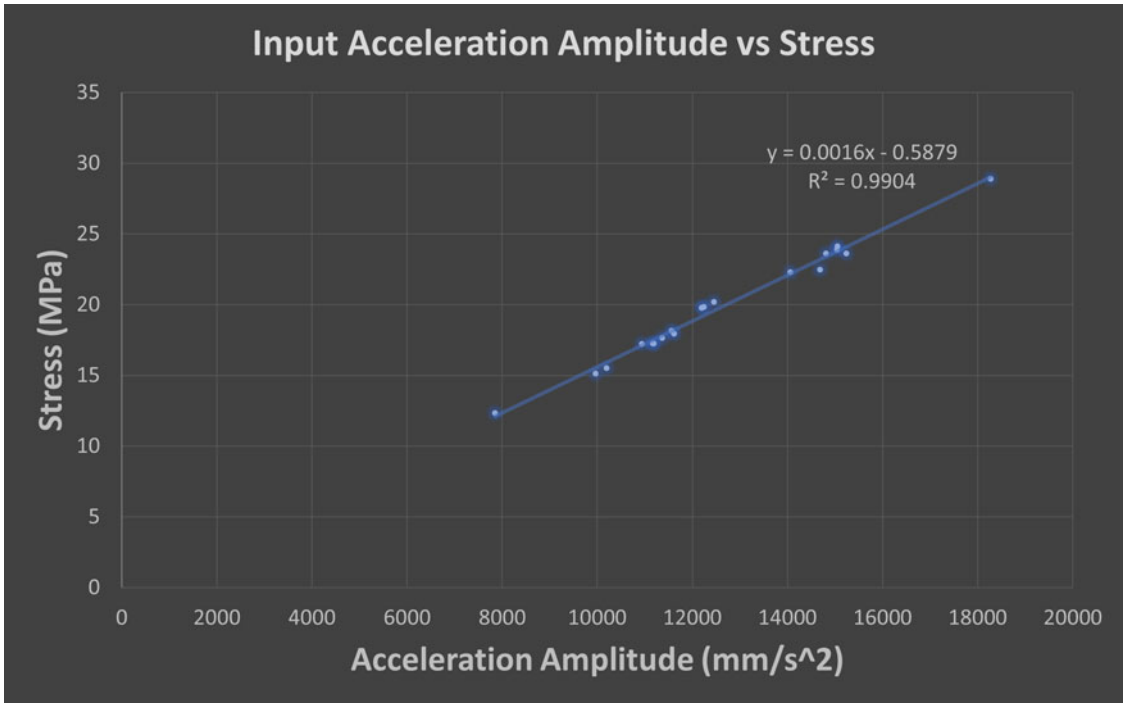

Fig. 1.8 Relationship between input acceleration and stress experienced by parts at failure

Table 1.1 Variable loading damage

	Starting amplitude		Ending amplitude		Damage
	Theoretical *N*	Experimental *n*	Theoretical *N*	Experimental *n*	
High to low loading	13,920	5670	26,757	12,269	0.87
	13,767	5670	26,759	15,574	0.99
	15,246	5670	27,505	13,176	0.85
Low to high loading	32,898	13,122	14,328	11,637	1.21
	33,032	13,122	14,184	15,849	1.51
	21,999	13,122	8362	10,303	1.83

1.3.3 Analysis of Miner's Rule and the Variability of AM Parts

A core motivation of this study was to use simulation and modeling to evaluate Miner's Rule for variable loadings to analyze the inaccuracies in the method in complex systems. The results, though limited in experimental variety, do speak to the expected result that using the simple method of Miner's Rule for damage estimation in complex systems under nonconstant loadings is not accurate enough to be reliable for serious applications. If damage is overestimated, a part will be pulled out of use too early. This wastes a portion of the usable lifespan of the part and in turn wastes the time and money of the engineers who produced the part due to their unnecessary effort spent putting an unneeded new part into circulation. Where this becomes very critical is when damage is underestimated, meaning the part is kept in service beyond its usable life. At this point, there is a severe risk of complete failure of the part while in use, which poses a threat to anyone using or near the part while in service.

The use of simulation and modeling in this study to more easily predict broad features of failure and fatigue in complex environments can, and should, be expanded to further investigate the applications of informing fatigue tests. Engineers who work on projects that require transport or other unstable use environments spend a large portion of their time and resources looking at fatigue testing and potential damage to the parts. While models are already in use for scenarios like this, they are not considered accurate enough to trust over physical data collection and therefore are not used in applications like this study in which purely simulated data is used to predict and inform real testing. In the future, this idea of utilizing models to evaluate fatigue and damage could be applied to less predictable environments like shock and random loading. These tests would provide a more accurate, realistic environment for the parts in use.

A key aspect of this study was the exploration of a material that is not widely studied and has little to no published studies to be found regarding its properties. AM plastic, and all AM materials at that, are still somewhat of a mystery regarding fatigue and failure due to their inherent variability and relative newness as a primary construction material. AM is starting to become quite a large interest to major industries like aerospace and defense who appreciate the manufacturing methods for their precision, ease of bulk production, and ability to be made hollow or latticed to save weight and material. Because of this interest, a further exploration into more materials and more complex failure methods such as the combination of bending and torsion seen in this study would be beneficial.

1.4 Conclusion

While the variability of composition and fatigue behavior in the additively manufactured ABS plastic parts created challenges in evaluating large groups of data, there were still important conclusions that could be drawn. The first is that because of these discrepancies in data, AM fatigue needs to be further evaluated for a variety of materials and failure methods. In this study, 53 vibration tests were run with single parts on the shaker and only 25 were considered to have viable data for analysis. Between this difficulty in testing, the discrepancies seen on the SN curve produced from the data, and the growing interest in AM for production in many industries, it is critical that analysis of the fatigue life and damage of AM parts are evaluated in much further detail. Within the scope of this study, the use of simulation and modeling to predict and inform complex tests such as these would greatly decrease the time and effort spent empirically collecting large amounts of data. If simulation could be better polished to have a near-perfectly validated model and be able to run far larger amounts of data in a short amount of time, the integrity of simulated data would be improved and therefore cause engineers and scientists to be more trusting in allowing modeling to take care of large amounts of data analysis and test prediction. Specifically looking at damage quantification, the methods of simulated modeling used in this study can be expanded to evaluate the efficacy of Miner's Rule in shock and random vibration environments. Even outside the scope of Miner's Rule, simulation has proven to be a viable method for informing test procedures and predicting real-world behaviors and would be useful in analyzing more complex loading environments.

Acknowledgements This research was funded by Los Alamos National Laboratory (LANL) through the Engineering Institute's Los Alamos Dynamics Summer School. The Engineering Institute is a research and education collaboration between LANL and the University of California San Diego's Jacobs School of Engineering. This collaboration seeks to promote multidisciplinary engineering research that develops and integrates advanced predictive modeling, novel sensing systems, and new developments in information technology to address LANL mission-relevant problems. Polyjet 3D printed fatigue parts were provided by Adam Kuiper, W-11 Additive Manufacturing LANL.

References

1. Miner, M.A.: Cumulative damage in fatigue. J. Appl. Mech. **12**(3), 159–164 (1945)
2. Safai, L., Cuellar, J.S., Smit, G., Zadpoor, A.A.: A review of the fatigue behavior of 3D printed polymers. Addit. Manuf. **28**, 87–97 (2019)
3. Head, A.K., Hooke, F.H.: Fatigue of metals under random loads. Nature. **177**(4521), 1176–1177 (1956)
4. Jang, J., Khonsari, M.M.: On the prediction of fatigue life subjected to variable loading sequence. Fatigue Fract. Eng. Mater. Struct. **44**(11), 2962–2974 (2021)
5. Manson, S.S., Halford, G.R.: Practical implementation of the double linear damage rule and damage curve approach for treating cumulative fatigue damage. Int. J. Fract. **17**(2), 169–192 (1981)
6. Henderson, G.R., Piersol, A.G.: Fatigue damage related descriptor for random vibration test environments. J. Sound Vib. **29**(10), 20–24 (1995)
7. Maatman, J.: A study of fatigue damage with application to vibration testing. Blucher Eng. Proc. **2**(1) (2015)
8. Van Baren, J., Van Baren, P., Jenison, M.I.: The fatigue damage spectrum and kurtosis control. J. Sound Vib. **46**(10), 10 (2012)
9. Lalanne, C.: Mechanical Vibration and Shock Analysis, Fatigue Damage, vol. 4. Wiley (2014)
10. Fatemi, A., Yang, L.: Cumulative fatigue damage and life prediction theories: a survey of the state of the art for homogenous materials. Int. J. Fatigue. **20**(1), 9–34 (1998)
11. Angeli, A., Cornelis, B., Troncossi, M.: Synthesis of Sine-on-Random vibration profiles for accelerated life tests based on fatigue damage spectrum equivalence. Mech. Syst. Signal Process. **103**, 340–351 (2018)
12. Ge, C.: Model of accelerated vibration test. Packag. Technol. Sci. **13**, 7–11 (2000)
13. Palanisamy, C., Raman, R.: Additive Manufacturing: A Review on Mechanical Properties of Polyjet and FDM Printed Parts, pp. 1–52. Polymer Bulletin (2021)
14. Kersch, K., Schmidt, A., Woschke, E.: Multiaxial fatigue damage evaluation: A new method based on modal velocities. J. Sound Vib. **476** (2020)
15. Gaberson, H.A., Chalmers, R.H.: Modal velocity as a criterion of shock severity. Shock Vib. **40** (1969)

Chapter 2
Producibility of Time domain Test Specification of Resonant Plate Shock Test

Washington J. DeLima, William Zenk, and Jonathan Hower

Abstract The shock response spectrum (SRS) is commonly used to characterize pyroshock environments created by mechanical impacts and explosives. One limitation is that a single SRS may be computed from different acceleration time histories (time domain signals). As a result, variables from acceleration time histories such as peak amplitude, duration have been introduced as an alternative method to better characterize pyroshock environments. This chapter investigates the producibility of resonant plate test when time domain variables are used as specifications parameters. Time domain variable will be evaluated for various test setup parameters such as plate, projectile weight, and projectile velocity.

Keywords SRS · Time domain · Mechanical shock · Pyroshock · Resonant plate

2.1 Introduction

Components in aerospace systems can be exposed to pyroshock events during their life time and therefore they need to be qualified for these events. Pyroshock tests are usually specified as SRS (shock response spectrum) of the acceleration time domain signal. SRS was initially proposed by Maurice Biot 1933 to evaluate the damage created by earthquake in buildings [1]. The SRS curves are obtained by modeling the device under test (DUT) as a series of single-degree-of-freedom oscillators. Over the years, SRS became the primary method to evaluate pyroshock events. Unfortunately, the method to find SRS curves has limitation since it is a process that guarantees existence of the SRS (give an acceleration: time history data, we can guarantee that there is an SRS associated to this time domain signal). However, it does not guarantee uniqueness in the transformation from acceleration time history data to SRS since more than one time domain signal can have the same SRS [2]. The lack of uniqueness creates problem during components qualification since it is not possible to know what time domain data was used to calculate the specified SRS, and information such as peak amplitude acceleration and duration of the shock event are completely lost.

Laboratory reproduction of pyroshock events is usually obtained by resonant fixtures machines (resonant plate or resonant beam) that simulates pyroshocks by launching a projectile toward the resonant fixture (plate or beam) using a gas gun at a specific firing pressure, and the projectile impact the resonant fixture with a correspondent velocity. The impact of the projectile with the plate/beam excites many structural modes resulting in oscillation of the plate/beam. In this chapter, we focus our attention to resonant plate system (Fig. 2.1). A resonant plate is designed to have a dominant bending mode at certain frequency. A material (programmer) is used at the projectile impact location to control how the impact force is transmitted to the resonant plate to create the pyroshock event. During a test for a given SRS specification and DUT, the operator of the resonant plate machine uses a combination of projectile weight, projective velocity, type of programmer, and resonant plate to achieve the desire SRS curve (Figs. 2.2). Damping bars (Fig. 2.3) can be attached to the plate to add constraint layer damping that helps control the high-frequency response of the plate.

In this chapter, it is evaluated the possibility to introduce acceleration time history parameters such as peak amplitude and duration back into the specification to improve the methods to evaluate pyroshock events by preserving the relation between the original acceleration time history and the specified SRS. The influence of test setup parameters (plate and projectile weight, damping bars and projectile velocity) on the test specification parameters (peak amplitude, duration, and knee frequency) is also investigated. This chapter investigates if for a given test specification that uses peak amplitude,

W. J. DeLima (✉) · W. Zenk · J. Hower
Kansas City National Security Campus, Kansas City, MO, USA
e-mail: wdelima@kcnsc.doe.gov; wzenk@kcnsc.doe.gov; jhower@kcnsc.doe.gov

J. Harvie (ed.), *Dynamic Environments Testing, Volume 7*, Conference Proceedings of the Society for Experimental Mechanics Series, https://doi.org/10.1007/978-3-031-34930-0_2

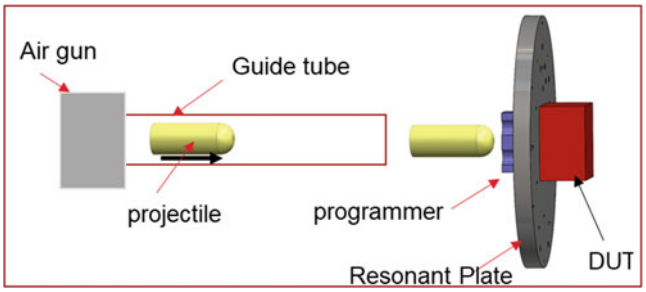

Fig. 2.1 Schematic representation of a resonant plate system used to simulate pyroshocks events

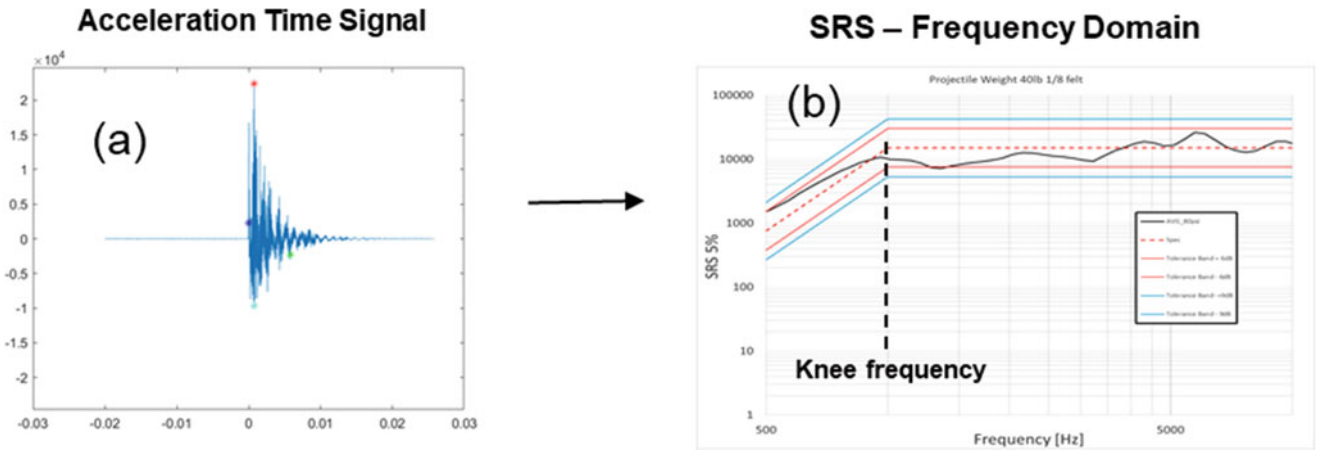

Fig. 2.2 Example of pyroshock acceleration events (**a**) with respective SRS (**b**)

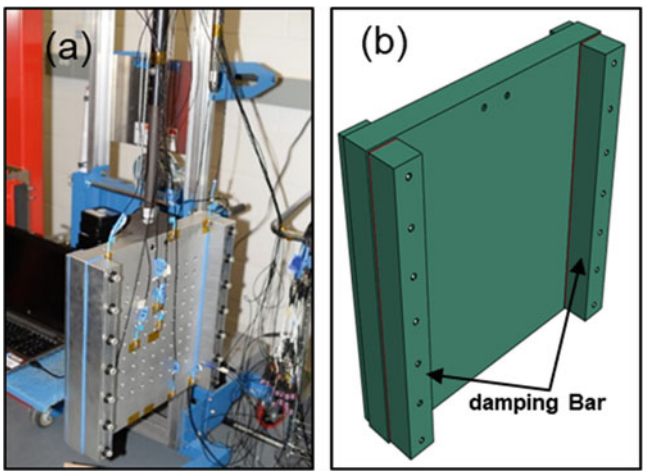

Fig. 2.3 Picture of a resonant plate test setup (**a**) and drawing of a resonant plate (**b**)

duration and knee frequency as specification parameters, it is possible find a resonant plate setup that realizes a shock event that satisfies the specification.

2.2 Definition of the Specification Parameters

Specification of shock events using time domain parameter is proposed as an alternative or addition to existent SRS specification. Peak amplitude and duration of the time event are two parameters commonly used to specify shock events

in the time domain, and they are usually used for classical shock test (haversine, half sine) specification but they are not used for pyroshock events. In addition to peak amplitude and duration, this chapter also investigated the possibility to use knee frequency as specification parameters for pyroshock tests to create a link between time domain and frequency domain information though it is not as time domain parameter.

2.3 Knee Frequency

Knee frequency (f_c) is the frequency in the SRS plot where the slope of the curve changes from positive to zero (Fig. 2.4). This frequency is also the first bending mode of the resonant plate (Fig. 2.5). If another structure such as device under test (DUT) and/or fixture is attached to the plate, the modes of the system (plate + DUT + fixture) will be different from the modes of the plate only. Figure 2.5 shows the bending mode of a resonant plate with free-free boundary conditions without (Fig. 2.5a) and with (Fig. 2.5b) damping bars.

In an SRS obtained experimentally the frequency where the slope change is not as well defined as it is showing in the theoretical curve in Fig. 2.4. Therefore, the definition of how to obtain the knee frequency in an actual SRS curve has to be included as part of test specification.

Two ways to find f_c are investigated in this chapter: (1) knee frequency is the frequency with highest SRS value in the frequency range of the test and (2) knee frequency is the frequency with highest amplitude value from fast Fourier transform (FFT) in the frequency range of the test. For test results as the one presented in Fig. 2.6a, the maximum value of the SRS is well defined, and the knee frequency can be easily found. However, it is possible to occur test whose the maximum SRS value is not well defined, as shown in Fig. 2.6b where there are two frequencies with highest SRS value and consequently two possible values for the knee frequency. Similar conclusion can be met if the maximum amplitude value for the FFT of the signal is used to define knee frequency (Fig. 2.7).

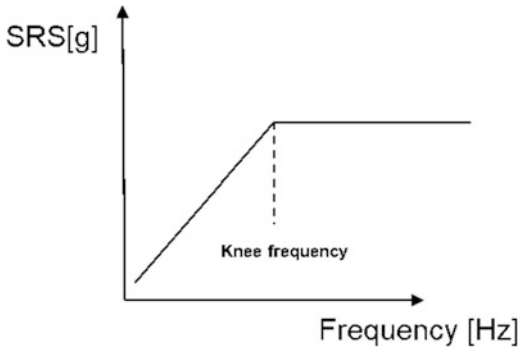

Fig. 2.4 Plot with SRS specification

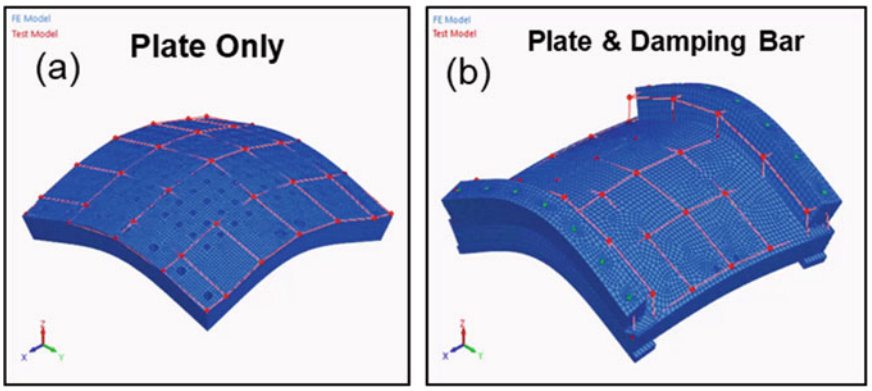

Fig. 2.5 Superposition of experimental and FEM first bending of plate (**a**) without damping bar (1080 Hz) and (**b**) with damping bars (1015 Hz)

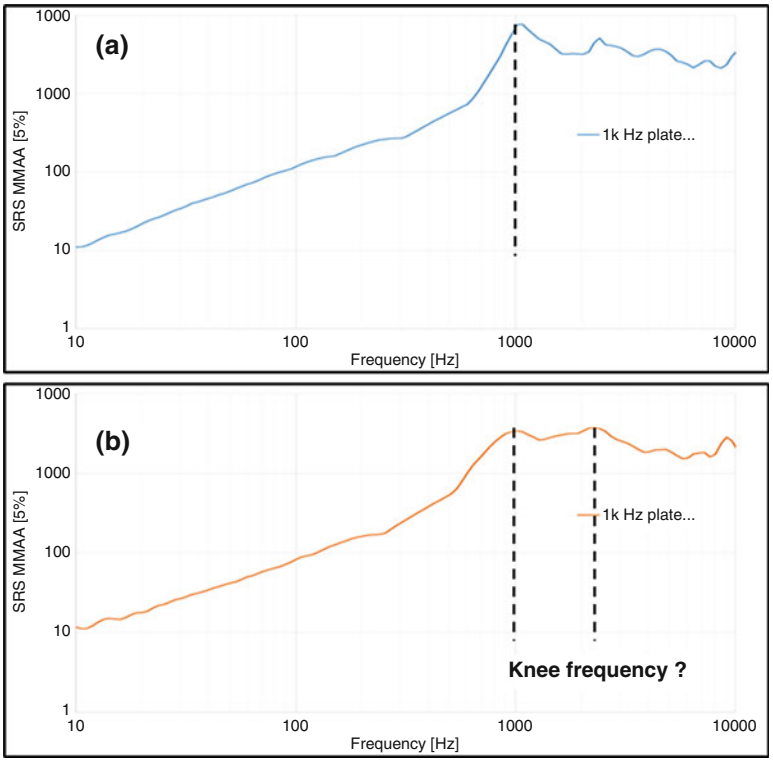

Fig. 2.6 Maximum SRS value method used to find knee frequency. (**a**) Plot of example where maximum SRS defined well the knee frequency. (**b**) Plot of example where maximum SRS failed to define the knee frequency

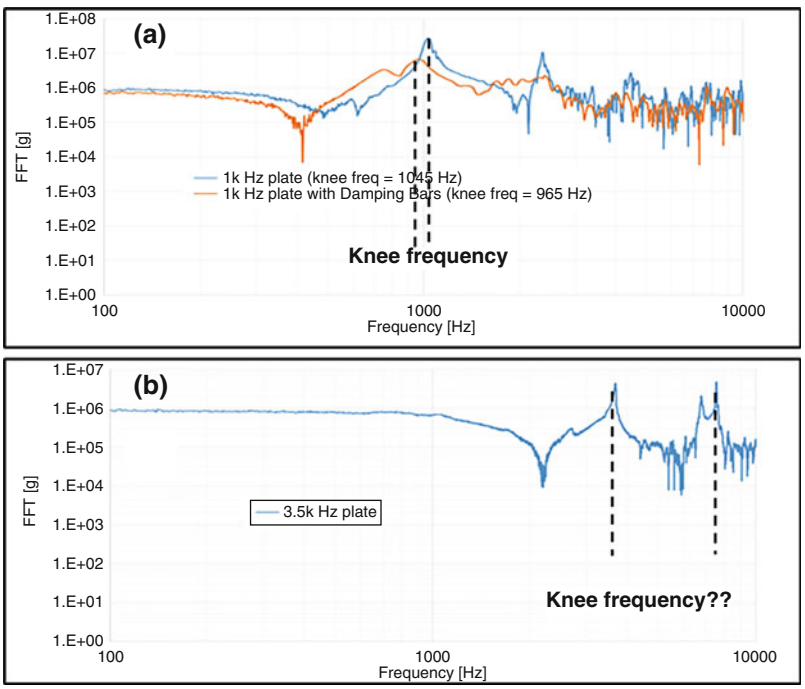

Fig. 2.7 Maximum FFT amplitude value method used to find knee frequency. Plot of example where maximum FFT defined well the knee frequency (**a**). Plot of example where maximum FFT failed to define the knee frequency

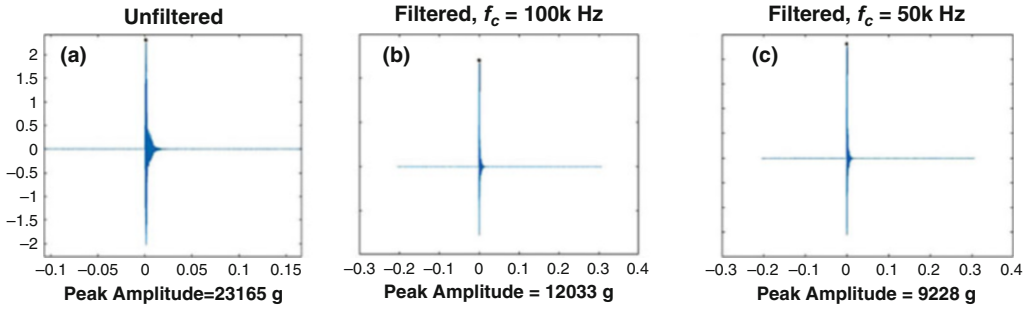

Fig. 2.8 (**a**) Peak amplitude using unfilted signal; (**b**) peak amplitude using $f_c = 100$ k Hz to faired the signal; (**c**) peak amplitude using $f_c = 50$ k Hz to faired the signal

2.4 Peak Amplitude

Peak amplitude is defined as the maximum absolute value of the faired acceleration time signal. The faired acceleration is found by applying a low pass filter with cutoff frequency *fc* to eliminate unrealistic peak amplitudes due to internal resonance of the accelerometer used in the test. As seen in Fig. 2.8, the peak amplitude is a function of the f_c, and it gets lower as the value of f_c is reduced. Note that actual force transmitted to the part by the impact of the projectile is a function of the projectile weight and velocity (acceleration) before hitting the plate and the programmer used in the test (Fig. 2.1). Therefore, all the three plots in Fig. 2.8 are results from the same test with different representation of the peak amplitude.

2.5 Duration

Duration of a shock signal is the effective length of the shock pulse. It is a measurement of the energy of the signal is first above zero (beginning of the shock) to the time the energy return to zero. This definition is easy to understand, but its application to actual test signals is not straightforward since the signal from actual test contains noise inherent to measurement. Sisemore and Babuska [2] give a good insight into this problem and present different definition of duration used in Mil-STD-810G. In this chapter, we will just present actual data showing how the definition of duration affects the interpretation of the data.

The two most common definitions of shock duration are as follows: Method 1: duration is defined as the time between the first and last 10% of the peak amplitude (Fig. 2.9); Method 2: the duration is defined as the interval between the first time the signal is above the noise floor and subsequent first time the signal returns to noise floor values (Fig. 2.10). Method 1 definition represents the time the signal raises up and decay relative to its peak amplitude. Note then that in this case duration is a function of the peak amplitude. Method 2 is independent of the peak amplitude, but it depends on the definition of noise floor. It is clear that the choice of method affects the physical interpretation of how long the event lasts.

2.6 Methodology and Analysis

In order to investigate the influence of test setups on the test results of time domain specification parameters, a sequence of tests was performed with the following constraints:

- Two resonant plates: plate 1 has a knee frequency of 1 kHz and a weight of 100 lb., and plate 2 has 3a knee frequency of .5 kHz and a weight of 130 lb.
- Projectile weight [lb.]: 20 and 40.
- Firing pressure [psi]: 20 and 60.
- Each test was repeated twice (repeatability test).
- Programmer: ¼" felt (replaced every test).
- Faired data filter: low pass filtered 50 kHz.

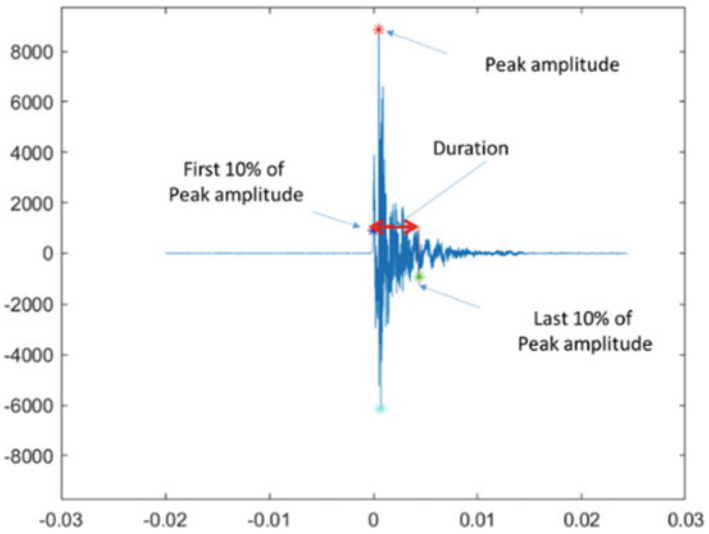

Fig. 2.9 Duration defined as the time between the fist 10% and last 10% of the peak amplitude

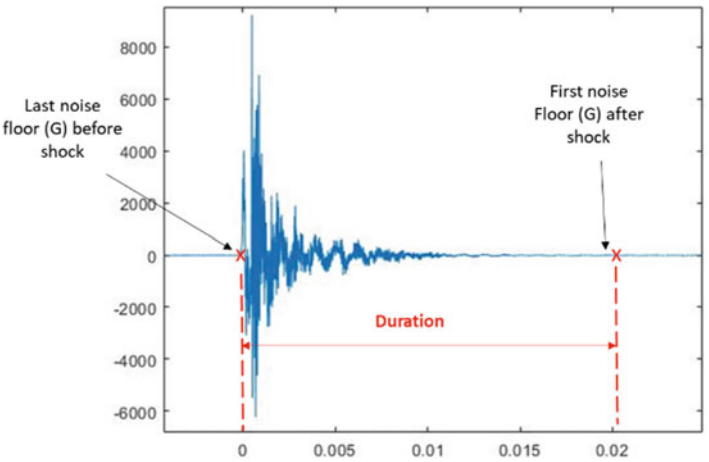

Fig. 2.10 Duration defined as the time between the last noise floor value before the shock and the first noise floor value after the shock

- Knee frequency was calculated by finding the frequency with maximum FFT values in the frequency range [100 Hz to 10 kHz].
- Duration was calculated using first and last 10% of peak amplitude (method 1).
- Each test was repeated twice (repeatability test).

The projectile velocities for each firing pressure were measured. 20 lb. projectile fired at 20 psi and 60 psi reaches impact velocities of 22 fps and 49 fps, respectively, and 40 lb. projectile fired at 20 psi and 60 psi reaches impact velocities of 16 fps and 34 fps, respectively. Table 2.1 shows the test sequence for both plates. Tables 2.2 and 2.3 present the results for tests with plate 1 (1 kHz plate) and plate 2 (3.5 kHz plate), respectively. The last three columns of Tables 2.2 and 2.3 show the repeatability variation for each test. In the repeatability tests, the operator did the best to maintain the same setups, but there is not anyway to prove that the setups were exactly the same and that there was no operator error. At least the setups investigated in this chapter (Table 2.1), the knee frequency and peak amplitude, show the lowest and highest repeatability variations, respectively.

As shown in Tables 2.2 and 2.3 show, a variation in the repeatability of 31%, 50%, and 51% was observed for peak, duration, and knee frequency, respectively, depending on the test setup. Figure 2.11 show the SRS plots up to 10 k Hz for tests 13 and 15 in Table 2.3 that corresponds to the repeatability tests with plate 2 (3.5 kHz plate), projectile weight 40 lb. and projectile velocity 16 fps. Figure 2.11a shows that the SRS is essentially the same up to 10 kHz, even though there is reasonable repeatability variation for peak, duration, and knee frequency values, while Fig. 2.11b shows that a great difference in SRS levels was observed as the frequency increases, which suggests that the content in high frequency is

Table 2.1 Test sequence

Test #	Projectile	Air gun pressure [psi]	Projectile velocity [fps]	Test repetition #	Damping bar
1	20	20	22	1	YES
2	20	20	22	2	YES
3	20	60	49	1	YES
4	20	60	49	2	YES
5	40	20	16	1	YES
6	40	20	16	2	YES
7	40	60	34	1	YES
8	40	60	34	2	YES
9	20	20	22	1	NO
10	20	20	22	2	NO
11	20	60	49	1	NO
12	20	60	49	2	NO
13	40	20	16	1	NO
14	40	20	16	2	NO
15	40	60	34	1	NO
16	40	60	34	2	NO

Table 2.2 Test results for plate 1 (1 kHz)

Test #	Projectile	Firing Pressure [psi]	Projectile Velocity [fps]	Test Repetition	Damping Bar	Peak	Duration	Knee Freq	Peak Variation [%]	Duration Variation [%]	Knee Freq Variation [%]
1	20	20	22	1	YES	8863	**4.35**	955	4	**50**	2
2	20	20	22	2	YES	9229	**2.90**	973			
3	20	60	49	1	YES	21971	**2.56**	949	0	**11**	1
4	20	60	49	2	YES	21964	**2.89**	955			
5	40	20	16	1	YES	**1954**	7.72	975	**14**	6	1
6	40	20	16	2	YES	**1710**	8.23	963			
7	40	60	34	1	YES	**12091**	**4.18**	947	**12**	**11**	0
8	40	60	34	2	YES	**13675**	**4.70**	949			
9	20	20	22	1	NO	11100	11.59	1033	8	0	0
10	20	20	22	2	NO	12016	11.60	1033			
11	20	60	49	1	NO	**25708**	8.03	1035	**31**	5	0
12	20	60	49	2	NO	**37203**	7.68	1035			
13	40	20	16	1	NO	2663	16.95	1035	5	3	0
14	40	20	16	2	NO	2805	17.52	1033			
15	40	60	34	1	NO	**15970**	10.15	1031	**13**	0	0
16	40	60	34	2	NO	**18284**	10.16	1033			

responsible for the difference in peak amplitude (35% variation). Figure 2.12 shows the amplitude FFT for test 13 (a) and 14 (b) of Table 2.3, where it shows that the maximum value of the amplitude FFT shift from 3674 Hz to 7547 Hz given two knee frequencies for the same test setup and test 14 (Fig. 2.12b) give an erroneous value since the plate used has 3.5 kHz bending mode. The high-frequency content also affects the duration because it changes the shape of the acceleration time history. However, as seen in Fig. 2.13 higher high-frequency content does not necessary translate in higher duration.

Tests 13 and 14 in Table 2.2, that correspond to a repetition test with plate 1 (1.0 kHz plate), projectile weight of 40 lb., and projectile velocity of 16 fps, present the lowest repeatability variation. By plotting the SRS for these tests (Fig. 2.14), it can be seen that there is very small variation between the SRS even in high frequency, which reinforces the idea that high-frequency contents can tell how similar the parameters of the acceleration time history of the tests are.

Table 2.3 Test results for plate 2 (3.5 kHz)

Test #	Projectile	Firing Pressure [psi]	Projectile Velocity [fps]	Test Repetition	Damping Bar	Peak [g]	Duration [ms]	Knee Freq	Peak Variation [%]	Duration Variation [%]	Knee Freq Variation [%]
1	20	20	22	1	YES	**2179**	4.08	3586	**23**	0	0
2	20	20	22	2	YES	**2815**	4.08	3582			
3	20	60	49	1	YES	9997	3.73	3545	9	0	0
4	20	60	49	2	YES	11020	3.73	3537			
5	40	20	16	1	YES	**1393**	**5.26**	7561	**30**	**35**	0
6	40	20	16	2	YES	**1997**	**3.91**	7561			
7	40	60	34	1	YES	**3250**	4.81	7551	**27**	3	0
8	40	60	34	2	YES	**2567**	4.68	7553			
9	20	20	22	1	NO	**2949**	12.00	3592	**10**	6	0
10	20	20	22	2	NO	**3272**	11.30	3594			
11	20	60	49	1	NO	**22831**	7.11	3529	**20**	0	0
12	20	60	49	2	NO	**18949**	7.10	3533			
13	40	20	16	1	NO	**1603**	**10.86**	**3674**	**35**	**31**	**51**
14	40	20	16	2	NO	**2475**	**8.27**	**7545**			
15	40	60	34	1	NO	**3163**	10.10	3604	**20**	6	0
16	40	60	34	2	NO	**3979**	9.53	3604			

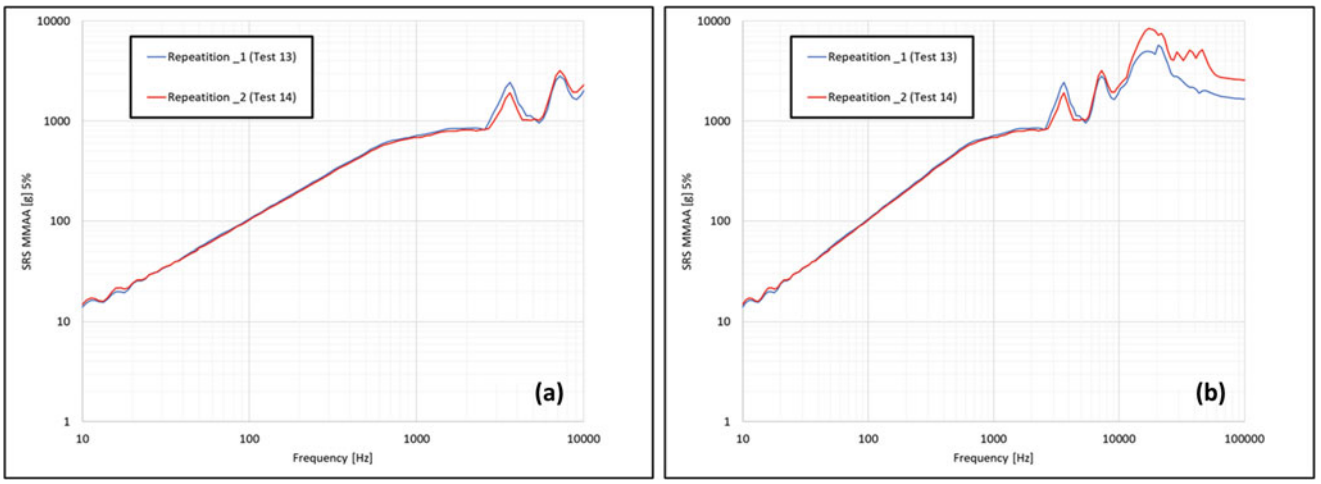

Fig. 2.11 SRS plots for test 13 and test 14 in Table 2.3. (**a**) SRS up to 10 kHz and (**b**) SRS up to 100 kHz

2.7 Conclusion

This chapter evaluates the application of time domain variables for test specification of pyroshocks events. Three variables were investigated (peal amplitude, duration, and knee frequency). The influence of test setup in the results for these variables was obtained from a sequence of test with different test setups. High test-to-test variation from same setup can occur and it is caused by the high-frequency content of the signal.

The addition of time domain variable into the SRS specification for pyroshock tests can help preserve the relation between the SRS and its original time event. However, the realization of these events in a resonant plate machine can be compromised by the lack of setup parameter that can control the SRS curves, time domain variables, and high repeatability variation.

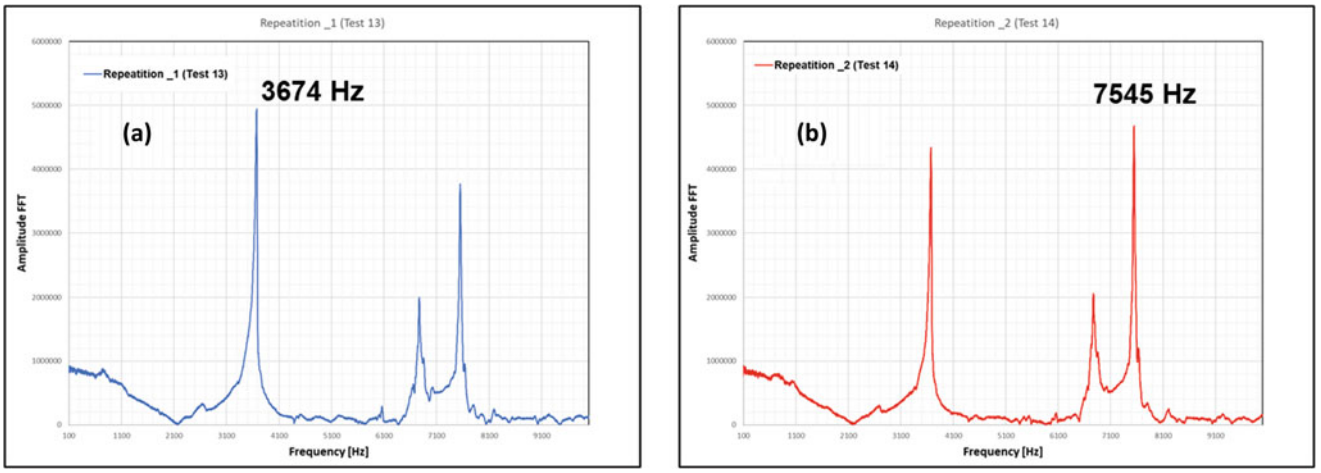

Fig. 2.12 FFT plots for test 13 (**a**) and test 14 (**b**) in Table 2.3

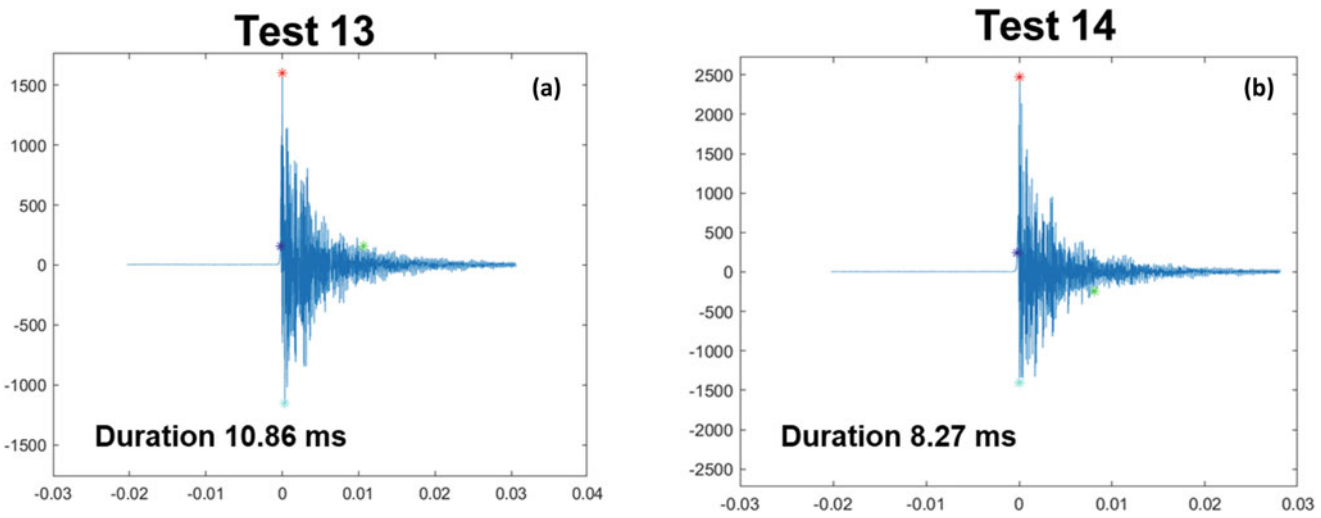

Fig. 2.13 Acceleration time history for test 13 (**a**) and test 14 (**b**) in Table 2.3

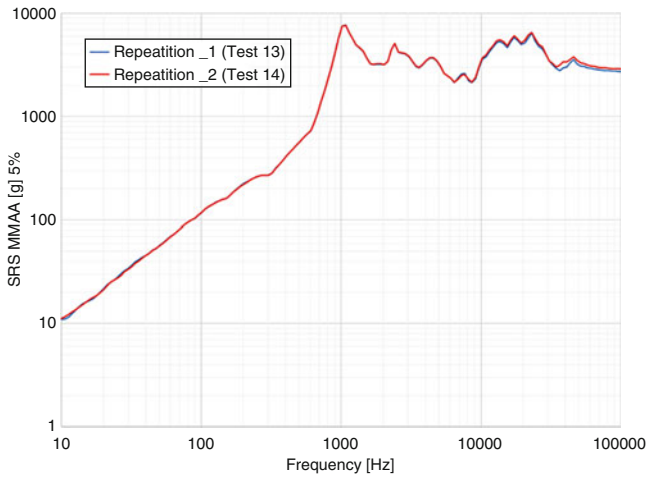

Fig. 2.14 SRS plots test 13 (**a**) and test 14 (**b**) in Table 2.2

Acknowledgements The authors gratefully acknowledge the Department of Energy's Kansas City National Security Campus, operated by Honeywell Federal Manufacturing & Technologies LLC, for funding this work under contract number DE-NA0002839.

References

1. Biot, M.A.: Theory of elastic systems vibrating under transient impulse with application to earthquake-proof building. Proc. Natl. Acad. Sci. **19**(2), 262–268 (1933)
2. Sisemore, C., Babuska, V.: The Science and Engineering of Mechanical Shock. Springer (2020)
3. Lalanne, C.: Mechanical Shock – Mechanical Vibration and Shock Analysis, vol. 2, 3rd edn. Wiley

Chapter 3
A Method to Expand Sparse Set Acceleration Data to Full Set Strain Data

Jonathan Hower, Raymond Joshua, and Tyler Schoenherr

Abstract Expansion methods are commonly used to compute the response at locations not measured during physical testing. The System Equivalent Reduction Expansion Process (SEREP) produces responses at finite-element degrees of freedom through the mode shapes of that model. Measurements used for expansion are often acceleration, strain, and displacement and operate only on like sets of data. For example, expanding acceleration data produces only additional acceleration data and does not provide insight into the test article's stress or strain state. Stress and strain are often desired to evaluate yield limits and create fatigue models. The engineer may have acceleration measurements available but desire a component's stress and strain state. This chapter evaluates a physical experiment from which acceleration is measured and a full set of strain, stress, and displacement data is obtained through SEREP and integration. Honeywell Federal Manufacturing & Technologies, LLC, operates the Kansas City National Security Campus for the United States Department of Energy/National Nuclear Security Administration under Contract Number DE-NA0002839.

Keywords SEREP · Expansion · Acceleration · Strain

3.1 Introduction

System Equivalent Reduction Expansion Process (SEREP) was initially developed by O'Callahan [1] as a global mapping technique to estimate rotational degrees of freedom (DOFs) for experimental modal data. Since inception, it has been used for multiple applications. One early application of the process involved model reduction to reduce large analytical models when performing correlation studies between a model and physical experiment. Recent applications of SEREP involve expanding a sparse set of measurements from a physical test to a full set by the mode shapes of a finite-element model [2, 3]. The goal of this effort is to compute the stress and strain states of a component under dynamic loads using only acceleration measurements and a finite-element model. Although this method is valid for both stress and strain, only strain results are presented because there are no means to directly measure stress state.

A simple physical test structure was created, known as the bobble head, and represents a cantilever beam with a mass at the tip. The structure was placed on an electrodynamic shaker and subjected to a multi-axis random vibration load. A set of accelerometers were placed about the structure to measure response and are used for strain computation. A set of strain

J. Hower (✉) · R. Joshua
Honeywell Federal Manufacturing & Technologies, Kansas City, MO, USA
e-mail: jhower@kcnsc.doe.gov; rjoshua@kcnsc.doe.gov

T. Schoenherr
Sandia National Laboratories, Albuquerque, NM, USA
e-mail: tfschoe@sandia.gov

J. Harvie (ed.), *Dynamic Environments Testing, Volume 7*, Conference Proceedings of the Society for Experimental Mechanics Series, https://doi.org/10.1007/978-3-031-34930-0_3

gauges were placed about the structure for validation of the proposed strain estimation method. These measured strains were not used in the strain estimation process.

An uncalibrated finite-element model was created, and all modes in the frequency band of interest were computed. The acceleration measurements were expanded through SEREP with the finite-element mode shapes and compared to the measured data for verification. Displacements were estimated by integrating and filtering the measured accelerations. These estimated displacements were then expanded through SEREP. The expanded displacement data were then converted into strain data by performing a linear transformation through the finite-element model. Finally, the expanded strains were compared to the strains measured during the physical test.

3.2 Background Theory

3.2.1 Expansion Method

This chapter applies SEREP as introduced by O'Callahan [1]. In the literature, SEREP has been performed on accelerations, displacements, and strains [2–4]. The equation for SEREP is shown as Eq. 3.1 and is performed by expanding a sparse set, $\overline{x}_a$, to a full set, $\overline{x}_n$, by performing a linear transformation through the transformation matrix, T. The transformation matrix is a function of the full, ϕ_n, and sparse, ϕ_a, mode shape matrices as shown in Eq. 3.2. The superscript ^{g} indicates the generalized inverse and is shown in Eq. 3.3.

$$\overline{x}_n(t) = T\overline{x}_a(t) \tag{3.1}$$

$$T = \phi_n {\phi_a}^g \tag{3.2}$$

$$\phi^g = (\phi^\top \phi)^{-1}\phi^\top. \tag{3.3}$$

3.2.2 Estimating Displacement from Acceleration

Displacement was estimated from accelerometer data by integration and bandpass filtering. Acceleration data were integrated twice via cumulative trapezoidal numerical integration. Prior to integration, data were filtered with a fifth-order Butterworth bandpass filter. The proposed approach is displayed visually in Fig. 3.1. It is thought that filtering out low-frequency response reduced the effect of drift when double integrating and filtering out high-frequency response reduced integration errors due to high frequency noise in the signal. The bandpass frequencies were set to 50 and 2000 Hz. Multiple techniques exist in the

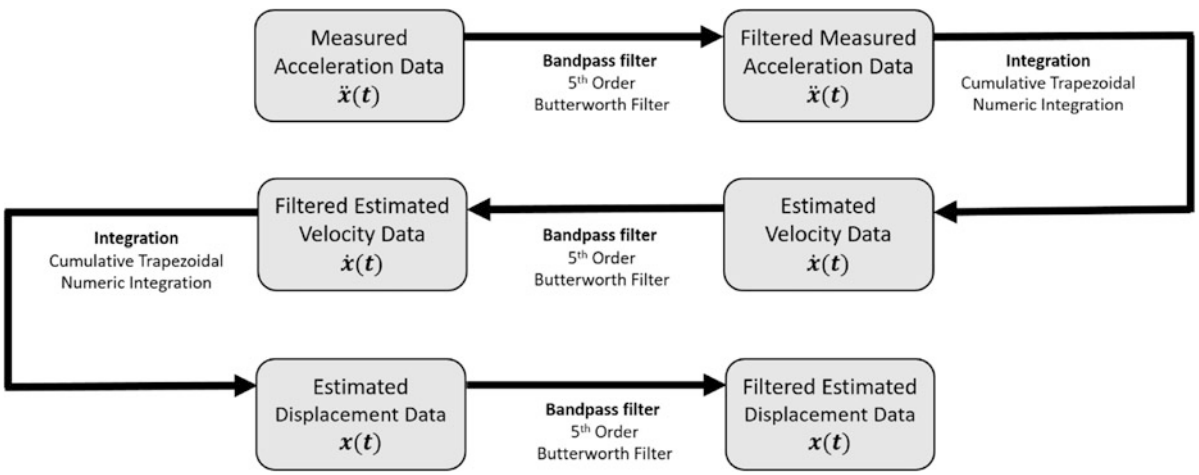

Fig. 3.1 Method to estimate displacement from acceleration

literature to estimate displacement from acceleration. The proposed technique is a simple approach to estimate displacement when compared to other methods [5, 6]. No displacement measurements were taken, so the accuracy of the proposed approach cannot be directly validated. Instead, the estimate is verified by a differentiating process as described in Sect. 3.2.4.

3.2.3 Transformation of Displacement into Stress and Strain

Generally, a set of DOF responses at a point in time, $\overline{\alpha}(t)$, may be written as a function of its mode shape matrix, ϕ, and a modal weighting vector, $\overline{P}(t)$ shown as Eq. 3.4.

$$\overline{\alpha}(t) = \phi \overline{P}(t). \tag{3.4}$$

Particularly, these DOFs may be defined as displacement, strain, and stress vectors shown in Eqs. 3.5, 3.6, and 3.7, respectively.

$$\overline{x}(t) = \phi \overline{P}(t), \tag{3.5}$$

where $\overline{x}(t)$ is the displacement vector at time, t, ϕ is the displacement mode shape matrix, and $\overline{P}(t)$ is the modal weighting vector at time, t.

$$\overline{\varepsilon}(t) = \phi_\varepsilon \overline{P}(t), \tag{3.6}$$

where $\overline{\varepsilon}(t)$ is the strain vector at time, t, ϕ_ε is the strain mode shape matrix, and $\overline{P}(t)$ is the modal weighting vector at time, t.

$$\overline{\sigma}(t) = \phi_\sigma \overline{P}(t), \tag{3.7}$$

where $\overline{\sigma}(t)$ is the stress vector at time, t, ϕ_σ is the stress mode shape matrix, and $\overline{P}(t)$ is the modal weighting vector at time, t.

For displacements, strains, and stresses, it holds true that the modal weighting vector, $\overline{P}(t)$, is constant. Therefore, Eqs. 3.6 and 3.7 may be written in terms of the displacement vector, the displacement mode shape matrix, and their respective mode shape matrices. Solving for the strain vector yields Eq. 3.8, and solving for the stress vector yields Eq. 3.9.

$$\overline{\varepsilon}(t) = \phi_\varepsilon \phi^g \overline{x}(t) \tag{3.8}$$

$$\overline{\sigma}(t) = \phi_\sigma \phi^g \overline{x}(t). \tag{3.9}$$

3.2.4 Verification Metrics

Modal Projection Error

The modal projection error (MPE), introduced by Schoenherr [7], provides insight on how well one set of mode shapes can be projected onto another set of mode shapes. For this research, it will indicate the model's ability to represent the measured data at some instance in time. For example, if a linear combination of the mode shapes computed from the finite-element model can properly represent the measured response at an instance in time, the MPE will be low. The equation for MPE as derived by Schoenherr [8] is shown as Eq. 3.10.

$$MPE(t) = 1 - \overline{X}_a(t)^g \phi_a \phi_a{}^g \overline{X}_a(t). \tag{3.10}$$

Double Differentiation

The estimated displacements cannot be directly compared to the physical displacements because there was no direct displacement measurement of the test hardware under load. In order to verify the displacement estimation, the estimated

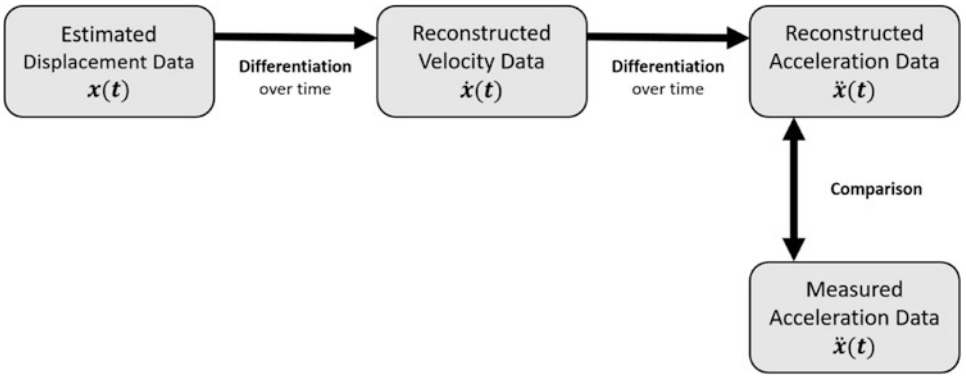

Fig. 3.2 Method to verify estimated displacements from reconstructed acceleration

displacements over time were differentiated twice to compute a reconstructed acceleration. This reconstructed acceleration was then compared to the measured acceleration. The workflow of this process is shown in Fig. 3.2.

3.2.5 Error Metrics

Multiple error metrics were used to evaluate the efficacy of the acceleration expansion and strain estimation methods. The values $\overline{X}$ may represent acceleration or strain data. The subscript $_{meas}$ represents data that have been physically measured, while $_{pred}$ represents data that were predicted through analysis. The subscripts $_t$ and $_f$ represent time-domain and frequency-domain data, respectively. The numbers of values in the time- and frequency-domain data sets are represented by n_t and n_f, respectively. For all frequency-domain error metrics, the power spectral density (PSD) values were used. PSDs were computed via Welch's method with a 50% overlap, a Hamming window, and a total of seven averages. Supplementary error metrics are introduced in Appendix 3.

Root Mean Square

The root mean square (RMS) values are used as error metrics and computed in both the time and frequency domains. The time-domain RMS value is computed by Eq. 3.11. The frequency-domain RMS, often called g_{RMS} for acceleration data, is the square root of the area under the PSD vs. frequency curve and was computed per Irvine [9].

$$RMS_{time} = \sqrt{\frac{1}{n_t}\sum_t |\overline{X}_t|^2}. \tag{3.11}$$

Mean Absolute Error

The mean absolute error (MAE) compares two signals by averaging the absolute values of the data set. It may be computed in the time or frequency domain, as shown in Eq. 3.12 and 3.13, respectively. A low MAE indicates good agreement between measured and predicted values.

$$MAE_{time} = \frac{1}{n_t}\sum_t |\overline{X}_{t,meas} - \overline{X}_{t,pred}| \tag{3.12}$$

$$MAE_{freq} = \frac{1}{n_f}\sum_f |\overline{X}_{f,meas} - \overline{X}_{f,pred}|. \tag{3.13}$$

3.3 Proposed Method

The goal of this chapter is to define and evaluate a process to compute full set stress and strain data from sparse accelerometer measurements. As stated, this chapter focuses on strain data because stress cannot be measured physically. The steps in the process are described below and visually displayed in Fig. 3.3.

The bobble head was subjected to random vibration loading. On the structure, a sparse set of acceleration data was collected for strain estimation and a sparse set of strain data was collected for validation. Next, sparse displacements were estimated through integration and filtering as described in Sect. 3.2.2. The sparse displacements were then expanded through SEREP, Eq. 3.1, and converted into strains through a linear transformation, Eq. 3.8. Displacement and strain mode shape matrices were computed from a finite-element model. The estimated strains were then compared to measured strains at sparse locations as described in Sect. 3.2.5. Additionally, sparse accelerations were expanded and compared in the same manner as described above. Acceleration expansion was performed to verify the expansion process prior to strain estimation.

There are a few limitations of this approach worth noting. First, the strain estimate is sensitive to the filter frequencies because it suffered from significant drift in the displacement estimation when the high-pass filter was not used. This error is created when estimating displacements and is carried through the entire process ultimately affecting the strain estimate. Second, the accuracy of the displacement estimate is not known because there was no direct measurement of displacement on the physical structure under load. Last, the accuracy of the finite-element mode shapes used for expansion and strain estimation is not known because experimental modal analysis on the physical test structure was not performed.

3.4 Physical Test Hardware and Environment

The bobble head represents a cantilever beam with a large mass at the tip. The structure is comprised of a base plate ($6'' \times 6'' \times 0.375''$), beam ($0.375'' \times 0.5'' \times 3.125''$), and block ($2'' \times 2'' \times 2''$). All components are made from aluminum and are mechanically fastened via bolts. For this test, the bobble head was mounted to an electrodynamic shaker as shown in Fig. 3.4.

The bobble head was subjected to a multi-axis random vibration loading. The test profile had a target of 3 g_{rms} for all axes and was controlled to 2 kHz. All data were filtered via a 5th-order Butterworth filter with bandpass frequencies of 50 and 2000 Hz. The bobble head was instrumented with ten triaxial accelerometers distributed about the base plate and block

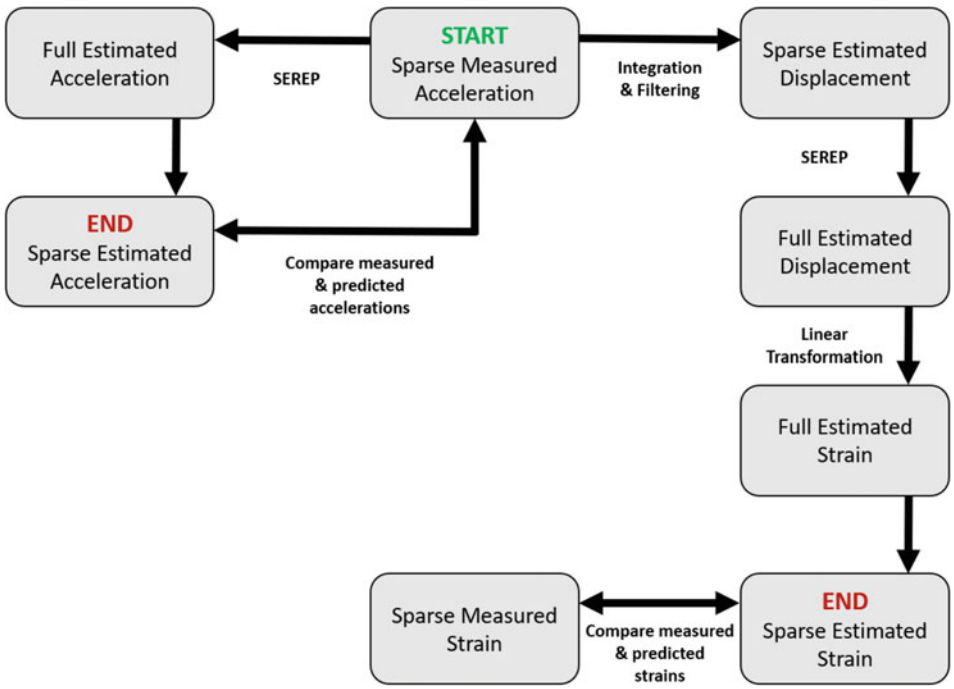

Fig. 3.3 Workflow for acceleration expansion and full set strain estimation from sparse set acceleration data

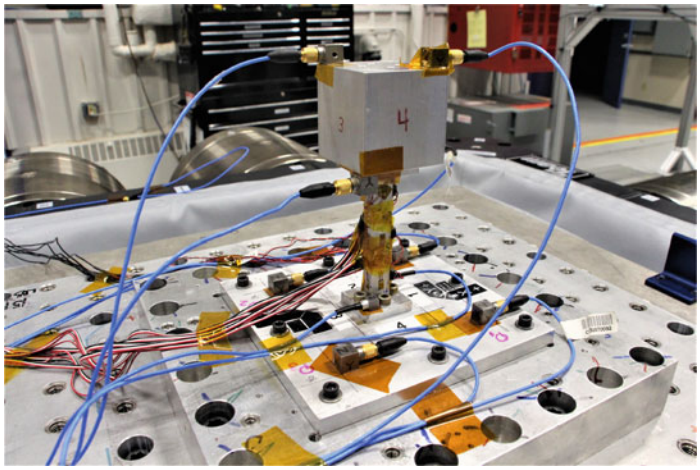

Fig. 3.4 Instrumented bobble head test structure mounted atop electrodynamic shaker

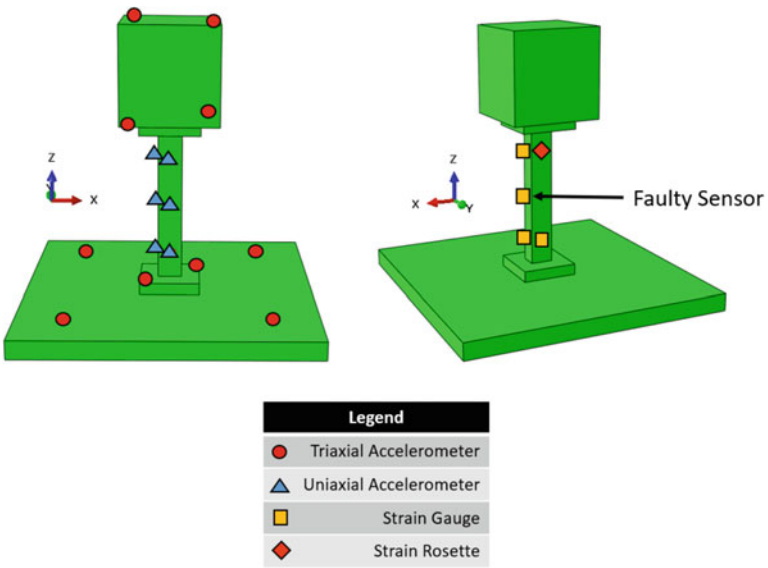

Fig. 3.5 Accelerometer and strain gauge locations during physical testing

and six uniaxial accelerometers distributed about the beam. Five strain gauges and one strain rosette were distributed along the beam. One of the strain gauges recorded poor data and was not used for this analysis. The locations of all instrumentation used for analysis are shown in Fig. 3.5.

When performing expansion about the entire structure, it was discovered that the twelve measured DOFs at the base had overall much lower accuracy than other locations. The DOFs used in the expansion are shown in Fig. 3.6. Section 3.6 studies the effect of including and excluding the twelve base DOFs.

3.5 Finite-Element Model

A finite-element model of the bobble head was created. The base, beam, and block were modeled as nominal dimensions of the test hardware. Aluminum material properties were assigned to all components with a modulus of elasticity of $10(10^6)$ psi and a density of 0.098 $\frac{lb}{in^3}$. A continuous mesh was used, meaning that components were completely tied at contact surfaces. The bolts and sensors were not modeled. The lower surface of the base of the structure was constrained in all 6 DOFs as shown in Fig. 3.7. The model consisted of 231,282 linear hexahedral elements and is shown in Fig. 3.8. A fine mesh on the beam was used to improve stress and strain computations of this component.

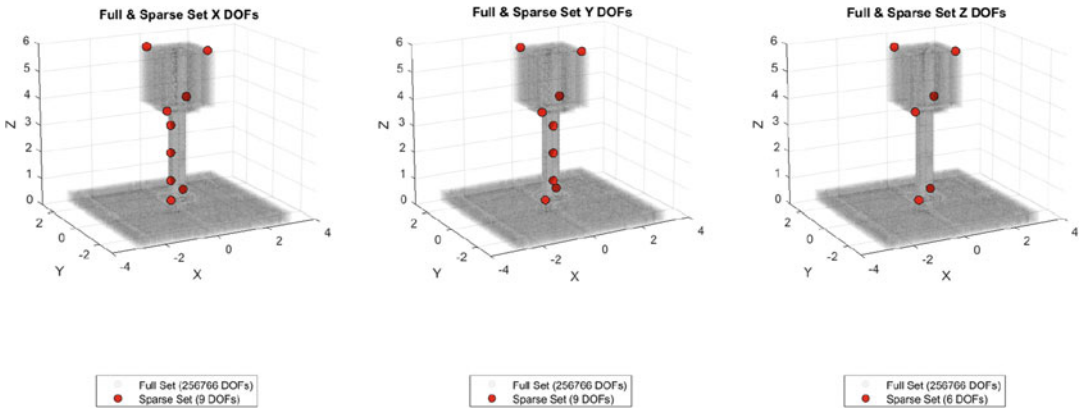

Fig. 3.6 Sparse and full set of each independent direction used for SEREP

Fig. 3.7 Finite-element model boundary condition highlighted in red and constrained in 6 DOFs

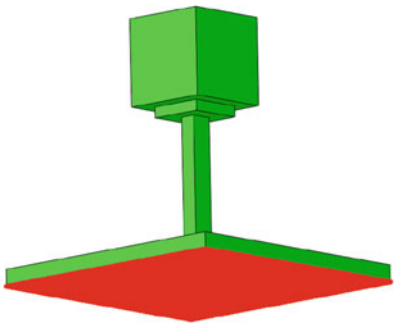

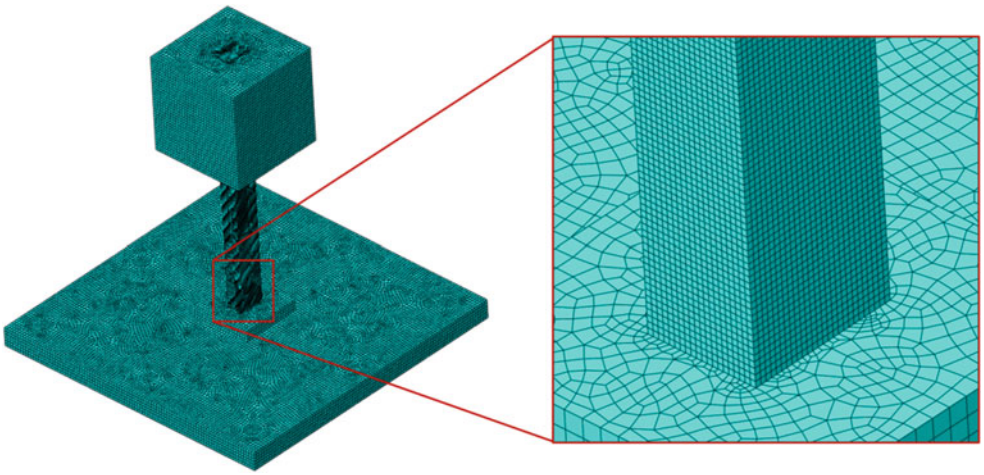

Fig. 3.8 Geometry and mesh of finite-element model

A total of 12 modes were used for expansion including 6 rigid body and 6 flexible modes. These modes were selected because they align with the frequency band of the test. The test was controlled to a maximum frequency of 2 kHz, and the frequency of the highest mode in the model was 2.46 kHz. The flexible displacement mode shapes and natural frequencies are shown in Appendix 1, and the flexible strain mode shapes and natural frequencies are shown in Appendix 2.

3.6 Verification

3.6.1 Modal Projection Error

The modal projection error was computed from Eq. 3.10 for two potential sparse data sets for expansion. It was computed from measured accelerometer data and the 12 finite-element displacement mode shapes described in Sect. 3.5. The first set contained all accelerometer data from the test for a total of 36 responses. The second set contained all accelerometer data except for the twelve base DOFs associated with the base plate for a total of 24 responses. The DOFs for these sets are shown in Fig. 3.9. The modal projection error associated with each data set is shown in Fig. 3.10. The second data set with excluded base DOFs was used for strain estimation because it had lower average modal projection error. An explanation for the higher MPE in the first set is because the boundary condition assigned to the model overconstrains the base DOFs.

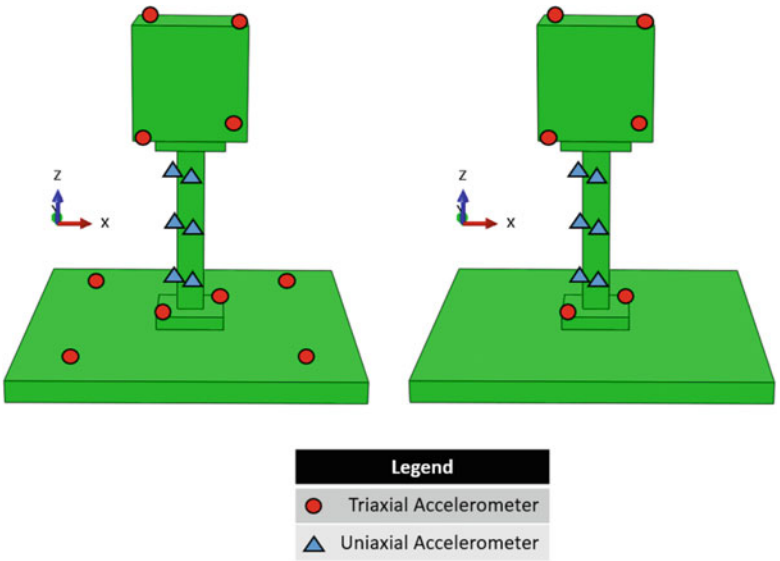

Fig. 3.9 Degrees-of-freedom locations for MPE calculation when including (Left) and excluding (Right) the 12 base DOFs

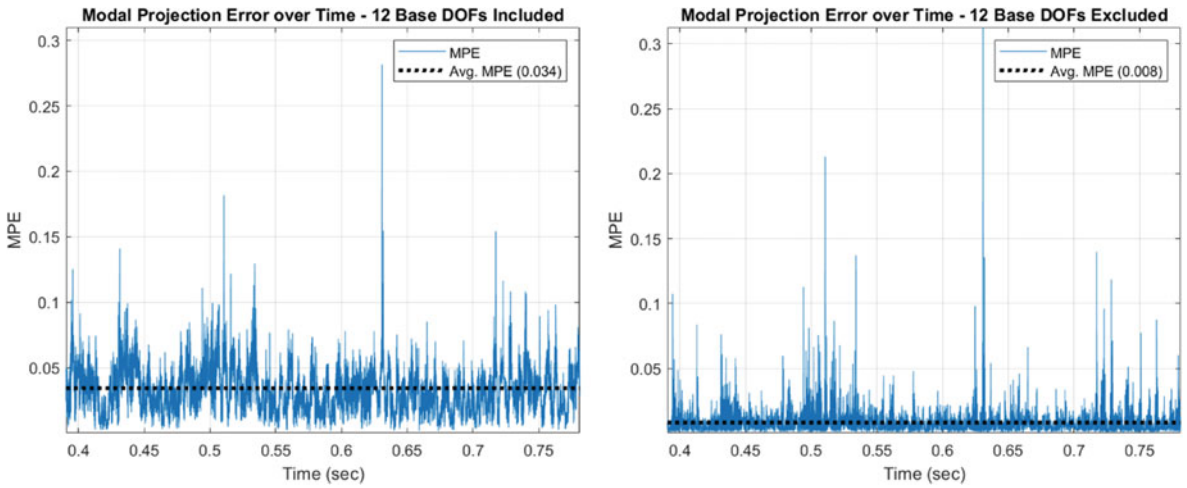

Fig. 3.10 Modal projection error when including (Left) and excluding (Right) the 12 base DOFs

3.6.2 Double Differentiation

The displacement estimation was verified by double differentiation as shown in Fig. 3.2. The method was verified in three directions and three locations, including the base of the beam, bottom of the bobble head, and the top of the bobble head. The time history and PSD of the results are shown in Figs. 3.11 and 3.12, respectively. Note from the RMS values in Figs. 3.11 and 3.12 that the reconstructed accelerations underpredict the measured values. This may be due to the multiple filters applied to the data during integration. Figure 3.12 shows the in-band response from 50–2000 Hz is reconstructed well.

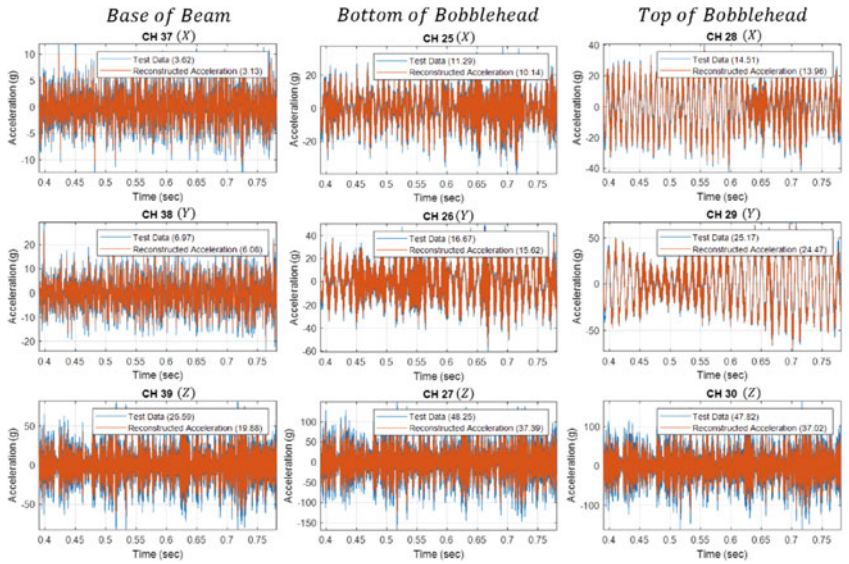

Fig. 3.11 Acceleration time history data from physical measurement and reconstruction by double differentiation of estimated displacement. The RMS values are displayed in parentheses

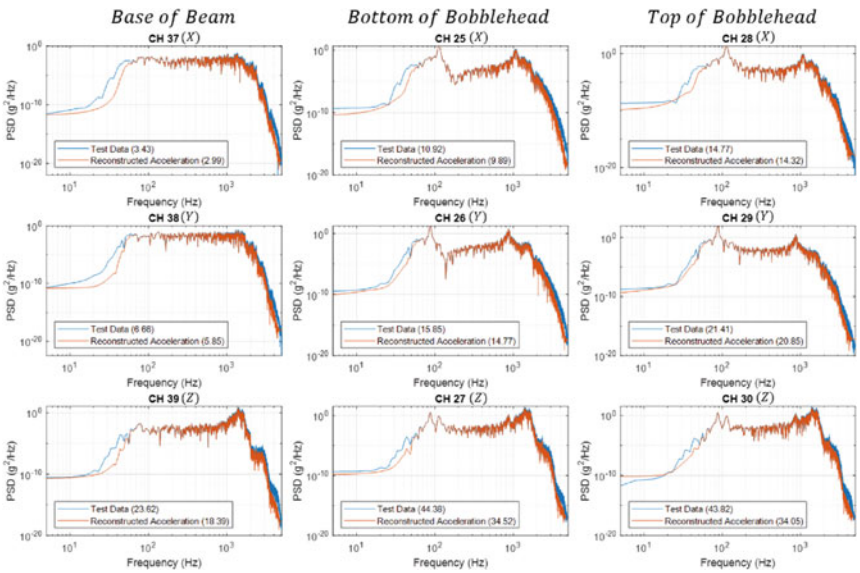

Fig. 3.12 Acceleration power spectral density data from physical measurement and reconstruction by double differentiation of estimated displacement. The RMS values are displayed in parentheses

3.7 Results

3.7.1 Acceleration Expansion

Acceleration expansion was performed prior to strain expansion to verify the expansion process. Acceleration was expanded over roughly a 0.4 second time interval. The measured and expanded acceleration data are overlaid in Fig. 3.13 at a single instance in time.

The expanded accelerations are compared to measured accelerations by the methods listed in Sect. 3.2.5. Figure 3.14 compares RMS and MAE values in both the time and frequency domains. The MAE and values were generally low when compared to their respective RMS values, implying the acceleration expansion was accurate. Supplementary results are presented in Appendix 4.

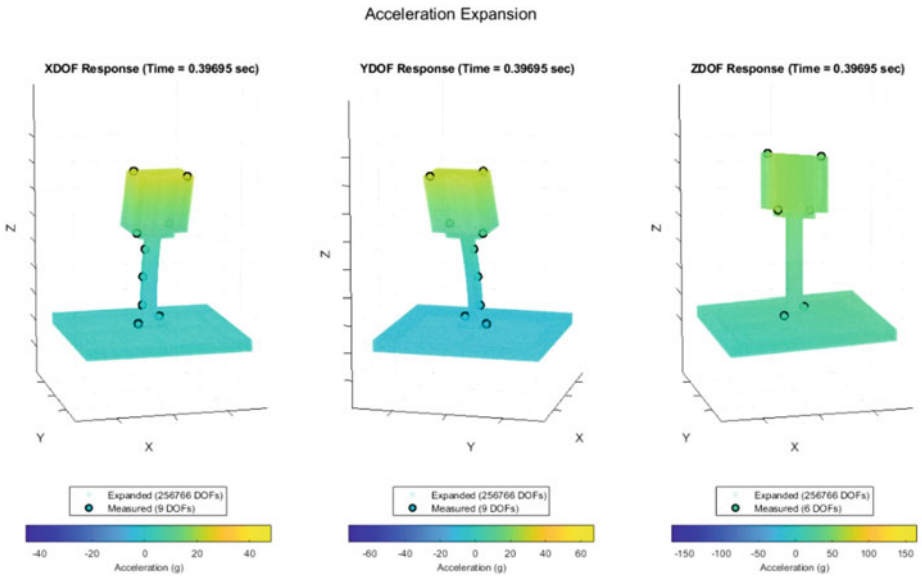

Fig. 3.13 Measured and expanded acceleration data for each principal direction at a single instance in time

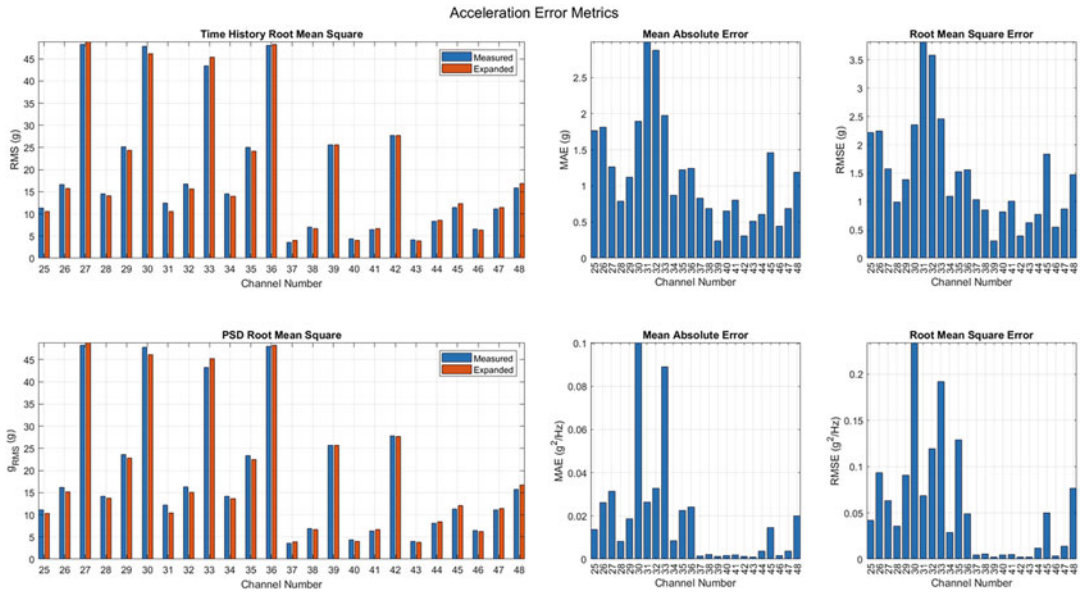

Fig. 3.14 RMS (Left) and MAE (Right) for measured and expanded acceleration signals. The time- and frequency-domain metrics are displayed on the top and bottom, respectively

3.7.2 Strain Expansion

In this section, strain values from the estimation method are compared to measured values at four points on the structure. The locations, directions, and sensor numbers are shown in Fig. 3.15. Note that all strains presented are in the Z direction per Fig. 3.15. The full estimated and sparse measured strains are shown at a single instance in time in Fig. 3.16.

The strains are compared in the time domain in Fig. 3.17 and the frequency domain in Fig. 3.18. The error metrics, RMS and MAE, for the time and frequency domains are presented in Fig. 3.19. Upon inspection of Figs. 3.17, 3.18, and 3.19, it can be noted that there is significant error between the estimated and measured strain values. Comparatively, the results from acceleration expansion per Sect. 3.7.1 had much lower error.

The frequency responses may be used to help characterize this error. Figure 3.18 shows two key characteristics of the strain responses. First, note that the peak in each signal around 100 Hz has a much greater amplitude than other peaks in the frequency range. Assuming the system response may be approximated by a linear combination of its natural frequencies and mode shapes, this indicates that the first few natural frequencies are the major contributors to the strain response. The strain mode shapes of the first two modes at 91 and 120 Hz are shown in Appendix 2, Figs. 3.26 and 3.27. The second observation is that the majority of the error is concentrated at lower frequencies. Note that all sensors exhibit relatively lower error at frequencies above 1000 Hz. In conclusion, there are significant errors in the strain estimate (Fig. 3.19), and the majority of these errors are due to the lower frequency response (Fig. 3.18). Potential sources of this error are discussed in the following section.

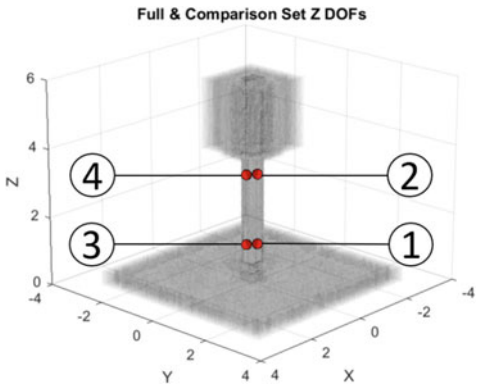

Fig. 3.15 Strain locations marked as red dots with corresponding sensor numbers. The direction of strain is Z per the axis shown

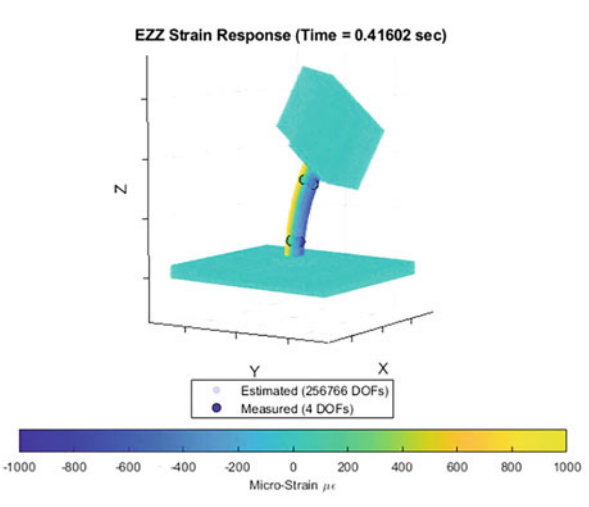

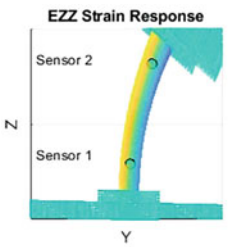

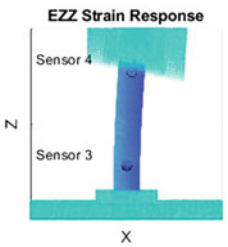

Fig. 3.16 Measured and estimated strains in vertical direction (Z) at a single instance in time

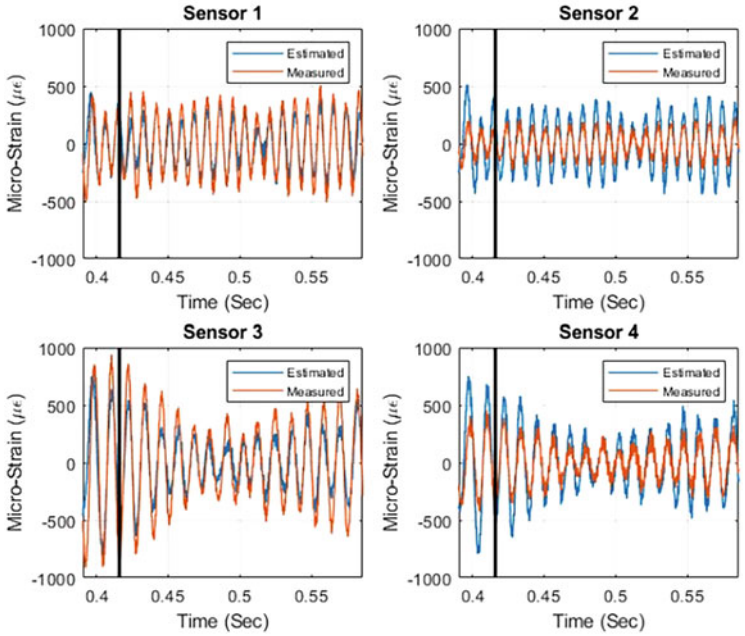

Fig. 3.17 Strain time histories of measured and estimated strains per the corresponding sensor numbers defined in Fig. 3.15. The vertical black line represents the instance in time associated with Fig. 3.16

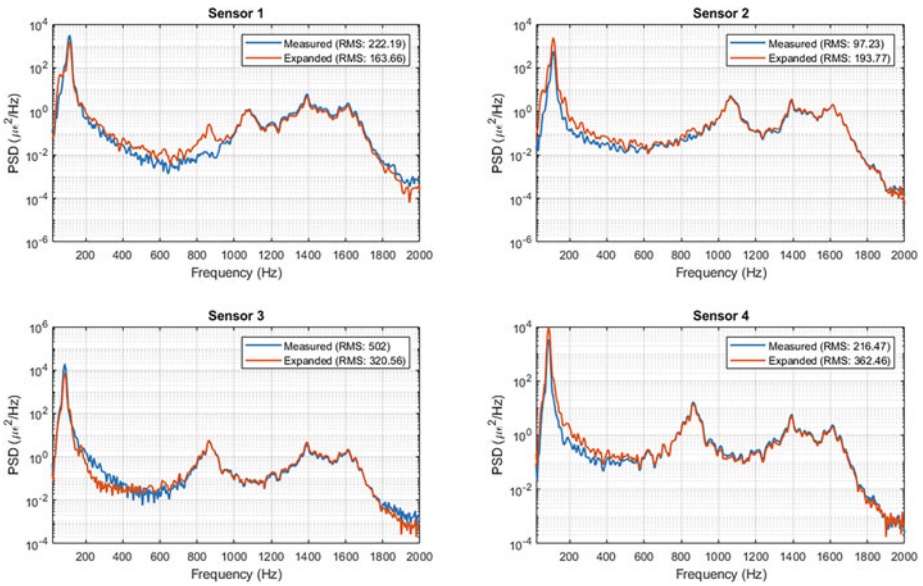

Fig. 3.18 Strain power spectral densities of measured and estimated strains per the corresponding sensor numbers defined in Fig. 3.15

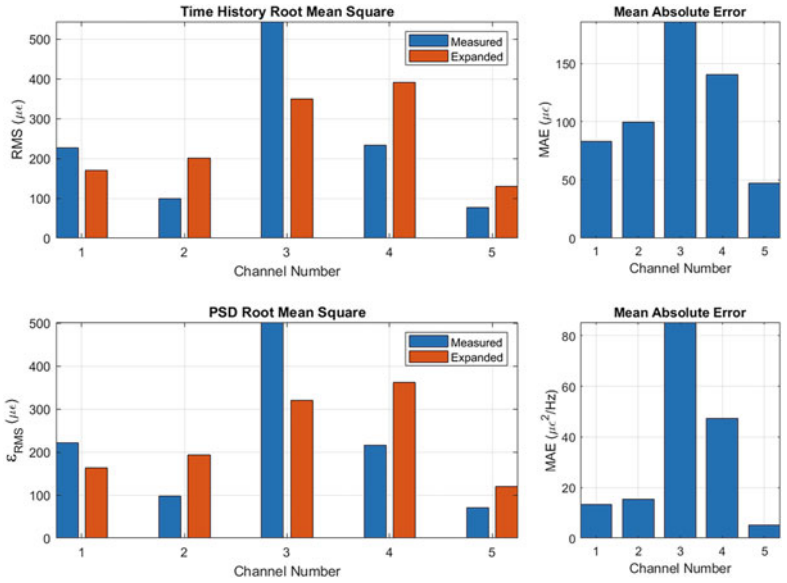

Fig. 3.19 RMS (Left) and MAE (Right) of measured and estimated strains per the corresponding sensor numbers defined in Fig. 3.15

3.8 Conclusion

Acceleration expansion and strain estimation were performed and evaluated on a physical test structure. Expansion of acceleration was shown to be accurate and enables assessment of the component's acceleration response at unmeasured locations. The strain estimation method produced significant error when compared to measured values. It can be concluded that accurate expansion of acceleration does not guarantee accurate estimation of strain when performing the proposed method.

Some anticipated sources of error are due to the following limitations. First, errors are introduced when estimating displacement from acceleration data. Other methods for estimating displacement from acceleration exist and could improve the strain estimate. Additionally, direct measurements of the displacement response would help validate displacement estimation techniques. Second, the uncalibrated mode shapes from the finite-element model are another source of error. This error occurs because the physically measured values are fitted via the finite-element mode shapes. Any discrepancies between experimental and model mode shapes will result in errors in this step. Further study of these limitations could improve the accuracy of strain estimation.

Appendix 1: Displacement Mode Shapes from Finite-Element Model

Displacement mode shapes for the first six flexible modes of the structure are shown in Figs. 3.20–3.25.

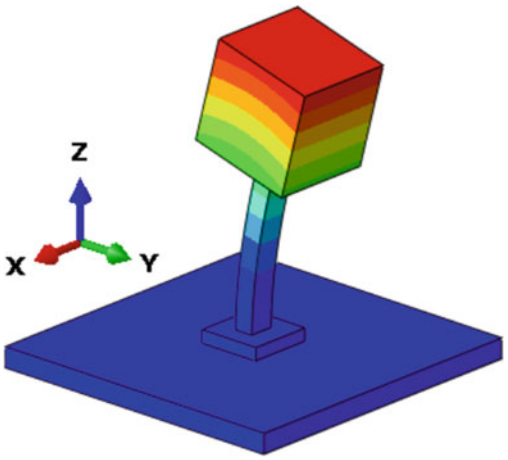

Fig. 3.20 First flexible mode. First-order bending in Y direction at 91 Hz

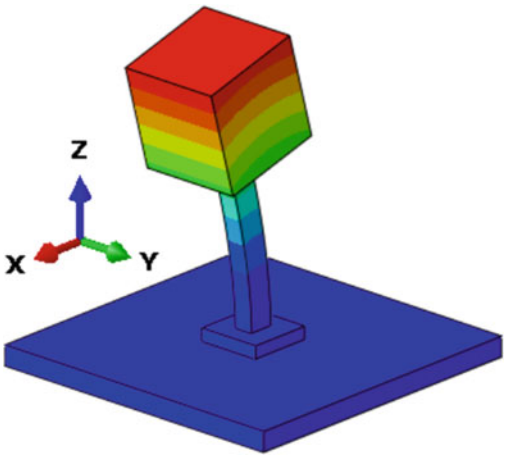

Fig. 3.21 Second flexible mode. First-order bending in X direction at 120 Hz

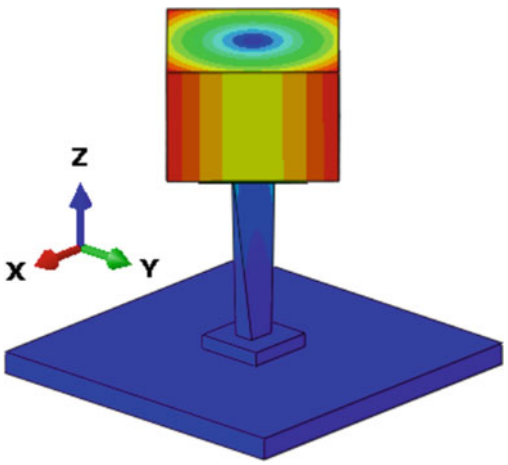

Fig. 3.22 Third flexible mode. First-order torsion in Z at 317 Hz

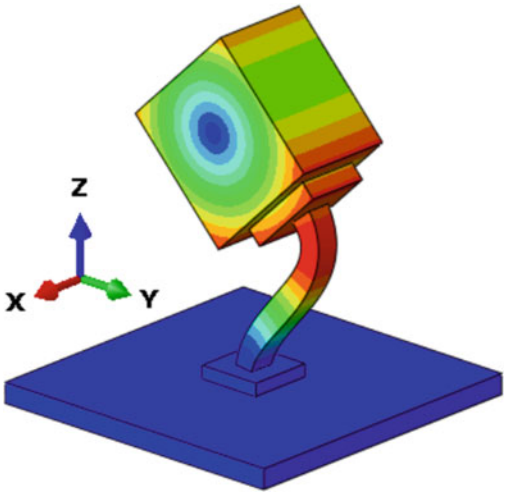

Fig. 3.23 Fourth flexible mode. Second-order bending in Y direction at 976 Hz

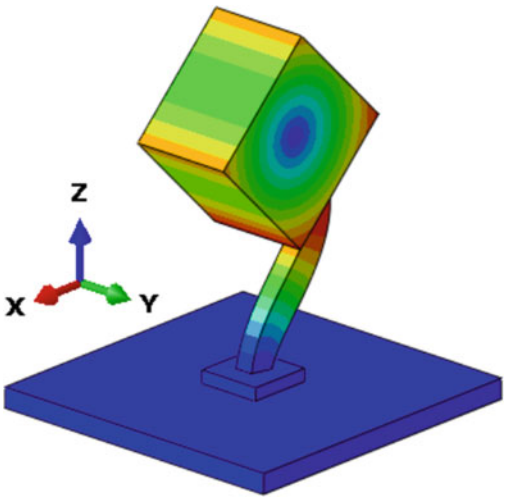

Fig. 3.24 Fifth flexible mode. Second-order bending in X direction at 1265 Hz

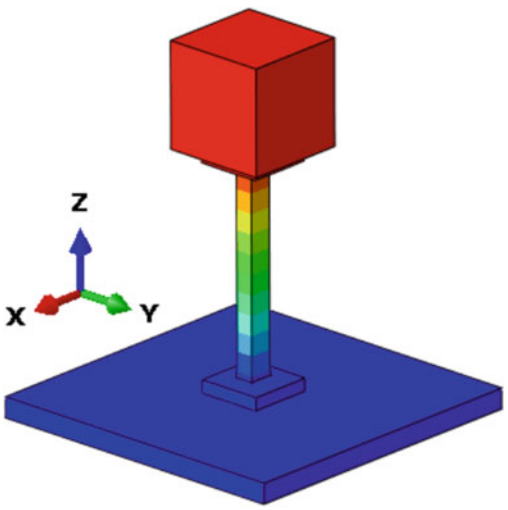

Fig. 3.25 Sixth flexible mode. First-order axial mode at 2462 Hz

Appendix 2: Strain Mode Shapes from Finite-Element Model

Strain mode shapes for the first six flexible modes of the structure are shown in Figs. 3.26–3.31.

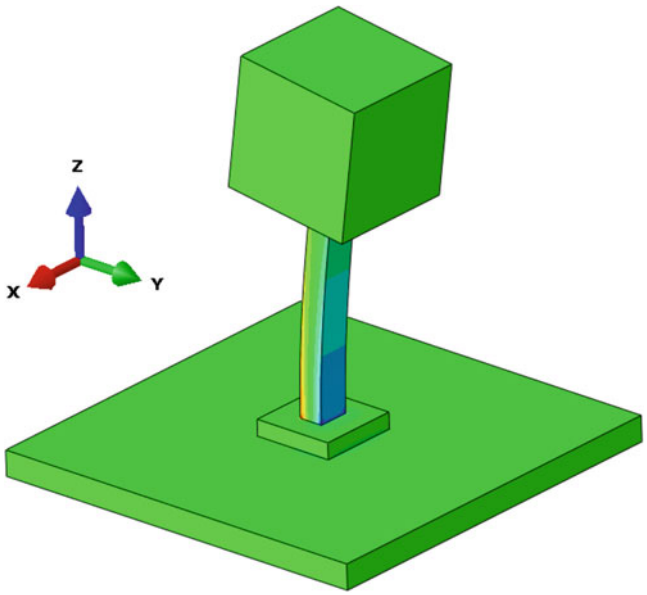

Fig. 3.26 First flexible mode. First-order bending in Y direction at 91 Hz

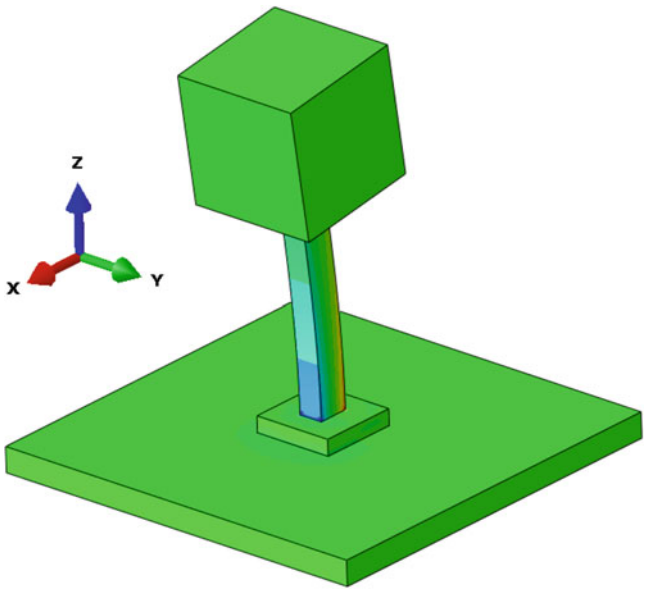

Fig. 3.27 Second flexible mode. First-order bending in X direction at 120 Hz

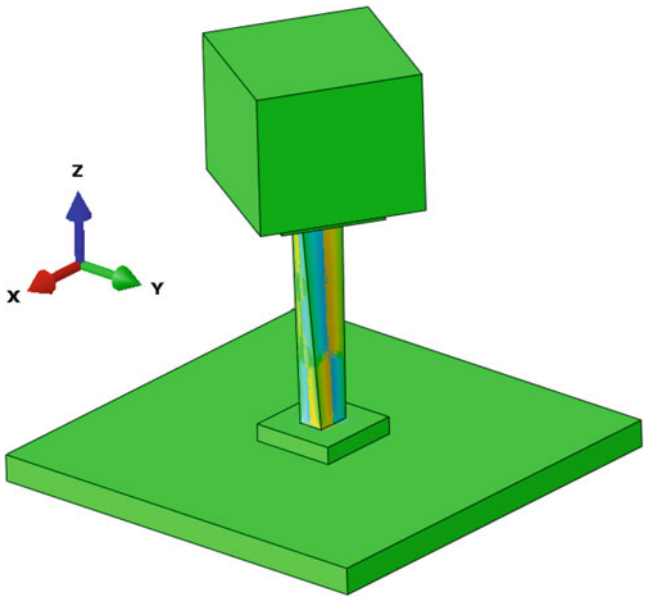

Fig. 3.28 Third flexible mode. First-order torsion in Z at 317 Hz

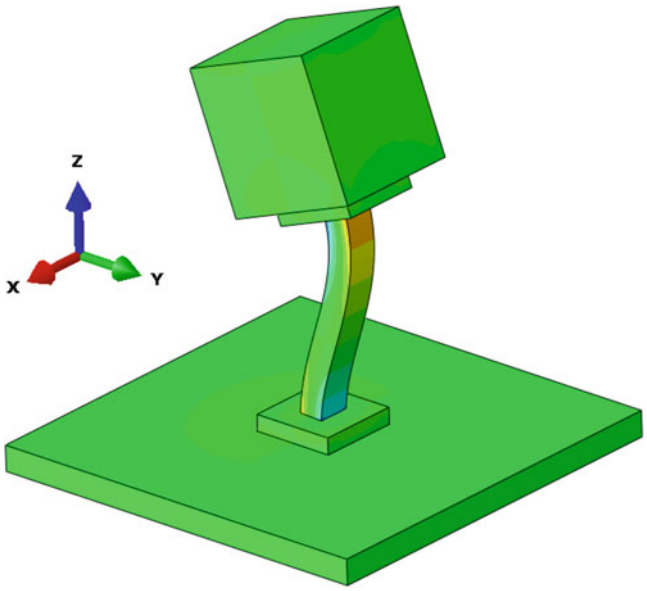

Fig. 3.29 Fourth flexible mode. Second-order bending in Y direction at 976 Hz

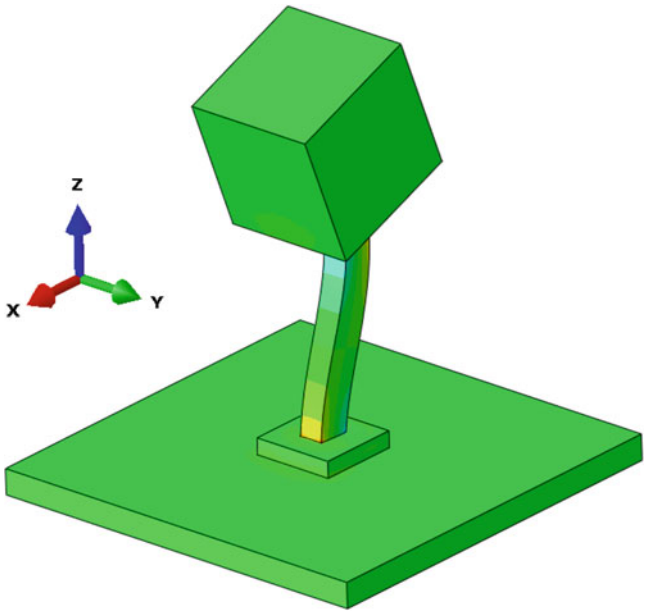

Fig. 3.30 Fifth flexible mode. Second-order bending in X direction at 1265 Hz

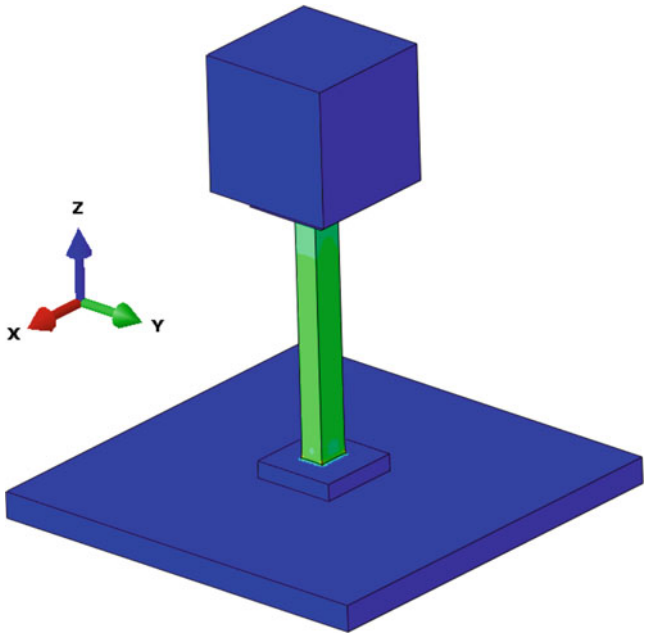

Fig. 3.31 Sixth flexible mode. First-order axial mode at 2462 Hz

Appendix 3: Supplementary Error Metrics

Time and Frequency Response Assurance Criterion

The time response assurance criterion (TRAC) and frequency response assurance criterion (FRAC) are both metrics that qualitatively compare two signals in the time and frequency domains, respectively. The equation for TRAC is shown as Eq. 3.14, and the equation FRAC is shown as Eq. 3.15 per dynamic design solutions [10]. A TRAC or FRAC of 1 indicates perfect consistency and 0 indicates inconsistency or orthogonal signals.

$$TRAC = \frac{(|\overline{X}_{t,meas}{}^{\top}||\overline{X}_{t,pred}|)^2}{(|\overline{X}_{t,pred}{}^{\top}||\overline{X}_{t,meas}|)(|\overline{X}_{t,meas}{}^{\top}||\overline{X}_{t,pred}|)} \tag{3.14}$$

$$FRAC = \frac{(|\overline{X}_{f,meas}{}^{\top}||\overline{X}_{f,pred}|)^2}{(|\overline{X}_{f,pred}{}^{\top}||\overline{X}_{f,meas}|)(|\overline{X}_{f,meas}{}^{\top}||\overline{X}_{f,pred}|)}. \tag{3.15}$$

Root Mean-Squared Error

The root mean-squared error (RMSE) compares two signals by computing the deviation between them. It may be computed in the time or frequency domain, as shown in Eq. 3.16 and 3.17, respectively. A low RMSE indicates good agreement between measured and predicted values.

$$RMSE_{time} = \sqrt{\frac{\sum_t (\overline{X}_{t,meas} - \overline{X}_{t,pred})^2}{n_t}} \tag{3.16}$$

$$RMSE_{freq} = \sqrt{\frac{\sum_f (\overline{X}_{f,meas} - \overline{X}_{f,pred})^2}{n_f}}. \tag{3.17}$$

Appendix 4: Supplementary Acceleration Expansion Results

The time- and frequency-domain responses of a few of the signals are studied in greater detail in Figs. 3.32 and 3.33, respectively. For succinctness, only three signals are shown. These signals were selected to represent a worst, average, and best expansion of the total 24 signals based on the various error metrics discussed above. The TRAC and FRAC values are listed generally as SAC, which stands for Signature Assurance Criterion.

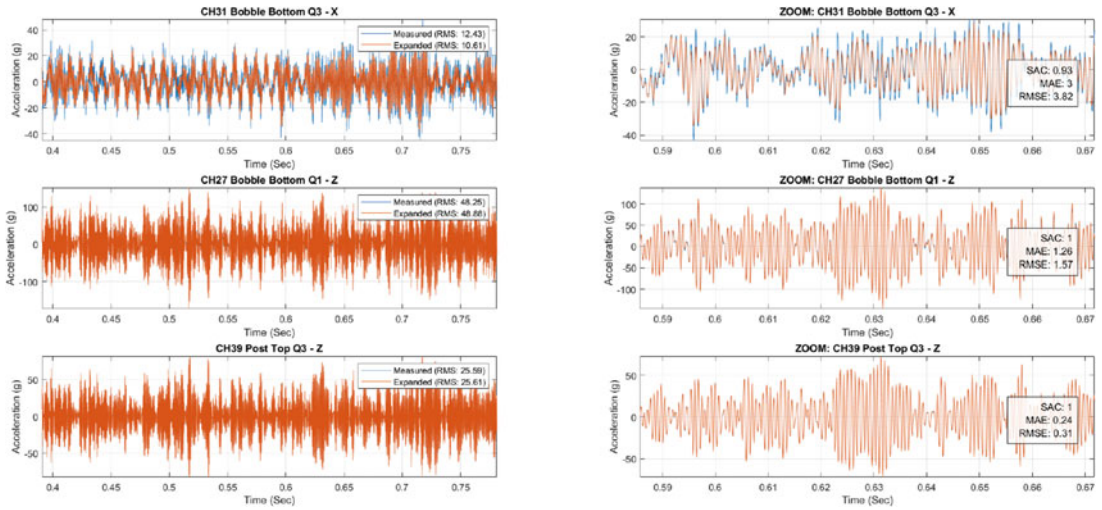

Fig. 3.32 Acceleration time history compared between measured and expanded data of worst (top), average (middle), and best (bottom) channels

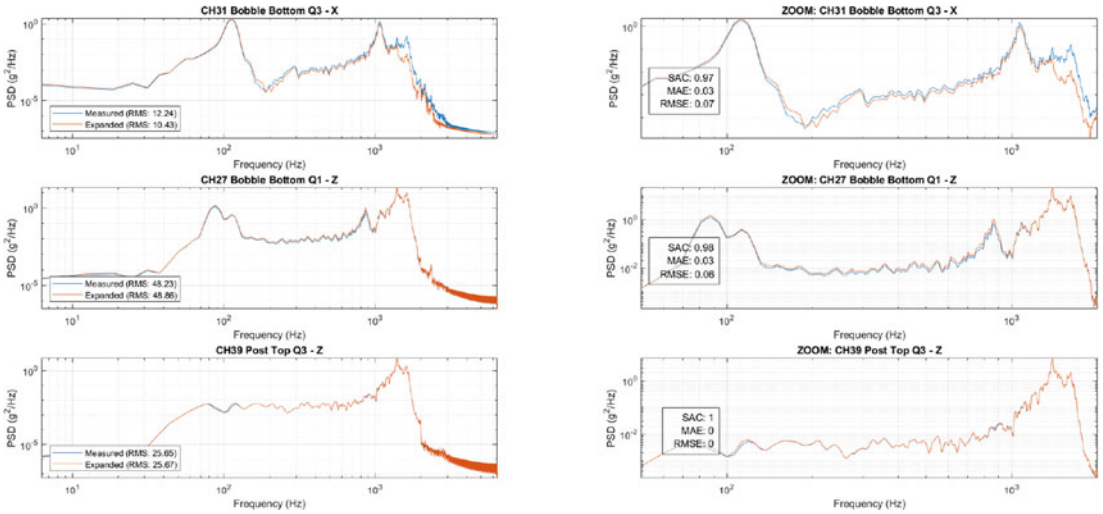

Fig. 3.33 Acceleration power spectral density compared between measured and expanded data of worst (top), average (middle), and best (bottom) channels

References

1. O'Callahan, J., Avitabile, P., Riemer, R.: System equivalent reduction expansion process (SEREP). In: Proceedings of the 7th International Modal Analysis Conference. IMAC (1989)
2. Zwink, B., et al.: Flight Environments Demonstrator: Part II - Ground Trials of a Sounding Rocket Experiment for Characterization of Flight. Tech. rep. SAND2018-12092C. Sandia National Laboratories (2019)
3. Baqersad, J., Bharaqwaj, K.: Strain expansion-reduction approach. Mech. Syst. Signal Process. **101**, 156–167 (2018)
4. Witt, B., Rohe, D., Schoenherr, T.: Full-Field Strain Shape Estimation from 3D SLDV. Tech. rep. SAND2018-12119C. Sandia National Laboratories (2018)
5. Almarshad. Building Drift Estimation Using Acceleration and Strain Measurements (2017)
6. How to 'correctly' integrate time data within Time Domain Integration? SIEMENS^{TM} (2016)
7. Schoenherr, T., Rouse, J., Harvie, J.: Characterizing dynamic test fixtures through the modal projection error. Tech. rep. SAND2020-1119. Sandia National Laboratories (2020)
8. Schoenherr, T., Paripovic, J.: Using modal projection error to evaluate SEREP modal expansion. In: Proceedings of the 38th International Modal Analysis Conference. IMAC (2021)
9. Irvine, T.: Power Spectral Density Integration. https://www.mathworks.com/matlabcentral/fileexchange/7600-power-spectral-density-integration. Accessed 10 June 2022
10. FEMTools^{TM} Model Updating Theoretical Manual (2017)

Chapter 4
Using Modal Acceleration to Compare Two Environments of an Aerospace Component

Tyler F. Schoenherr and Moheimin Khan

Abstract Engineers are interested in the ability to compare dynamic environments for many reasons. Current methods of comparing environments compare the measured acceleration at the same physical point via a direct measurement during the two environments. Comparing the acceleration at a defined point only provides a comparison of response at that location. However, the stress and strain of the structure are defined by the global response of all the points in a structure. This chapter uses modal filtering to transform a set of measurements at physical degrees of freedom into modal degrees of freedom that quantify the global response of the structure. Once the global response of the structure is quantified, two environments can be more reliably and accurately compared. This chapter compares the response of an aerospace component in a service environment to the response of the same component in a laboratory test environment. The comparison first compares the mode shapes between the two environments. Once it is determined that the same mode shapes are present in both configurations, the modal accelerations are compared in order to determine the similarity of the global response of the component.

Keywords Modal filter · Modal projection error · Modal acceleration · Environment · Aerospace

4.1 Introduction

A dynamic environment is defined in this chapter as the response of a structure to a dynamic load. Dynamic environments are of interest to designers and engineers because these environments can cause large stresses in their structures and cause them not to function as intended. Defining, comparing, and reproducing dynamic environments have a long history well laid out by Daborn [1]. Although there are many advances in the past century on defining, comparing, and reproducing dynamic environments, all common techniques compare dynamic response at a point or sometimes a limited set of points. This limited set of information is not sufficient to determine the strain field since strain is the relative displacement between two adjacent points. Therefore, global response information is needed to quantify the damage of a structure.

If mechanical failure of the structure is the concern with respect to the environment, mechanical strain is the quantity of interest. Since mechanical strain is the relative displacement of two points on a structure, rigid body motion does not cause strain within the structure. However, the acceleration due to rigid body motion is captured during environments and is included in the environments definition that is subsequently used in a laboratory test. This extra excitation is unnecessary and could be removed to increase the capacity of the testing facilities.

Instead of using the response at a single or small subset of points to characterize the response of a structure, this chapter demonstrates how the environment can be characterized in the modal domain and the corresponding benefits. Transforming

T. F. Schoenherr (✉) · M. Khan
Sandia National Laboratories, Albuquerque, NM, USA
e-mail: tfschoe@sandia.gov; mkhan@sandia.gov

J. Harvie (ed.), *Dynamic Environments Testing, Volume 7*, Conference Proceedings of the Society for Experimental Mechanics Series, https://doi.org/10.1007/978-3-031-34930-0_4

physical response into modal response makes use of a modal filter. Modal filters have been used in modal theory for techniques such as modal parameter estimation, force reconstruction, and expansion [2–4]. This transformation has errors associated with how it fits mode shapes to the measurements. This chapter uses the modal projection error to quantify the error in the modal filtering process [5].

There are many ways to use a characterized environment as previously stated. This chapter focuses on comparing two environments, specifically, the environment of an aerospace structure, while it is mounted in its service configuration, and the environment of the same aerospace structure when attached to an electrodynamic shaker in a laboratory configuration. This chapter utilizes the modal domain responses from each of the environments, quantifies the global response, and compares the global response of the two environments.

4.2 The Aerospace Structure

The structure of interest is a relatively small component in a larger system. The component is bolted to a bracket in a cantilevered configuration. For the service configuration, the bracket is bolted to another component in a large assembly. The laboratory configuration has the same component and bracket assembly bolted rigidly to a single-axis shaker system. A finite-element model of this structure and its bracket is shown in Fig. 4.1. Representations of the service and laboratory configurations of the component are shown in Fig. 4.2.

4.3 Computing Modal Acceleration

Computing the modal acceleration of a structure produces an understanding of the global response of the structure. This global understanding is obtained because the modal acceleration is uniquely tied to a single mode shape of the structure. Modal acceleration is defined in this chapter as the coefficients that scale the mode shapes to approximate the physical accelerations of a structure shown as

$$\ddot{\bar{x}} \approx \boldsymbol{\phi}\ddot{q}, \tag{4.1}$$

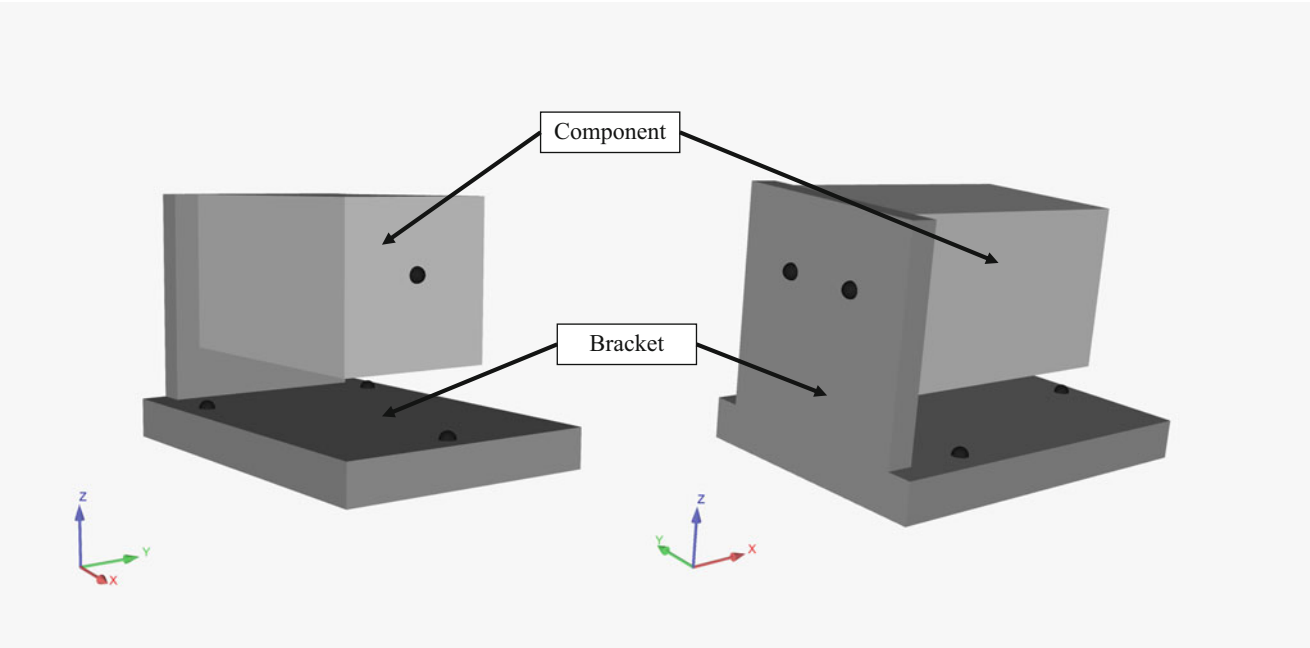

Fig. 4.1 Finite-element model of the component and its bracket. Triaxial accelerometers used are indicated by black dots

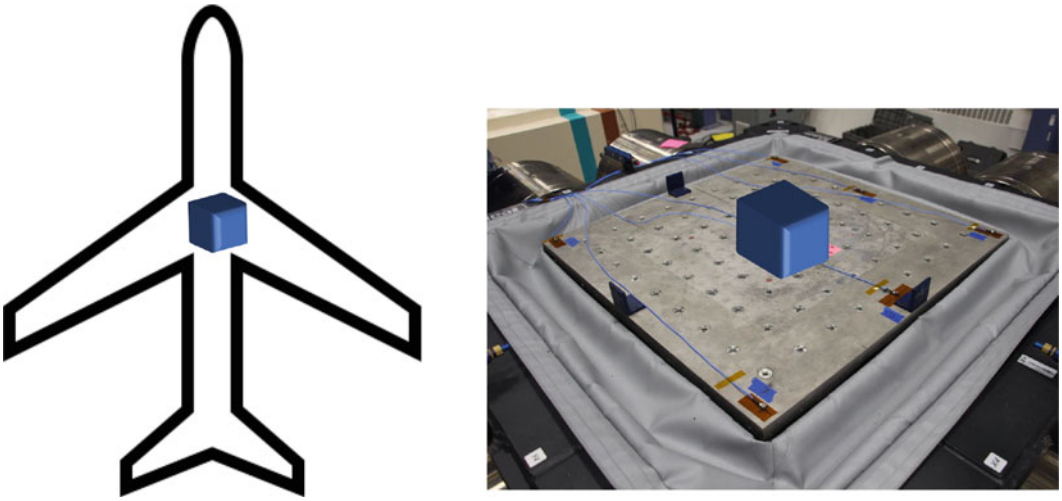

Fig. 4.2 Representation of the component in its service environment (left) and its laboratory environment (right)

where $\ddot{\bar{x}}$ is the vector of accelerations at the measured degrees of freedom, $\boldsymbol{\phi}$ is the mode shape matrix at the measured degrees of freedom, and $\ddot{\bar{q}}$ is the modal acceleration for each corresponding mode. The linear combination of modes in Eq. 4.1 is approximately the acceleration due to modal truncation.

In order to transform the physical accelerations into modal accelerations, the measured accelerations are projected on to the mode shapes by using the pseudoinverse of ϕ,

$$\boldsymbol{\phi}^{+}\ddot{\bar{x}} \approx \ddot{\bar{q}}, \tag{4.2}$$

where the $^{+}$ superscript denotes the pseudoinverse of a matrix. Equations 4.1 and 4.2 are written generally as the shapes used in the pseudoinverse can be from test data or a finite-element model.

For the structure in Fig. 4.1, the measured accelerations in both the service and laboratory environments are transformed using mode shapes generated from a finite-element model to acquire the modal accelerations. Because there are two sets of data being transformed into the modal domain, Eq. 4.2 is executed once per set of data. In order to compare the modal accelerations between the two environments, the same set of mode shapes must be used. However, the same degrees of freedom do not need to be measured. Being able to have two sets of instrumentation is especially important because it is common for sets of data to not measure exactly the same degrees of freedom. This chapter uses data where one of the triaxial accelerometers is in a different location between the two sets.

Equation 4.2 provides an estimate of the modal acceleration as there are sources of error that influence the computation. The first source of error is in the measured accelerations. There is standard measurement error and location error. The location error manifests itself when the location of the accelerometer is thought to have a certain coordinate location, but the measurement actually happens at an alternate location. This results in mismatched degrees of freedom in the mode shapes. The magnitude of the location error is dependent on the gradient of the mode shape at the measured degree of freedom and the magnitude of the response. The standard measurement error comes from the inherent error in the accelerometer after calibration. This error is minimized through the least squares fitting of the random measurement error to the mode shapes.

Another large source of error to the computation in Eq. 4.2 is in the projection of the measured accelerations onto the mode shape space. In order to understand this error, it is important to discuss the projection of the test data onto the mode shapes as a curve-fitting process. The mode shapes are scaled independently in order to best fit the data in a least squares sense. The scale factors are the modal accelerations. The least squares fitting is all done through the computation of the pseudoinverse of the mode shape matrix.

The error of the curve-fitting process can be quantified by use of the modal projection error (MPE) [6]. The MPE is analogous to the coefficient of determination and can provide insight into how well a set of basis vectors can be combined to reproduce a set of data. The MPE, $\Psi^2(t)$, is computed by

$$\Psi^2(t) = 1 - \ddot{\bar{x}}(t)^{+}\boldsymbol{\phi}\boldsymbol{\phi}^{+}\ddot{\bar{x}}(t). \tag{4.3}$$

In order to obtain a least squares estimation of the modal accelerations, the mode shapes need to be independent, and the matrix needs to be rectangular with more rows than columns representing more degrees of freedom than modes. The more

rectangular the mode shape matrix is, the more reliable the MPE is in being a metric for the success of the modal filter. In order to make the mode shape matrix more rectangular, only the necessary modes are included in the pseudoinverse. Greedy algorithms are used to iteratively down-select mode shapes until a satisfactory minimum number of modes are selected with a satisfactory MPE.

Another important aspect is the independence of the mode shapes relative to each other. There are many ways to determine if two shapes or vectors are independent, but this chapter uses the modal assurance criteria (MAC). If there is a high MAC value between two shapes, then they will counteract each other and give artificially high magnitudes in the projection using Eq. 4.2.

4.4 Comparing Service and Laboratory Environments

The component shown in Fig. 4.1 has a service and laboratory configuration. There are two service environments each excited in the X, Y, and Z directions. Service environment 1 is a low-level environment, while service environment 2 is a high-level environment. Additionally, there is a laboratory configuration where the component in Fig. 4.1 is attached directly to an electrodynamic shaker. This laboratory environment is excited in the X, Y, and Z directions. All of the service and laboratory environments are considered to have random vibration excitation. The modal accelerations for all environments and excitation directions are calculated per Eq. 4.2 using the mode shapes from the finite-element model. The mode shapes from the finite-element model are used because they are the only set of shapes that had all of the degrees of freedom from both configurations.

Six rigid and four elastic modes from the finite-element model are used to represent the motion of the component in all of the environments compared. The four elastic modes are not the four modes with the lowest natural frequencies, but the four modes that minimize the MPE along with being independent with respect to the other basis shapes. This combination provides a mode shape matrix that includes 18 degrees of freedom measured and 10 modes. The pseudoinverse of the mode shape matrix of these dimensions provides an overdetermined estimation of the modal accelerations when computing the pseudoinverse. Only the modal accelerations of the elastic modes are used to define the response of the environment because rigid body modes do not induce stresses in the structure. The four elastic modes that this analysis uses are shown in Fig. 4.3.

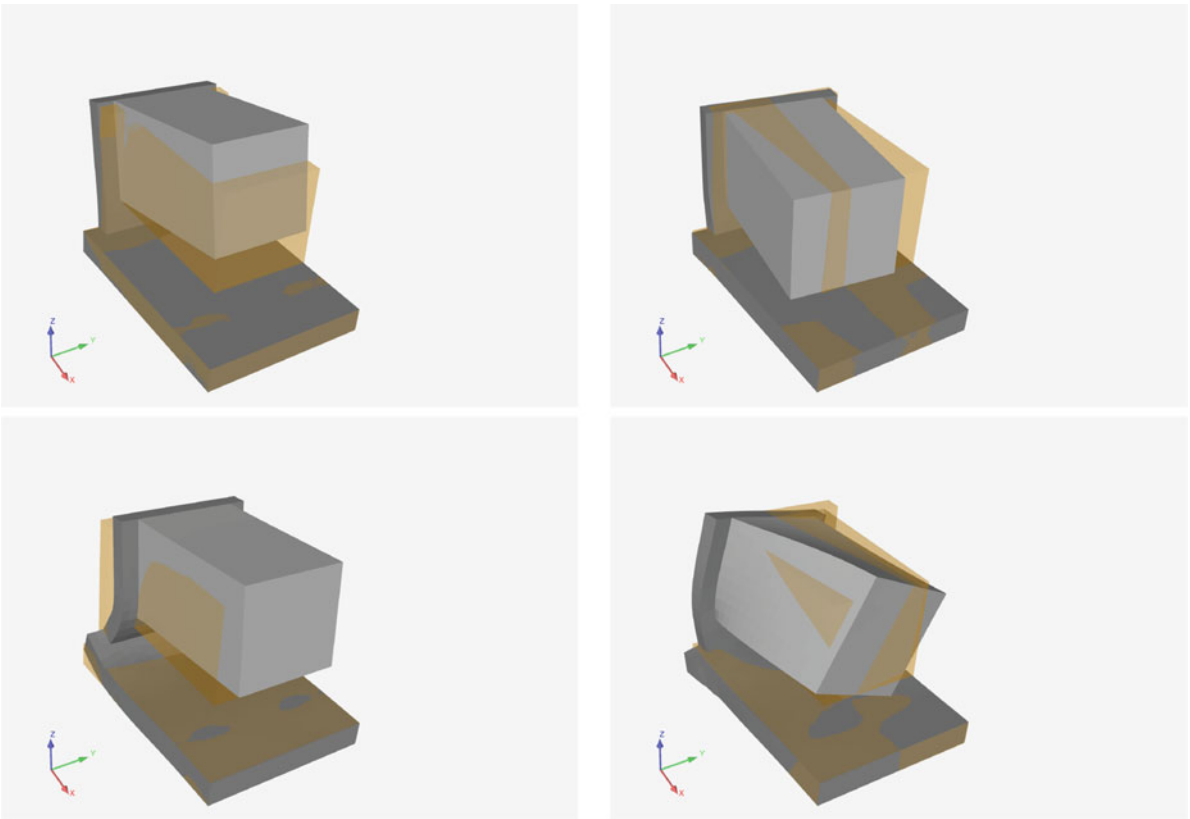

Fig. 4.3 Deformed (gray) and undeformed (orange) shapes of the 1st (upper left), 2nd (upper right), 3rd (lower left), and 4th (lower right) mode shapes used in the modal filter

Table 4.1 Average modal projection errors for the modal filter per environment

Environment	Direction	Avg MPE
Service 1	X	12.6e-3
Service 1	Y	19.7e-3
Service 1	Z	14.3e-3
Service 2	X	8.6e-3
Service 2	Y	10.6e-3
Service 2	Z	9.2e-3
Laboratory 1	X	4.4e-3
Laboratory 1	Y	4.4e-3
Laboratory 1	Z	4.7e-3

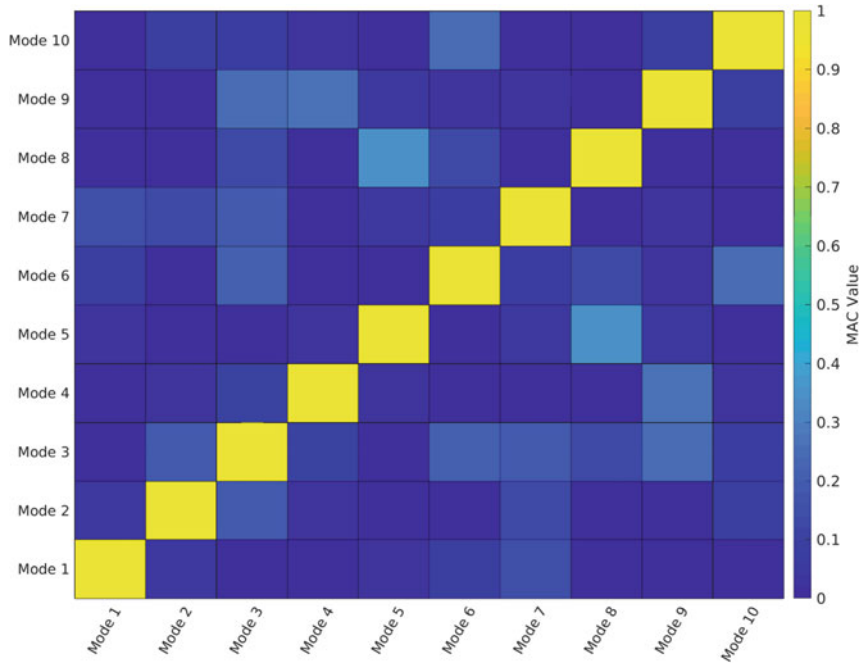

Fig. 4.4 Self-modal assurance criteria plot of the mode shapes used in the modal filter

The MPE is calculated for every environment at each time step. The average MPE over the time history of each environment is in Table 4.1. The significance of the MPE is relative to the ratio of degrees of freedom to the number of modes used in the pseudoinverse as shown in [6] and to what degrees of freedom are chosen. In an overdetermined pseudoinverse calculation, values under 0.02 typically result in excellent projections [6]. The low values of MPE provide evidence of how well the ten finite-element modes fit the test data. This low error provides confidence that the ten modes acting as the basis vectors for the test data are accurate representations of the modes of the structure in both service and laboratory configurations. It also shows no other modes of the structure are excited in any of the environments. This low error for both environments indicates that the test fixture attaching the component to the electrodynamic shaker produces the same mode shapes for the structure of interest in the laboratory configuration as in the service configuration, which is necessary for a successful laboratory test.

The independence of the mode shapes as basis vectors is critical in using a modal filter. If the basis vectors are similar to each other, then the pseudoinverse will use what small differences there are between the similar vectors to fit noise or other data not represented by the basis vectors. It will also inflate the magnitude of the modal accelerations. The self MAC of the mode shape matrix verifies the independence of the mode shapes and is shown in Fig. 4.4.

Another check on the validity of Eq. 4.2 is to use the modal accelerations for modal expansion. This process removes one of the degrees of freedom from the mode shape matrix and then uses the full finite-element shapes to calculate the acceleration at that degree of freedom and compare to the measurement. This process is done for the Y direction degree of freedom at the point indicated in Fig. 4.5. Although this method of validating the modal filter appears intuitive, it is

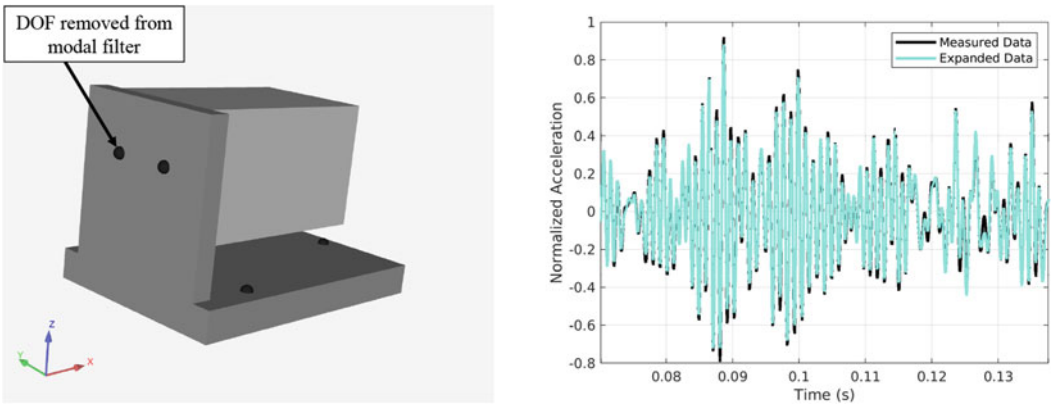

Fig. 4.5 Reproduction of the acceleration response through SEREP expansion not utilized in the expansion technique

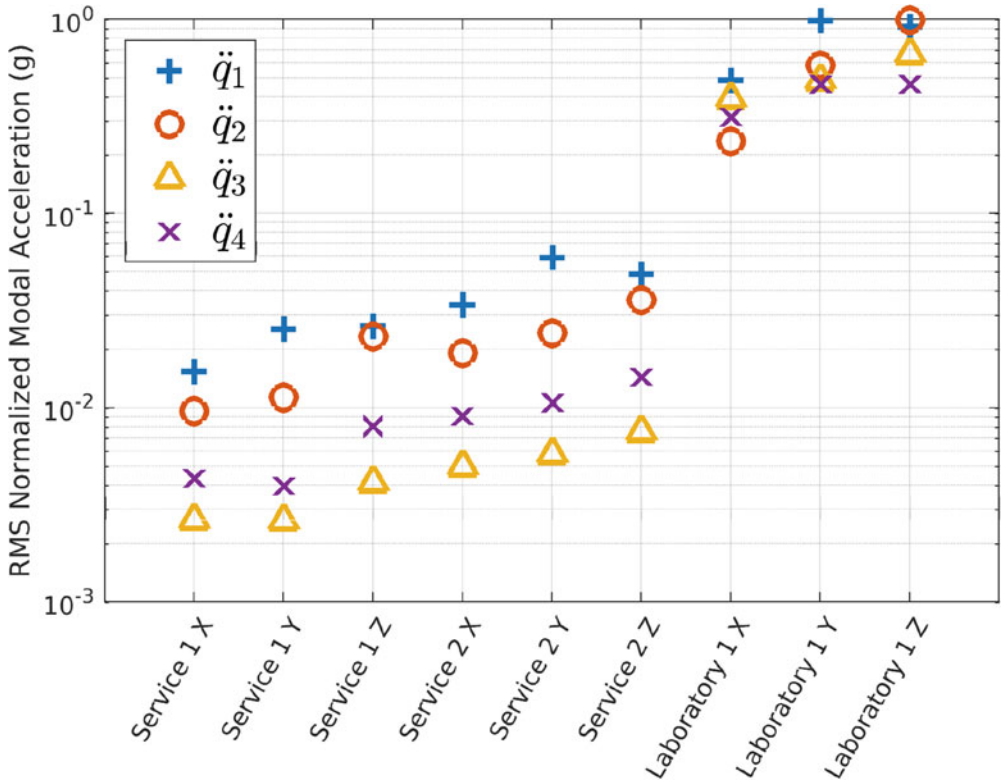

Fig. 4.6 Normalized modal accelerations from service and laboratory environments

only useful if the modal accelerations are overdetermined as removing a degree of freedom from the modal filter can cause errors in the pseudoinverse. The reconstruction of that degree of freedom response is shown in Fig. 4.5 and has an average point-by-point error of 5% over the entire time history.

The modal filter in Eq. 4.2 uses the 10 basis modes and calculates the modal accelerations. The root mean-squared values of the modal acceleration time histories are calculated and normalized for each environment. The root mean-squared values of the modal accelerations for the elastic modes are shown in Fig. 4.6 for each environment. Being able to examine just the elastic motion removes any rigid body motion from the response. The rigid body response does not induce any stress but can account for a lot of the acceleration in any structure. Examination of the root mean-squared values of each of the modal accelerations provides additional information that cannot be determined from comparing physical accelerations. Because the modal acceleration is a measure of the global response, the modal acceleration provides a better estimate of the energy in the system when comparing the energy at a single degree of freedom.

The service and laboratory environments shown in Fig. 4.6 are typical in that they are executed with a single degree of freedom shaker in three orthogonal directions, X, Y, and Z. Although the structure of interest is excited in orthogonal directions, the four elastic modes of the structure are excited in each direction. By examining the response in the modal domain, the assumptions of only X degrees of freedom being excited during an X direction laboratory test can be abandoned. This revelation is important because current testing assumes that testing in the X, Y, and Z directions separately provides orthogonal response and that the damage can be superimposed, which is false.

The modal accelerations alone cannot be used to state which modes are the most damaging as each mode will scale to stress at different locations on the structure; however, each mode can be directly compared to the same mode in different environments. It is observed that the laboratory tests are exciting the same elastic modes to approximately an order of magnitude more acceleration than the two service environments. It is also observed that the order of the modal accelerations in the laboratory environment does not match the order in the service environments. This order of which mode is excited the most is controlled by the test apparatus or shaker system. An alternate forcing function or multi-degree of freedom excitation can gain additional control of the different modes to make the laboratory test behave more like the service environments.

Typically, the purpose of the laboratory test is to determine if the component will survive in the service environment. In that scenario, it can be said with confidence that the stresses in the laboratory environment are greater because the excitation of each of the elastic modes is greater than any of the service environments. In addition, Fig. 4.6 shows that each of the laboratory environments excites all of the modes more than the service environment. Therefore, the traditional test in three orthogonal directions is unnecessary, and only one test setup is needed.

These results quantify the difference in damage responses between environments because the amplitudes of the same mode shapes excited are compared. However, it is important to address the uncertainties in the analysis. The highest amount of uncertainty in this process of computing and comparing modal accelerations comes from the curve-fitting process in the projection of the mode shapes onto the time histories. The finite number of modes included can cause change the calculated modal accelerations and should be examined when computing the modal accelerations. This case study had low errors with respect to the MPE, and there is high confidence in the results. This result may not be common for all case studies. Additional work should be done to investigate these sensitivities. This analysis uses random vibration as the excitation. Additional work could utilize this process for a transient response as the computation works on the time domain and should be robust against light nonlinearities due to mode shapes being the basis of the analysis [7].

4.5 Conclusion

This chapter demonstrates the process of computing modal accelerations and using specific tools to determine the validity of the process. Modal accelerations provide a framework for comparing the global response of a structure in different environments and greatly reduce the errors associated with comparing single physical accelerations between two environments. These errors include differences in physical location of the accelerometer and the inclusion of rigid body acceleration in the comparison. This chapter uses an aerospace component and compares its modal accelerations in service and laboratory environments. The results show a transparent and intuitive approach to comparing the elastic response between environments.

The process also provides evidence of the laboratory environment's representation of the service environment through the modal projection error. The low MPE indicates that the same modes existed between the service environments and the laboratory environments because the shapes are independent and the pseudoinverse is overdetermined. Having the same mode shapes in each environment would be impossible if the test fixture did not represent the dynamic impedance of the next level of assembly in the service configuration.

This process comes with challenges. There are many sources of errors when computing the modal accelerations. One challenge is ensuring that there is an appropriate set of basis vectors with enough instrumentation to independently observe them. If the basis set of mode shapes is inadequate, then the values of modal accelerations are meaningless. Use of the MPE, MAC and making sure that the modal accelerations are overdetermined are critical in gaining confidence in the modal acceleration calculation.

One unknown of this process is the effect of the accelerometer placement in the pseudoinverse calculation. Because the pseudoinverse is a least squares fitting process, if one shape has more measurements participating over other shapes, then the fitted modal accelerations will be weighted toward that shape. Also important is how independent the elastic shapes are with respect to the rigid shapes. Any misfitting of the elastic shapes to the measurements is typically compensated by rigid body modes, which can also skew the results. Additional research in these areas can improve the quality and repeatability of the modal acceleration calculation.

References

1. Daborn, P.: Smarter Dynamic Testing of Critical Structures. Thesis, 2014
2. Carne, T.G., Bateman, V.I., Dohrman, C.R.: Force reconstruction using the inverse of the mode-shape matrix. Report SAND-90-2281C, Sandia National Labs., Albuquerque, NM (United States), 1991
3. Mayes, R.L., Klenke, S.E.: SMAC modal parameter extraction package. Shock Vib. Digest **32**(1), 57 (2000)
4. O'Callahan, J.C.: System equivalent reduction expansion process. In: Proc. of the 7th Inter. Modal Analysis Conf., 1989
5. Schoenherr, T.F., Rouse, J.W., Harvie, J.: Characterizing dynamic test fixtures through the modal projection error. Report SAND2020-1119, Sandia National Lab.(SNL-NM), Albuquerque, NM (United States), 2020
6. Schoenherr, T.F., Paripovic, J.: Using Modal Projection Error to Evaluate SEREP Modal Expansion, pp. 111–138. Springer, Berlin (2022)
7. Eriten, M., Kurt, M., Luo, G., McFarland, D.M., Bergman, L.A., Vakakis, A.F.: Nonlinear system identification of frictional effects in a beam with a bolted joint connection. Mech. Syst. Signal Process. **39**(1–2), 245–264 (2013)

Chapter 5
Equivalencing of Sine-Sweep and Random Vibration Specification with Considerations of Nonlinear Statistics

Arup Maji

Abstract Comparison of pure sinusoidal vibration to random vibration or combinations of the two is an important and useful subject for dynamic testing. The objective of this chapter is to succinctly document the technical background for converting a sine-sweep test specification into an equivalent random vibration test specification. The information can also be used in reverse, i.e., to compare a random vibe spec with a sine-sweep, although that is less common in practice. Because of inherent assumptions involved in such conversions, it is always preferable to test to original specifications and conduct this conversion when other options are impractical.

This chapter outlines the theoretical premise and relevant equations. An example of implementation with hypothetical but realistic data is provided that captures the conversion of a sinusoid to an equivalent ASD. The example also demonstrates how to account for the rate of sine-sweep to the duration of the random vibration.

A significant content of this chapter is the discussion on the statistical distribution of peaks in a narrow-band random signal and the consequences of that on the damage imparted to a structure. Numerical simulations were carried out to capture the effect of various combinations of narrow-band random and pure sinusoid superimposed on each other. The consequences of this are captured to provide guidance on accuracy and conservatism.

Keywords Vibration · Random · Sinusoid · Testing · Simulation

5.1 Background

Random vibe can be due to various sources of vibration typically propagated through structural connections while the sine sweep could be due to engine humming at different rpm over time. The random vibe environment is specified as ASD (autospectral density) as g^2 vs. frequency (typically log scale), while the sine-sweep is specified as g vs. frequency (typically linear scale). The overall premise for equivalencing the two is to consider how these inputs lead to resonance in the structure being tested. For simplicity, structural dynamic equations pertaining to a single degree of freedom (SDOF) structure will be used, but the results are universally applicable.

Amplification at resonance $Q = 1/(2\xi)$ where ξ is the viscous damping factor. The half-power (3db) bandwidth (Δf) captures the frequency band around the resonant frequency fn within which most of the energy associated with resonance is concentrated: $\Delta f = 2\xi f_n = f_n/Q$. The time constant $t_n = T/(2\pi\xi)$ represents the duration for decay to $1/e$ of initial amplitude for free vibration (T is the period of vibration). It is also an indicator for the time needed for resonance to develop; in this application, it is small enough for resonance to develop during the sine-sweep. The basic premise of equivalencing is to look at each frequency, consider the energy within the half power (3db) bandwidth (Δf), and evaluate the equivalent imparted damage (note: $\Delta f = f_n/Q$).

Sandia National Laboratories is a multimission laboratory managed and operated by National Technology & Engineering Solutions of Sandia, LLC, a wholly owned subsidiary of Honeywell International Inc., for the U.S. Department of Energy's National Nuclear Security Administration under contract DE-NA0003525.

This paper describes objective technical results and analysis. Any subjective views or opinions that might be expressed in the paper do not necessarily represent the views of the U.S. Department of Energy or the United States Government.

A. Maji (✉)
Sandia National Laboratories, Albuquerque, NM, USA
e-mail: amaji@unm.edu

J. Harvie (ed.), *Dynamic Environments Testing, Volume 7*, Conference Proceedings of the Society for Experimental Mechanics Series, https://doi.org/10.1007/978-3-031-34930-0_5

The root-mean-square acceleration g (g-rms) of a pure sinusoid of amplitude G_s is $G_s/\sqrt{2}$, g-rms of response is therefore $QG_s/\sqrt{2}$. The g-rms of an ASD (where G_{xx} is the ASD at frequency f_n) within the half-power (3db) bandwidth Δf is $\sqrt{(G_{xx}\,\Delta f)} = \sqrt{(G_{xx}\,f_n/Q)}$.

The g-rms response of a SDOF oscillator to a wide band (Δf) random vibe is captured by the Miles' equation: The g-rms $= \sqrt{(\pi Q G_{xx} f_n/2)}$. Note that this is similar to amplification factor x the g-rms of input, $Q \times \sqrt{(G_{xx}\,f_n/Q)}$, but differs by the factor $\sqrt{(\pi/2)}$. This is due to the fact that the peaks of the response to a narrow-band random vibe follow a Raleigh distribution due to the superposition of various frequencies and random phase.

The implication of this Raleigh distribution is the greater possibility of peak amplitudes that are farther from the mean. Since fatigue damage follows a power law, these larger peaks have a far more significant effect. Cap [1] did a detailed analysis with various fatigue damage parameters to determine the appropriate factor N_σ to capture this effect. N_σ is defined as the ratio between the peak of a pure sinusoid and the g-rms of the corresponding narrow-band random that provides the same damage (note: ratio of g-rms of pure sinusoid to g-rms of equivalent narrow-band $= N_\sigma/\sqrt{2}$).

Our specifications are based on low-cycle-fatigue coefficient of 6.67, which corresponds to a 3 dB increase for time compression of factor of 10. Cap's numerical analyses [1] provided a N_σ value ≈ 2 for a fatigue coefficient of 6.67. This N_σ is based on the following equivalencing that considers both the root-mean-square (rms) response and the consequence to fatigue damage between a sine tone of peak amplitude G_s and an ASD of G_{xx}:

From [1] $G_s = N_\sigma\ \sqrt{(\pi Q G_{xx} f_n/2)}/Q = N_\sigma\ \sqrt{(\pi G_{xx} f_n/2Q)}$.

Therefore,

$$G_{xx} = 2QG_s{}^2/\left(\pi f_n N_\sigma{}^2\right) \approx \quad QG_s{}^2/\left(2\pi f_n\right) \qquad \text{(Assumed } N_\sigma \approx 2\text{)} \tag{5.1}$$

Note that ignoring N_σ (assuming $= \sqrt{2}$) leads to a more conservative (higher) value of G_{xx}.

Equation 3–19 in document by Fackler (page 55) provides an equation for equivalent stress imparted $= C_r\sqrt{(\pi Q G_{xx} f_n/2)}$. This is identical in form to the equations used here. This reference [2] also provides detailed discussion on numerous technical aspects relevant to this memo.

5.1.1 Equivalencing of Duration of Sine-Sweep Versus Random Vibe

The time duration for which sine-sweep is within each subsequent half-power bandwidth is $\Delta f/R = f_n/QR = 2\xi f_n/R$, where R is the rate of sine-sweep (example: if sine sweep is between 1 and 4 khz for a 30 min test, $R = 100$ Hz/min). If the equivalent random vibe test has a duration of t minutes, G_{xx} needs to be multiplied by $(2\xi f_n/Rt)^{0.3}$ to account for the relative durations. The time-compression factor 0.3 in the last equation depends on the relevant low-cycle fatigue parameter (0.3 for ASDs corresponds to 0.15 for G and is inverse of the fatigue coefficient of 6.67 used).

It is now important to recognize that the random vibe occurs simultaneously with the sine-tone and therefore the ASDs need to be added. However, the individual sine-tones occur in sequence (at different points in time that add up to 30 min).

5.2 Implementation Process with Example

The specifications shown in Table 5.1 were used to illustrate the process. The moving sine-tone is to occur simultaneously with the random vibe ASD for a duration of 30 min. Hence the sine-sweep rate is to go from 1 to 4 kHz over 30 min (= 100 Hz/min). Damping factor is 0.05 ($Q = 10$). The ASD has a g-rms of 2.45 in the 1–4 kHZ regime, comparable to the sine-tone g-levels.

Step1: Determine desired octave spacing based on half-power bandwidth (Δf).
Step2: Convert the straight-line specs into octave-spaced data.
Step3: Convert each sine-tone into equivalent narrow-band ASD using (Eq. 5.1).

This is shown in Fig. 5.1; dashed blue and green lines are original sine-tone and random data, solid green line is octave-spaced random data, and solid blue line is sine-tone converted to equivalent ASD for each octave-spaced data point. It is now important to recognize that the random vibe occurs simultaneously with the sine-tone and therefore the ASDs need to be added. However, the individual sine-tones occur in sequence (at different points in time that add up to 30 min).

Table 5.1 Data (specifications) used in example

Original sine-tone spec		Original random spec	
Freq (Hz)	(g)	Freq (Hz)	ASD (g^2/Hz)
1000	1.5	1000	0.002
1600	2	4000	0.002
2100	1		
2500	1		
3200	1.9		
4000	2.2		

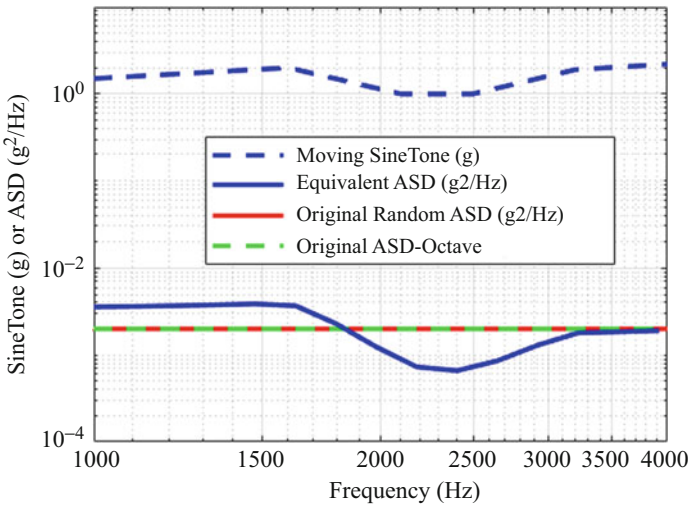

Fig. 5.1 Sine-tone converted to ASD

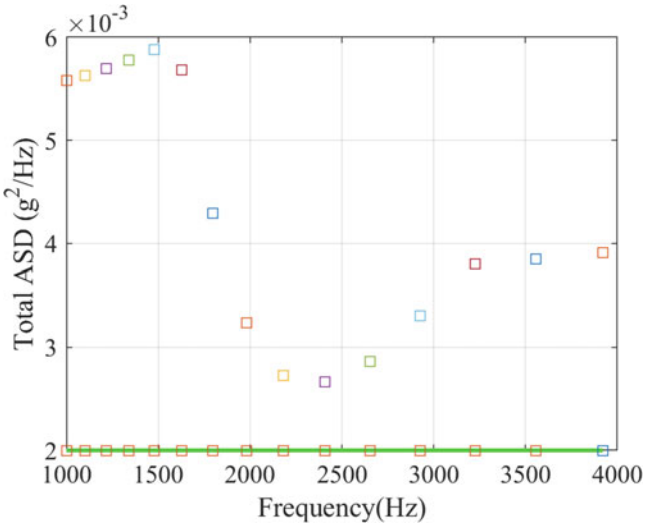

Fig. 5.2 Total ASDs vs. Stage5 ASD

Step 4: Each equivalent sine-tone ASD is added to the Stage5 ASD (solid blue and green lines in Fig. 5.1) since they occur simultaneously. Result is shown in Fig. 5.2 (original Stage5 ASD is shown in green).

Step 5: Since the different ASDs (examples shown in Fig. 5.3a–c) occur in sequence, they are combined using fatigue-time-compression algorithm (based on Miner's rule and the time-compression factor mentioned earlier).

Figure 5.4 shows the final combined specification (red) along with the original Stage5 spec and the sine-tone equivalent ASD separated from the random spec (same as solid blue line in Fig. 5.1).

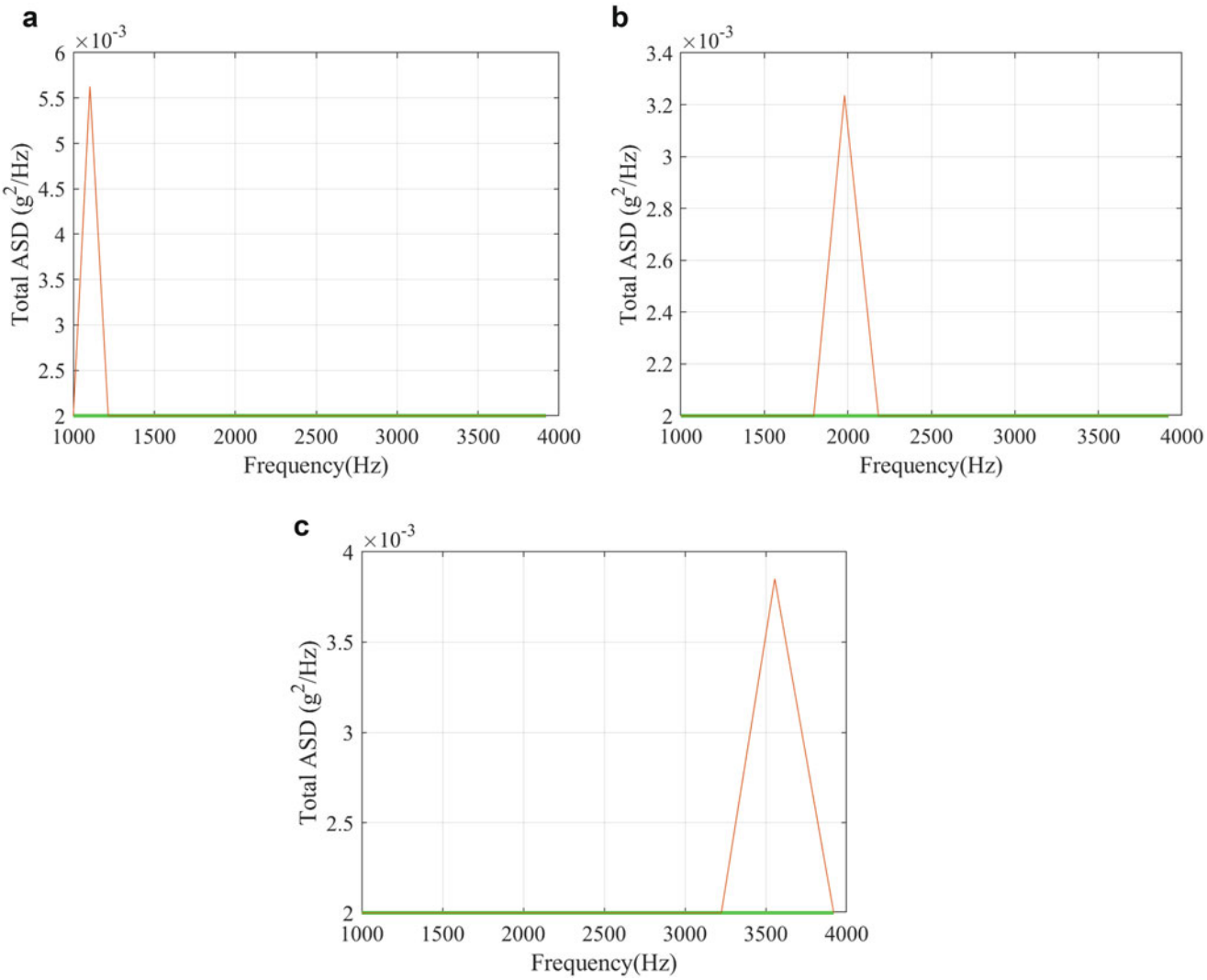

Fig. 5.3 (**a**) Total ASD at 2nd time interval. (**b**) Total ASD at 8th time interval. (**c**) Total ASD at 14th time interval

5.3 Nonlinear Statistics and Equivalent Fatigue Damage

This section examines through numerical simulations how to account for the parameter N_σ defined earlier in (Eq. 5.1). N_σ captures the nonlinear effect of statistical distribution of peaks in a narrow-band random signal and the consequent damage imparted. The issues and the consequent effects are captured for both pure sine-tone and that superimposed on a random vibration. Effect of various fatigue damage coefficients is also demonstrated.

Narrowband signal was created with ASD = 0.01 g^2/Hz between 950 and 1050 Hz (bandwidth = $\Delta f = 2\,\xi\, f_n = 100$ Hz for $f_n = 1000$ Hz). Therefore, g-rms = (100 × 0.01)ˆ0.5 = 1.0. A realization of this ASD for a 10 second duration with sampling rate of 10,000 is shown in Fig. 5.5. A zoomed-in version of the time series is also shown to illustrate the modulated sinusoid.

Figure 5.6 shows the histogram of 10,033 peaks into 40 bins demonstrating Raleigh distribution with a peak value at 1.0 (equal to the g-rms of the signal) and max beyond 4.0. A normalized Raleigh distribution [Eq. 5.2] is superimposed on the histogram (red line). The formula for Raleigh distribution of peaks (x) of a narrow-band random signal formula is shown below for a waveform of g-rms = σ.

$$P\,(x/\sigma) = \frac{x}{\sigma^2} e^{\frac{-x^2}{2\sigma^2}}. \tag{5.2}$$

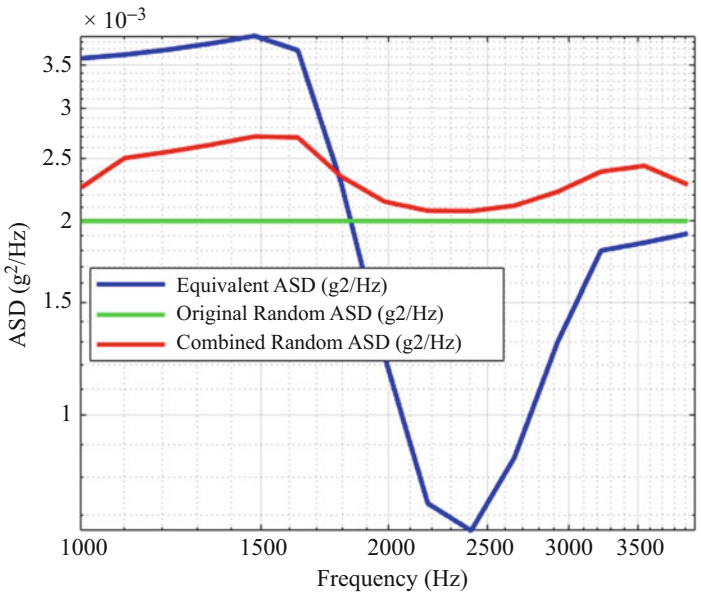

Fig. 5.4 Equivalent test specification (red)

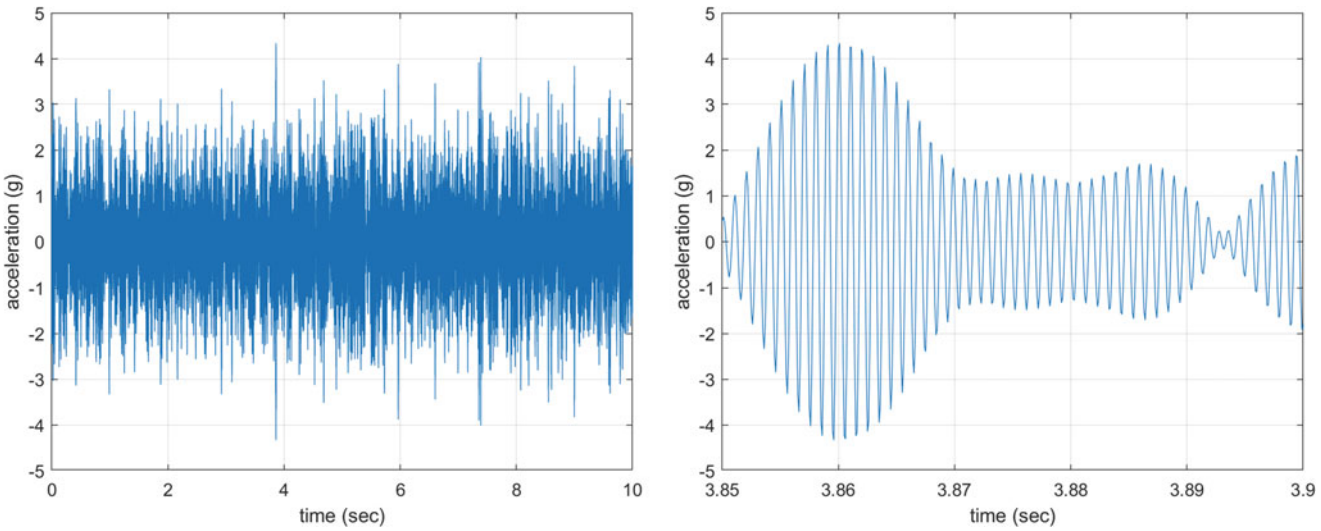

Fig. 5.5 Time-domain realization of a narrowband ASD of g-rms = 1.0

Figure 5.6 shows that the narrow-band random has many peaks above $\sqrt{2} \approx 1.4$ (which corresponds to the peak of a pure sinusoid of the same g-rms =1.0). This leads to a higher imparted damage since the low-cycle-fatigue damage law ($damage = \Sigma stress\hat{}b$) exaggerates the effect of higher amplitudes. The exponent b depends on the type of failure; $b = 6.65$ (ductile failure) is typically used in our analyses. Based on this Raleigh distribution of the sinusoid peaks, the corresponding damage can be calculated. An equivalent sinusoid (single frequency) that imparts the same damage can be determined by adjusting the peak of that pure sine-tone. This equivalency leads to various values of the factor N_σ, discussed earlier (Eq. 5.1) for corresponding values of b. These are shown in Fig. 5.7 ($b = 2$, 4, and 16.65 corresponds to energy, fretting corrosion, and quasi-brittle failure, respectively, $b = 6.65$ leads to $N_\sigma \approx 2$ shown by the red line).

Figure 5.8 shows the time-domain realization of pure sinusoid superimposed on a narrowband ASD, each with g-rms = 1.0. The narrow-band random had an autospectral density (ASD) of 0.01 between 950 and 1050 Hz.m and the sinusoid had a peak amplitude of $\sqrt{2}$ at 1000 Hz. The resulting signal has an rms value of $\approx\sqrt{2}$. The same zoomed-in portion is also shown to compare with the realization of only the narrow-band signal. Note that in contrast with Fig. 5.5 (narrow-band random only), the new signal has many exceedences above 4 g and a few above 5 g.

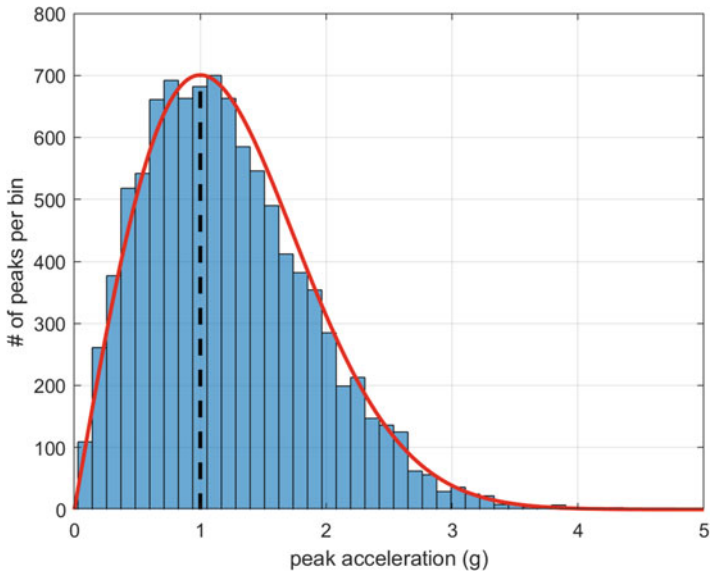

Fig. 5.6 Distribution of peaks of the narrow-band random signal (g-rms = 1.0)

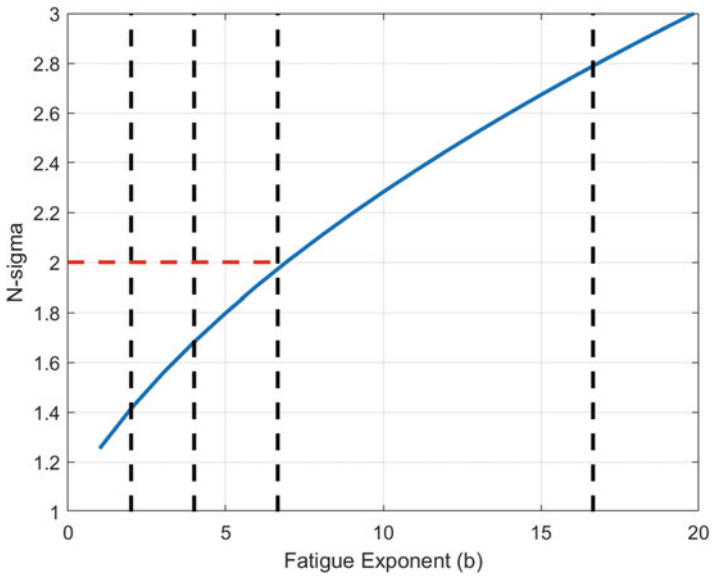

Fig. 5.7 Factor N_σ for various values of b

A "rainflow" analysis was done on several combined (sinusoid + narrow-band random) time-domain signals each with correspondingly greater ratio of the g-rms values of the sinusoid to the narrow-band random signals. The signals with this ratio of 0 (random only) and 1.0 (same g-rms) have been shown earlier in Figs. 5.5 and 5.8. Signals with this ratio = 2.0 and 5.0 (g-rms of pure sine-tone = 5.0) were also generated and added to the narrow-band random.

Figure 5.9 shows the histograms of the cycles from the "rainflow" analyses on the four signals described earlier (progressively increasing ratios). For comparison, the histograms were all normalized for the g-rms of the total signal being 1.0. It can be seen that the narrow-band random had a Raleigh distribution discussed earlier with a most probably occurrence near 1.0, when the pure sinusoid dominates (ratio = 5) the distribution is more "normal" with peak close to 1.4 (peak of a pure sinusoid of g-rms = 1.0 is $\sqrt{2}$). On the other hand, when the sinusoid gets smaller compared to the narrow-band random, the distribution is progressively closer to that of the narrow-band random (blue line depicting Raleigh distribution). Since with decreasing ratio of sinusoid/narrow-band-random the resulting distributions progressively deviate from that of the pure sine-tone (single peak at $\sqrt{2}$), it can be presumed that Nσ will decrease progressively from ≈2.0 to ≈1.0.

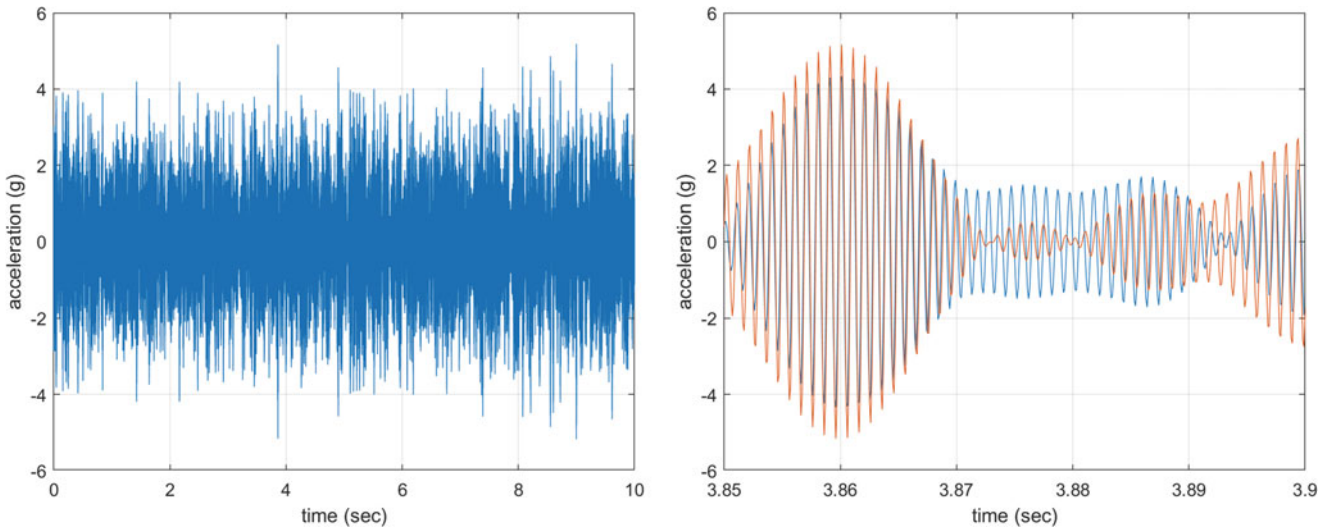

Fig. 5.8 Realization of pure sinusoid superimposed on a narrowband ASD

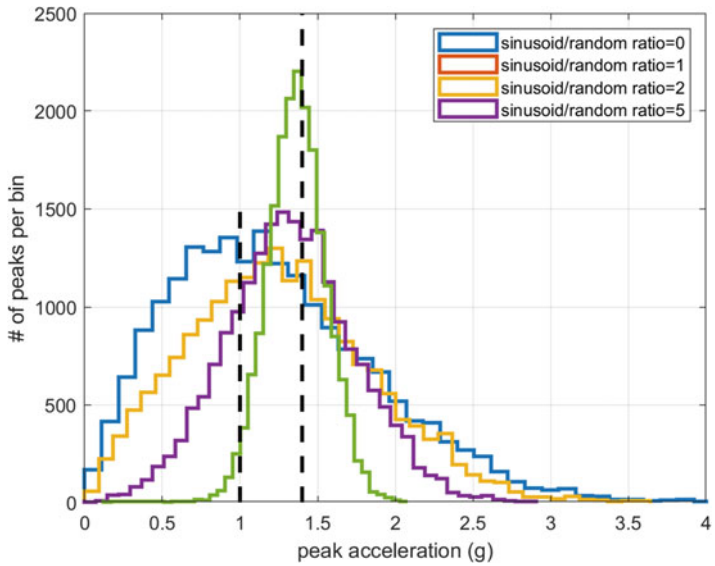

Fig. 5.9 Distribution of cycles for signals with different sinusoid/narrow-band random

Figure 5.10 shows this change of N_σ for various ratio of sinusoid to narrow-band random using simulations described in the steps below. The total simulation time was extended to 100 s to get more statistically representative results.

- Signals were created by adding (in time domain) the narrow-band random signal to the sinusoid multiplied by various factors (0.25, 0.5, 1.0, 2.0, 3.0, 4.0, 5.0).
- "Rainflow" analysis was done to determine the number of fatigue cycles of various magnitude; some of them are shown in Fig. 5.9.
- Total damage for each combined signal was determined using the equation for damage above ($D_{\text{total}} = \Sigma$(fatigue cyclesˆ6.65)).
- A total equivalent g-rms of a narrow-band random that would have the same damage was determined $g\text{-rms}_{\text{total}} = {D_{\text{total}}}^{1/6.65}$.
- This $g\text{-rms}_{\text{total}}$ is due to both the original narrow-band random $g\text{-rms}_{\text{random}}$ plus the sinusoid (of g-rms = 1.0) converted to an equivalent narrow-band random with $g\text{-rms}_{\text{sine}}$. Hence:
- ${g\text{-rms}_{\text{sine}}}^2 = {g\text{-rms}_{\text{total}}}^2 - {g\text{-rms}_{\text{random}}}^2$
- By original definition

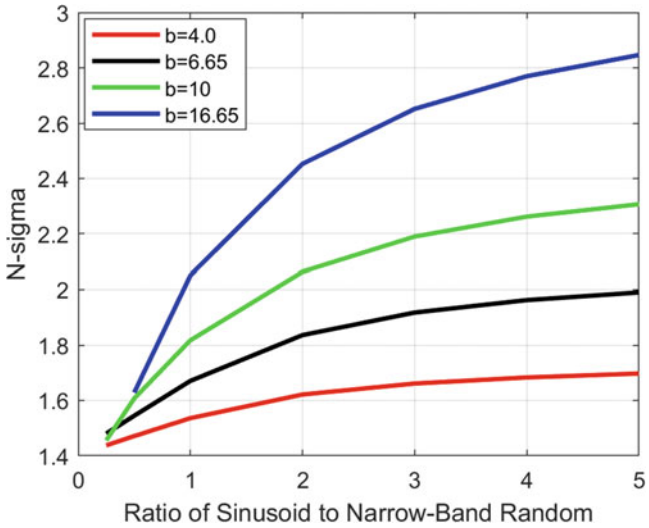

Fig. 5.10 Value of N_σ for various ratio of sinusoid to narrow-band-random

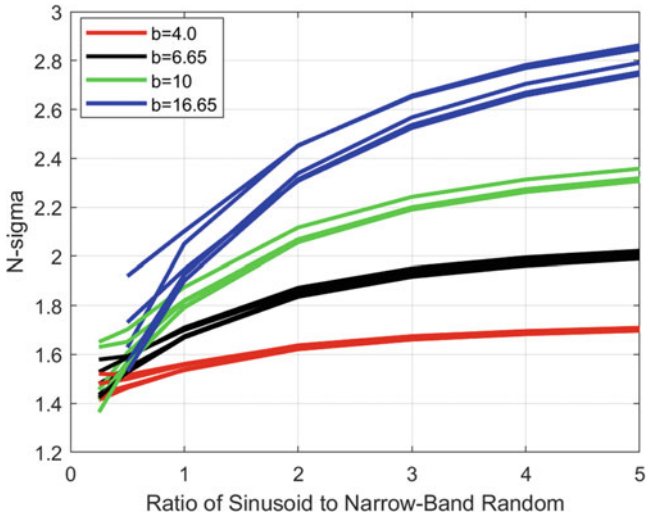

Fig. 5.11 Variation of N_σ for various recreations of narrow-band-random

$$N_\sigma \;=\; \text{sinusoid-peak}/g\text{-rms}_{\text{sine}} = \text{sinusoid-peak}/\sqrt{\left(g\text{-rms}_{\text{total}}{}^2 - g\text{-rms}_{\text{random}}{}^2\right)} \tag{5.3}$$

Figure 5.10 shows that N_σ approaches the values corresponding that of the pure sinusoid for ratios approaching 5. The effect of N_σ is insignificant ($\approx\sqrt{2}$) for small values of sinusoid (based on relative g-rms values) and approaches 2.0 when the sinusoid is dominant. Figure 5.11 shows the variation of N_σ for various recreations of time-domain signals from the same ASD (due to randomly generated relative phase). The variation is greater for higher values of the fatigue coefficient (b) since that amplifies the effect for the few instances the signal has high amplitude. The variation is also greater for small relative values of the sinusoid since the denominator of Eq. 5.3 is small and hence subject to greater fluctuations for each generation of random signal from the same ASD. For values of $b < 10$, the variation is <5% for higher ratio of sinusoid to random, which is negligible compared to most other sources of errors in real-life data. For small ratio of sinusoid to random, if the goal is to convert a sinusoid to an equivalent narrow-band ASD (G_{xx}), it is conservative to assume the lower limiting value of $\sqrt{2}$ (i.e., simply ignore this issue), since per Eq. 5.1, a lower value of N_σ would lead to a greater value of ASD.

References

1. Cap, J.: “Environments specifications short course, sinusoidal vibration”, es2p3_sinevibration_103120.pptx
2. Fackler, W.C.: 1972, “Equivalence Techniques for Vibration Testing”, SVM-9, Shock and Vibration Monograph Series (DTIC, 1987)

Chapter 6
Evaluation of a Multiaxis Shock Fixture Concept

David E. Soine, Tyler F. Schoenherr, and Jack D. Heister

Abstract Mechanical shock testing utilizing different types of resonating fixtures is an aerospace environmental testing practice useful in simulating mid-field pyroshock. Qualification tests using these methods may be specified in single or multiple test axes, with each axis performed individually or sometimes all at once. Simple structures such as bars, beams, and plates have been used to repeatably perform single-axis resonant shock tests, while plates of varying sizes along with a 90 degree bracket have been used to perform tests that meet all axes requirements in a single shock test event.

This work will evaluate a different fixture concept, used in conjunction with a resonant plate. The fixture is designed to create a controlled resonant response in two axes, which when combined with the plate motion in the third axis can achieve a repeatable resonant shock response in all axes at once, with minimal setup time or operator trial and error. Modal properties of a combined fixture and plate assembly are used as performance objectives for the fixture design. Finite element modeling is used to evaluate and modify the fixture design. A fixture is then fabricated and tested in several configurations to evaluate modal response characteristics, shock response performance, and the performance of the model when predicting those quantities of interest.

Keywords Mechanical shock · Pyroshock · Modal analysis · Resonant fixture · Plate

6.1 Introduction

Pyroshock is a high-acceleration transient transmitted to a structure due to the use of an explosive bolt, joint, or other device containing energetics. These devices have been used to perform critical structure separation activities, such as stage separation in spacecraft. In the 1960s and early 1970s, the identification of pyroshock as a significant cause of electronics failure on spacecraft and other aerospace vehicles led to the development of pyroshock simulation techniques, and those test techniques began to be used to demonstrate that aerospace components can withstand these types of events. Resonant fixture shock testing was adopted as a technique for pyroshock simulation, and methods were developed utilizing simple plates, bars, or beams to provide a resonating platform for test article attachment. The test is performed by striking the resonant fixture assembly with a projectile or hammer in an appropriate direction, resulting in a rapid onset acceleration followed by a decaying sinusoidal acceleration corresponding to the excited resonant frequencies of the assembly. When a test is carefully

Sandia National Laboratories is a multi-mission laboratory managed and operated by National Technology & Engineering Solutions of Sandia, LLC, a wholly owned subsidiary of Honeywell International Inc., for the US Department of Energy's National Nuclear Security Administration under contract DE-NA0003525. SAND2022-14150 C

Disclaimer: This chapter describes objective technical results and analysis. Any subjective views or opinions that might be expressed in this chapter do not necessarily represent the views of the US Department of Energy or the U S government.

D. E. Soine (✉) · T. F. Schoenherr · J. D. Heister
Sandia National Laboratories, Albuquerque, NM, USA
e-mail: desoine@sandia.gov; tfschoe@sandia.gov; jdheist@sandia.gov

J. Harvie (ed.), *Dynamic Environments Testing, Volume 7*, Conference Proceedings of the Society for Experimental Mechanics Series, https://doi.org/10.1007/978-3-031-34930-0_6

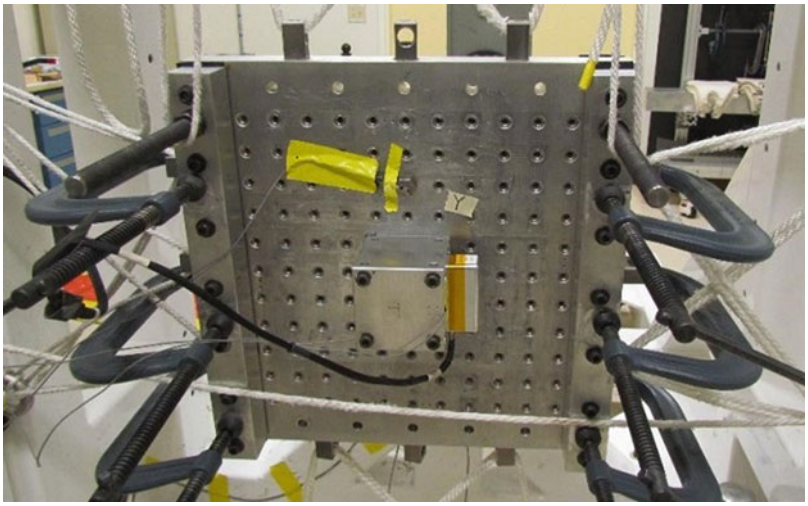

Fig. 6.1 A rope-suspended resonant plate with isolated damping bars and clamps added to achieve the desired shock response spectrum. A test fixture with a test unit is attached to the center of the plate. The projectile impact occurs on the opposite side of the plate

designed and performed, the acceleration measured near the test article has a shock response spectrum similar to that of actual pyroshock events measured during vehicle field tests (Fig. 6.1).

6.2 Resonant Fixture Fundamentals and Extension to Multi-axis Response

The fundamentals of resonant fixture design for uniaxial shock response, as developed at Sandia National Laboratories, were documented by Neil Davie and Vesta Bateman [1, 2]. Three techniques were developed, exploiting the fundamental modes of vibration of simple structures. Handbook formulas were used as the primary design tool. The resonant bar technique exploits the extensional natural frequency and mode shape of a bar (free-free boundary conditions), with the resonant frequencies estimated by Eq. 6.1. Dimensions of the resonant bar are selected such that the natural frequency of the extensional mode aligned with the desired peak in the shock response spectrum.

$$f_n = \frac{nc}{2L} \tag{6.1}$$

$n = 1, 2, 3 \ldots$
$c =$ wave speed in the bar (~199,000 in/sec for aluminum)
$L =$ bar length

When the end of the resonant bar is struck with a projectile, the resulting wave travels the length of the bar, and reflections within the bar result in excitation of the extensional modes. The test unit is mounted to the end of the bar opposite the impacted end, and the bar end motion provides the shock simulation to the unit. The resonant beam and resonant plate techniques were developed in a similar fashion to resonant bar, except they exploit the first bending mode of the beam or plate. Design dimensions of the plate and beam are similarly estimated from handbook equations. The design approach for resonant beam can be found in the references [2] and are not discussed here. Regarding resonant plate, the method has been implemented primarily on square plates suspended to simulate free boundary conditions. The first three flexural modes of a square plate are the twist (torsion) mode, the saddle mode, and the breathing (plate bending) mode, respectively. The plate is struck with the projectile in the center, perpendicular to the plane of the plate. This location takes advantage of the fact that the twist and saddle modes both have node lines through the center point of the plate, whereas the center of the plate is a point of maximum motion of the breathing mode; therefore, response of the twist and saddle modes are minimized while the breathing mode is strongly excited. The test unit is mounted to the center of the plate opposite the projectile impact point.

The fundamental lessons from successful uniaxial designs for resonant shock test structures are (1) utilize the lowest flexural modes possible when designing to the intended peak frequency, and (2) exploit the mode shape (node lines, etc.) to

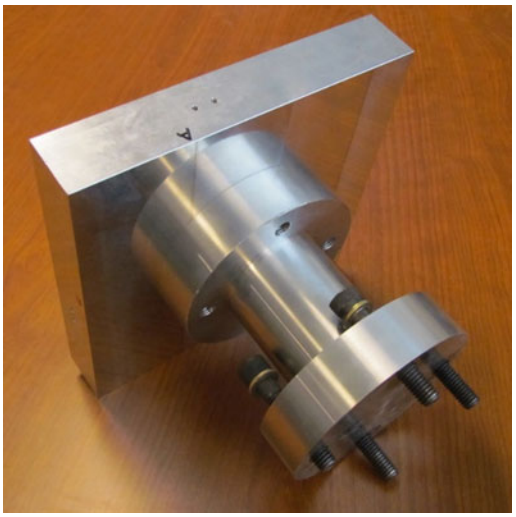

Fig. 6.2 Cylindrical concept fixture with a 7 × 1.25 inch square plate to simulate loading with a small test article

suppress or enhance the modal response as needed. The approach taken in this work will attempt to extend these principles by combining simple structures into an assembly that responds strongly in three axes to a single projectile impact.

6.3 Cylindrical Concept Fixture Design

A cylindrical adapter fixture to be attached between the resonant plate and the test article was designed and fabricated. With the cylinder attached perpendicular to the plate surface, the fundamental design concept was for the plate bending motion to provide one axis of shock response perpendicular to the plate, while the cantilevered cylinder bending response would dominate the motion parallel to the plane of the plate. The test article is mounted to the end of the cantilevered cylinder. For this work, "impact direction" or "Z-axis" motion will refer to motion perpendicular to the plate, while "transverse" or "X- and Y-axis" refers to motion parallel to the plane of the plate.

The design goal of the cantilevered cylinder was for a first bending frequency between 500 and 600 Hz. The fixture design was modeled in CAD, with a simulated test unit consisting of a seven-inch square plate. Initial dynamic modeling and tailoring of the cylinder dimensions resulted in an estimated frequency of 593 Hz for cylinder bending of a combined plate, cylindrical fixture, and simulated test unit, which was deemed adequate to proceed with fabrication and testing. Flanges and bolted interfaces at each end of the cylinder were designed to match the standard bolt pattern (1.5 inch) common to the resonant plates in the test laboratory (Fig. 6.2).

Resonant plate testing was developed to perform single-axis shock tests, with a high response in the test direction and very low transverse response. One concern for the cylindrical concept fixture was how to excite the bending modes that would hopefully dominate the transverse acceleration response of the test article. Methods considered to enhance the transverse response included changing the projectile impact location, impact direction, and location of the fixture on the plate. It is known that for the bending mode, the surface of the plate exhibits rotation at locations away from the plate center [3], and the team investigated the phenomenon to achieve excitation of the fixture in the transverse direction. Only results obtained by changing the location of the cylindrical fixture on the plate are reported here.

6.4 Modeling and As-Built Response

To enhance model-driven test design in the mechanical shock laboratory, a substantial finite element modeling (FEM) effort was undertaken prior to and in conjunction with the testing. Several challenges to accurate modeling were observed – one significant observation was the contribution of bolted interfaces to the measured shock acceleration and shock response. To mitigate these effects, precision steel spacers were added to cylindrical fixture interface. This interface modification was found to improve agreement between the shock response of the test and FEM [4, 5] (Fig. 6.3).

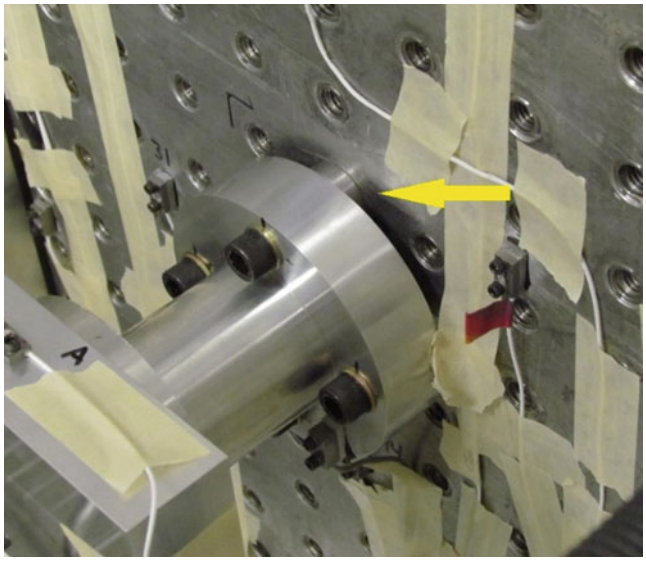

Fig. 6.3 A precision steel spacer (yellow arrow) installed between the cylindrical fixture and the resonant plate. In the future, this linearization of the physical system could be integrated into the machined surface of the fixture via a boss

Table 6.1 Natural frequency estimates from finite element modeling (FEM) and shock testing

	Initial FEM	High-fidelity FEM	High-fidelity FEM	Shock test	Shock test
Plate configuration	20.1 × 2.5″ plate	20 × 2″ plate assy.	20 × 2″ plate assy.	20 × 2″ plate assy.	20 × 2″ plate assy.
Fixture location	Center	Center	Offset 4.5,4.5″	Center	Offset 4.5,4.5″
Fixture Interface	Full surface	Linearized	Linearized	Linearized	Linearized
Cylinder transverse “X” (Hz)	593	495	487	462	510
Cylinder transverse “Y” (Hz)	593	503	502	500	462
Plate saddle/bending (Hz)	–	710	769	677	724
Plate bending (Hz)	–	927	995	887	968

One goal of model-driven test design is to accurately estimate the natural frequencies of the resonant fixture assembly, since the actual natural frequencies delivered by the shock test need to be within approximately 10–20% of the design target to be successful. Table 6.1 contains some of the resonant frequencies of interest, derived from both finite element modeling and testing. The frequencies from testing are the peak frequencies of the FFT of the shock acceleration response.

6.5 Test Results

Shock testing was conducted on a 20 × 20 × 2 inch resonant plate assembly. For these results, the plate was struck in the center by a 24 pound projectile at a velocity of approximately 34 feet per second, with one half inch of felt placed between the plate and projectile to lengthen the input pulse rise time. Two locations for the cylindrical fixture are reported here: center of the plate and offset 4.5 inches in both the *X* and *Y* dimensions (see Fig. 6.4). Shock acceleration measurements were made on the simulated test article.

Resonant plate shock testing is usually specified using the shock response spectrum (SRS), with typical specifications having an initial slope of approximately 12 dB/octave, with the specification rising to the target natural frequency for the test. Above the target natural frequency, the specification has zero slope. Typical test tolerances are ±6 dB from the reference. A reference shock response spectrum is used in this document for visual comparison to the measured shock response, see Table 6.2. Note that the initial slope of the reference spectrum in Table 6.2 is 9 dB/octave. In these results, the same reference spectrum is used for both the impact direction and transverse directions, but a better reference spectrum might have a target frequency of 550 Hz for the transverse axes, since that assumption was made (target natural frequency 500–600 Hz) during the design phase of the cylindrical fixture.

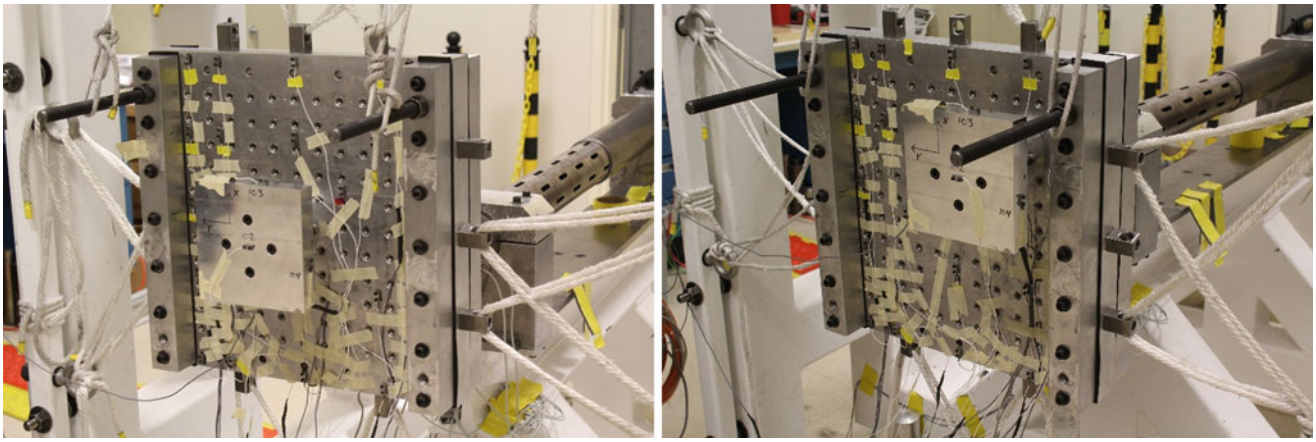

Fig. 6.4 Fixture centered (left) and offset 4.5 inches in the *X*- and *Y*-directions (right)

Table 6.2 Reference shock response spectrum used for visual comparison of results. The target natural frequency, sometimes called the "knee frequency," is 1000 Hz in this example

f_n (Hz)	MMAA SRS (g)
250	500
1000	4000
10,000	4000

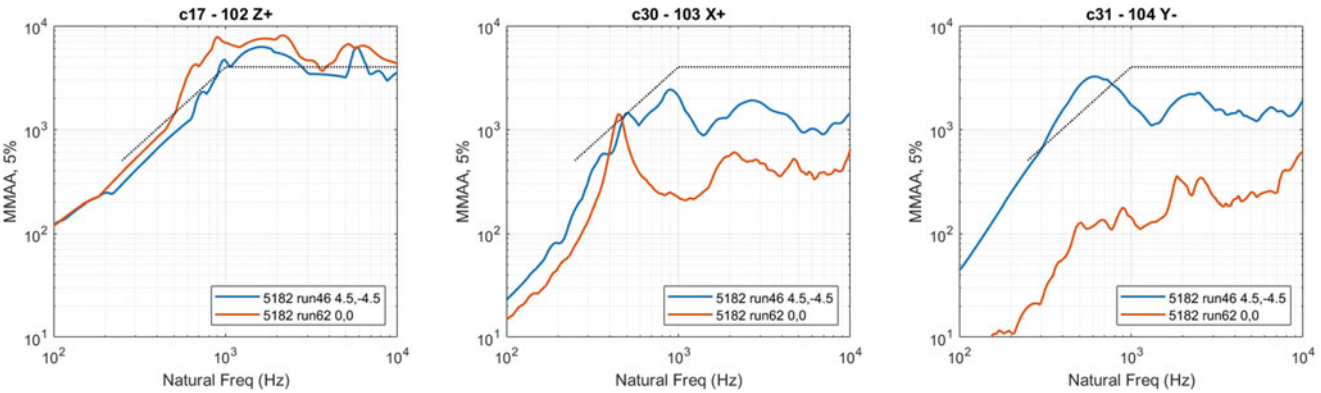

Fig. 6.5 SRS response at the simulated test article, with the fixture in the center of the plate (run62), and the fixture offset 4.5 inches in *X*- and *Y*-axes (transverse axes) (run46)

Figure 6.5 shows the plots of the shock response spectra achieved with the test article in the center location on the plate (represented by Run 62), and with the test article offset (Run 46). When the fixture is located at the plate center, a low transverse response is expected at the test article. This proved to be the case and the transverse shock response spectra were generally more than 18 dB below the response in the impact direction. The exception is at approximately 450 Hz in the *X* direction, where the transverse response slightly exceeded that of the impact direction. It appears that the cylinder bending response is excited by some aspect of the full test assembly motion. The plate assembly bending frequency has a peak at 887 Hz. Figure 6.6 shows the FFT of the acceleration response for both test cases.

With the fixture located in an offset location, 4.5 inches from the center in both the *X*- and *Y*-axes, the response in the impact direction (Z-axis) is 2–6 dB less than response when on-center, with a higher bending mode frequency of 968 Hz. Transverse response appears less than 12 dB below response in the impact direction and reflects the transverse cylinder bending frequencies at 462 and 510 Hz.

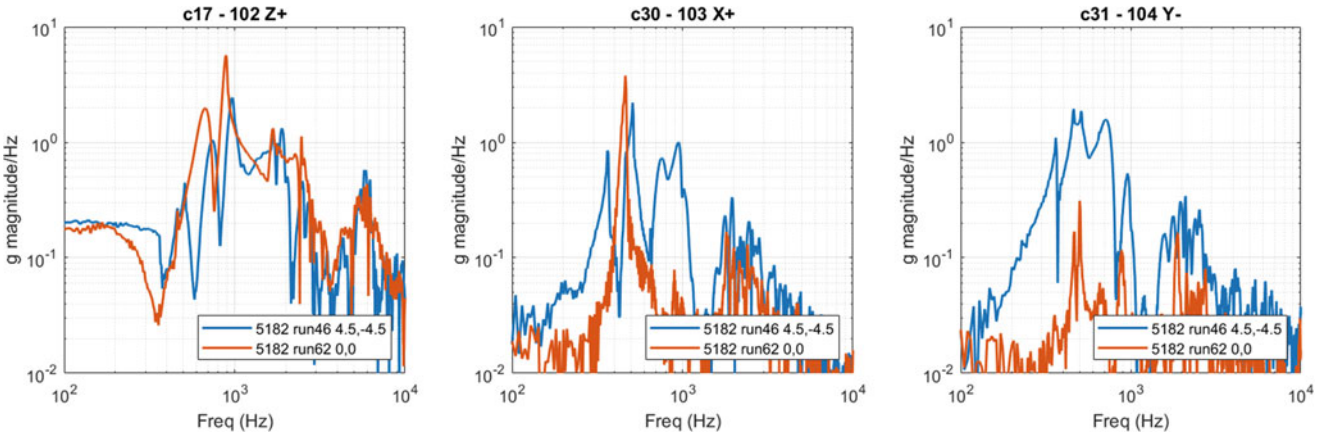

Fig. 6.6 FFT magnitude of Run 62 and Run 46

Table 6.3 Example of a plausible SRS profile that the test assembly in this work would come close to meeting with a single impact

f_n (Hz)	MMAA SRS (g) Impact direction	f_n (Hz)	MMAA SRS (g) Transverse
250	250	125	44
1000	4000	500	1400
10,000	4000	10,000	1400

Note in the impact direction, the initial slope is 12 dB/octave; in the transverse, initial slope is 15 dB/octave. The flat portion of the transverse SRS level is 9 dB below that of the impact direction

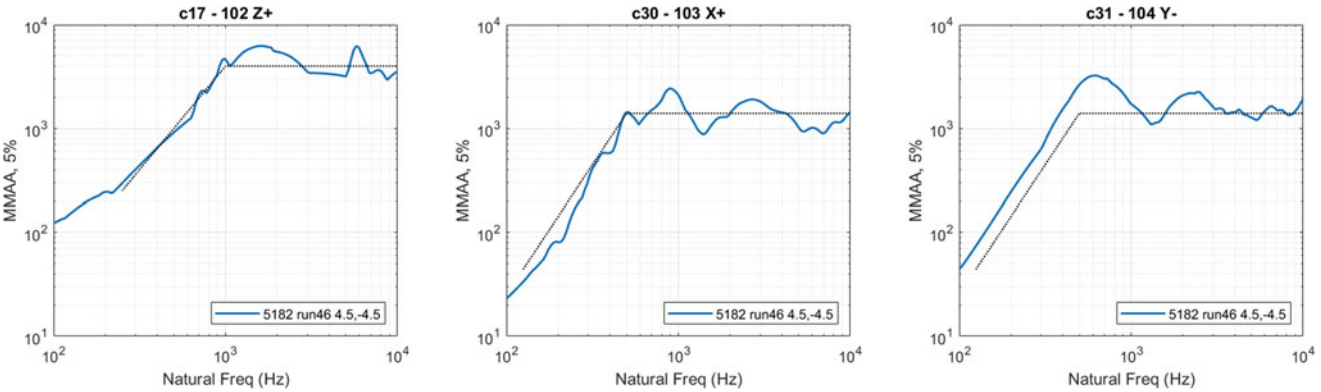

Fig. 6.7 Run 46 data, plotted with the reference SRS from Table 6.3

6.6 Specification Guidance and Test Equipment Development

This work demonstrates that the design approach used to develop the cylindrical fixture is viable to meet potential three-axis test specifications, with limitations. The specified SRS level of the transverse axes must be about 6–12 dB lower than the impact direction specification, and the frequency target for the transverse direction should be lower than the plate bending resonant frequency. Increasing the slope of the initial SRS profile in the transverse axes to 15–18 dB/octave would make the specification more producible, since the smaller expected velocity change in the transverse axes should drive a steeper slope in the SRS. Using this current work as an example, for the offset fixture location, the impact direction response would meet a specification like the reference SRS profile in Table 6.2. An example of a reference specification adjusted according to these guidelines is given in Table 6.3, and the data is plotted with the alternative reference specification in Fig. 6.7.

In practice, an appropriate test specification could be developed according to these guidelines if the flight test or ground test data supported it. The test article fixture, cylindrical fixture, and resonant plate would subsequently be developed with CAD and FEM according to the design guidance given above.

6.7 Conclusion

Resonant plate shock testing has been a versatile and productive test method for simulation of mid-field pyroshock. Addition of the cylindrical test fixture concept to resonant plate techniques can expand the method to repeatably perform shock tests that provide a controlled response in three axes to a single projectile impact, by design, with minimal intervention from the shock testing practitioner.

References

1. Davie, N.: The controlled response of resonating fixtures used to simulate pyroshock environments. In: *The Shock and Vibration Bulletin*. Bulletin 56 Part 3, The Shock and Vibration Information Center, Naval Research Laboratory (August 1986)
2. Davie, N., Bateman, V.: Recent Developments in Pyroshock Simulation Using Fixtures with Tunable Resonant Frequencies. Proceedings – Institute of Environmental Sciences (1994)
3. Sisemore, C., Babuska, V., Flores, R.: Multi-axis Resonant Plate Shock Testing Evaluation and Test Specification Development. Report SAND2020-10224, Sandia National Lab. (SNL-NM), Albuquerque (2020)
4. Schoenherr, T., Soine, D., Witt, B.: Experimental modal analysis of a resonant plate during a mid-field pyroshock replication test. In: Sensors and Instrumentation, Aircraft/Aerospace and Dynamic Environments Testing, vol. 7. Springer (2022)
5. Schoenherr, T., Soine, D., Witt, B.: Testing, Characterization, and Modeling of the Resonant Plate Test Environment. Report SAND2022-0780, Sandia National Lab. (SNL-NM), Albuquerque (2022)

Chapter 7
Operational Analysis of a Structure with Intermittent Impact

Ryan Wolfe and Dagny Beale

Abstract Modal characterization of a structure is necessary to inform predictive simulation models. Unfortunately, cost and schedule limitations tend to prioritize other dynamic tests, which can lead to inadequate or nonexistent modal testing. To utilize the dynamic test data that is acquired, analysts can extract operational deflection shapes (ODS) which can then be used as a substitute for modal data in model updating and structure characterization. However, extremely high levels of excitation during vibration testing may introduce nonlinear behavior that distorts the ODS prediction. This chapter investigates the reliability of using ODS as a replacement for traditional modal testing on an academic structure designed to respond with intermittent impact. This chapter calculates ODS from responses at several input excitation levels, and the influence of nonlinear impact on the resulting operating modes is discussed.

Keywords ODS · Model updating · Modal analysis · Dynamic environments testing

7.1 Introduction

Knowing the modal parameters of a structure is an important step toward understanding how that structure responds to dynamic excitation, as well as a key step in model validation. Traditional modal testing, however, is not always possible. As a substitute, operational techniques such as operational modal analysis (OMA) and operational deflection shapes (ODS) can be used to estimate the mode shapes and frequencies of a structure without traditional modal testing. Contrary to modal testing, structural response is measured during the operation of the structure, such as while a machine is running or in response to wind blowing past a building. Operational techniques are historically used to predict mode shapes of structures that cannot be tested with traditional modal techniques, such as extremely large structures like buildings or bridges [1]. The techniques can provide accurate predictions of the structure's modes, but only if the structure is properly excited. Operational techniques will miss modes if certain directions or subcomponents of a structure are not adequately excited. Similarly, if the excitation spectra do not include a certain frequency range, any mode shapes in that frequency range will not be captured. This is very likely in operational measurements where the excitation of the structure is uncontrolled.

More recently, operational techniques have been used to gain insight about structures that could be modal tested when modal data does not exist. Test schedules may not prioritize modal testing, but other test data such as shaker table vibration data are acquired. Performing operational techniques on the existing test data can give analysts some indication of the mode shapes and frequencies, which can help validate models. In addition, the excitation input spectra of vibration testing are known. Although the actual inputs to the structure in a vibration test are not measured, there is some insight about the

R. Wolfe · D. Beale (✉)
Sandia National Laboratories, Albuquerque, NM, USA
e-mail: djoffre@sandia.gov

J. Harvie (ed.), *Dynamic Environments Testing, Volume 7*, Conference Proceedings of the Society for Experimental Mechanics Series, https://doi.org/10.1007/978-3-031-34930-0_7

structural excitation that is captured and can be used to help identify frequency ranges or components that may have mode shapes missed in the operational shape estimation due to inadequate excitation.

As operational techniques are used more often and for smaller complex structures, an investigation of potential pitfalls is needed. Nonlinear structural response in combination with varying levels of dynamic excitation have the potential to affect the ODS predictions. Excitation level has previously been shown to affect operational frequencies and shapes of a bridge and bell tower [2]. However, the modal parameters of those structures were not measured or analytically predicted, so the difference between the operational shapes and frequencies and the actual shapes and frequencies was not quantified.

This chapter investigates the influence of excitation levels on the predicted ODS of an academic structure with and without components with observable nonlinear contact in order to understand the reliability of predicted ODS from high-amplitude vibration test data.

7.2 Theory

Modal analysis is a powerful tool to characterize the frequencies, damping, and mode shapes of a structure. In traditional modal analysis, these characteristics are measured in a controlled test environment where all forces acting on the structure are measured. The response of the structure to a given load can be predicted once these characteristics of a structure are known. However, excitation forces required for traditional modal analysis may not be measured, either due to unknown forces acting on a structure in an operational setting or due to testing constraints. Operational modal analysis (OMA) and operational deflection shapes (ODS) are two similar approaches that can estimate the mode shapes of the structure without performing traditional modal analysis. The key differences between traditional modal, OMA, and ODS are based on the forces that are measured in the test and how the modal parameters are estimated [3].

In modal analysis, an excitation force and location are chosen to excite the full structure up to a frequency of interest. The relationship between the response of the structure and the excitation is calculated as a frequency response function (FRF). The H_1 formulation of the FRF is given in Eq. 7.1, where G_{xf} is the cross power spectrum between the response spectrum and the force spectrum, and G_{ff} is the auto power spectrum of the force. An FRF is calculated between each response measurement channel and each excitation channel, creating an FRF matrix.

$$\text{FRF} = \frac{G_{xf}}{G_{ff}} \tag{7.1}$$

The FRF matrix is then used to estimate the poles of the system, which are also estimates of the modal frequencies of the system. The partial fraction form of the FRF is given in Eq. 7.2, where $H(j\omega)$ is the FRF at a chosen frequency line given by the summation of m modes of the system, A_k is the residue matrix for the k^{th} mode, and p_k is the pole for the k^{th} mode. When the chosen frequency line is at the pole of a mode the term for that mode becomes very large, dominating the overall response of the structure. For systems with well-spaced modes, the response of the system at that frequency line will resemble a mode shape of the structure [4].

$$[H\,(j\omega)] = \sum_{k=1}^{m} \frac{[A_k]}{(j\omega - p_k)} + \frac{\left[A_k^*\right]}{\left(j\omega - p_k^*\right)} \tag{7.2}$$

One common method to estimate poles, and the method used in this chapter, is the complex mode indicator function (CMIF). The CMIF is a plot of the singular values of the FRF matrix at each frequency line. The singular value decomposition equation is given in Eq. 7.3, where A is a matrix, Σ is the diagonal matrix of singular values of A, U and V are singular vector matrices of A, and † indicates the Hermitian transpose [5]. Once the poles of the system have been estimated, the modal parameters of the structure can be estimated using curvefitting techniques, such as polyMAX, to extract the modal parameters of the structure.

$$A = U \Sigma V^{\dagger} \tag{7.3}$$

OMA attempts to use response data without measured force data to estimate the mode shapes of a structure. Instead, the structure is measured during an operating condition with the assumption that the excitation of the structure is broadband. A true FRF cannot be computed because the excitation force is not measured. However, a reference measurement can be selected, and transmissibility functions can then be calculated between the chosen reference measurement and all other measurements. An example transmissibility function, *TF*, is given in Eq. 7.4, where G_{xr} is the cross correlation spectra between the response spectra and the reference spectra, and G_{rr} is the auto power spectra of the reference.

$$TF = \frac{G_{xr}}{G_{rr}} \tag{7.4}$$

The same steps as modal analysis are followed using the *TF* instead of the FRF: poles are estimated and the *TF* is curvefit to estimate the modal parameters of the structure. However, there is no guarantee that the excitation is broadband or that the structure is fully excited. If so, mode shapes that are not excited will not be present in the data. The choice of reference point may also distort the predicted modal parameters, for example, if the reference point is located at a node of a mode.

ODS also attempts to use response data without measured force data by selecting a reference point and computing the *TF*. However, ODS does not attempt to curvefit the *TF*. Instead, ODS assumes that the response of the structure at an estimated pole of the system is dominated by the motion of that single mode. Because ODS does not require curvefitting to estimate the mode shapes, it is a simpler post-processing technique. Instead, the CMIF of the *TF* is calculated, and peaks in the CMIF are used to predict modal frequencies of the system. The response of the structure at a given frequency is the imaginary component of the *TF* at that frequency line, so the estimated mode shapes are easily obtained by selecting response motion at the predicted modal frequencies. As in OMA, the excitation is assumed to be distributed and broadband which can lead to missed modes if these assumptions are not met. In addition, the modes are assumed to be adequately spaced such that the response at a predicted modal frequency is dominated by only one mode. If there are two closely spaced modes in the system, ODS is likely to predict a single mode with a shape that is the combination of the two modes.

Operational shapes will be compared to the predicted true modes of the structure by computing the modal assurance criterion (MAC), given in Eq. 7.5 where e_i and e_j are the chosen shape vectors being compared.

$$\text{MAC}_{ij} = \frac{\left[\{e_i\}^T \{e_j\}\right]^2}{\left[\{e_i\}^T \{e_i\} \{e_j\}^T \{e_j\}\right]} \tag{7.5}$$

MAC values can range from a value of one, which indicates that the two vectors are correlated, to a value of zero, which indicates that the vectors are uncorrelated. The MAC is traditionally calculated between all modes of two data sets, such as between all measured modes and all FEA predicted modes, and presented as a color plot. Values on the diagonal of the color plot are expected to be near one, indicating that the modes between two sets are the same shapes and in the same order. Values of diagonal are expected to be near zero, indicating that the modes of the system are orthogonal to each other.

7.3 Structure Configurations

An academic structure shown in Fig. 7.1 was designed to respond to dynamic excitation with intermittent impact, thus inducing nonlinear contact. This structure was composed of five primary components: platforms, springs (essentially columns), blocks, L-brackets, and the impact stack. The impact stack is shown in Fig. 7.2 and consists of an impact hammer tip, a force gauge, an accelerometer cap, and an accelerometer. The L-brackets and impact stack will be collectively referred to as the impact assembly. The intermittent impact in the structure resulted from the impact stack colliding with the lower L-bracket.

Throughout this chapter, several variations of the structure are referenced. Table 7.1 identifies all of the variations of the structure discussed in the chapter. In addition, Table 7.1 identifies if modal test data was acquired in those configurations.

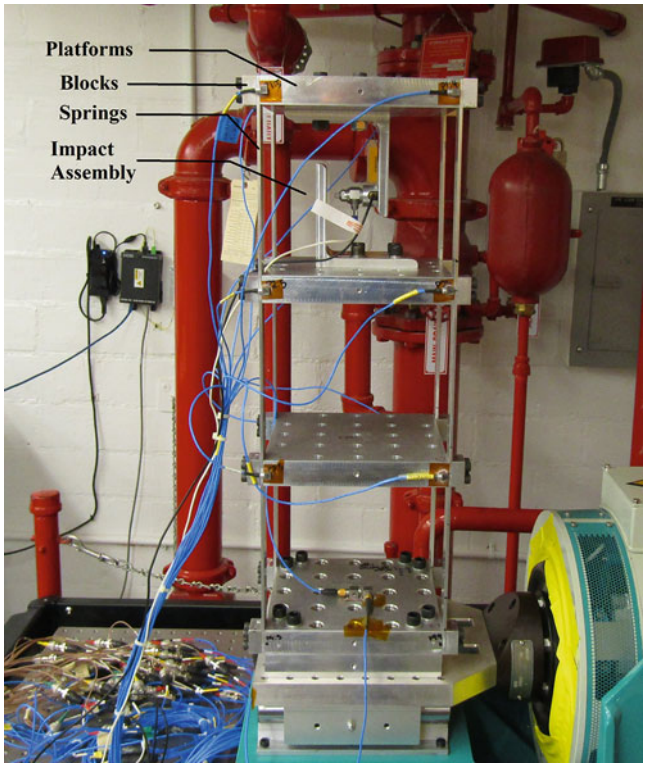

Fig. 7.1 Structure used to study the effect of nonlinear impact on ODS

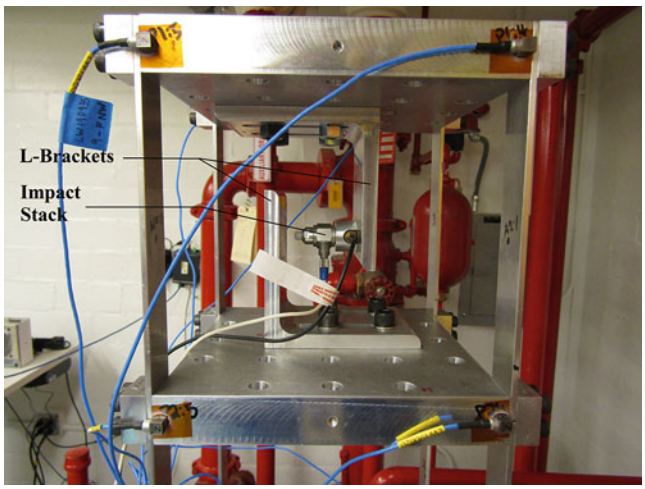

Fig. 7.2 Impact assembly used to induce intermittent impact in the structure

7.4 Approach

To assess the effect of excitation level on the calculated ODS, the structure was tested at six excitation levels: 0.57 Grms, 0.95 Grms, 1.06 Grms, 1.5 Grms, 2.12 Grms, and 3 Grms. Each test was a random vibration test (5–1000 Hz) performed on the same shaker table and instrumented using accelerometers placed at points on the platforms and impact assembly. Internal impact occurred at each excitation level; however, higher excitation levels experienced more frequent impact, resulting in increased levels of nonlinear behavior. The measurement locations were chosen to capture the dominant motion of the structure. Figure 7.1 shows the structure in the vibration test configuration.

Table 7.1 All configurations of the structure modeled and tested

	Structure without the impact assembly in free-free	Structure with the impact assembly in free-free	Structure without the impact assembly on the vibration shaker	Structure with the impact assembly on the vibration shaker
FEA	✓	✓	✓	✓
Modal test	✓	✓	X	X
Vibration test	X	X	✓	✓

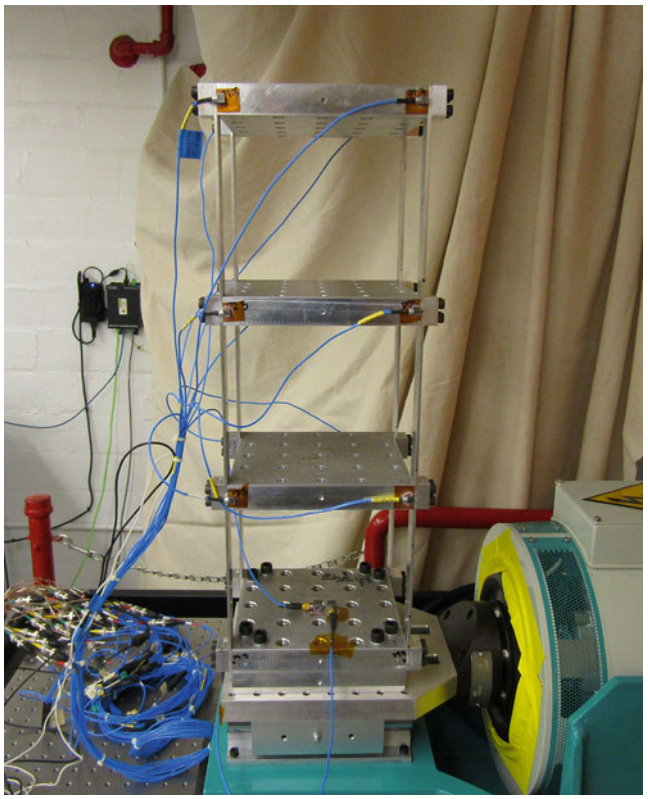

Fig. 7.3 Structure without the impact assembly on the vibration shaker

To assess the effect of excitation level on ODS consistency independent of impact, the structure was also tested at the same levels with the impact assembly removed, as seen in Fig. 7.3. Without the impact assembly, the structure's response was linear.

To assess the reliability of ODS with intermittent impact, a combination of traditional modal testing and finite element modeling was used to compare the ODS with the predicted true mode shapes of the structure. Modal testing in the same boundary condition as the vibration tests (i.e., structure fastened to the vibration shaker) was not possible due to equipment unavailability, so no test modes are available to compare to the ODS calculated shapes.

Instead, a calibrated finite element model was used to predict the mode shapes of the structure in the vibration test configuration to compare to the ODS. To aid in model calibration, a traditional modal test of the structure was performed in a free-free boundary condition. This test was performed using an impact hammer to excite the structure, and data was acquired using a laser Doppler vibrometer (LDV) to capture the structural response across more of the structure than would be possible using accelerometers. Impact between the impact assembly and the L-bracket was avoided during the modal testing by removing the hammer tip component from the impact stack because the unmeasured impact of the structure would have introduced forcing not accounted for in the calculation of modal parameters.

7.4.1 Model Calibration

A model of the structure with the impact assembly on the vibration shaker was built to compare predicted modes to the ODS that will be discussed in a later section. The model was built in Cubit [6], and all simulation results were run using the Sierra SD finite element codes [7]. Figure 7.4 shows the model with and without the impact assembly.

First, the measured free-free modal test data was used to calibrate the model of the structure in free-free conditions, initially without and then with the impact assembly. The modal test setup for each configuration is shown above in Fig. 7.5. The MAC plots between the modal test and calibrated model for the free-free structures are shown in Fig. 7.6.

The high MAC values along the diagonals of these two MAC plots indicate that the mode shapes are very consistent between model and test. Additionally, the natural frequencies are within a 5 Hz difference between the finite element model and modal test data, further indicating the model and test are closely matched. The portions of the MAC table at middle and high frequencies where there is no correlation indicated between model and test are closely spaced, repeated root modes of the springs in the structure. The lack of shape correlation can be explained by observing a typical shape comparison

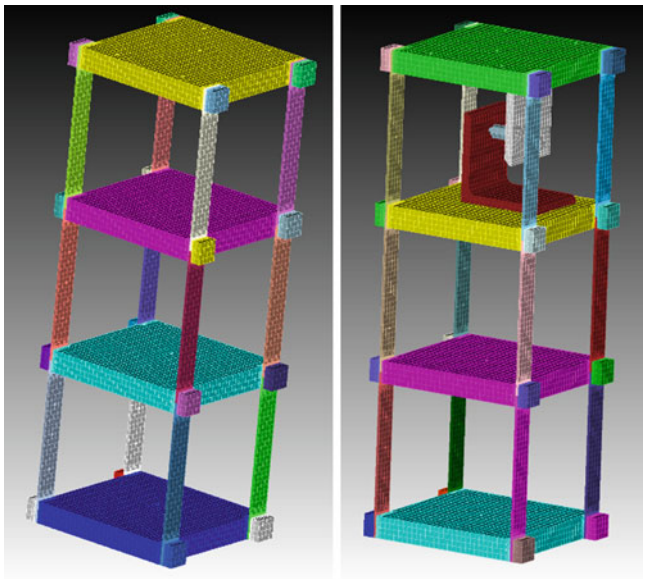

Fig. 7.4 Finite element model of structure without (left) and with (right) impact assembly

Fig. 7.5 Free-free modal test setup for structure without (left) and with (right) impact assembly

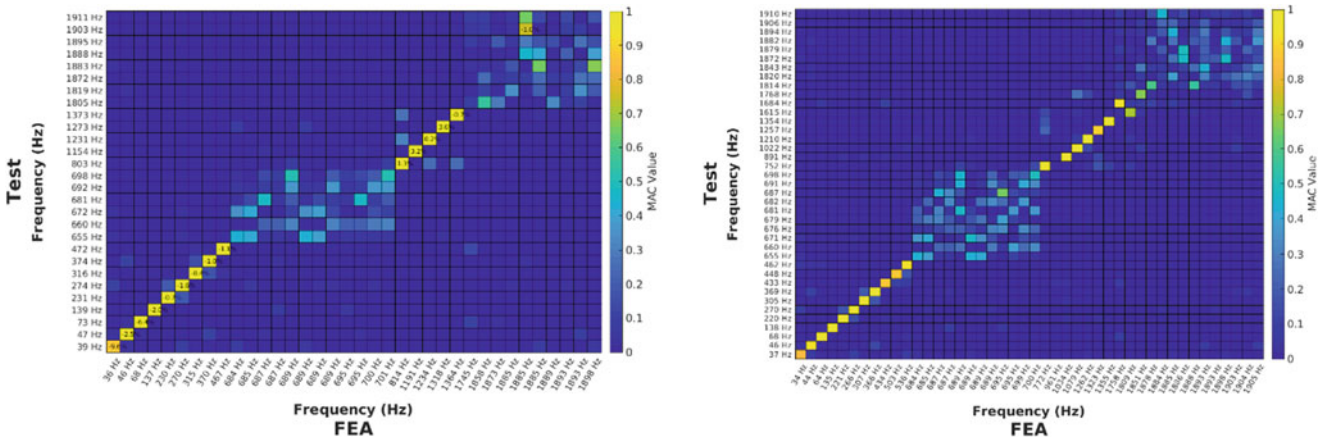

Fig. 7.6 MAC comparing model without impact assembly (left) and model with impact assembly (right) to free-free modal test

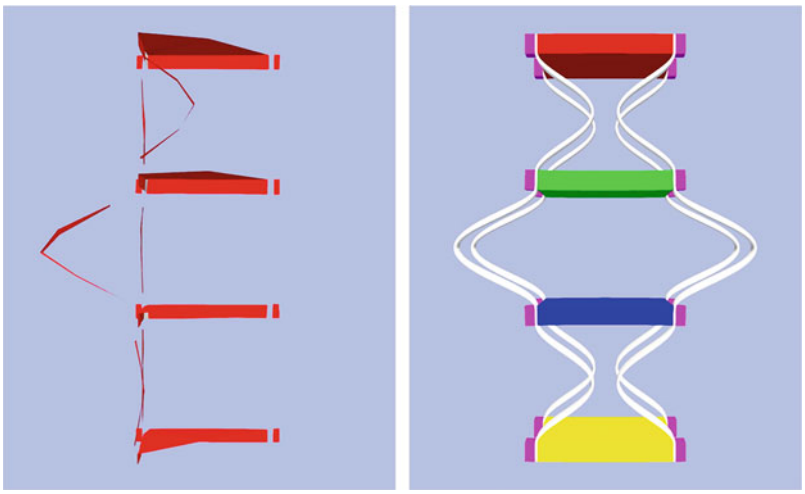

Fig. 7.7 Free-free modal test (left) and free-free model (right) first spring bending mode

in Fig. 7.7, which shows the first of the spring bending modes. Only two of the six measured springs show significant response for the selected mode, despite the model predicting that all modes will respond. The model predicts all of the springs in the structure will respond symmetrically at each level. This is unlikely to be captured in test data for three reasons: bolt tightness variations, boundary condition effects, and challenges resolving closely spaced modes from test data. Bolt tightness variations will result in non-symmetric spring responses, which can lead to poor matches between test and data unless every spring connection is individually tuned. The foam boundary condition used to test the structure in "free-free" was not included in the model, so some differences in shape are expected. This is represented in Fig. 7.8, where you can see the base of the structure in contact with the foam in the test data has less displacement than the top of the structure that is not in contact with the foam. And finally, resolving closely spaced repeated root modes with a single excitation is a known challenge in modal testing [4]. These modes clustered in a small frequency band are each a different combination of which springs are bending and their phase.

Figures 7.8 and 7.9 show the mode shapes obtained from the model for the structure in free-free with and without the impact assembly as compared to the corresponding mode shapes from the free-free modal testing. The primary discrepancy of note is the lack of symmetry in the 39 and 36 Hz mode shapes in Fig. 7.8, likely resulting from the non-zero stiffness of the foam the structure was sitting on in the free-free modal testing. Ultimately, these models were considered to be adequately calibrated to the test data and were then updated to have a fixed-base boundary condition. The modes from these fixed-base models were then used to compare to the shapes obtained from ODS. The model fixed base boundary condition is more severe than the actual shaker boundary condition shown in Fig. 7.1, so some differences are expected between the model predicted modes and the ODS obtained shapes and frequencies.

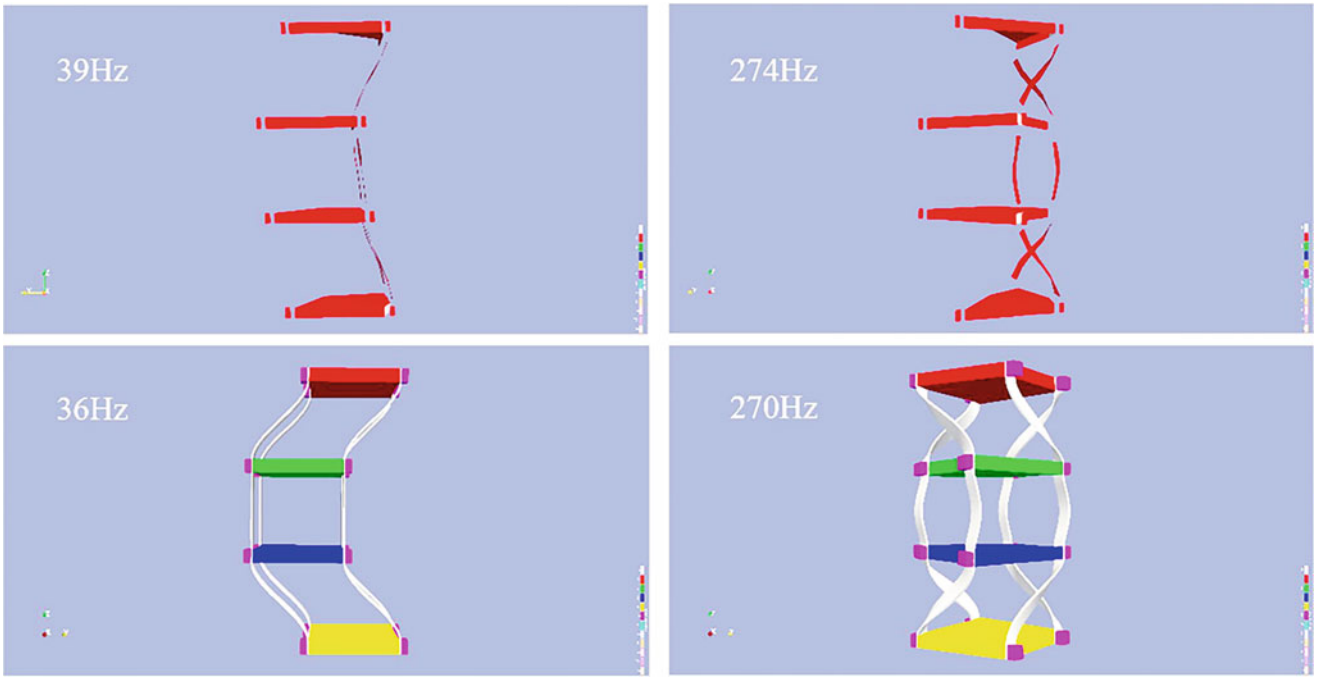

Fig. 7.8 Mode shape comparisons for structure without impact assembly

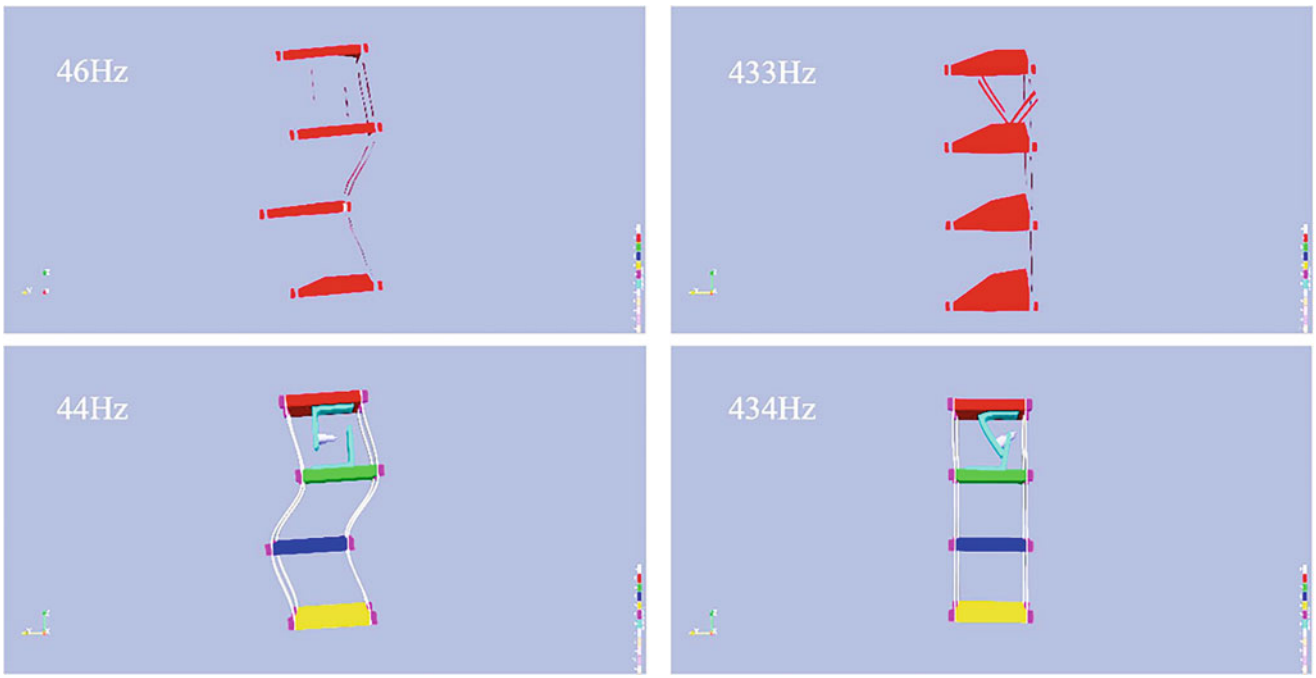

Fig. 7.9 Mode shape comparisons for structure with impact assembly

7.4.2 ODS

ODS were obtained for each excitation level using the acceleration time history data from the vibration tests. The selected reference node for the ODS procedure was located at the base of the structure, closest to the shaker. It was chosen because it most closely represented the input motion which helped to better capture the relative motion of the rest of the structure. Resonant frequencies were estimated by computing the CMIF of the *TF*s calculated using the reference node, and then using

the peak-picking function in Matlab to select peaks in the CMIF. Shape orthogonality was also enforced by computing a MAC of all shapes at each possible peak in the CMIF. If several peaks had a similar shape, the frequency with the highest CMIF value was chosen to be the estimated modal frequency. All other possible modal frequencies with that similar shape were not selected.

The primary method for comparing the mode shapes obtained from ODS and those obtained from the calibrated finite element model was also by using the MAC. Additionally, the MAC was used to compare the ODS obtained mode shapes at different excitation levels to more closely inspect the sensitivity of ODS to excitation level.

7.5 Results

Once the ODS procedure was conducted for each excitation level, the mode shapes from each excitation level were compared to one another in a "bigMAC" plot. With and without impact, the modal consistency across excitation levels is high overall. For both testing configurations (with and without the impact assembly), the primary region of low consistency is in the low frequency range less than 20 Hz. Figures 7.10 and 7.11 show these bigMAC plots for the structure with and without the impact assembly, respectively.

Next, the ODS obtained modes are compared to the finite element model obtained modes in Figs. 7.12, 7.13, 7.14, 7.15, 7.16 and 7.17. Additionally, the ODS obtained natural frequencies are compared to the finite element model modal frequencies in Tables 7.2 and 7.3. Bolded values in these tables indicate high modal consistency between the finite element model and ODS at that frequency. Tables 7.4 and 7.5 show only the frequencies for which the finite element model predicts mode shapes, with blanks in the ODS columns when ODS fails to predict that mode shape.

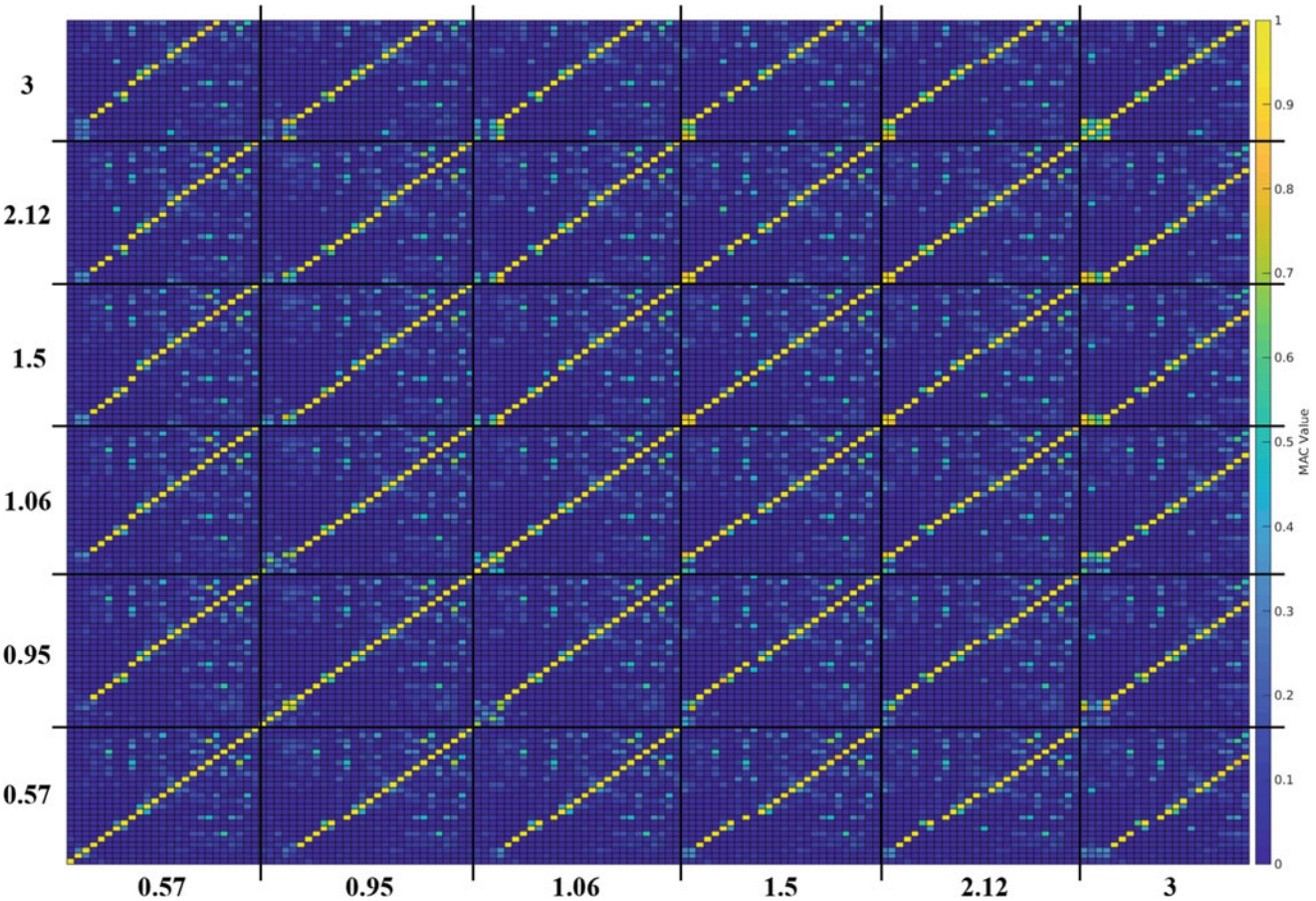

Fig. 7.10 MAC plot comparing consistency of ODS mode shapes across excitation level for structure with impact assembly

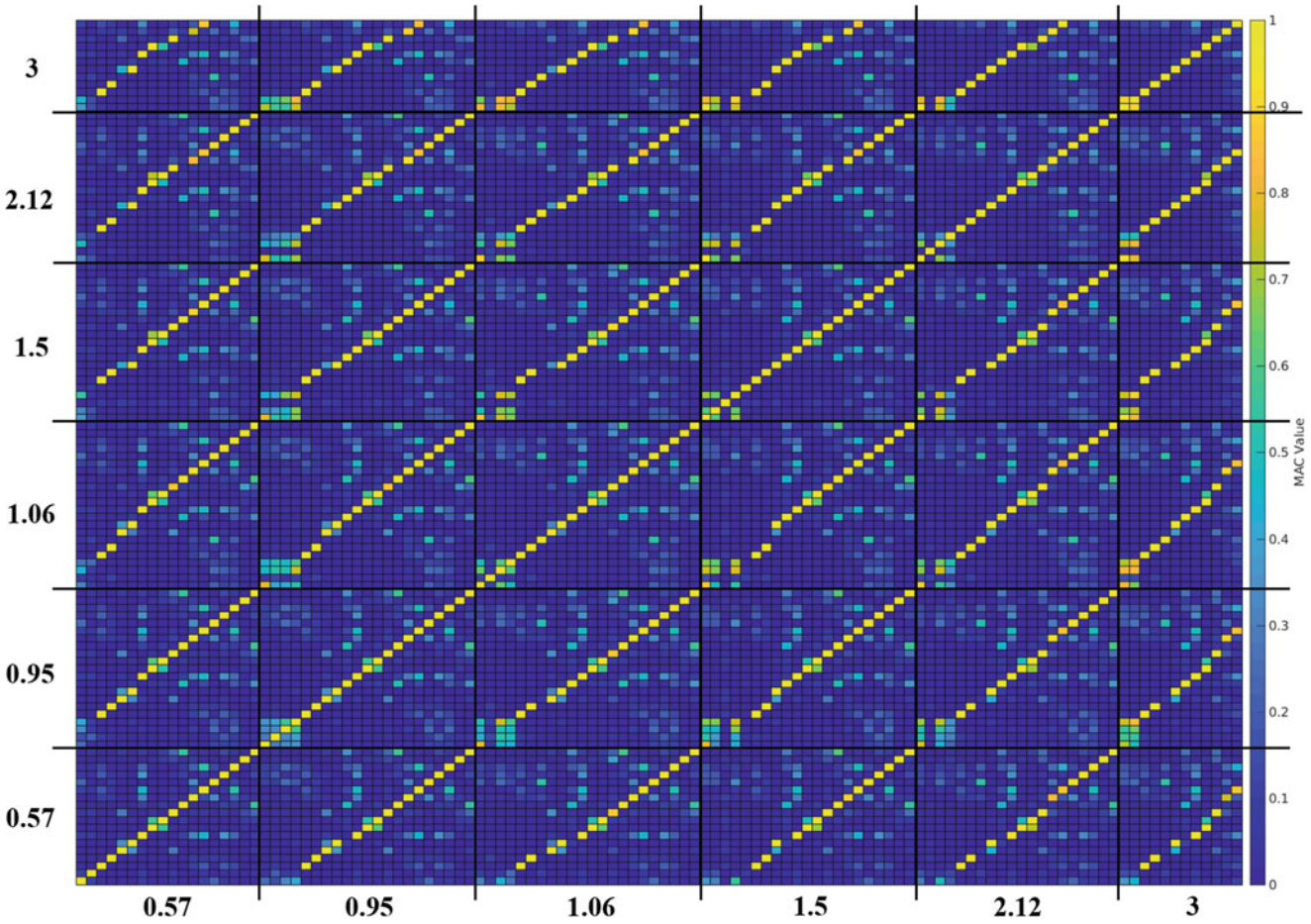

Fig. 7.11 MAC plot comparing consistency of ODS mode shapes across excitation level for structure without impact assembly

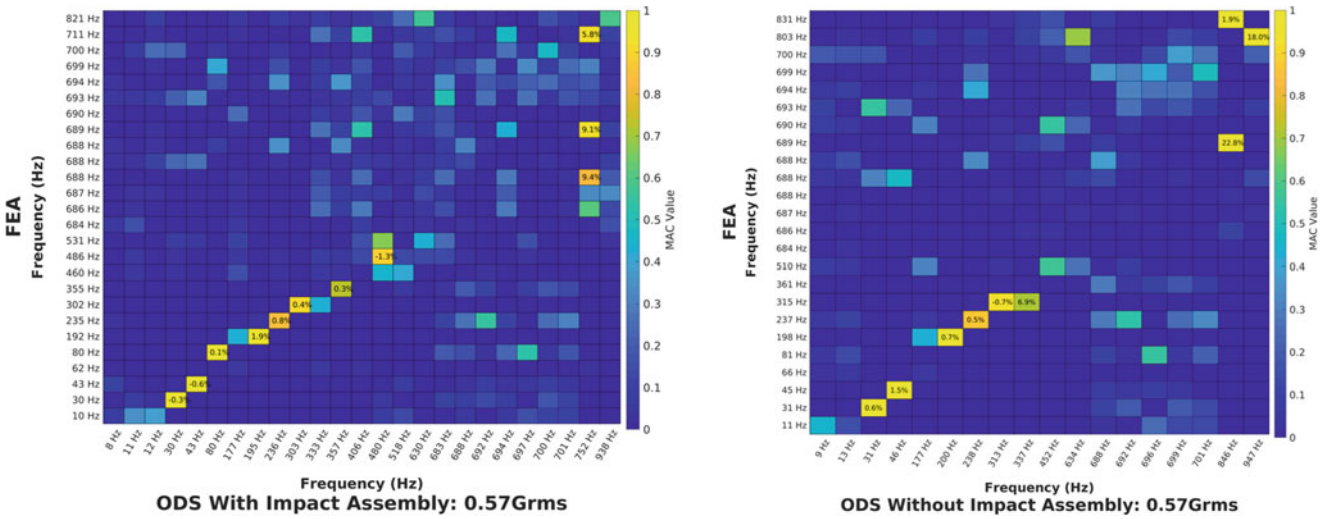

Fig. 7.12 MAC plots comparing ODS to finite element model mode shapes for structure with (left) and without (right) impact assembly at 0.57 Grms

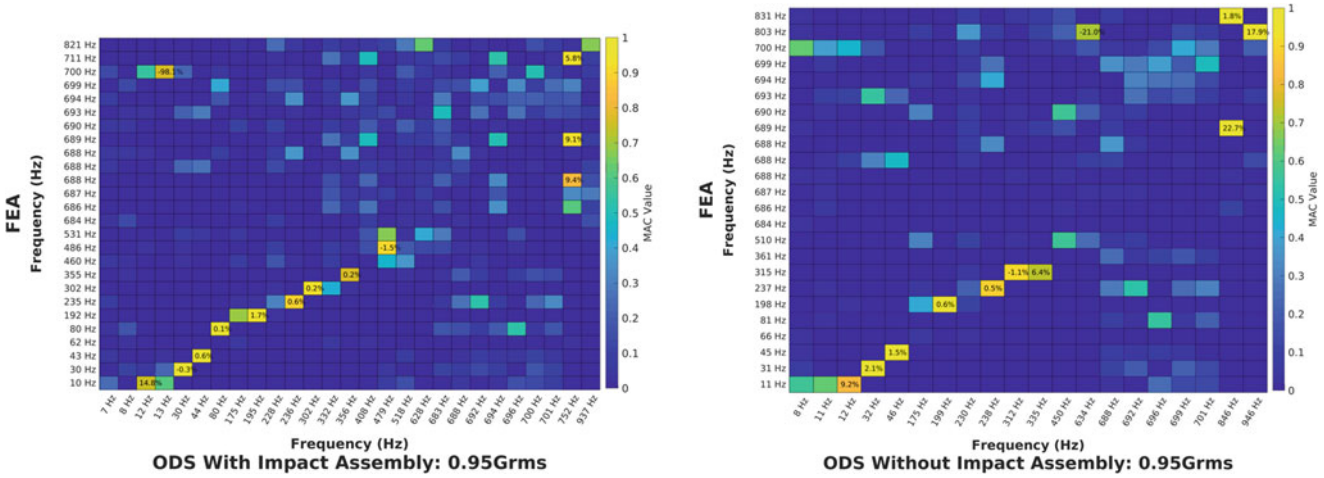

Fig. 7.13 MAC plots comparing ODS to finite element model mode shapes for structure with (left) and without (right) impact assembly at 0.95 Grms

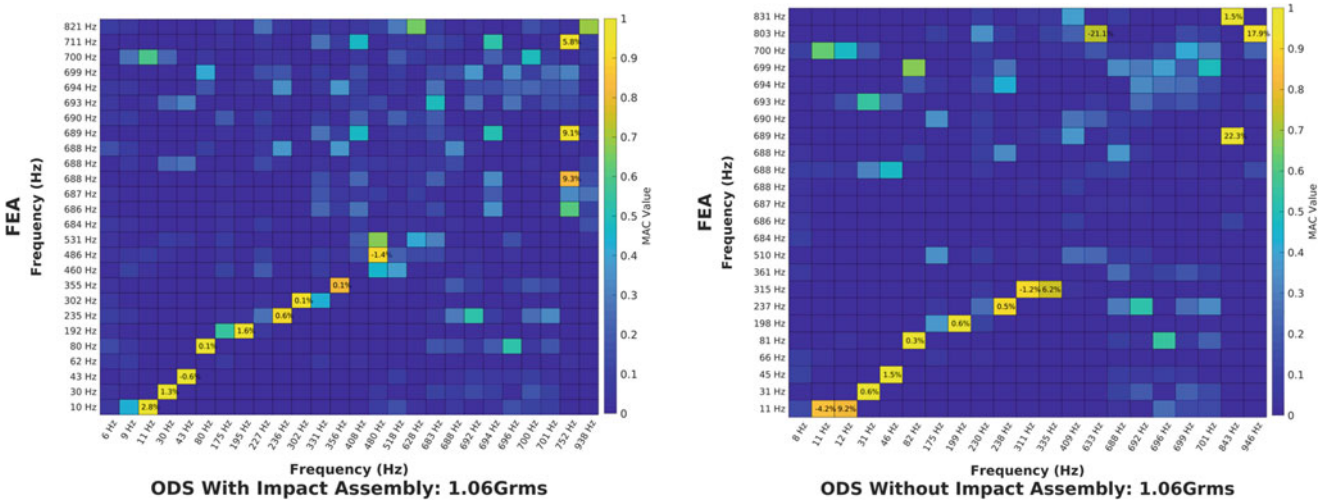

Fig. 7.14 MAC plots comparing ODS to finite element model mode shapes for structure with (left) and without (right) impact assembly at 1.06 Grms

Across all excitation levels and both structure configurations, the ODS procedure resolves a handful of mode shapes and their corresponding frequencies with high consistency with the finite element model. There is little difference in consistency from one excitation level to next; however, the higher excitation levels tend to have mode shapes exhibiting slightly more consistency and natural frequencies slightly closer to those shapes and frequencies of the finite element model. A possible explanation for this observation is that having higher levels of excitation could be increasing the response of the structure, making response peaks more prominent relative to noise. It is also worth noting that the ODS method picks up the first L-bracket bending mode for all permutations of excitation level and structure configuration. Some selected mode shapes highlighting the overall consistency between the ODS and finite element model obtained mode shapes are shown in Figs. 7.18, 7.19 and 7.20.

Across all excitation levels, the ODS procedure picks up modes that don't exist in the finite element model. These are a result of peaks in the *TF*s that are likely noise and not truly representative of actual modes. Another discrepancy worth noting is that the ODS procedure fails to resolve the mode at 66 Hz for the structure without the impact assembly and 62 Hz for the structure with the impact assembly across all excitation levels. The missed mode shape is an out-of-plane rocking motion, as

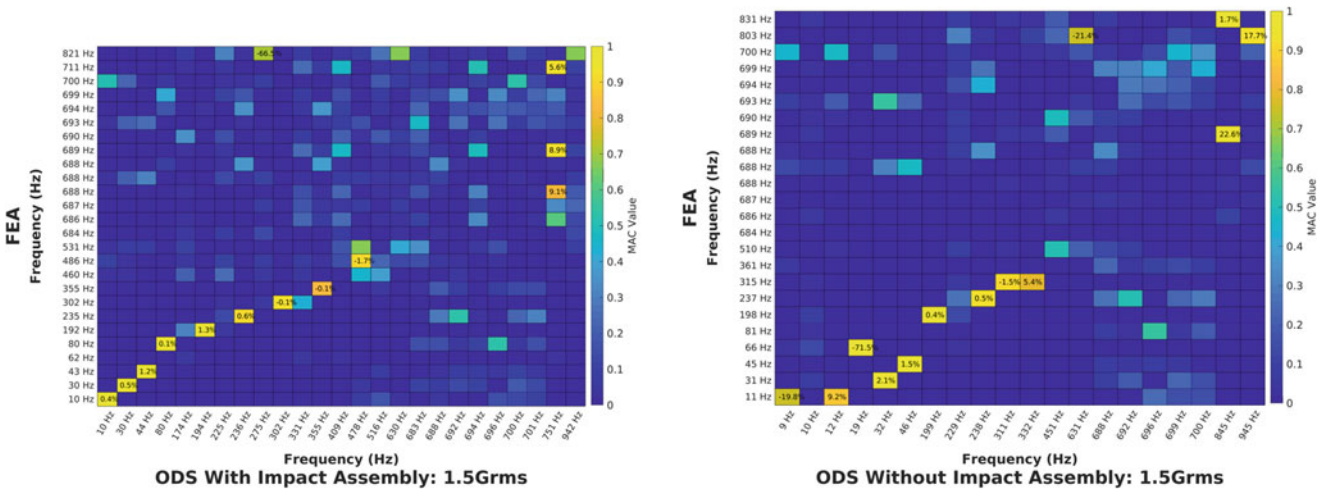

Fig. 7.15 MAC plots comparing ODS to finite element model mode shapes for structure with (left) and without (right) impact assembly at 1.5 Grms

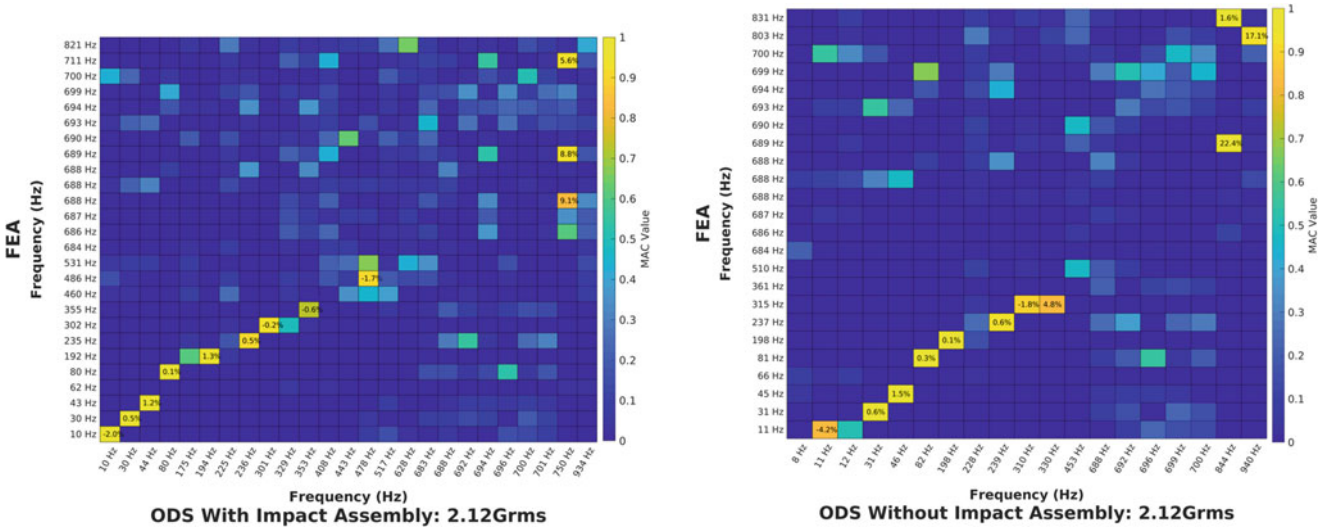

Fig. 7.16 MAC plots comparing ODS to finite element model mode shapes for structure with (left) and without (right) impact assembly at 2.12 Grms

can be seen in Fig. 7.21, while the excitation for the vibration testing was only in-plane. Since operational techniques only predict modes that are excited, this and other unexcited modes are unable to be estimated by ODS, as is emphasized in Tables 7.4 and 7.5.

Despite introducing observable nonlinear behavior, the addition of the impact assembly does not result in a significant decrease in consistency with the model obtained modes. In fact, at some excitation levels, it results in notably higher consistency. A possible explanation for this is that the induced impact provides more excitation to the structure that wouldn't have been induced by base excitation alone. The other primary difference between the configurations with and without the impact assembly is an increase in *TF* peaks for the structure with the impact assembly that are not representative of modes in the finite element model. This is somewhat expected since the structure with the impact assembly is essentially subjected to additional impulse forcing upon each impact. Ultimately, the impact assembly appears to result in somewhat better prediction of modes obtained from the finite element model, while also predicting more modes that likely are not actually modes.

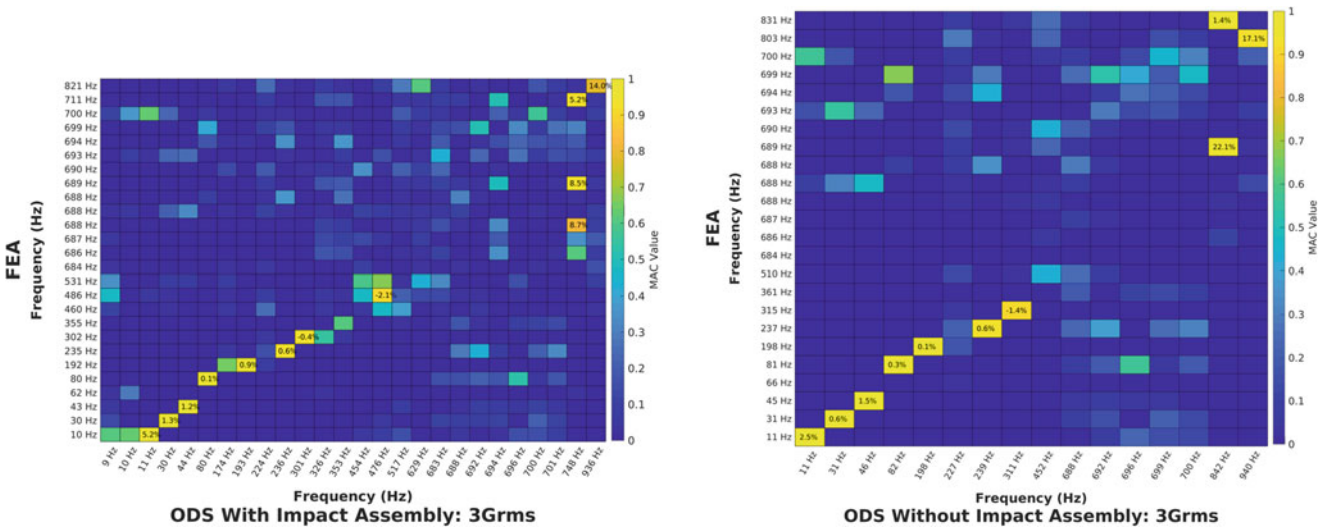

Fig. 7.17 MAC plots comparing ODS to finite element model mode shapes for structure with (left) and without (right) impact assembly at 3 Grms

Table 7.2 Resonant frequencies of structure with impact assembly from finite element model and ODS

	Finite element model	ODS: 0.57 Grms	ODS: 0.95 Grms	ODS: 1.06 Grms	ODS: 1.5 Grms	ODS: 2.12 Grms	ODS: 3 Grms
Modal frequencies (Hz)	**10**	8	7	6	**10**	**10**	9
	30	11	8	9	**30**	**30**	10
	43	12	12	**11**	**44**	**44**	**11**
	62	**30**	13	**30**	**80**	**80**	**30**
	80	**43**	**30**	**43**	174	175	**44**
	192	**80**	**44**	**80**	**194**	**194**	**80**
	235	177	**80**	175	225	225	174
	302	**195**	175	**195**	**236**	**236**	**193**
	355	**236**	**195**	227	275	301	224
	460	**303**	228	**236**	**302**	329	**236**
	486	333	**236**	**302**	331	**353**	**301**
	531	**357**	**302**	331	**355**	408	326
	684–700	406	332	**356**	409	443	353
	711	**480**	**356**	408	**478**	**478**	454
	821	516	408	**480**	516	517	**476**
		630	**479**	518	630	628	517
		683–701	518	628	683–701	683–701	629
		752	628	683–701	**751**	**750**	683–701
		938	683–701	**752**	942	934	**748**
			752	938			936
			937				

Table 7.3 Resonant frequencies of structure without impact assembly from finite element model and ODS

	Finite element model	ODS: 0.57 Grms	ODS: 0.95 Grms	ODS: 1.06 Grms	ODS: 1.5 Grms	ODS: 2.12 Grms	ODS: 3 Grms
Natural frequencies (Hz)	**11**	9	8	8	9	8	**11**
	31	13	11	11	10	11	**31**
	45	**31**	12	12	12	12	**46**
	66	**46**	**32**	**31**	19	**31**	**82**
	81	177	**46**	**46**	**32**	**46**	**198**
	198	**200**	175	**82**	**46**	**82**	227
	237	**238**	**199**	175	**199**	**198**	**239**
	315	**313**	230	**199**	229	228	**311**
	361	337	**238**	230	**238**	**239**	452
	510	452	**312**	**238**	**311**	**310**	688–700
	684–700	634	335	**311**	332	330	**842**
	803	688–701	450	335	451	453	940
	831	**846**	634	409	631	688–700	
		947	688–701	633	688–700	**844**	
			846	688–701	**845**	940	
			946	**843**	945		
				946			

Table 7.4 High consistency frequencies for structure with impact assembly

	Finite element model	ODS: 0.57 Grms	ODS: 0.95 Grms	ODS: 1.06 Grms	ODS: 1.5 Grms	ODS: 2.12 Grms	ODS: 3 Grms
Modal frequencies (Hz)	10	–	–	11	10	10	11
	30	30	30	30	30	30	30
	43	43	44	43	44	44	44
	62	–	–	–	–	–	–
	80	80	80	80	80	80	80
	192	195	195	195	194	194	193
	235	236	236	236	236	236	236
	302	303	302	302	302	–	301
	355	357	356	356	355	353	–
	460	–	–	–	–	–	–
	486	480	479	480	478	478	476
	531	–	–	–	–	–	–
	684–700	683–701	683–701	683–701	683–701	683–701	683–701
	711	752	752	752	751	750	748
	821	–	–	–	–	–	–

Table 7.5 High consistency frequencies for structure without impact assembly

	Finite element model	ODS: 0.57 Grms	ODS: 0.95 Grms	ODS: 1.06 Grms	ODS: 1.5 Grms	ODS: 2.12 Grms	ODS: 3 Grms
Natural frequencies (Hz)	11	–	–	–	–	–	11
	31	31	32	31	32	31	31
	45	46	46	46	46	46	46
	66	–	–	–	–	–	–
	81	–	–	82	–	82	82
	198	200	199	199	199	198	198
	237	238	238	238	238	239	239
	315	313	312	311	311	310	311
	361	–	–	–	–	–	–
	510	–	–	–	–	–	–
	684–700	688–701	688–701	688–701	688–700	688–700	688–700
	803	–	–	–	–	–	–
	831	846	846	843	845	844	842

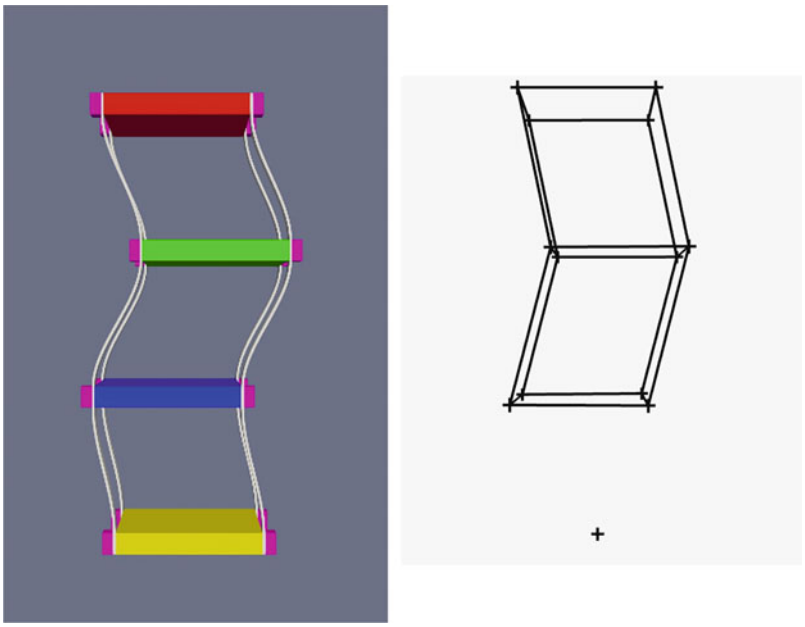

Fig. 7.18 Finite element model mode shape at 45 Hz (left) and ODS at 46 Hz (right) for 0.95 Grms

7.6 Conclusion

Without traditional modal testing to use as a basis for assessing the accuracy of the ODS obtained modal parameters, no conclusive statements can be made regarding the accuracy of the ODS obtained shapes and frequencies. The finite element model can be used to estimate the consistency but is not a perfect representation of the structure and cannot be used as a "truth" estimate of the actual mode shapes and frequencies. Most importantly, the model's fixed base approximation fails to represent the dynamics of the vibration shaker used for the vibration testing. Despite these limitations, there are some important takeaways from this research regarding the effect of excitation level and intermittent impact on the ODS obtained modal parameters. Especially for the structure without the impact assembly, as excitation level increases, the modal consistency appears to increase slightly. Without more reference data, concluding that increasing excitation level results in higher modal consistency would be unreasonable; however, it is a noteworthy observation worth further investigation. The addition of the impact assembly appears to result in somewhat higher modal consistency; however, it also results in noisier

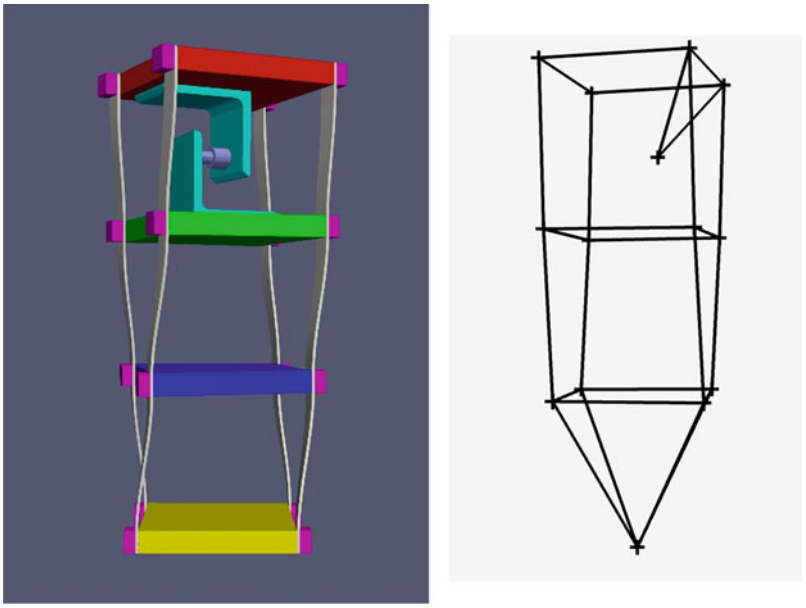

Fig. 7.19 Finite element model mode shape at 80 Hz (left) and ODS at 80 Hz (right) for 1.06 Grms

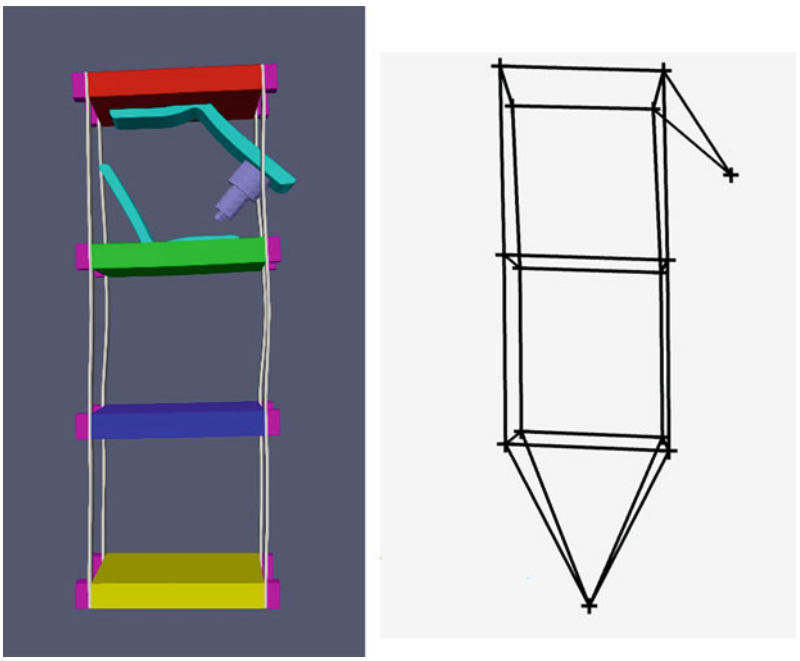

Fig. 7.20 Finite element model mode shape at 486 Hz (left) and ODS at 478 Hz (right) for 2.12 Grms

data, leading to more peaks that aren't representative of modes. This research suggests that the usage of the ODS method for modal parameter estimation is promising for structures with varying levels of excitation and known nonlinear impact. However, further research is needed to fully understand the limitations of using ODS as a substitute for modal data.

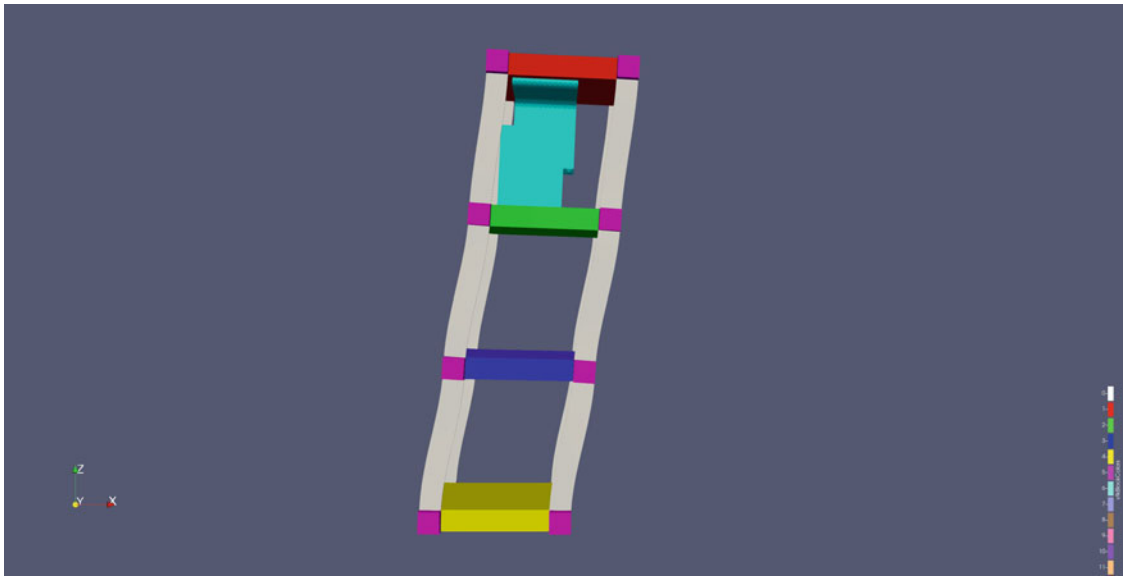

Fig. 7.21 Finite element model mode shape at 62 Hz showing out of plane response

Acknowledgments The authors would like to especially thank Dan Roettgen, Bryan Witt, and Anthony Jaramillo for acquiring and sharing the vibration and modal data of the academic structure used in this chapter.

References

1. Hermans, L., Auweraer, H.V.D.: Modal testing and analysis of structures under operational conditions: industrial applications. Mech. Syst. Signal Process. **13**(2), 193–216 (1999)
2. Gentile, C., Saisi, A.: Operational modal testing of historic structures at different levels of excitation. Constr. Build. Mater. **48**, 1273–1285 (2013)
3. Siemens, "OMG! What is OMA? Operational Modal Analysis," Siemens, 10 July 2020. [Online]. Available: https://community.sw.siemens.com/s/article/OMG-What-is-OMA-Operating-Modal-Analysis
4. Avitabile, P.: Modal Testing: a practitioner's Guide. Wiley (2017)
5. The MathWorks, Inc, "Singular Values," 2022. [Online]. Available: https://www.mathworks.com/help/matlab/math/singular-values.html
6. CUBIT Development Team, *CUBIT Geometry and Mesh Generation Toolkit,* SAND2022-9299 W (2022)
7. Sierra, S.D.: Team, *Sierra SD,* SAND2022-12518 (2022)

Chapter 8
Finite Element Simulation of Electromagnetic Shaker for Environmental Test

Adam P. Bruetsch and Washington J. Delima

Abstract The Environmental Test group at KCNSC performs various mechanical tests to evaluate the production lifetime of components. The majority of these tests are performed on an electromagnetic (EM) shaker. An EM shaker is a device that converts electrical energy to mechanical vibrations using the principles of electromagnetism. This vibration testing is highly useful for field testing components that are routinely subjected to repetitive vibrations and shocks.

In order to facilitate a reduction in unnecessary testing time, simulation of the shaker using finite element modeling (FEM) is an invaluable tool to predict real-world outcomes. Full dynamic characterization of the shaker as well as its interaction with adapters and test fixtures is difficult to capture but is nonetheless fundamental to understanding the response of a unit undergoing test. Inputs to achieve reliable predictive simulation results require accurate design, a proper understanding of coupling behavior, and precise test article definition.

At KCNSC, we are performing modal and dynamic analyses using our FEM model of an electromagnetic shaker. This abstract intends to examine some of the design challenges our team has faced such as model creation, boundary condition definition, and response matching to test specifications. We will also examine future challenges we are working to overcome which could allow for better prediction of input parameters prior to simulation.

Keywords Electromagnetic · Shaker · FEM · Simulation · Environmental

8.1 Introduction

An EM shaker is a widely used environmental test apparatus that is used to subject a variety of components to random vibration testing. Its design consists of an armature containing a magnetic coil. The passing of AC current through this coil generates an axial force upward toward the shaker table that is imparted onto the device under test (Fig. 8.1).

The shaker functions as a closed feedback loop vibration test to impart a random vibration impulse to a part under test that is attached to a fixture affixed to an adapter atop the shaker table. A vibration controller sends a voltage to a power amplifier which then sends the amplified signal to the shaker. The voltage imparts a mechanical shock to the part under test. A feedback response is then sent back to the vibration controller [1].

Simulating this process would provide many benefits to the test engineer, such as time saving and cost reduction when compared to experimental testing. In order achieve accurate results, a robust model of the shaker is critical. Previous efforts at KCNSC have made a significant amount of progress toward building a shaker simulation model with known limitations. This effort intends to expand upon the existing work and address some of the current challenges and how to best resolve them moving forward.

Honeywell Federal Manufacturing & Technologies, LLC, operates the Kansas City National Security Campus for the U S Department of Energy/National Nuclear Security Administration under Contract Number DE-NA0002839 NSC-614-4885 10/22 Unclassified Unlimited Release

A. P. Bruetsch (✉) · W. J. Delima
U.S. Department of Energy's Kansas City National Security Campus, Managed by Honeywell FM&T, Kansas City, MO, USA
e-mail: abruetsch@kcnsc.doe.gov; wdelima@kcnsc.doe.gov

J. Harvie (ed.), *Dynamic Environments Testing, Volume 7*, Conference Proceedings of the Society for Experimental Mechanics Series, https://doi.org/10.1007/978-3-031-34930-0_8

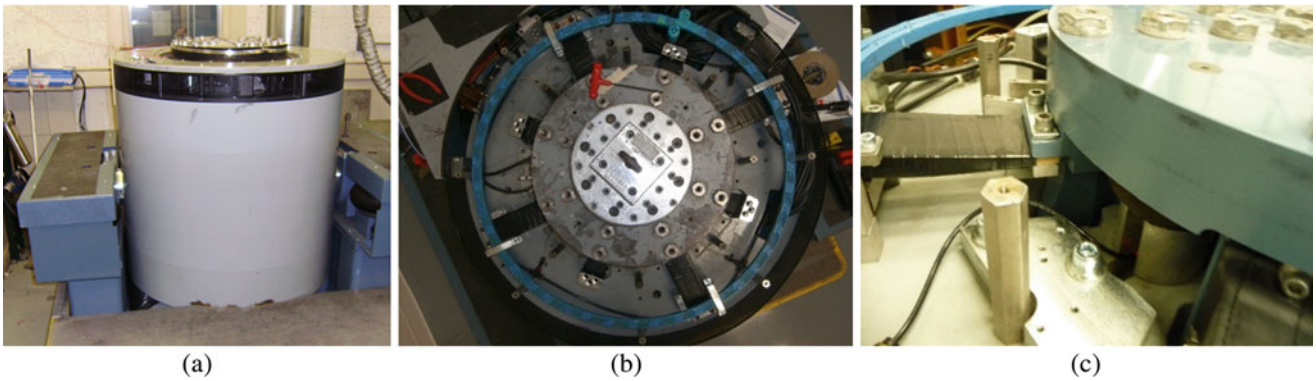

Fig. 8.1 EM shaker: (**a**) full view, (**b**) view showing flexible shear mounts, (**c**) view of table showing flexible beam mounts

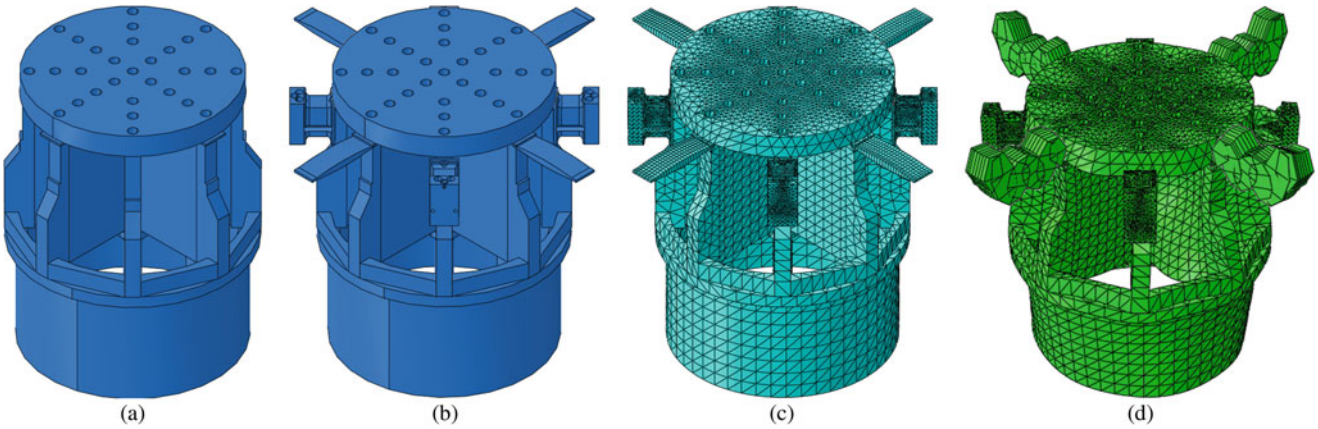

Fig. 8.2 Progression of modeling efforts. (**a**) EM shaker with boundary conditions applied at locations of flexible beam mount and flexible shear mount geometry without geometry modeled, (**b**) EM shaker with flex and shear mount geometry added in, (**c**) full model with meshing complete, (**d**) completed simulation showing 2487 Hz axial mode shape

8.2 Background

In examining the approaches used in previous publications, a lumped mass 3DOF model has been used to model axial shaker motion [1]. For this model, a full geometry assembly was built up for the entire shaker and a random vibration modal and steady-state dynamic tests were performed capable of capturing the influence of off-axis motion as well, which is present during the shaker tests (Fig. 8.2).

KCNSC possesses several different shakers on which tests are regularly performed. Despite similar design specification, significant differences in frequency response are present for each individual shaker when performing a test with the same random vibration input values. Specifically, there is considerable variation in the high-frequency range. There is also a differing voltage generated from the vibration controller to drive the shaker coil for each shaker. One of the ongoing challenges of this modeling endeavor is predicting the variation in signal response that will be present in each different shaker and normalizing the input force given the variation in voltage. Currently, each simulation needs to be calibrated to match the empty shaker response for each separate shaker.

8.3 Analysis

A simulation was completed for an empty shaker test for a random vibration analysis using a range from low frequency to above the first natural mode. The results were compared against experimental test data from two separate shakers that exhibit different frequency response behaviors at higher frequencies. Input force was tuned to match the output amplitude magnitude of the test data. In addition to input force, boundary condition definition and modal damping had significant

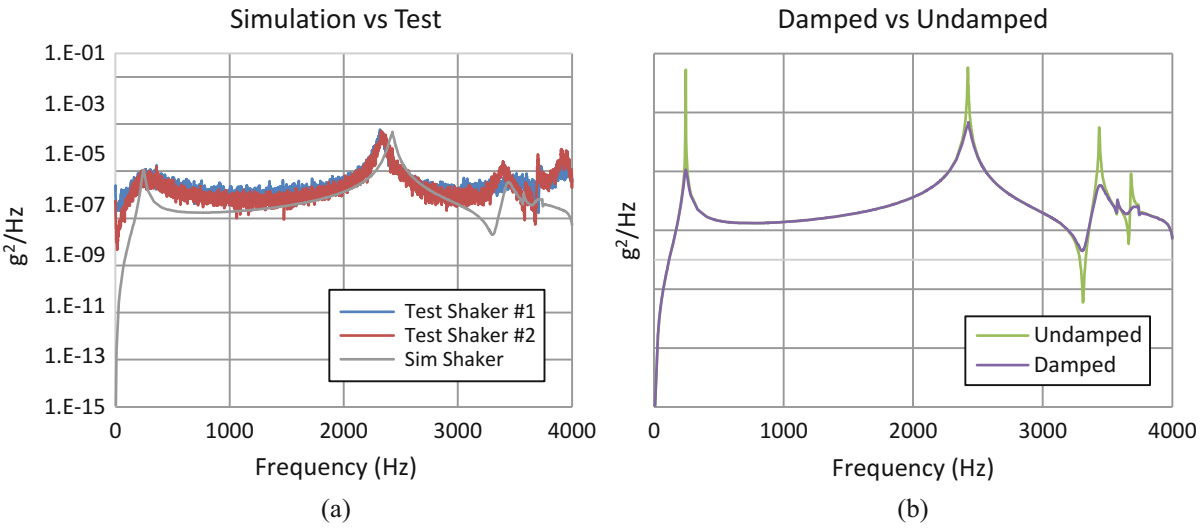

Fig. 8.3 Simulation results: (**a**) comparison of FEM simulation frequency response vs test results from two different shakers showing differences in responses in the higher frequency range and (**b**) comparison of FEM simulation results undamped vs modal damping

impacts on accurately replicating the response. Low and middle frequency eigenvalue peaks as well as overall response curve shape were reasonably well captured. Higher frequency responses were challenging to capture, and efforts to more accurately capture this area will be made with subsequent simulations (Fig. 8.3).

Boundary conditions had a significant impact on producing the correct locations of the eigenfrequencies. If the boundary condition stiffness was incorrect, the peaks would appear at the incorrect frequency. Ultimately it was determined to constrain the model in all degrees of freedom at the location of the flex and shear mount attachments to produce the most accurate results.

Applying individual modal damping to each eigenmode was also necessary to improve the accuracy of the response. A higher critical damping fraction was applied to the first eigenmode and a lower fraction to the remaining eigenmodes. For the rest of the system, very minimal damping was applied. This damping reduced the amplitude of the eigenmode response to match the experimental test data without removing it entirely.

Other modifications can be employed to alter the response characteristics of the system. Mass modifications to various components alter the location of the eigenfrequencies. This was not necessary to produce these results but is a useful tool that will likely be employed for future simulations.

8.4 Conclusion

Initial efforts to replicate the empty shaker response for a standard random vibration test have produced reasonably accurate results when compared to test data after determining how to properly apply appropriate damping fractions and apply boundary conditions.

Primary challenges moving forward include refining the optimal location of boundary conditions and damping values as well as quantifying the relationship between voltage input and dynamic force.

Acknowledgments I would like to thank my colleagues at KCNSC for their assistance, specifically Washington DeLima and Jonathan Hower.

Reference

1. DeLima, W.J., Ambrose, M.N.: Experimental Characterization and Simulation of Vibration Environmental Test. Proceedings of the SEM 2015 IMAC XXXIII A Conference and Exposition on Structural Dynamics (2015)

Chapter 9
Rapid, Approximate Multi-axis Vibration Testing

Ethan Cramer, Dustin Harvey, and Richard Zhang

Abstract Sequential single-axis vibration testing strategies often produce over-testing when qualifying system hardware. Rarely does the test article experience equivalent cumulative vibration response between laboratory and service environments when using traditional single-axis testing methodologies. Multi-axis excitation techniques can simulate realistic service environments, but the hardware and testing-strategies needed to do so tend to be costly and complex. Test engineers instead must execute sequential tests on single-axis shaker tables to excite each degree of freedom, which the previous two decades of vibration testing literature have shown to cause extensive over-testing when considering cross-axis responses in assessing the severity of the applied test environments. Traditional assessments assume that the test article responds only in the axis of excitation, but often significant response occurs in the off-axes as well. This chapter proposes a method to address the over-testing problem by approximating a simultaneous multi-axis test using readily available, single-axis shaker tables. By optimizing the angle of excitation and the boundary condition through dynamic test fixture design, the test article can be rapidly and inexpensively tested using a single-input, multiple-output (SIMO) test in a way that approximates a multiple-input, multiple-output (MIMO) test. This chapter shows the proposed method in simulation with a 2D finite-element box assembly with removable component (BARC) model attached to springs with variable stiffness. The results include quantified test quality assessment metrics with comparison to standard sequential testing. The proposed method enables wide access to rapid, approximate multi-axis testing using existing hardware, thereby reducing the over-conservatism of sequential single-axis tests and requisite over-design of systems.

Keywords Multi-axis · Vibration · Testing · Fixture · Design

9.1 Introduction

In vibration testing, single-axis shaker excitation is often the tool chosen to qualify systems and their components to their intended service environments. However, it is difficult to reproduce the multi-axis nature of many service environments with a laboratory test. Hardware that can excite a test article in multiple axes simultaneously is costly and requires complex test control strategies. A common approach is to vibrate the test article sequentially in each primary axes of motion, with the assumption that three sequential single-axis tests are equivalent to a single multi-axis test. This assumption neglects the cross-axis responses that occur in axes other than the primary test axis. In most test assessments, the cross-axis responses are assumed to be zero or negligible, but in reality, they often meet or even exceed the on-axis response [1]. If a test article experiences non-negligible, full-duration response in all three primary axes more times than required by the service environment, then that article has been over-tested. Over-testing causes unnecessary costs in strengthening the design and

E. Cramer (✉)
Department of Mechanical and Energy Engineering, College of Engineering at University of North Texas, Denton, TX, USA

Los Alamos National Laboratory, Los Alamos, NM, USA

D. Harvey
Los Alamos National Laboratory, Los Alamos, NM, USA
e-mail: harveydy@lanl.gov

R. Zhang
Department of Mechanical and Energy Engineering, College of Engineering at University of North Texas, Denton, TX, USA
e-mail: Zihao.Zhang@unt.edu

J. Harvie (ed.), *Dynamic Environments Testing, Volume 7*, Conference Proceedings of the Society for Experimental Mechanics Series, https://doi.org/10.1007/978-3-031-34930-0_9

may result in designs that do not accurately account for the service environment. Therefore, there is a need for a vibration testing method that better reproduces the service environment while avoiding excessive cost and test complexity.

For a single-axis laboratory test, the test article is typically connected to the shaker by a fixture providing a rigid boundary condition. In the space of all possible boundary conditions, there likely exists some non-rigid boundary condition that can produce an improved approximation of the service environment when excited by a single-axis shaker. A previous study showed that a single-axis vibration test of a satellite system was able to adequately match the maximum RMS values for the coupled system tests with only one test at an optimized offset angle [2]. The method proposed in this chapter builds upon the optimized offset angle approach by also dynamically optimizing the test fixture stiffness. The goal is to produce a test which approximates the service environment using one excitation from a single-axis shaker. The method is rapid because it requires only one test, saving the time needed to setup and test an article three times. In comparison to multiple-input, multiple-output (MIMO) testing, the proposed method saves the time required for a more complex setup and execution process. The method is approximate because it is unlikely to result in a test equivalent to one achieved using a multi-axis shaker. The goal of this chapter is to assess the quality of this approximation.

The vibration testing literature has long acknowledged the over-testing implicit in sequential single-axis vibration testing [3–5]. Strategies such as impedance-matched multi-axis testing (IMMAT) attempt to address the issue by employing multiple single-axis shakers [6], yet the community has been so far unsuccessful in finding test fixtures which recreate the service environment boundary conditions. Topological optimization [7] and N + 1 fixtures [8] have been explored, as well as modal- and frequency-based substructuring. The variety of approaches saw a need for a common test bed to compare strategies, which led to the creation of the boundary condition round Robin challenge [9]. The challenge introduced hardware called the box assembly with removable component (BARC), which is used as a model in this chapter to implement the proposed method.

The following sections of this chapter will (1) overview a set of five case studies used to validate the proposed method, (2) introduce a finite-element BARC model to use in each case study, (3) describe a service environment and test quality metrics, and (4) discuss the results of each of the case studies.

9.2 Case Studies

The following subsections set up a series of five case studies to compare the proposed method with traditional testing approaches. First, the Finite-Element Model subsection describes the model used in each of the case studies, including mesh properties, dimensions, mode shapes, and output locations. Then the Service Environment subsection describes the service environment used in each of the case studies. The case studies vary in three aspects: boundary condition, control location, and test sequence. All three aspects have their own subsection to show how they fit into each case study. The Boundary Conditions subsection discusses rigid and dynamically optimized test fixtures. The Control Locations subsection compares controlling a test with a single control location to controlling using all control locations. The Test Sequence subsection describes sequential single-axis testing and the proposed alternative of single-input, multiple-output (SIMO) multi-axis testing. Table 9.1 summarizes the variations in boundary condition, control location, and test sequence for each of the case studies with Case 1 representing traditional sequential single-axis testing and Case 5 representing the proposed method. Metrics to assess the quality of each case study are introduced in the Test Quality Metrics subsection. The optimization scheme used to dynamically optimize the test fixture in Case 3 and Case 5 is described in the Optimization Scheme subsection.

Table 9.1 Five case studies

Case	Test sequence	Fixture	Control locations
1	Sequential single axis	Rigid	Single
2	Sequential single axis	Rigid	All
3	Sequential single axis	Optimized	All
4	SIMO multi axis	Rigid	All
5	SIMO multi axis	Optimized	All

Case 1 is intended to be the simplest, traditional test strategy, while Case 5 is the proposed method of rapid, approximate multi-axis testing with single-axis techniques

Table 9.2 Finite element properties

Mesh density	0.003
Number of elements	681
Element type	4-node bilinear plane strain quadrilateral, reduced integration, hourglass control (CPE4R in Abaqus)
Material	Aluminum 6061
Outer dimensions	15.24 × 12.7 cm [10]

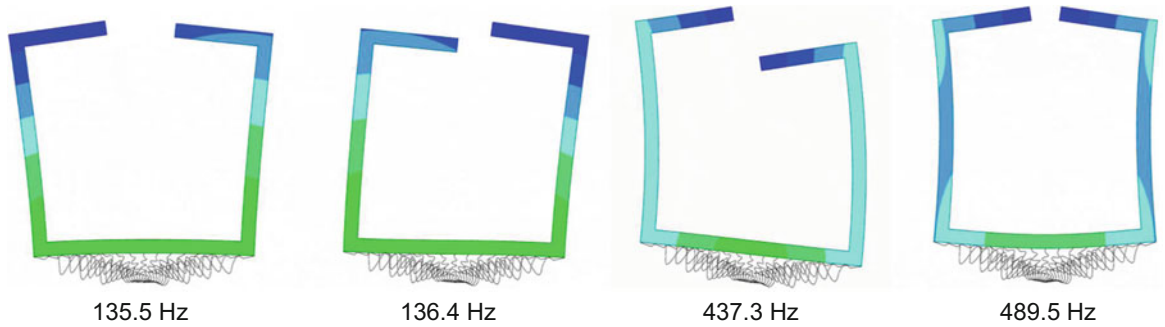

Fig. 9.1 First four mode shapes of the BARC model with their natural frequencies

Fig. 9.2 BARC model with output locations shown in red. Four locations are called out

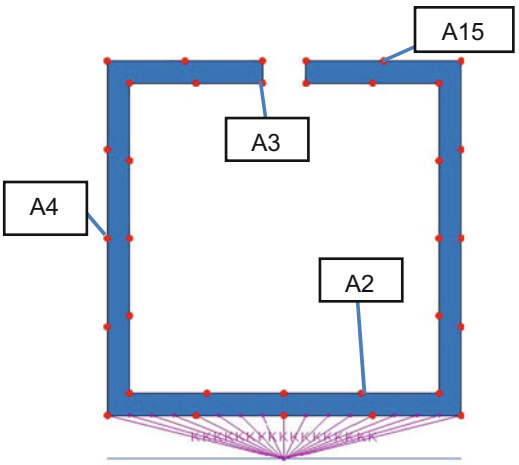

9.2.1 Finite-Element Model

Each case study is performed on a finite-element model. The model is a two-dimensional assembly composed of a part, a test fixture, and a rigid base. The part is a solid aluminum BARC model [10] with the removable component not included. The BARC is meshed with 681 plane strain elements. Table 9.2 has a more detailed description of the mesh and other model properties, while Fig. 9.1 shows the first four mode shapes of the model. The BARC is attached to the base by a test fixture consisting of seventeen parallel springs. The test fixture springs have a separate vertical and longitudinal stiffness and are attached to a rigid base. The base is modeled as a 10,000 kg analytical rigid shell and is stiffly connected to the ground. The base is meant to represent a vertically oriented, single-axis shaker; therefore, the acceleration input is always applied vertically at the base.

9.2.2 Output Locations

Acceleration transfer functions between the base and selected output points on the BARC were calculated for use in testing simulations. Thirty-four outputs were chosen: seventeen evenly spaced on the outside edge and seventeen evenly spaced on the inside edge as shown by the red points in Fig. 9.2. The rigid base has one output at the center which is used as a reference location to compute transfer functions between the part and the base. Initially, transfer functions are computed using the

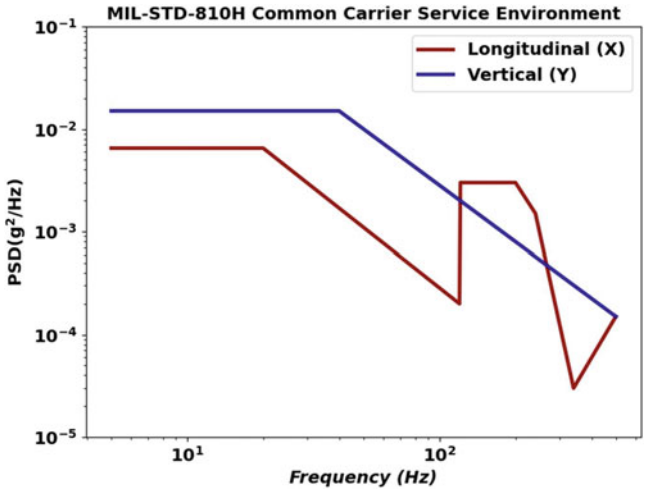

Fig. 9.3 Common carrier (US highway truck) service environment [11]

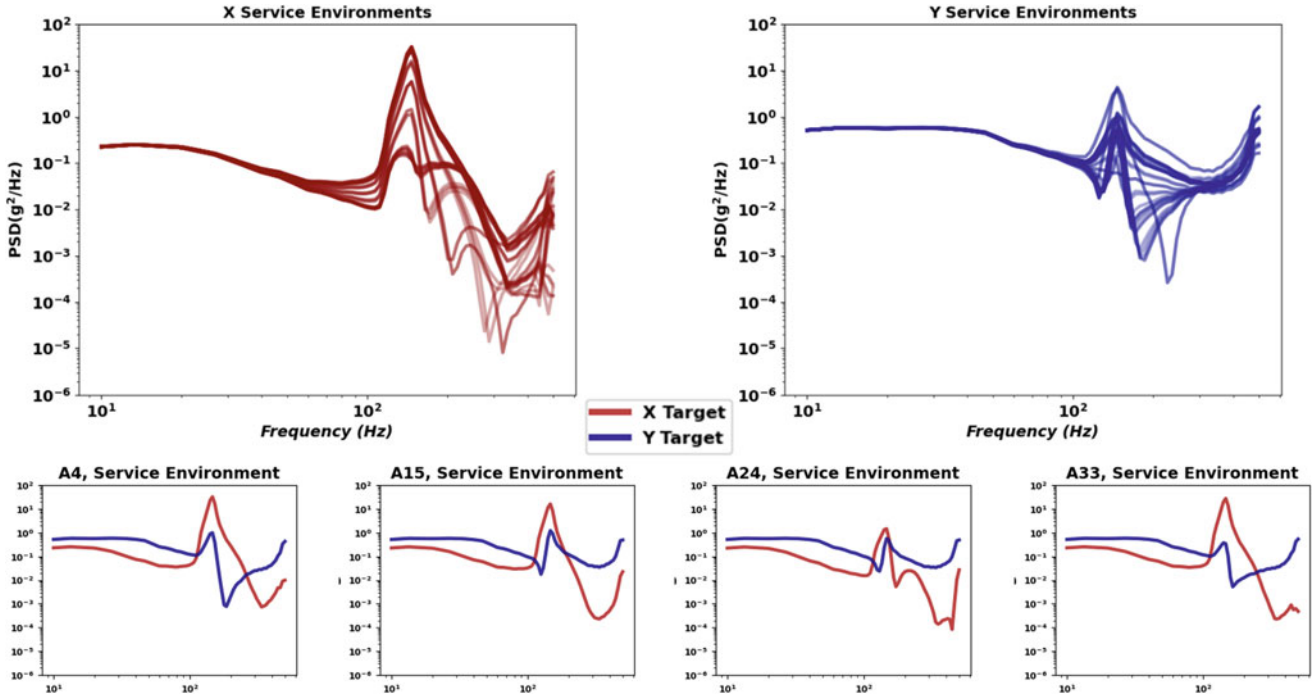

Fig. 9.4 Service environments derived from simultaneous *X* and *Y* input of the MIL-STD-810H common carrier service environment on the BARC model. The bottom row shows *X* and *Y* targets at select locations on the BARC annotated on Fig. 9.2

modal solution provided by the Lanczos eigensolver, then acceleration responses for testing simulations are calculated at each output location by passing a power spectral density (PSD) input applied at the base through those transfer functions.

9.2.3 Service Environment

A service environment is the real environment a test article is expected to experience in its lifetime. From hereon, the service environment will be referred to as the target. For the following simulations, the targets are generated using the MIL-STD-810H Common Carrier environment shown in Fig. 9.3 [11]. The vertical and longitudinal PSD were transformed into timeseries data and simultaneously applied to the base. Acceleration time responses at each output location were recorded and then transformed back into PSDs shown in Fig. 9.4. The goal of this target generation was to produce a set of test article responses in a representative multi-axis service environment to be recreated in a response-matching laboratory test.

The targets were generated using a flexible boundary condition. All springs had a stiffness of 10^6 N/m, which was chosen to achieve a boundary condition between a fixed-fixed and free-free condition. This type of boundary condition is common in real systems and is often difficult to match in a laboratory test.

9.2.4 Control Location Variations

In a response-matching test, control locations are used to control the measured response a shaker should try to produce on the test article. Typically, control locations are chosen to be accessible and instrumentable in both the service and laboratory settings. The case studies discussed in the results section consider two control scenarios: "single location" and "all locations." In the "single location" case, the acceleration input is derived to achieve the lowest possible error between the target and response at the chosen location. In the "all locations" case, the input is derived to achieve the lowest possible error between target and response averaged at all locations.

9.2.5 Boundary Condition Variations

In a laboratory test, the test article's boundary conditions are determined by the test fixture. Test fixtures are typically rigid even though the real boundary conditions experienced in the service environment are often flexible. For the optimized fixture cases, Case 3 and Case 5 from Table 9.1, the stiffness of the test fixture is optimized to best achieve the targets. Although the test fixture is composed of many parallel springs, each spring's stiffness is not varied individually. The group of spring's vertical and longitudinal stiffness are treated as the two optimization parameters.

9.2.6 Test Sequence Variations

The primary goal of this chapter is to compare sequential single-axis testing to the proposed method of SIMO multi-axis testing using single-axis hardware. In the sequential single-axis case, the vertical and longitudinal axes are tested sequentially. An input is derived to hit only the targets for the test axis, and error is computed with respect to those targets. In the SIMO multi-axis case, a single input attempts to hit both the vertical and longitudinal targets simultaneously. To adjust the relative amount of excitation energy applied in both directions, the test article, test fixture springs, and rigid base are all rotated such that the vertical shaker excitation is applied to the entire system at an angle. This method is visualized in Fig. 9.5 where $\Theta = 0°$ corresponds to excitation in the vertical (Y) part axis and $\Theta = 90°$ to excitation in the longitudinal (X) part axis.

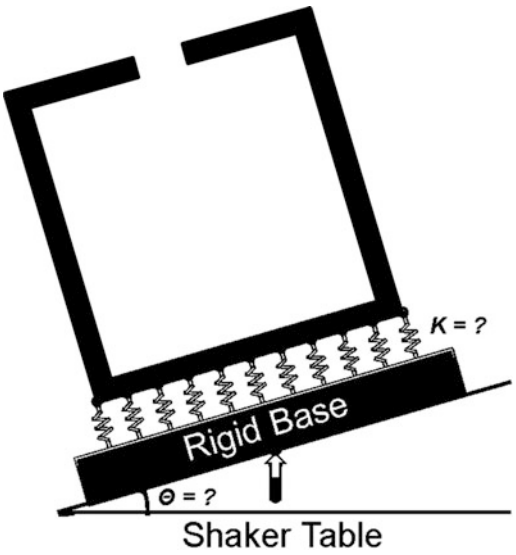

Fig. 9.5 Test fixture rotated to adjust relative excitation energy applied to each test article primary axis

9.2.7 Test Quality Metrics

Two scalar measures of test quality are introduced to quantify the difference between test targets and responses: RMS dB error (RDBE) and the percentage of frequency lines within a 3 dB tolerance (% FL).

The RMS dB error between two PSDs can be calculated to supply a scalar metric sensitive to large differences on a log scale. The RMS dB error value between a response PSD and a target PSD is a representation of the average mismatch between the response and the target across all frequencies.

$$\text{RDBE} = \sqrt{\frac{\sum_{i=1}^{n}\left(10\log_{10}\frac{\hat{y}_i}{y_i}\right)^2}{n}} \tag{9.1}$$

In Eq. 9.1, $\hat{y}_i$ is the value of a response PSD at the i^{th} frequency line and y_i is the value of the target PSD at the i^{th} frequency line. The squared decibel error between the response and target PSDs is summed at every frequency line up to the n^{th} frequency line. The resulting sum is divided by the total number of frequency lines, n, and the square root of that quantity is the RMS dB error.

Another metric employed is the percentage of frequency lines within a 3 dB tolerance. This metric counts the percentage of frequency lines where the response PSD differs from the target PSD by less than 3 dB. While the RDBE metric should be minimized to improve test quality, % FL should be maximized.

$$\%FL = 100 * \frac{1}{n}\sum_{i=1}^{n}\begin{cases} 1\ if & \left|10\log_{10}\frac{\hat{y}_i}{y_i}\right| \leq 3\ dB \\ 0\ if & \left|10\log_{10}\frac{\hat{y}_i}{y_i}\right| > 3\ dB \end{cases} \tag{9.2}$$

In each test simulation, the input PSD is derived to minimize RDBE across control locations, which is not optimal for maximizing % FL.

9.2.8 Optimization Scheme

There are a maximum of three optimization parameters in the most complex simulation case: vertical stiffness (K_y), longitudinal stiffness (K_x), and excitation angle (Θ). For the sequential single-axis case with optimized test fixture, only stiffness optimization is needed. For the SIMO multi-axis case with a rigid test fixture, only angle optimization is needed. The SIMO case with optimized test fixture is the only case to require all three parameters as shown in Table 9.3.

The stiffness parameters are optimized using a simple grid search over a grid of log-spaced stiffness values. At the lower bound of the grid, the springs behave freely, and at the upper bound, they behave rigidly. The angle optimization is a brute force search over every angle between 0° and 90° in 1° increments.

In general, the stiffness and angle optimizations can be treated independently, since only the stiffness optimization affects the mode shapes of the system. The angle optimization can best be thought of as a way to adjust the relative amount of excitation energy applied in each direction. When stiffness and angle are optimized together, as in Case 5, the stiffness optimization occurs in an outer loop and the angle optimization in an inner loop. This means that, for every pair of K_x and K_y, the optimization checks every angle for a best solution before trying the next stiffness pair.

Table 9.3 Parameters optimized for each case

Case	Test sequence	Fixture	Optimization parameters
1	Sequential single axis	Rigid	*No optimization*
2	Sequential single axis	Rigid	*No optimization*
3	Sequential single axis	Optimized	K_x, K_y
4	SIMO multi axis	Rigid	Θ
5	SIMO multi axis	Optimized	Θ, K_x, K_y

9.3 Results and Discussion

The results of all case studies are summarized by the test quality metrics shown in Table 9.4. In all cases, the test quality metrics indicate a general improvement in test quality when the test fixture design and control locations are strategically chosen.

In Case 1, a sequential single-axis test controlled at a single location with a rigid test fixture achieved 4.5–7.5 dB error in the X test and 2.8–3.7 dB error in the Y test. The percentages of frequency lines within a 3 dB tolerance were 69–77% for the X test and 69%–86% for the Y test. The errors are a range instead of a single value because they vary with respect to the control location chosen. The range captures possible errors for picking any of the thirty-four possible control locations. Although the Case 1 test is being controlled to a single location, the metrics are computed as an average over all thirty-four locations. Case 1 is the simplest, traditional testing approach and provides a baseline to assess the following cases. By controlling at all locations instead of only one, Case 2 is able to improve the RDBE over Case 1 for both the X and Y tests. The frequency lines within tolerance are an improvement over some control locations from Case 1. In Case 3, a sequential single-axis test with an optimized test fixture improved every test quality metric over the previous two cases, with the most significant improvement in the X axis due to higher variability among the target population. The optimal test fixture was one with $K_x = 10^6$ N/m and $K_y = 10^6$ N/m, which is the stiffness used to derive the target.

Case 4 and Case 5 achieved errors only slightly worse than their sequential single-axis counterparts in Case 2 and 3. In these cases, the angle was optimized to minimize the RDBE. As shown in Fig. 9.6, the angle optimization returned 26 degrees as the optimal input angle in both Case 4 and Case 5. The SIMO multi-axis tests are no more than 3.2 dB worse than the best performing sequential test in Case 3, and similar to the average performing sequential test in Case 1. Since Case 4 and Case 5 avoid the cross-axis responses implicit in sequential single-axis testing, a slight decrease in test quality metrics may be justified. Interestingly, neither test quality metric improved significantly between Case 4 and Case 5. Case 3 saw the X axis RDBE almost halved from Case 2 by optimizing the test fixture, but that did not occur between Case 4 and Case 5. Fig. 9.8 shows that the RDBE was nearly invariable across a broad set of test fixture stiffnesses in Case 5.

The primary motivation of this chapter was to investigate the possibility of replacing a series of sequential single-axis tests with a SIMO multi-axis test. When looking only at on-axis responses for a SIMO multi-axis test, the error between those responses and targets will always be worse than the same test performed sequentially. However, when cross-axis responses are considered, as in Figs. 9.7a–c, it becomes difficult to dismiss the benefit of the SIMO multi-axis test. Compare the

Table 9.4 Case study results

Case	Test sequence	Fixture	Control locations	RMS dB error (RDBE)		% frequency lines in tolerance (% FL)	
				X (dB)	*Y (dB)*	*X*	*Y*
1	Sequential single axis	Rigid	Single	[a]4.5–7.5	[a]2.8–3.7	[a]69–77%	[a]69–86%
2	Sequential single axis	Rigid	All	4.1	2.6	73%	85%
3	Sequential single axis	Optimized	All	2.2	2.4	92%	87%
4	SIMO multi axis	Rigid	All	5.4	4.3	68%	73%
5	SIMO multi axis	Optimized	All	5.0	4.2	71%	72%

In the sequential cases, the X and Y errors are only computed from the X and Y targets for their respective X and Y test simulation, while in the SIMO cases, the X and Y errors are all computed from a single test simulation

[a]In the single control location case, error varies depending on control location used; the resulting range of metric values is provided

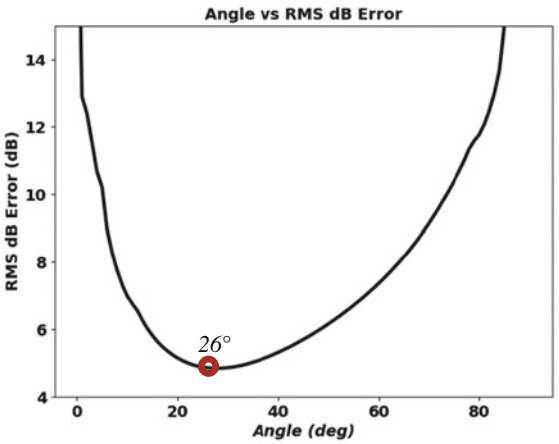

Fig. 9.6 RMS dB error minimization by adjusting excitation angle, Case 4 on the BARC model

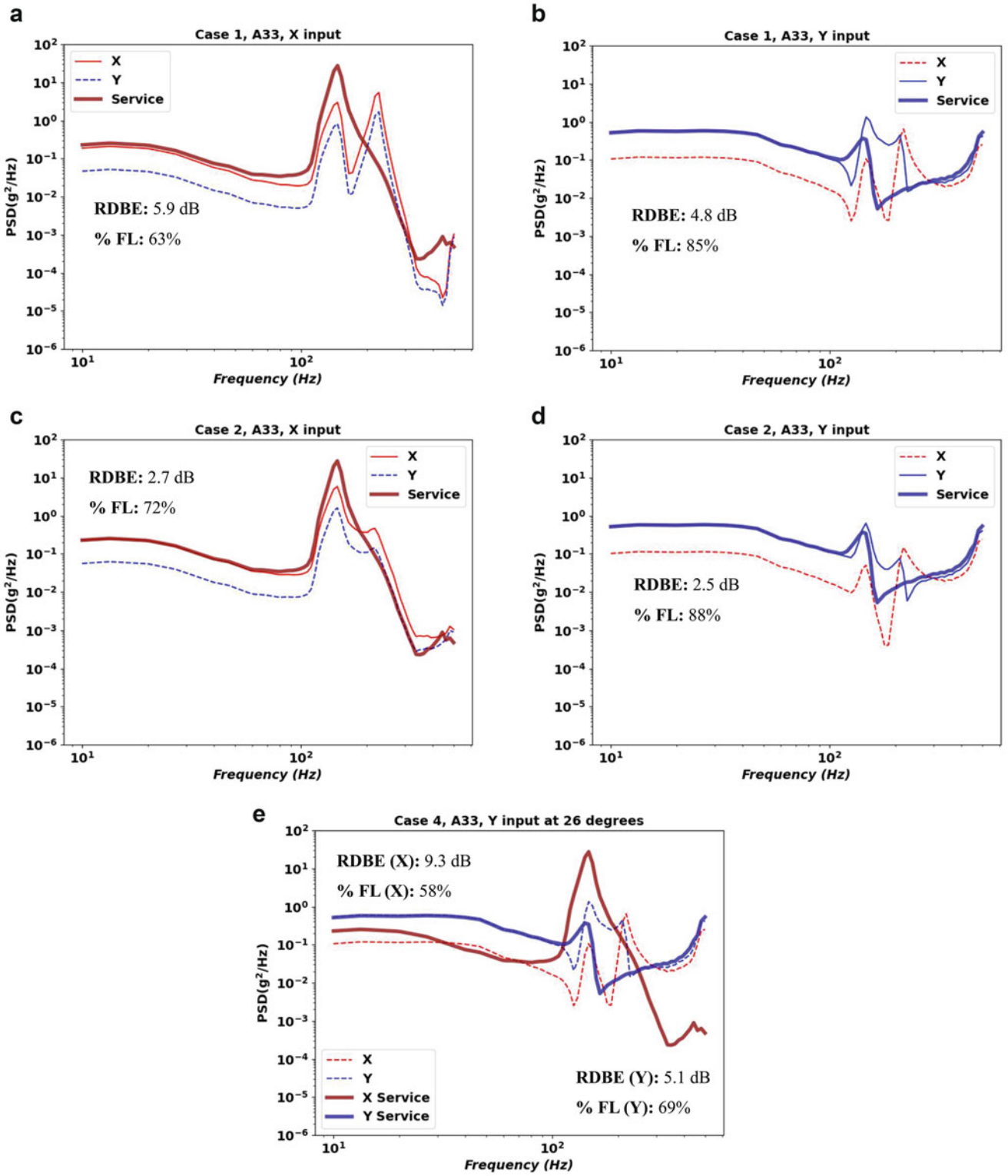

Fig. 9.7 (**a**) A33 response during Case 1 on the BARC model, controlled at A15. The off-axis response is dashed. In both tests, at frequencies above 100 Hz, the off-axis responses occasionally exceed their target. On-axis test quality metrics are displayed next to each response line. (**b**) A33 response during Case 2 on the BARC model, controlled at all locations. The off-axis response is dashed. In both tests, at frequencies above 100 Hz, the off-axis responses occasionally exceed their target. On-axis test quality metrics are displayed next to each response line. (**c**) A33 response during simulation Case 4 on the BARC model. The dashed lines are the *X* and *Y* responses to a single, angled input. On-axis test quality metrics are displayed next to each response line

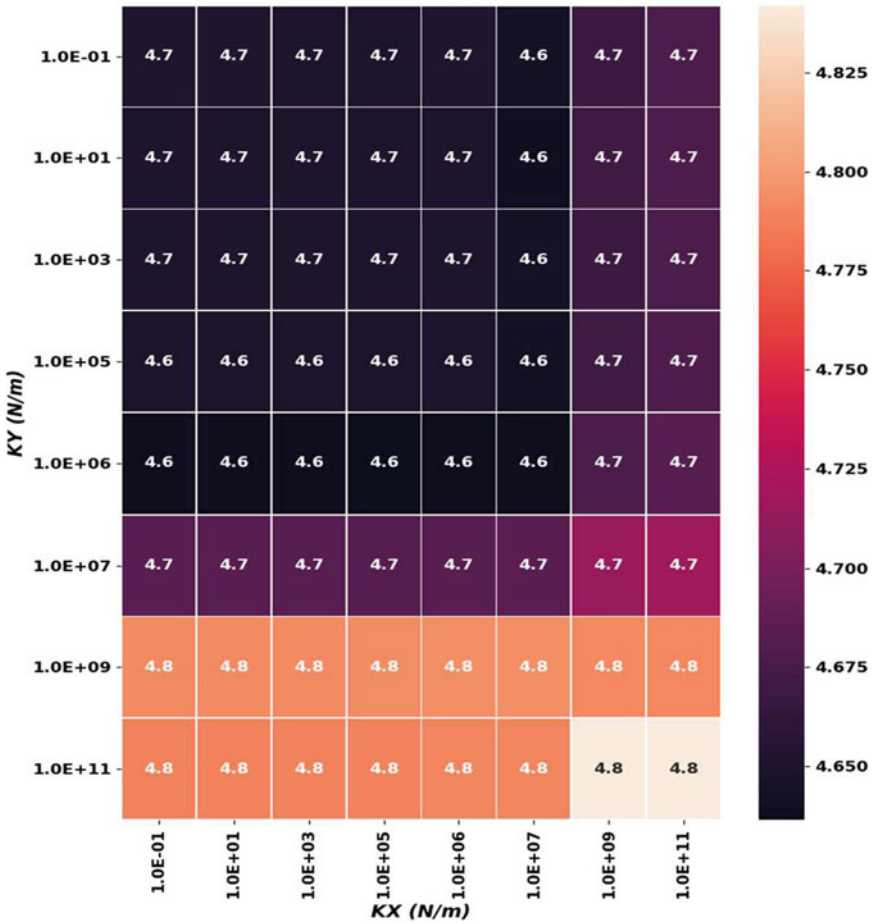

Fig. 9.8 RMS *dB* error over a coarse grid of K_x and K_y stiffness values for Case 5 on the BARC model

responses of the Case 1 and Case 2 sequential single-axis tests in Fig. 9.7a, b to the Case 4 SIMO multi-axis test in Fig. 9.7c. Although the on-axis responses in the sequential tests closely match the service environment, the cross-axis responses are large. In the SIMO test, the responses approximate the service environment, but since only one test was performed, there are no cross-axis responses.

The next step for this research is to increase the test fixture design complexity and to identify successful test fixture optimization methodologies. The test fixture design complexity could be increased by tuning the stiffness of individual springs rather than the entire spring population. Increasing the number of springs also increases the difficulty of the search problem, so work must be done to decide the best number of parameters to use. The test fixture optimization method used in this chapter was a simple grid search, which, as shown in Fig. 9.8, succeeded in finding a test fixture stiffness more optimal than rigid but did not broadly explore the possible dynamic test fixture design space. A more advanced strategy seeded with good starting locations could more effectively search the space and further reduce error.

9.4 Conclusion

The proposed method was compared to several sequential single-axis strategies through a series of case studies. The case studies were presented to assess the viability of approximating a MIMO multi-axis test with a SIMO single-axis test. In the proposed method, a vertical shaker input excites the angled 2D test article simultaneously in both axes, thereby eliminating the excess lifetime damage that would have accrued from the cross-axis responses over several sequential tests. Applying the proposed method to a 3D test article would increase the complexity of the test fixture design optimization problem, but the fundamental approach is still applicable.

A finite-element model of the BARC was used to simulate each case. The cases included variations in test sequence, boundary condition, and control location. With an optimized boundary condition stiffness and angle of excitation, a single excitation test produced slightly worse on-axis errors than the sequential single-axis tests, while avoiding detrimental cross-axis responses seen in the sequential single-axis tests. Cross-axis responses are often neglected in sequential single-axis testing, which obscures the over-testing often produced by sequential single-axis testing. The proposed method provides access to approximate multi-axis testing using existing single-axis testing hardware, mitigating the need for costly multi-axis excitation setups or complex test control strategies.

References

1. Bouma, A., Campbell, A., Roberts, T., Taylor, S., Haynes, C., Harvey, D.: Accumulated Lifetimes in Single-Axis Vibration Testing, vol. 7. In Sensors and Instrumentation, Aircraft/Aerospace, Energy Harvesting & Dynamic Environments Testing (2019)
2. Knight, C., Remedia, M., Aglietti, G.S., Richardson, G.: Satellite vibration testing: angle optimisation method to reduce overtesting. Acta Astronaut. **147**, 205–218 (2018). https://doi.org/10.1016/j.actaastro.2018.04.004
3. French, R.M., Handy, R., Cooper, H.L.: A comparison of simultaneous and sequential single-Axis durability testing. Exp. Tech. **30**, 32 (2006)
4. Gregory, D.L., Bitsie, F., Smallwood, D.O.: Comparison of the Response of a Simple Structure to Single Axis and Multiple Axis Random Vibration Inputs. United States: N. p., 2009. Web (2009)
5. Roberts, C., Ewins, D.: Multi-axis vibration testing of an aerodynamically excited structure. J. Vib. Control. **24**, 427 (2016)
6. Daborn, P.M., Roberts, C., Ewins, D.J., Ind, P.R.: Next-Generation Random Vibration Tests, pp. 397–410. In Topics in Modal Analysis II, Volume 8: Proceedings of the 32nd IMAC, A Conference and Exposition on Structural Dynamics (2014)
7. Schoenherr, T.: "Designing an Impedance Matched Test Fixture Using Parameterized Optimization and the Modal Projection Error," n.d., 25. (2020)
8. Hall, T.M.: Analytically investigating impedance-matching test fixtures. In: Sensors and Instrumentation, Aircraft/Aerospace, Energy Harvesting & Dynamic Environments Testing, vol. 7, pp. 21–31. Society of Experimental Mechanics (2020)
9. Soine, D.E., Jones, R.J., Harvie, J.M., Skousen, T.J., Schoenherr, T.F.: Designing Hardware for the Boundary Condition Round Robin Challenge. Sandia National Laboratories (2018)
10. Rohe, D.P.: Modal Data for the BARC Challenge Problem Test Report. United States: N. p. (2018) https://doi.org/10.2172/1418738
11. MIL-STD-810H, Department of Defense Test Method Standard: Environmental Engineering Considerations and Laboratory Tests. Defense Logistics Agency, United States. 31 Jan 2019

Chapter 10
Operational Replication of Strain Responses During MIMO Random Control Tests

Umberto Musella, Raphael Hallez, and Bart Peeters

Abstract The main goal of a successful environmental vibration control test is ultimately to replicate in the laboratory the same load path and stress responses that a test article experiences when subjected to operational vibrations. Poor replications can lead to an unacceptable time to failure estimation for the unit under test and different failure modes. When performing a vibration control test, it is however necessary to deal with the differences between real-life and testing boundary conditions and excitation mechanisms. In case of in-flight random vibration environments, these differences become particularly critical due to the distributed nature of the aerodynamic loads. Multi-input multi-output (MIMO) random vibration control is a technology that allows to explore new possibilities for the replication of these environments. With MIMO random control, it is possible to increase the number of inputs and the number of acceleration control channels on the structure; when combined with the operational impedance matching, the approach can lead to an optimal replication of the in-service acceleration responses. The main goal of this work is to show a new possibility in the MIMO random control testing practice: simultaneous control of multiple strain responses. The underlying idea is to directly target the replication of stress propagation mechanisms while making use of the well-known advantages of MIMO random control.

Keywords Environmental testing · Random vibration · MIMO · Multi-axis · Strain control

10.1 Introduction

Random vibration control tests are performed to verify that a system and all its sub-components can withstand a random vibration environment during the operational life. These tests aim to accurately replicate via controlled shaker excitation the in-service structural response of a device under test (DUT) in the main axis of vibration and in all the possible axes where the levels exceed the acceptance thresholds. In the recent years, great visibility has been given to the problem of accurately replicating in the laboratory the operational conditions that the DUT will eventually experience in-service. The work of different authors (for example [1–4]) highlights how multiple-input multiple-output (MIMO) random control testing allows for a close replication of the nature of the operational loads. The works of Daborn et al. [1, 2] on aerodynamically excited structures show how increasing the number of control channels and trying to match the operational mechanical impedance, on top of a successful random test, also allow to closely match the response in locations that are not controlled. These observations are at the basis of the so-called IMMAT (impedance-matched multi-axial test). Roberts in [3] shows that the environmental replication further improves by increasing the number of shakers and adopting rectangular control strategies. The work of Musella et al. [4] extend the findings of [1–3] to the use-case of a multi-axial transportation load applied to the so-called BARC demonstrator (Box Assembly with Removable Component) [5]. The ultimate goal of these studies is to converge towards a solution that will lead to a laboratory test that will eventually lead to damage mechanisms closer to the one that the component would experience in service. The objective of this paper is to continue the investigation extending the findings of [1–4] to the physical quantities that can be actively controlled. This work attempts to answer the following research question: since the failure of the unit under test is directly related to the stresses and hence the strains, could MIMO random control techniques applied directly to strain measurements improve the replication of the operational strain field?

U. Musella (✉) · R. Hallez · B. Peeters
Siemens Industry Software NV, Leuven, Belgium
e-mail: umberto.musella@siemens.com; raphael.hallez@siemens.com; bart.peeters@siemens.com

J. Harvie (ed.), *Dynamic Environments Testing, Volume 7*, Conference Proceedings of the Society for Experimental Mechanics Series, https://doi.org/10.1007/978-3-031-34930-0_10

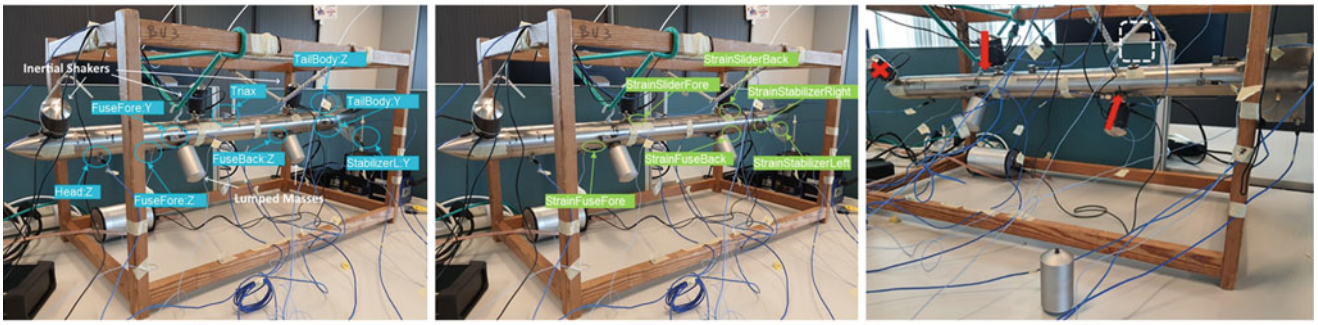

Fig. 10.1 Test setup adopted for the "pseudo-operational" conditions

10.2 Background and Methodology

To address the research question defined in the introduction, a set of experiments was carried out on the setup shown in Fig. 10.1.

Figure 10.1a, b shows the setup adopted for definition of the "pseudo-operational" conditions, highlighting the locations of the sensors for recording strain and acceleration responses. The inputs for the definition of the pseudo-operational conditions were white-pink noise uncorrelated voltages sent from a Siemens Simcenter SCADAS system to Siemens Simcenter Q-Sources inertial shakers attached to the frame of the DUT. Lumped calibrated masses were also attached to the lower side of the DUT allowing for simulating mass loading differences during the "pseudo-test" conditions.

Figure 10.1c shows the setup adopted for definition of the "pseudo-test" conditions. The test complexity was gradually increased introducing differences between "pseudo-operational" and "pseudo-test" conditions and changing control strategy.

10.3 Analysis

The first tests were simple random control tests performed without changing the test setup ("pseudo-test" and "pseudo-operational" setup were physically the same), but simply changing the control sensors and quantities (an accelerometer and a strain sensor). The results are shown in Fig. 10.2. The results illustrated in the figure confirm the findings extensively discussed in the references [1–4]: a multi-input operational environments can be replicated using one exciter in exactly one control location. Measure sensors will respond according to the dynamic of the system and will be subjected to the difference in excitation mechanism (single- versus multi- input) and boundary conditions. This can impact to a certain extent the fatigue failure mechanism of the DUT, given that the strain response will also be impacted. Controlling directly on a strain sensor allows however for the exact replication of a single *strain* response, which can be crucial, for example in case of a single critical point identified during the design of the DUT.

Next step of the study was to improve the strain response in multiple strain channels adopting MIMO control strategies. The results from the simple test case controlling all the strain responses without introducing a difference between the "pseudo-test" and "pseudo-operational" setup will not be shown. More interesting is however the case where a difference in the excitation mechanism is introduced by deactivating the inertial shaker located in correspondence of the DUT head and adopting the remaining two inertial shakers as inputs during the tests. Figure 10.3 illustrates the results of three different control strategies: two acceleration channels adopted as controls (FuseFore: +Z, FuseBack: +Z), all the acceleration channels adopted as controls and finally all the strain channels adopted as controls.

The results illustrated in the figure show that using MIMO control enables replication of multiple responses simultaneously. In this sense, increasing the number of control sensors on the structure improves the replication of multi-input operational responses. This propagates to uncontrolled channels too (measure). Figure 10.3 shows a drastic improvement of the measured strains when controlling just only two acceleration channels. Deviations are still observed but are much limited if compared with the strain responses of Fig. 10.2, where only one acceleration was defined as control, even though the excitation mechanisms were substantially different in this test case (one missing input). The deviations further reduce when controlling all the acceleration channels and lead to a perfect replication when all the strain sensors are used as controls.

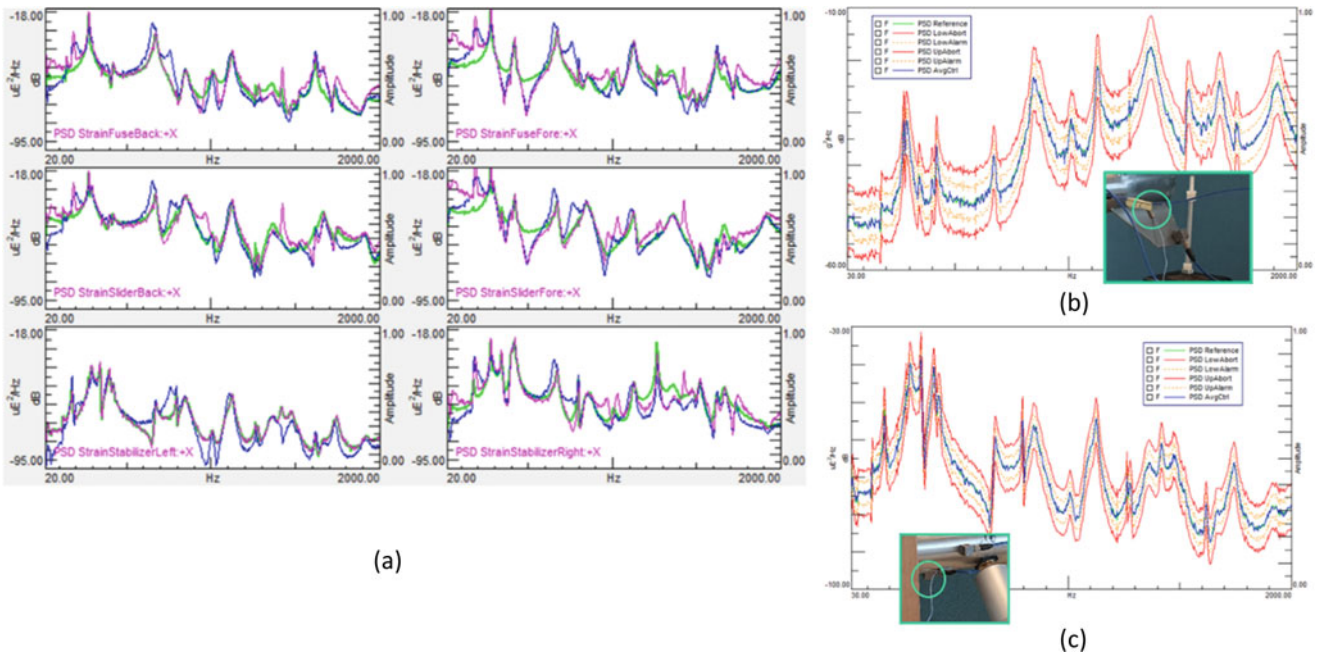

Fig. 10.2 Random control results without changing the pseudo-operational system. (**a**) Strain response PSDs; solid green, pseudo-operational responses; solid blue, control on acceleration (FuseBack: +Z channel); solid magenta, control on strain (StrainStabilizerLeft channel). (**b**, **c**) Random control results for the control on acceleration and on strain, respectively

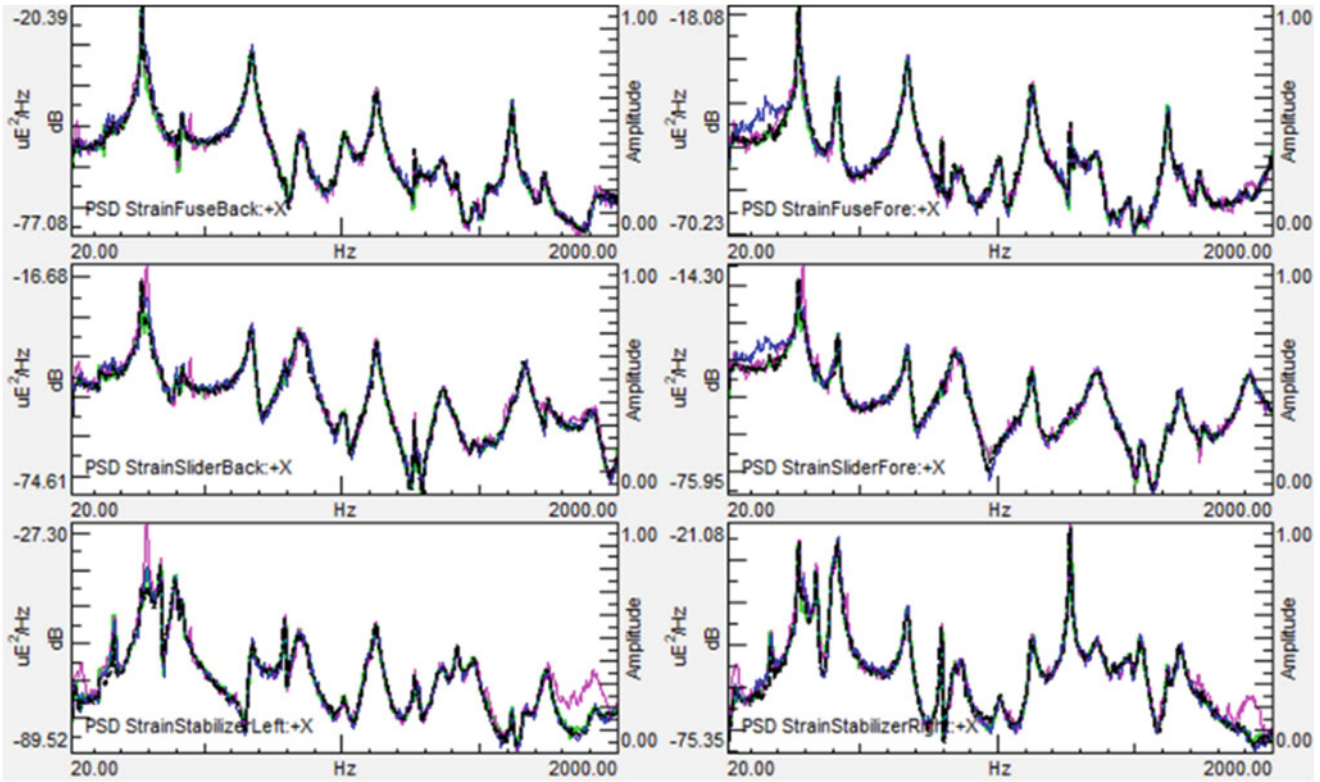

Fig. 10.3 MIMO random control results in term of strain response PSDs. Solid magenta: MIMO random, two acceleration control channels (FuseFore:+Z, FuseBack:+Z); solid blue: control on all the acceleration channels; solid black: rectangular control on all the strain channels

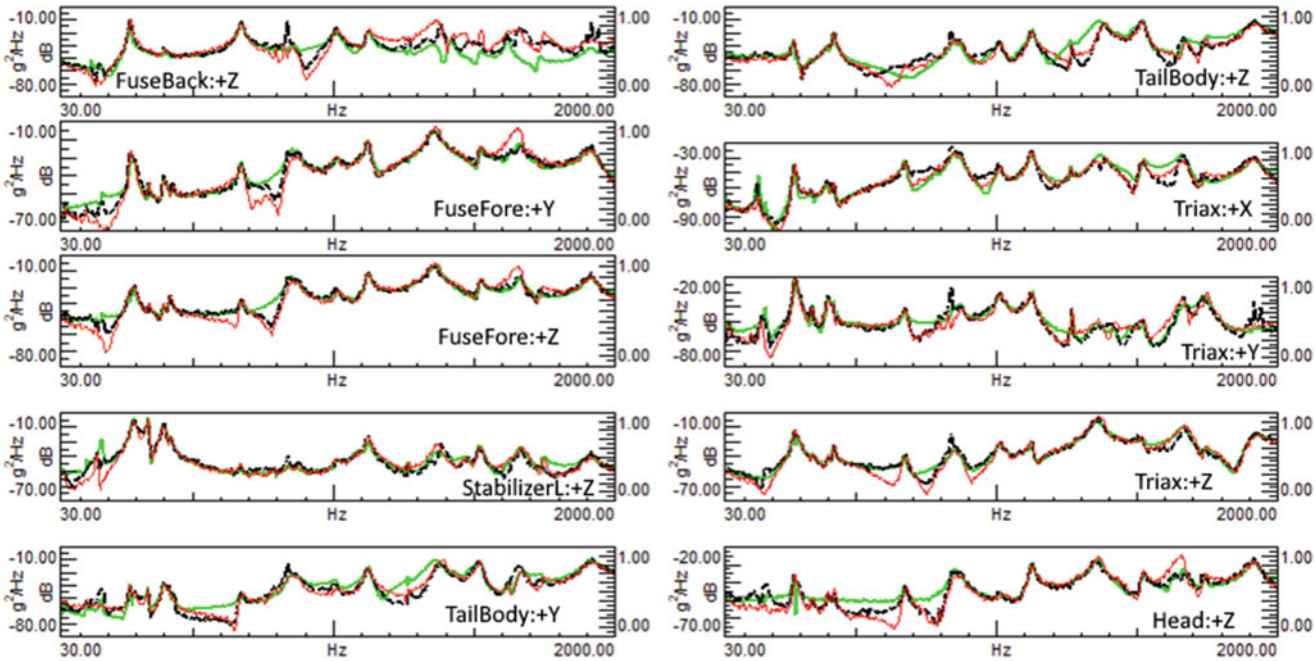

Fig. 10.4 MIMO random control acceleration response PSDs. Solid green: operational measurements. Dashed black: control on acceleration. Solid red: control on strain sensors

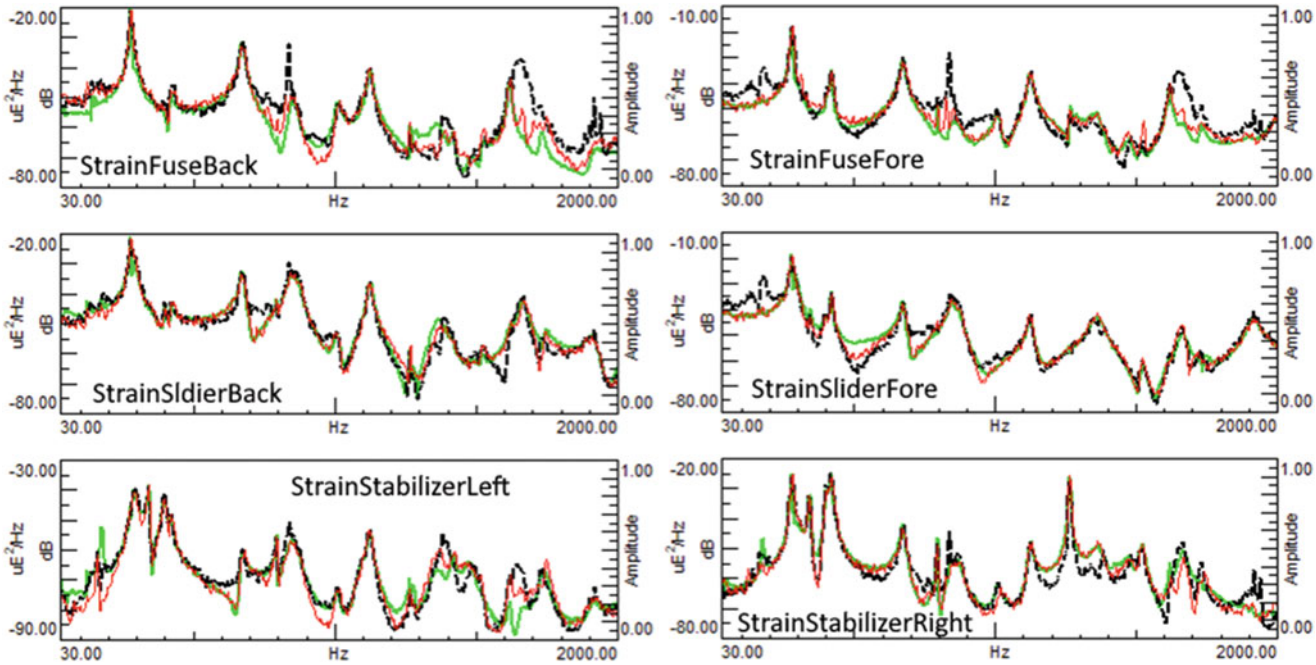

Fig. 10.5 MIMO random control strain response PSDs. Solid green: operational measurements. Dashed black: control on acceleration. Solid red: control on strain sensors

Figure 10.1c shows the configuration adopted for final test. The setup has been modified to introduce dramatic differences in the setup with respect to the pseudo-operational tests. The inertial shaker on the DUT head was deactivated. The shaker attached to the upper part of the DUT tail was moved to the lower part and the collocated lumped mass was completely removed.

Figures 10.4 and 10.5 show the MIMO random control results in terms of acceleration and strain response PSDs, respectively. Although bigger deviations are observed with respect to the previous use-cases due to the dramatic difference

between “pseudo-operational” and “pseudo-test” conditions, also for this use-case, the results show that controlling directly on strain improves the replication of the strain field (at the price of the replication of acceleration responses).

10.4 Conclusion

Adopting multi-input multi-output (MIMO) random control enables the replication of multiple random responses simultaneously. MIMO random control therefore allows for a better replication of multi-input operational responses compared to legacy single-input single-output (SISO) random control. Increasing the number of control channels (controls) allows for a better replication also for uncontrolled responses (measure). These considerations, well known in the MIMO testing communities, are shown in this work to apply also for control on strain responses. Because the differences in strain response of the device under test (DUT) are correlated to differences in stress distribution, controlling directly on multiple strain sensors may lead to a closest replication of the fatigue failure mechanisms of the DUT during random vibration control tests.

References

1. Daborn, P.M., Ind, P.R., Ewins, D.J.: Enhanced ground vibration testing for aerodynamic environments. Mech. Syst. Signal Process. **49**, 165–180 (2014)
2. Daborn, P.M., Ind, P.R., Ewins, D.J.: Next-generation random vibration tests. Topic Modal Anal. **II**(8), 397–410 (2014)
3. Roberts, C., Ewins, D.J.: Multi-Axis vibration testing of an aerodynamically excited structure. J. Vib. Control. **1**, 427 (2016)
4. Musella, U., Alvarez Blanco, M., Mastrodicasa, D., Monco, G., Di Lorenzo, E., Manzato, S., Peeters, B., Mucchi, E., Guillaume, P.: Combining Test and Simulation to Tackle the Challenges Derived from Boundary Conditions Mismatches in Environmental Testing, vol. 7, pp. 259–269. Sensors and Instrumentation, Aircraft/Aerospace, Energy Harvesting & Dynamic Environments Testing (2020)
5. Harvie, J., Soine, D.E., Jones Jr., R.J., Skousen, T.J., Schoenherr, T.F.: Mike Starr Boundary Conditions in Environmental Testing Round Robin. In Proc. of the IEST (2018)

Chapter 11
Using Cell Phone Videos to Diagnose Machinery Faults

Dan Ambre, Brian Schwarz, Shawn Richardson, and Mark Richardson

Abstract Nearly everyone carries a cell phone in their pocket, including field technicians, engineers, and plant managers. Extracting vibration signals from a cell phone or tablet video offers a low-cost alternative to traditional methods for monitoring the health of plant operating equipment.

In this chapter, two case studies are presented where vibration signals are extracted from cell phone videos and used to diagnose machinery faults. It is shown how time-based or frequency-based operating deflection shapes (ODSs) of a machine or structure can be used to visualize and analyze machine faults.

In each case study, diagnosis of a real-world machine fault is presented. In the second case study, the video results are compared with accelerometer results to confirm the validity of this new non-contacting measurement method.

Keywords Operating deflection shape (ODS): The deflection of two or more points and directions on a machine or structure · Time waveform (TWF): A time waveform in digital form · extracted either from frames of a video or from an analog accelerometer signal · Digital Fourier transform (DFT): A DFT is calculated from a TWF using the fast Fourier transform (FFT) algorithm · ODS-FRF: a frequency domain function with magnitude equal to the auto spectrum of a response signal combined with the phase of the response relative to a fixed reference response

11.1 Introduction

Most power plants, oil refineries, and manufacturing plants worldwide have implemented route-based machinery health monitoring programs for accessing the health of their rotating machinery and equipment. Digital vibration signals are typically acquired and processed to detect and diagnose faults in operating equipment.

Traditionally, machine health monitoring has been done by attaching accelerometers to the surfaces of the operating equipment, and vibration signals are acquired from the accelerometers with a portable digital spectrum analyzer. This method of acquiring data is expensive and time consuming, and cannot be used on hot or inaccessible parts of a machine or structure.

Over the past 20 years, optical flow algorithms [1, 2] have been developed for extracting dynamic features and time waveforms from a high-speed video recording. These algorithms are now being used in many new applications, including autonomous vehicles, robotic vision, and other non-contacting measurements such as vibration.

In a previous paper [3], we presented this new method of extracting time and frequency waveforms from frames of a video. Time or frequency waveforms can then be used to deform points in each frame of a video so that the operating deflection shape *(ODS)* [4–6] of an operating machine can be visualized in animation.

In this chapter, two different case studies are discussed, and the video processing capability of the MEscope software package [7] is used to derive and present the results.

D. Ambre
Full Spectrum Diagnostics, Plymouth, MN, USA

B. Schwarz · S. Richardson · M. Richardson (✉)
Vibrant Technology, Inc., Centennial, CO, USA
e-mail: mark.richardson@vibetech.com

J. Harvie (ed.), *Dynamic Environments Testing, Volume 7*, Conference Proceedings of the Society for Experimental Mechanics Series, https://doi.org/10.1007/978-3-031-34930-0_11

11.2 Video ODS Analysis

MEscope Video ODS™ is a vibration analysis software package that extracts TWFs, DFTs, and ODS-FRFs from a high-speed digital video recording. A video clip is processed with the optical flow algorithm [1, 2], which enhances the subtle displacements and rescales the amplitudes.

This processing allows the user to *"see"* what the human eye cannot perceive in a raw video playback either because the event is too fast or because the displacements are too small, or both.

Video ODS makes vibration analysis visible and understandable to customer's entire management team, so everyone can be involved in defining and implementing asset management solutions to machinery health problems.

11.2.1 Time-Based Sweep Animation

A time-based Video ODS is animated by sweeping a line cursor through a set of TWFs extracted from a video.

11.2.2 Frequency-Based Dwell Animation

A frequency-based Video ODS is animated with sinusoidal modulation at the frequency of the line cursor in a set of DFTs or ODS-FRFs.

11.2.3 Case #1: Induced Fan Vibration Analysis

This unit was located in a power plant. Data was captured with a cell phone camera mounted on a tripod.

Video camera: iPhone 10 SE
Frame rate: 240 fps
Resolution: 1080p HD
Video mode: "Slo-Mo"
Trigger: Blue Tooth (start/stop)
Clip Duration: 15–20 s

11.3 Signal Processing

Time domain (TWF): extracted from the video using the optical flow algorithm.
Frequency domain (DFT): each DFT was calculated from a TWF.
Operating deflection analysis (ODS-FRF): each ODS-FRF was calculated from a TWF.
Overlap processing: 25 spectrum averages with 95% overlap processing between averages.
Cell phone frame rate: 240 fps → 240 Hz.
F_{MAX} *of the FFT:* 120 fps → 7200 RPM.

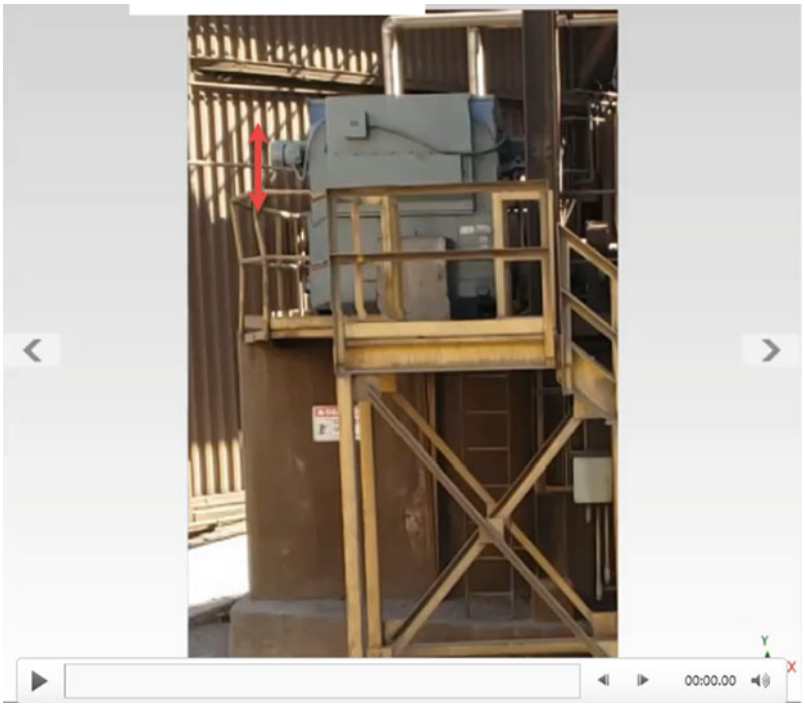

Fig. 11.1 Vertical motor motion

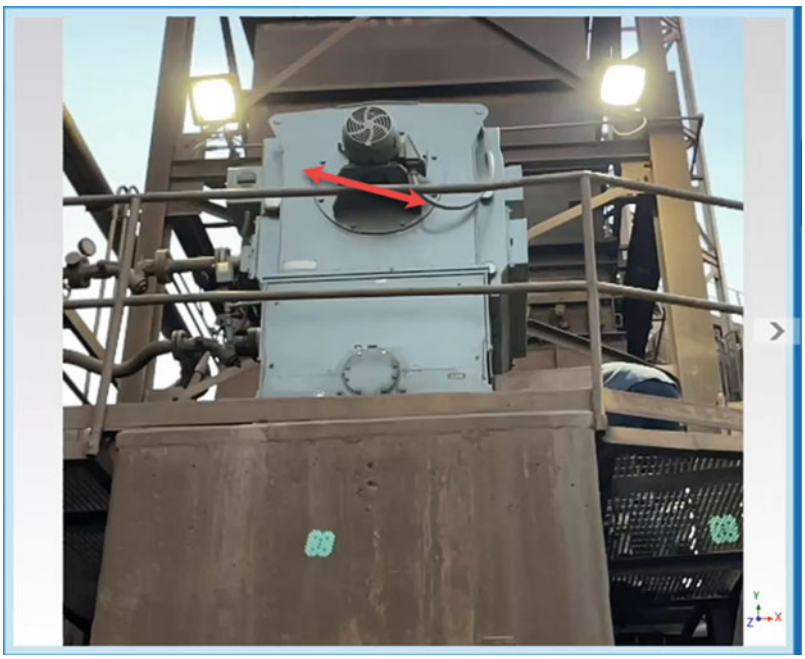

Fig. 11.2 Horizontal motion or "list" of the motor

11.3.1 Case #1 Analysis Summary

The customer noticed elevated and increasing vibration levels in the outboard motor location. The video ODS analysis quickly pin-pointed an odd vertical motion in the motor (Fig. 11.1). The perpendicular (axial) view suggested a horizontal "list" in the motor (Fig. 11.2). The elevated vantage point (Fig. 11.3) showed an overall torsional response in the motor.

The video ODS analysis quickly pin-pointed a soft foot issue at the motor outboard mount.

Fig. 11.3 Torsional vibration

Even though it was late in the day and the unit was *"in shadow,"* no external lighting was required.

Most applications require only a cell phone camera and do not require additional lighting.

Figure 11.4 shows that both the DFT and the ODS-FRF identified the running speed, or first order, of the machine at *893 RPM*. The second order peak is also very prominent at *1790 RPM* in both frequency functions.

The video ODS analysis indicated a *horizontal twisting response* in the motor.

The video ODS analysis quickly pin-pointed a soft foot issue at the motor outboard mount.

11.3.2 Case #2: Concentrator Processing Vessel Vibration Analysis

This unit was located in a sugar refinery. Data was captured with a cell phone camera mounted on a tripod.

Video camera: iPhone 10 SE
Frame rate: 240 fps
Resolution: 1080p HD
Video mode: "Slo-Mo"
Trigger: Blue Tooth (start/stop)
Clip duration: 15–20 s

The customer noticed vibration problems initially from the lights mounted on the framework. A structure of this size is a challenge for performing a traditional accelerometer-based ODS analysis. The six I-beam columns were 70 feet tall. Overall, the structure was 70 × 35 × 15. The video ODS made easy work of defining the structural natural frequencies. A traditional accelerometer-based analysis of the structure verified the frequencies and amplitudes (Figs. 11.5 and 11.6).

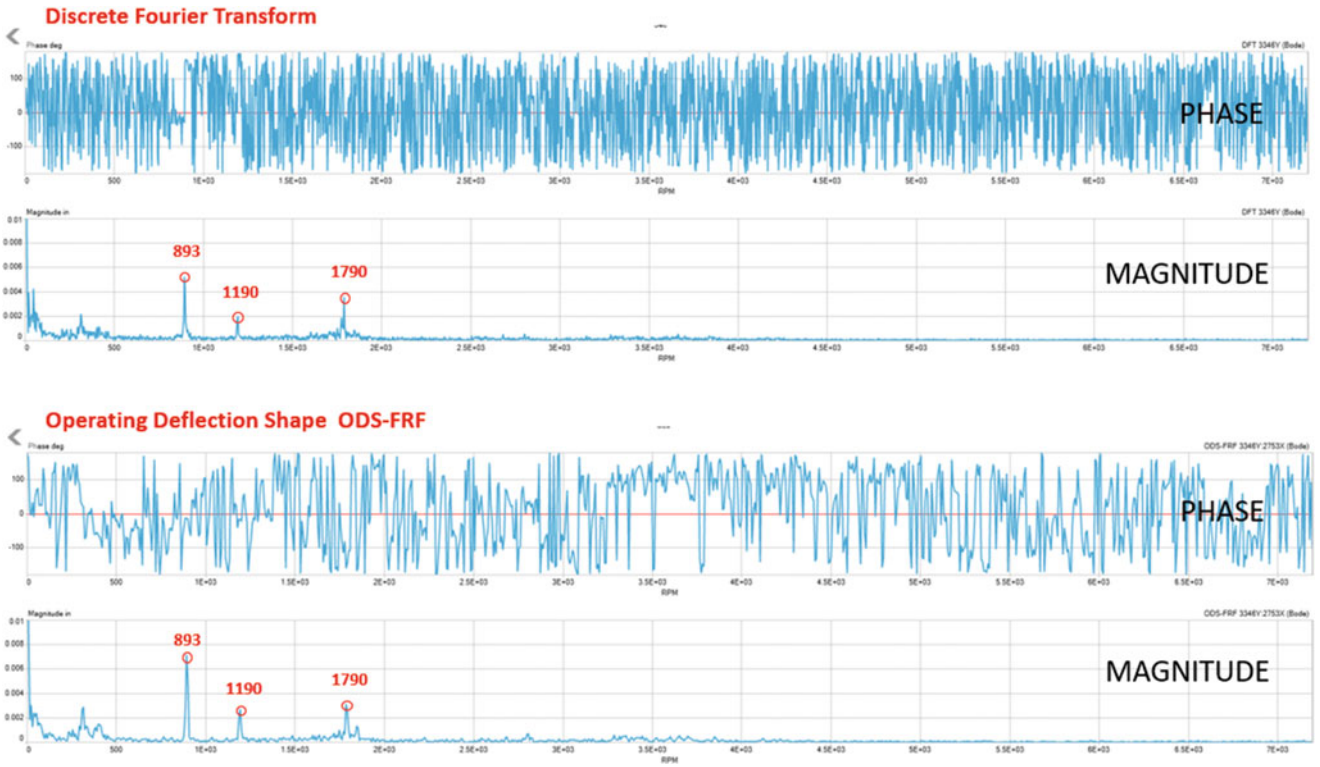

Fig. 11.4 DFTs and ODS-FRFs

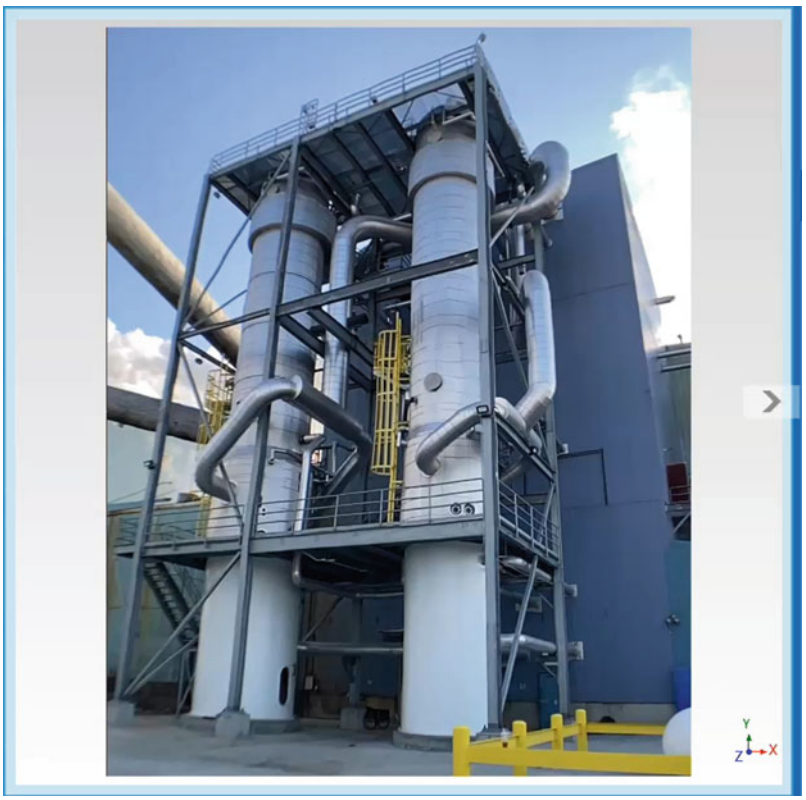

Fig. 11.5 70 Foot-tall sugar refiner

Fig. 11.6 Column with light attached

11.4 Asset Description

This tower is the main part of a concentrator process. There is no rotating equipment on the framework platform to provide excitation. The only source of excitation is internal turbulence in the process itself or possible wind loadings that might induce unstable vortex shedding around the tanks.

11.5 Video Analysis

A series of cell phone video clips were acquired on the tower at various locations and directions. The camera was an iPhone 10 with frame rate set to 240 frames-per-second (fps). The 1080p videos was set to "Slo-Mo." The video clips were processed with the MEscope Video ODS™ software.

11.6 Analysis Summary

The video ODS analysis revealed a definite frame and tank motion at 180 CPM (3 Hz). The excitation source was likely random wind gusts (vortex shedding).

11.7 Traditional ODS Analysis

A traditional operating deflection shape (ODS) analysis was performed on the tower structure. This analysis is an accelerometer-based vibration analysis. Roving vibration measurements were acquired which provided amplitudes and phases throughout spatial locations on the tower structure. A fixed reference accelerometer response is compared to each

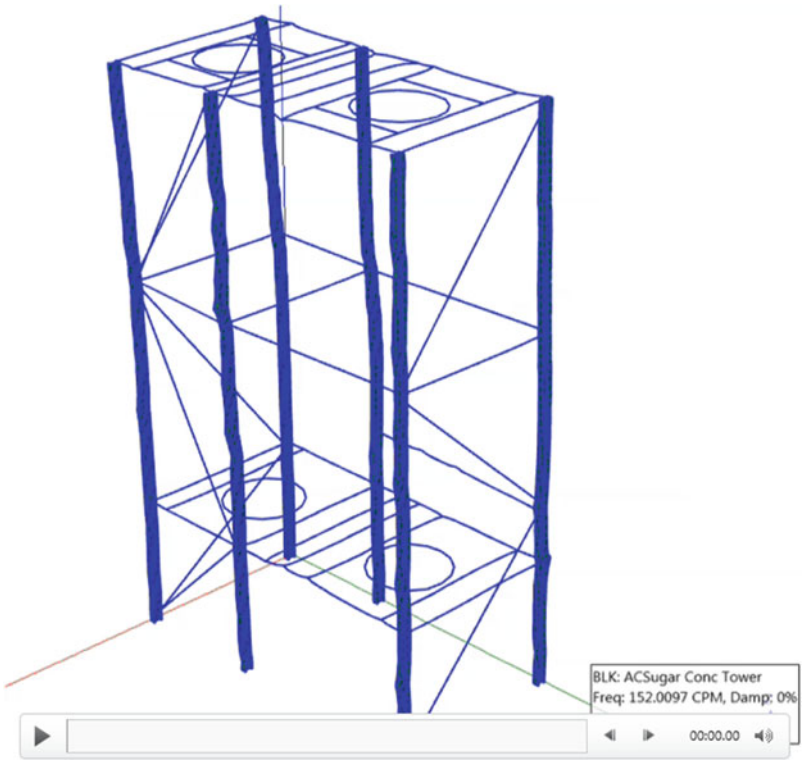

Fig. 11.7 ODS of the tower from accelerometers

roving response to define the magnitude and phase of its motion relative to the reference. When the data is animated, a visual ODS of the structure immerges (Fig. 11.7).

11.8 ODS Analysis Summary

A resonance peak was identified in this spectral response of the tower at *152 CPM (2.53 Hz)*. The ODS of this response confirmed this mode shape as the first bending (1B) mode shape of the frame structure.

11.9 Conclusions

Most rotating machines and attendant structures have phase-related problems such as unbalance, eccentricity, looseness, misalignment, bent shafts, and resonance amplification. Video ODS analysis is ideal for detecting and defining these phase-related problems.

To analyze phase-related vibration below *120 Hz (or 7200 CPM)*, a cell phone is more than adequate as a low-cost non-contacting device for acquiring data and displaying it in animation as a video ODS. Another benefit is that artificial lighting is not required in most cases.

Time waveforms (*TWFs*) can be extracted from *any digital video recording using the MEscope Video ODS*™ software. Both time-based and frequency-based ODSs can be extracted from this data and displayed in animation on frames of the video to give a quick look at vibration problems in any operating machine or its attendant structure. When ODS data is used in this way, deflections of the test article are clearly seen, giving plant maintenance engineers, vibration analysts, and management a clear picture of the probable cause of a machinery health problem.

Video ODS makes vibration analysis visible and understandable to the entire management team so everyone can be involved in defining and implementing asset management solutions to machinery health problems.

References

1. Farnebäck, G.: Two-frame motion estimation based on polynomial expansion. In: Bigun, J., Gustavsson, T. (eds.) Image Analysis. SCIA 2003. Lecture Notes in Computer Science, vol 2749. Springer, Berlin, Heidelberg (2003)
2. https://nanonets.com/blog/optical-flow/
3. Schwarz, B., Richardson, S., Tyler, J., Spears, R., Richardson, M.: Post-Processing ODS Data from a Vibration Video. IMAC XXXVIII Houston, TX, February 10–13, 2020
4. Richardson, M.H.: Is it a mode shape or an operating deflection shape? Sound and Vibration Magazine, March 1997
5. Schwarz, B, Richardson, M.H.: Measurements Required for Displaying Operating Deflection Shapes. In: Proceedings of IMAC XXII, January 26, 2004
6. Schwarz, B., Richardson, M.H.: Introduction to Operating Deflection Shapes. CSI Reliability Week, Orlando, FL (October 1999)
7. MEscope™ is a trademark of Vibrant Technology, Inc. www.vibetech.com

Chapter 12
Influence of Shaker Limitations on the Success of MIMO Environment Reconstruction

Marcus Behling, Matthew S. Allen, Randall L. Mayes, Washington J. DeLima, and Jonathan Hower

Abstract Several factors can prevent MIMO environment reconstruction tests from being successful, including the locations of the shakers and their directions, the set of accelerometers that are controlled to, and the upper and lower bounds of a shaker's dynamic range. This work explores these issues for a simple component that flew on a sounding rocket in 2019, and which was instrumented with accelerometers to capture the operational environment in detail. Electrical models were estimated for three modal shakers to predict whether a certain configuration of shakers can recreate the environment without exceeding their input voltage capabilities. Tests are performed controlling to various sets of accelerometers. Finally, the condition number threshold and stinger length are investigated as potential solutions to insufficient shaker dynamic range. These factors are all studied by simulating a MIMO test using transfer functions measured in impact hammer testing, and physical MIMO testing is performed on the most promising test configurations using six modal shakers.

Keywords Shaker test · Dynamic environment · Reconstruction · Dynamic modeling · Dynamic range

12.1 Introduction

To determine if a part can withstand its intended operational environment, vibration qualification tests are performed. In these tests, a shaker is driven to excite the device under test (DUT), hopefully recreating the stresses it experiences in operation. If the part survives the qualification test, it is assumed to be ready to withstand its operational environment. Traditionally, these tests have been performed using a single axis shaker table, wherein the part of interest is rigidly fixed to the table and excited in a single direction. These single axis tests fail to match the DUT's boundary impedance and wrongly excite off-axis motion, often resulting in overly conservative qualification tests; past tests have exceeded the intended environment by 10 to 100 times [1]. Parts sometimes fail these overly conservative tests and must be redesigned when they would have survived in the field environment. This redesign involves more qualification tests which needlessly waste time and money.

One method that has been traditionally used to improve reconstruction accuracy is force limiting. Dynamic environments have historically been created by enveloping an acceleration power spectral density (PSD) with straight lines. This enveloping process along with the impedance mismatch between the operational environment and the shaker table to which the part is mounted in a lab test has historically caused significant over-testing at certain frequencies in a bandwidth [1]. If the voltage input to the shaker is notched at these frequencies, the response is reduced. At which frequencies and how much to notch the voltage are decided by force limits. Marchand et al. determined these force limits by multiplying the apparent mass at the shaker-DUT interface by the maximum interface acceleration, finding that this method provided significant notching, particularly at anti-resonances of the Shaker-DUT system [2]. Reyes and Avitabile developed a modular method to minimize shaker-DUT dynamic interactions that have historically caused over-testing [3]. Van Fossen and Napolitano proposed a

M. Behling (✉) · M. S. Allen
Brigham Young University, Provo, UT, USA
e-mail: mebehlin@student.byu.edu; matt.allen@byu.edu

R. L. Mayes
Mayes Consulting, Albuquerque, NM, USA

W. J. DeLima · J. Hower
Honeywell Federal Manufacturing & Technologies, Kansas City, MO, USA
e-mail: wdelima@kcnsc.doe.gov; jhower@kcnsc.doe.gov

J. Harvie (ed.), *Dynamic Environments Testing, Volume 7*, Conference Proceedings of the Society for Experimental Mechanics Series, https://doi.org/10.1007/978-3-031-34930-0_12

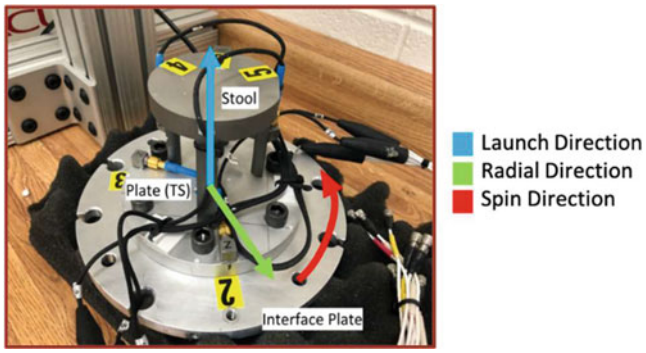

Fig. 12.1 DUT used in MIMO tests

method whereby the forces are computed from a set of acceleration measurements, eliminating the need for load cells, which can be problematic to include the mounting hardware [4].

While force limiting fixes some of the problems associated with single axis testing, off-axis motion remains a problem. An alternative to single-axis testing is multiple input-multiple output (MIMO) testing, in which the part of interest is excited in multiple degrees of freedom at the same time. These tests can be performed with six-degree of freedom shaker tables. Paripovic and Mayes showed that these tables could reproduce an acoustic environment in multiple directions much more accurately than a single-axis table [5]. While these tables have great potential, they are not yet widely available, and shaker modes can introduce additional uncontrolled dynamics.

Alternatively, MIMO tests can be performed using the impedance matched multi-axis testing (IMMAT) method proposed in [6]. This method involves attaching multiple smaller shakers to the DUT to excite it in multiple directions simultaneously. The shakers are attached via thin metal rods called "stingers" in order to change the DUT's boundary impedance as little as possible in the directions orthogonal to the excitation. While tests performed using the IMMAT Methodology have shown promising results [7], the increased potential for accurate reconstruction comes with increased complexity, which is evidenced by the broad range of relevant studies currently being performed. Rohe et al. performed MIMO tests using various topology optimized fixtures, finding these fixtures to have more modes that are active in a testing bandwidth and to be more difficult to control [8]. Jankowski et al. investigated the effect of the BARC structure's boundary stiffness on its PSD, finding no significant correlation [9]. Schultz and Avitabile presented an algorithm that selects and uses constraint vectors to coordinate input voltage PSDs for multiple shakers [10]. Schultz and Nelson explored how to create a test environment specification in the absence of operational data on a DUT [11]. Pacini et al. showed that a shaker's output force can be distorted due to structural nonlinearities and dynamic interactions between the shaker and structure [12]. Beale et al. compared two methods for selecting accelerometer locations and orientations, finding that both a mean square error minimization and a more complex optimal experimental design method provided reasonable locations [13]. Dumont et al. tested how various accelerometer mounting methods impact measurements, while discussing the potential impact of accelerometer mass on the dynamical properties of a DUT [14]. IMMAT testing requires a target cross spectral density (CPSD) matrix from multiple accelerometers and MIMO control equipment, which is often not available, so traditional vibration testing methods are often employed despite their well-known inaccuracy.

This study is a continuation of [7, 15, 16], and [17]. The DUT is shown in Fig. 12.1; the plate and interface plate together function as a transmission simulator, where forces are applied to the interface plate and transmitted through the plate with the goal of recreating the response on the stool. Tuman et al. found that MIMO tests performed using this configuration yielded more accurate reconstruction results than two other tested configurations where more or less of the flight hardware was included [7]. The plate and stool were each instrumented with three triaxial accelerometers for a total of 18 channels which measured in the radial, spin, and launch directions, and all shakers were attached to the interface plate. The operational environment was obtained from the boost portion of a sounding rocket's flight performed by Kansas City National Security Campus in July 2019. It excludes significant shock events.

12.2 IMMAT Theory

For a linear system, an input F and its steady-state response X are related by a frequency response function (FRF) as shown in Eq. (12.1). For a system with multiple inputs and multiple outputs, the inputs at locations i and outputs at locations s are

related by an FRF matrix H, with the superscript "S + TS + V" referring to the system that is being considered, which in this case is the stool (S), transmission simulator (TS), and vehicle (V), which are all present when the DUT's response is measured in the operational environment. The forcing inputs that cause the stool's response in its operational environment can theoretically be determined by inverting the FRF matrix as seen in Eq. (12.2). Since there are typically more measured outputs than inputs, the inverse of the FRF matrix is generally performed as a Moore-Penrose pseudoinverse, denoted as a "+" in the exponent. Though the distributed drag and thrust loads cannot be recreated in a lab, one could determine the forcing input at many locations on the rocket, attach shakers to each of these locations, and reproduce the operational environment on the stool.

$$X_{s,\text{env}}(\omega) = H_{s,i}^{S+\text{TS}+V}(\omega)\, F_{i,\text{env}}(\omega) \tag{12.1}$$

$$F_{i,\text{env}}(\omega) = \left(H_{s,i}^{S+\text{TS}+V}(\omega)\right)^{+} X_{s,\text{env}}(\omega) \tag{12.2}$$

In a lab, testing the whole rocket is generally not practical, so lab vibration tests use only a part of the vehicle in a lab reconstruction test, reducing the required number of shakers but also changing the DUT's dynamics. The forcing inputs can be determined using Eqs. (12.3) and (12.4), where the superscript "S + TS + Sh" refers to the fact that the lab setup includes the dynamics of the stool (S), transmission simulator (TS), and the attached shakers (Sh) which are used to excite the structure.

$$X_{s,\text{lab}}(\omega) = H_{s,i}^{S+\text{TS}+\text{Sh}}(\omega)\, F_{i,\text{lab}}(\omega) \tag{12.3}$$

$$F_{i,\text{lab}}(\omega) = \left(H_{s,i}^{S+\text{TS}+\text{Sh}}(\omega)\right)^{+} X_{s,\text{lab}}(\omega) \tag{12.4}$$

The goal of a lab vibration test, as previously mentioned, is to recreate the stress state a part will experience in its operation environment. Though strain measurements at various locations on the DUT would be best, it is often assumed that a stress state is accurately recreated if the acceleration response at multiple points on a structure is matched, or if $X_{s,\text{lab}} = X_{s,\text{env}}$.

In [7], the authors describe two main sources of error in reconstruction tests: error due to modes that shakers cannot control and errors in the controlled response caused by other factors. Poorly chosen shaker locations, insufficient shaker dynamic range, and poor conditioning in the FRF matrix, among many others, cause this second type of error. This chapter discusses possible solutions for some of these sources of error.

12.3 Simulating a MIMO Test

To predict how successful an IMMAT test will be and to select shaker locations, it is useful to simulate the test beforehand. To perform this simulation, the FRF from input force to the response of each accelerometer channel is necessary. This can be obtained using a finite element model or by performing a roving hammer test at a set of marked locations on the DUT, which is the method employed here. In practice, the target response is calculated as a CPSD matrix to mitigate the effect of noise. The environment CPSD, S_{XX}, can therefore be written as a function of the FRF matrix and some environmental forcing power spectrum, S_{FF}, as shown in Eq. (12.5). By inverting the FRF matrix, the forcing CPSD of the shakers can be estimated using Eq. (12.6). This forcing power spectrum can then be inserted into Eq. (12.5), allowing for estimation of the reconstructed lab response using Eq. (12.7). We presume that the same control method is employed by the data acquisition system in the MIMO tests presented in this study, except that DAQ obtains the FRF matrix by sending random, uncorrelated voltage inputs to each shaker during a pretest and measuring the responses at each location.

$$S_{\text{XX}}(\omega) = H_{\text{XF}}(\omega)\, S_{\text{FF}}(\omega)\, H_{\text{XF}}^{*}(\omega) \tag{12.5}$$

$$S_{\text{FF,EST}}(\omega) = H_{\text{XF}}{}^{+}(\omega)\, S_{\text{XX}}(\omega) \left[H_{\text{XF}}^{+}(\omega)\right]^{*} \tag{12.6}$$

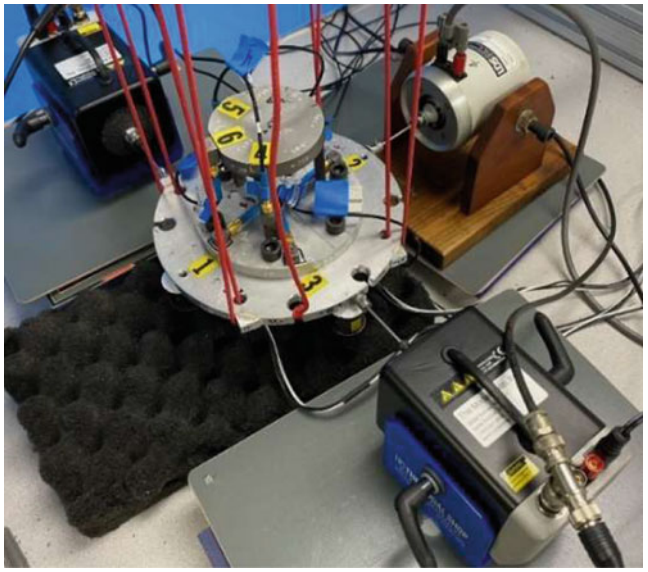

Fig. 12.2 MIMO test Setup 1 (includes launch, spin, and radial excitation)

$$S_{\mathrm{XX,EST}}(\omega) = H_{\mathrm{XF}}(\omega)\, S_{\mathrm{FF,EST}}(\omega)\, H_{\mathrm{XF}}^{*}(\omega) \tag{12.7}$$

In order to measure the accuracy of the reconstructed response, the error metric used in [7] is employed again here. The PSDs (diagonal terms of the CPSD) of the lab and environment response are converted to decibels, and the root mean square error between the lab and environment for all accelerometer channels is taken at a frequency line as shown in Eq. (12.8). The root mean square (RMS) of each of these frequency line errors is then taken, resulting in a single error for a given set of accelerometers in Eq. (12.9). This value is presented for the accelerometers on the plate and the stool in the results that follow.

$$e_{\mathrm{ASD}}(f_i) = \sqrt{\frac{1}{n_{\mathrm{accels}}} \sum_{k=1}^{n_{\mathrm{accels}}} \left[dB\left[\boldsymbol{S}_{X_k X_k}(f_i)\right] - dB\left[\boldsymbol{S}_{X_k X_k,\mathrm{lab}}(f_i)\right]\right]^2} \tag{12.8}$$

$$e_{\mathrm{ASD}} = \sqrt{\frac{1}{n_{\mathrm{freq}}} \sum_{i=1}^{n_{\mathrm{freq}}} e_{\mathrm{ASD}}(f_i)^2} \tag{12.9}$$

The MIMO simulation can be used to select shaker locations for a MIMO test. Though the simulation would ideally check every potential set of shaker locations, an iterative shaker selection algorithm has been found to yield reasonable results using far fewer calculations [18]. For each potential shaker location, this algorithm simulates the response $S_{XX,EST}$ and calculates the RMS dB error. The shaker that yields the lowest error is removed from the pool of potential locations and added to a vector of selected locations. The algorithm then selects the next shaker location, iterating through each available location and adding one at a time to the selected locations vector to calculate $S_{\mathrm{XX,EST}}$. The best location is kept in the selected locations vector, and this process is repeated until the desired number of shakers is obtained. We have found that many sets of shaker locations yield similar results, so a reasonable set of locations was obtained by selecting shaker locations to excite the modes of the DUT. This setup is shown in Fig. 12.2 and will be referred to as "Setup 1," providing the bulk of the results in this chapter. This intuitive set of shakers utilizes the three Q sources on the bottom of the interface plate to control the rigid body vertical, pitch and yaw degrees of freedom, two radial shakers to control the two lateral rigid body modes, and the torsional shaker to give roll rigid body control. Six shakers were used in all the tests in this study. Three Siemens Q Source Miniature Shakers excited the structure in the launch direction. Two Modal Shop (MS) Shakers and a Ling Dynamic Systems (LDS) Shaker excited the structure in the radial and spin directions.

12.4 Modeling Shaker Dynamics in Simulation

Tests performed using the IMMAT framework tend to use smaller shakers than a traditional shaker table test, so it is possible that shaker voltage limits are exceeded during a test. Hence, it is useful to be able to predict a shaker's RMS voltage in simulation, so one can predict whether a certain shaker setup will work. To this end, the dynamic model shown in Fig. 12.3 (similar to the model employed in [12]) was implemented in the MIMO simulation. This model was only implemented for the MS and LDS shakers, as the Q sources have different dynamics and higher voltage limits than the other shakers. To estimate the values of the model's parameters for each shaker, a uniaxial accelerometer was glued to the head of a 10-32x1/2″ bolt which threaded into each shaker's armature (shown in Fig. 12.4), and an experimental FRF from the amplifier voltage to acceleration was obtained. The same FRF was determined analytically from the model, and its magnitude was plotted alongside the magnitude of the experimental FRF. The parameter values were manually varied until the model and experimental FRFs matched with little error. This process was done once for the LDS shaker and once for one of the MS shakers, as it was assumed that both MS shakers would have identical characteristics. While most parameters could be obtained through direct measurement or consultation of the shaker data sheets, some of these parameters were varied from their measured or listed values to match the model FRF to the experimental FRF more closely. The model used to simulate the MIMO test is shown in Fig. 12.14, and the calibration plots for the MS and LDS shakers are shown in Figs. 12.15 and 12.16 respectively. Selected shaker parameters are shown in Table 12.5.

In order to estimate the FRF between shaker voltage and acceleration for the stool on plate assembly, the FRF obtained from the hammer test was multiplied by the analytical FRF from DAQ voltage to output force, $K_f * i_a$, at each frequency line, resulting in an FRF from voltage to acceleration as shown in Eq. (12.10). To account for the mass of the DUT and the

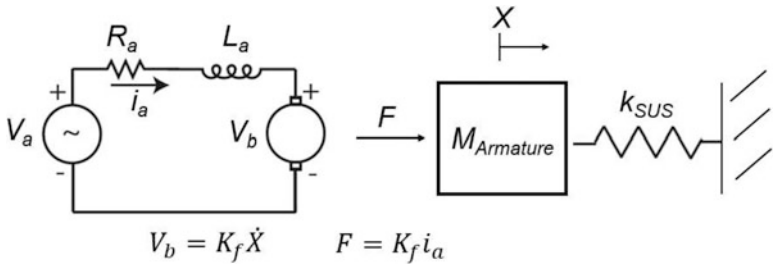

Fig. 12.3 Shaker model used to determine model parameters

Fig. 12.4 Setup used in shaker characterization tests

stiffness of the stinger, this analytical FRF was taken from a slightly different model which is shown in the Appendix. The simulation can then estimate the voltage power spectra for a set of shakers using Eq. (12.11), and these power spectra can be numerically integrated and square rooted to estimate the RMS voltage as shown in Eq. (12.12). Note that this is an estimate of the RMS voltage output by the DAQ that is sent to each shaker; this is a more relevant metric than the voltage coming out of the amplifier since most shaker data sheets list voltage limits in terms of the input to the amplifier. The amplifier voltage is obtained by multiplying the DAQ voltage by the amplifier gain.

$$H_{\mathrm{XV}}(\omega) = H_{\mathrm{XF}}(\omega)\, H_{\mathrm{FV}}(\omega) \tag{12.10}$$

$$S_{\mathrm{VV,EST}}(\omega) = H^{+}_{\mathrm{XV}}(\omega)\, S_{\mathrm{XX}}(\omega) \left[H^{+}_{\mathrm{XV}}(\omega)\right]^{*} \tag{12.11}$$

$$V_{\mathrm{RMS}} = \sqrt{\int S_{\mathrm{VV,EST}}(\omega)\, d\omega} \tag{12.12}$$

Before proceeding, it is important to note that this approach makes one important assumption that could limit the accuracy of these simulations. This approach inherently assumes that the dynamics of the shaker are not affected by its attachment to the structure. In essence, the velocity of the armature of the shaker is assumed to always be the same as it was in the test in Fig. 12.4. A more accurate approach would be to use substructuring [19] to couple the shaker model to the model of the structure, such that equal displacement (or velocity) is enforced where the shaker joins the structure. Mayes et al. used this approach, finding voltage predictions to be a bit conservative but generally accurate [20]. Unfortunately, this approach requires a drive-point measurement (both force and acceleration) at each point on the structure where the shaker is to be attached, and these are not currently available, so the simple approach outlined above was used instead.

Table 12.1 compares the RMS drive voltage from a MIMO test using Setup 1 to the RMS voltage predicted in simulation. The simulation predicts RMS voltages that are four to six times larger than those obtained in a test. As seen in Fig. 12.5, the voltage auto spectra from the data acquisition system (which we assume is obtained using Eq. (12.11)) and the voltage auto

Table 12.1 Comparison of simulated RMS voltage and MIMO test drive voltage

RMS voltage (V)	Simulation	MIMO test
MS Shaker 1 (radial)	0.410	0.066
LDS Shaker (radial)	0.189	0.053
MS Shaker 2 (spin)	0.313	0.059

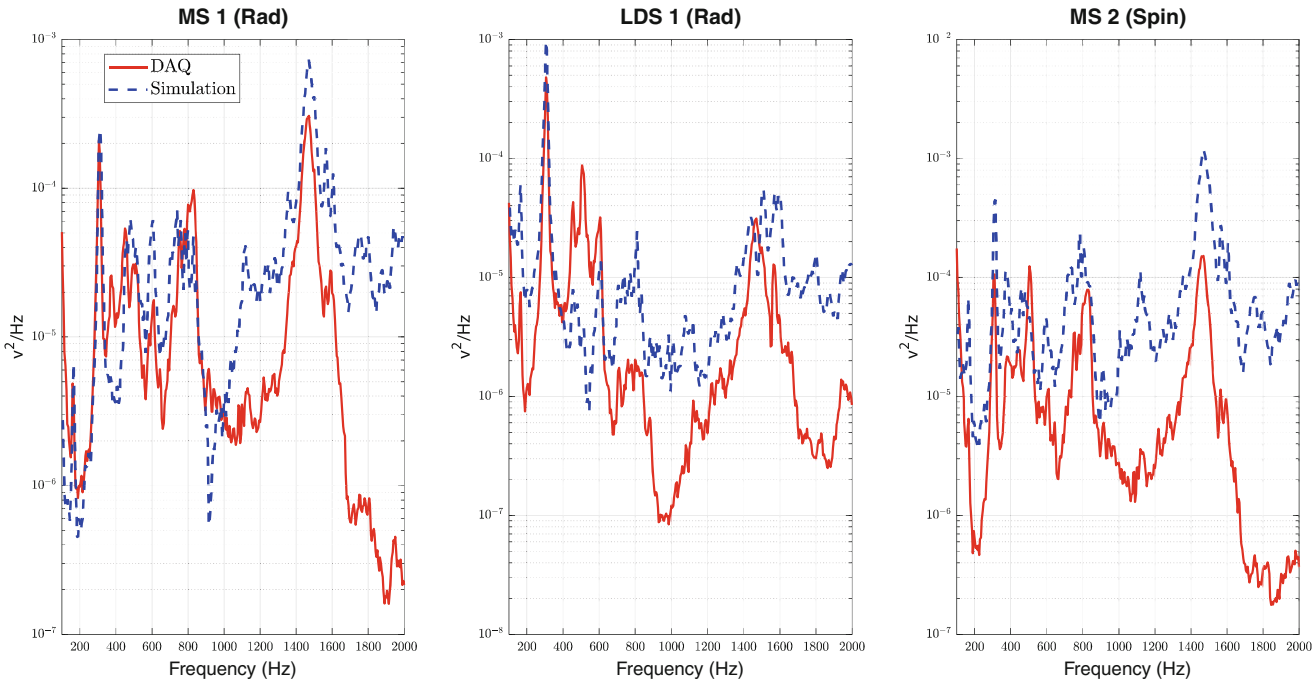

Fig. 12.5 Comparison of DAQ and simulation voltage auto spectra for Modeled Shakers

spectra predicted in simulation vary noticeably, though the simulation predicts general patterns in the spectra reasonably well. Perhaps these would match more closely if parameters were decided using an optimization algorithm rather than manually; not including the mass of the shaker casing in the model (as was done in [12]) might cause some of this error. Most likely, the dynamics of the shaker change significantly enough from the configuration in Fig. 12.4 to the MIMO test configuration that dynamic substructuring is required for a closer match on a spectral basis. The method presented here could still serve as a rough alternative to more rigorous modeling methods if sufficient time and data are not available.

12.5 Effect of Control Accelerometers

References [7, 15, 16, and 17] focused on gaining insight into the transmission of the response from the plate to the stool. As such, they only controlled to the accelerometers on the plate, using the environment data on the stool for comparison only. Since this study is focused less on transmissibility than improving the accuracy of controlled responses, MIMO tests were performed controlling to the plate, stool, and both simultaneously to determine which set of accelerometers yielded the best results. Since these past studies found that the reconstructed plate response was more accurate than the reconstructed stool response when the plate was controlled to, we expected that controlling to the stool would result in decreased stool error and increased plate error. It then seemed logical that controlling to all accelerometers would result in reasonable errors on both components due to the increased challenge of controlling to more accelerometers with a constant number of shakers.

Results of these tests are shown in Table 12.2, with the "Average Error" being the average RMS dB error over all available accelerometers on the plate and stool. The first two radial channels on the plate were excessively noisy during lab tests, so there were 7 available channels on the plate and 9 available channels on the stool. As expected, the plate error was significantly lower than the stool error when only controlling to the plate. A similar trend was observed for the stool, although the difference between plate and stool error was much less significant in that case. This seems to indicate that there are fewer ways to correctly recreate the stool response than the plate response, which seems reasonable given that the stool is not directly excited in the lab or operational environment while the plate response is. This also underscores how important it can be to choose shaker locations wisely. Controlling to the plate and stool simultaneously yielded the best average results; while this intuitively makes sense, it seemed likely that the increased number of control accelerometers would result in decreased controllability. Though using even more shakers could improve results, the six-shaker setup still yielded the best results on average when controlling to all accelerometers.

While it is difficult to predict how many shakers are generally needed for a given number of control accelerometers, or whether it is best to control to all available data on any given part, controlling to all accelerometers yielded the lowest average error for this DUT, so all tests shown in the remainder of this chapter were performed controlling to all accelerometers. It is interesting to note that the simulation tends to result in worse reconstruction than physical tests. This seems reasonable given that the simulation uses FRFs from a roving hammer test which approximate the shaker-stinger-DUT FRFs determined and used in a physical MIMO test.

12.6 Upper Bound of Shaker Dynamic Range

Vibration tests cannot be performed if shaker voltage limits are exceeded in a test. Consider the MIMO test setup shown in Fig. 12.6, which will be referred to as "Setup 2." This setup uses three shakers in the launch direction and three shakers in the radial direction to attempt to control responses in the radial, spin, and launch directions. This setup runs into a couple of

Table 12.2 Effect of control accelerometers on reconstruction error

		Control accelerometers		
		Plate	Stool	Plate + stool
Simulation	Plate error (dB)	1.1	8.8	4.8
	Stool error (dB)	15.7	5.3	8.3
	Average error (dB)	9.3	6.9	6.8
MIMO test	Plate error (dB)	1.4	5.5	4.2
	Stool error (dB)	11.2	3.5	4.1
	Average error (dB)	6.9	4.4	4.1

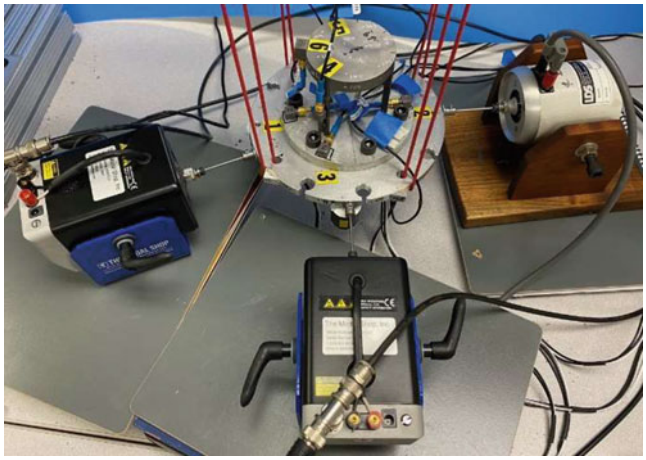

Fig. 12.6 MIMO test Setup 2 (includes launch and radial excitation)

problems. First, the shakers "fight" against each other, as one is oriented close to 180 degrees from another. Second, there is no direct torsion input to the DUT. Any spin input to the system is a result of small setup errors that cause eccentricity in the radial shakers. The RMS voltage required of each shaker is artificially increased, and shaker voltage limits are exceeded, preventing a test from running on this setup. Incidentally, a similar setup was chosen in [16] because the modal test data did not contain any DOF in the spin direction, and so the shaker placement algorithm could not select any shakers in the spin direction. In order to address this, it was necessary to glue angle blocks onto the plate and repeat the tests with hammer hits on those blocks.

One way to lower shaker voltages is to limit them to a specified number of standard deviations around the mean; most controllers have a setting such as this because a random voltage with a Gaussian distribution has the potential to return infinite values, saturating the hardware. In the Data Physics® system used in this study, this is called the Sigma Clip setting. A Sigma Clip of 3 is generally used in vibration tests as three standard deviations includes 99.7% of the data for a gaussian distribution; only the top and bottom 0.15% of voltages are clipped in such a test. While lowering the Sigma Clip parameter could reduce shaker voltage levels sufficiently to perform a test, it can affect reconstruction results significantly; Kihm and Delaux mention high-frequency distortions, reductions in shaker dynamic range, and reductions in damage potential as reasons against reducing the Sigma Clip parameter in vibration fatigue tests [21]. Though fatigue is not being tested here, the same conclusions are likely to apply.

Another option is to implement a condition number threshold on the FRF matrix that is determined in the pretest. Since the FRF matrix is inverted using Eq. (12.11) to determine the voltage CPSD, frequencies where the FRF matrix is poorly conditioned are particularly sensitive to noise resulting in artificial amplification of the voltage power spectrum at these frequencies. A condition number threshold can be implemented by taking the singular value decomposition of the matrix, calculating the ratio of each singular value to the largest singular value, and truncating the matrix to remove any singular values that are too small, as demonstrated in [7]. The same study found that implementing the condition number threshold tended to cause MIMO test results to match their simulation counterparts more closely; this is generally true, and the effect of the condition number threshold is further investigated here. When we refer to the condition number threshold, we use the inverse of the condition number as it is traditionally defined. A condition number threshold of 0.01, for example, removes all singular values that have a condition number of 100 or above, or those singular values that are less than 0.01 times the largest singular value.

Since the condition number threshold is implemented on the FRF matrix, which changes with every set of shaker locations, the effect of the condition number threshold also tends to vary from one set of shaker locations to another; one set of shaker locations can yield a more poorly conditioned FRF matrix than another set. This is demonstrated in Fig. 12.7, which compares the condition number spectrum of the FRF matrix for the two setups shown in Figs. 12.2 and 12.6. Since Setup 2 controls spin indirectly, the response is very sensitive to a small change in the shaker inputs, and the FRF matrix is poorly conditioned. Implementing a condition number threshold of 0.1 on the FRF matrix allows a test to be performed using Setup 2 because it lowers the required voltage level; the auto spectral densities of the corresponding voltages are shown in Fig. 12.8. Intuitively, the most significant notching in voltage auto spectra occurs at the most poorly conditioned frequency lines. Performing a MIMO test with this setup and a condition number threshold of 0.1 results in the reconstruction shown in Fig. 12.9. As seen in the figure, implementing a large condition number threshold tends to result in undertesting, particularly in valleys in the

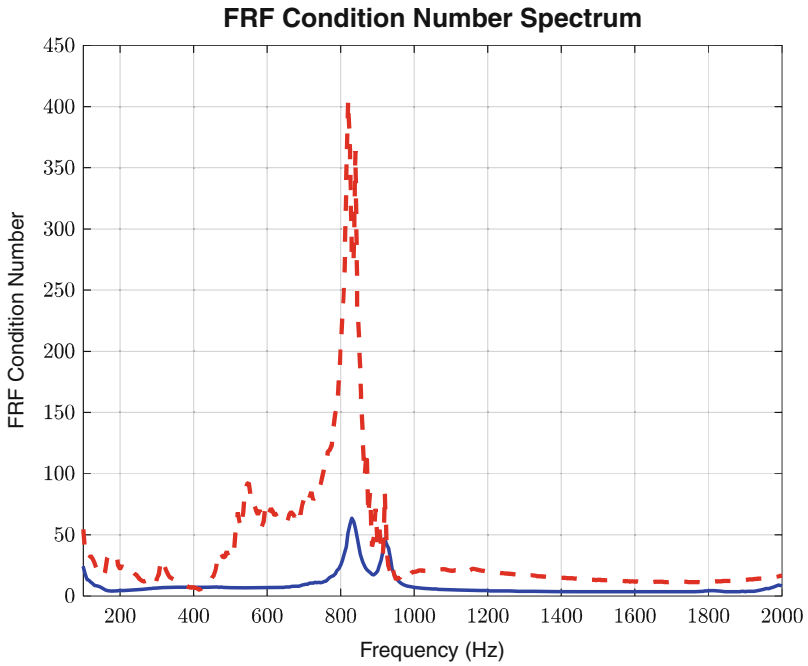

Fig. 12.7 Condition number spectrum of MIMO test FRF for Setup 1 (blue) and 2 (red)

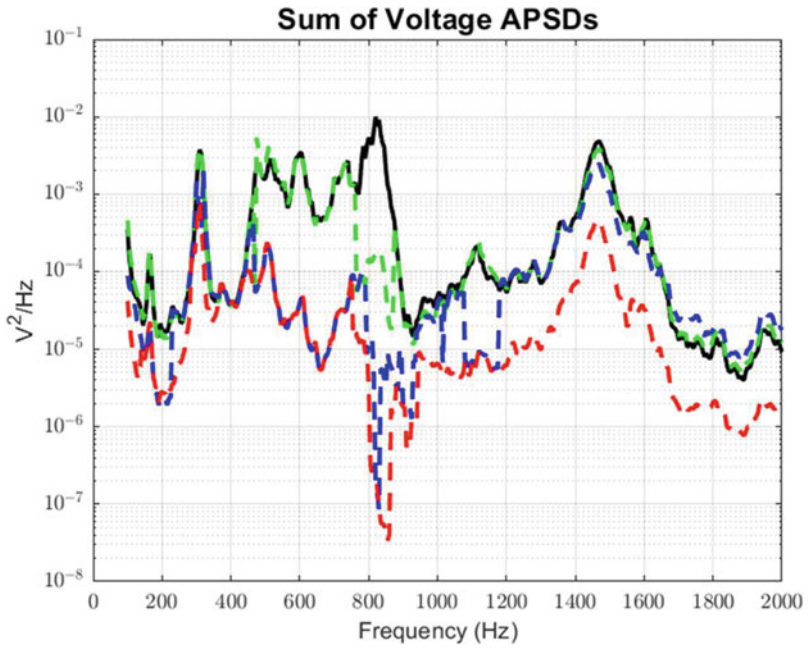

Fig. 12.8 Sum of MIMO test voltage auto spectra for Setup 2 with a condition number threshold of 0 (black), 0.01 (green), 0.05 (blue), and 0.1 (red)

environment. The condition number threshold is therefore a trade-off; while it can reduce shaker exertion so that a test can be performed, it removes information from the FRF matrix, resulting in worse reconstruction.

Now consider Setup 1, shown previously in Fig. 12.2. Since this setup orients shakers so they fight less and inputs torsion directly, a MIMO test can be performed with no condition number threshold (or the threshold set to zero), reconstructing the environment as shown in Fig. 12.10. Clearly, it is better to avoid implementing a condition number threshold altogether; when a small threshold (~0.01) is implemented on this setup, reconstruction results do not change significantly, and when a larger threshold is implemented, results worsen.

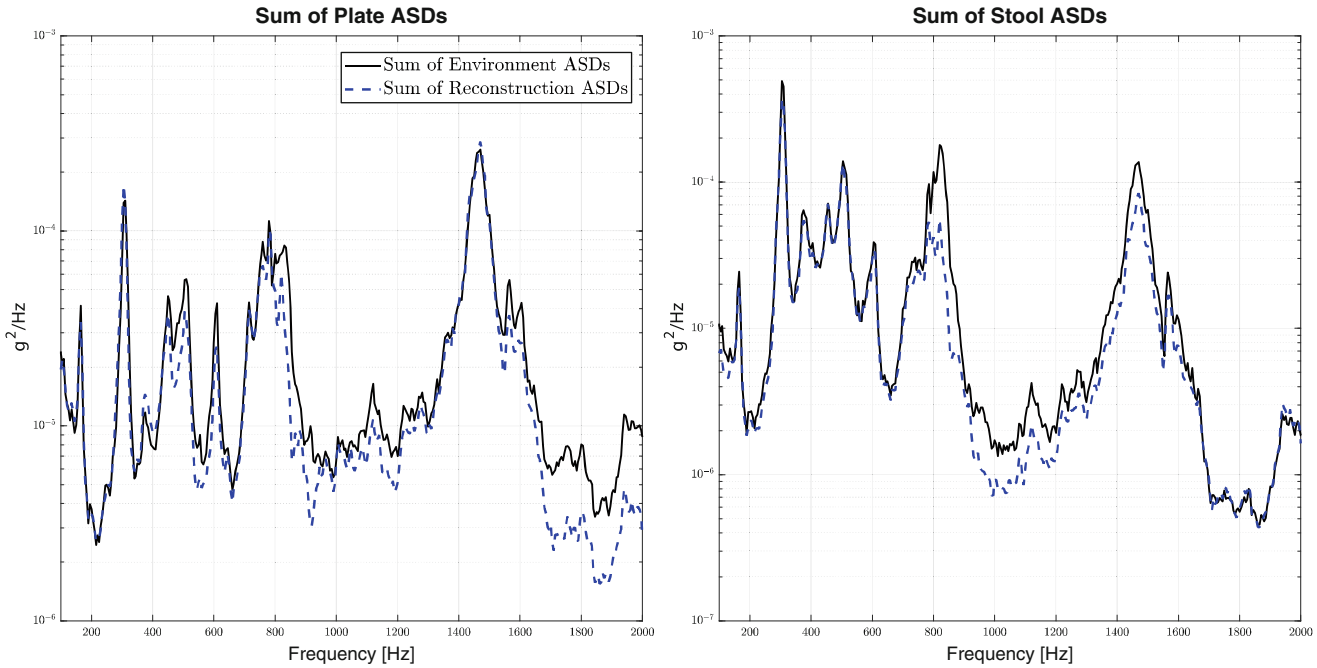

Fig. 12.9 MIMO test results for Setup 2 with condition number threshold = 0.1

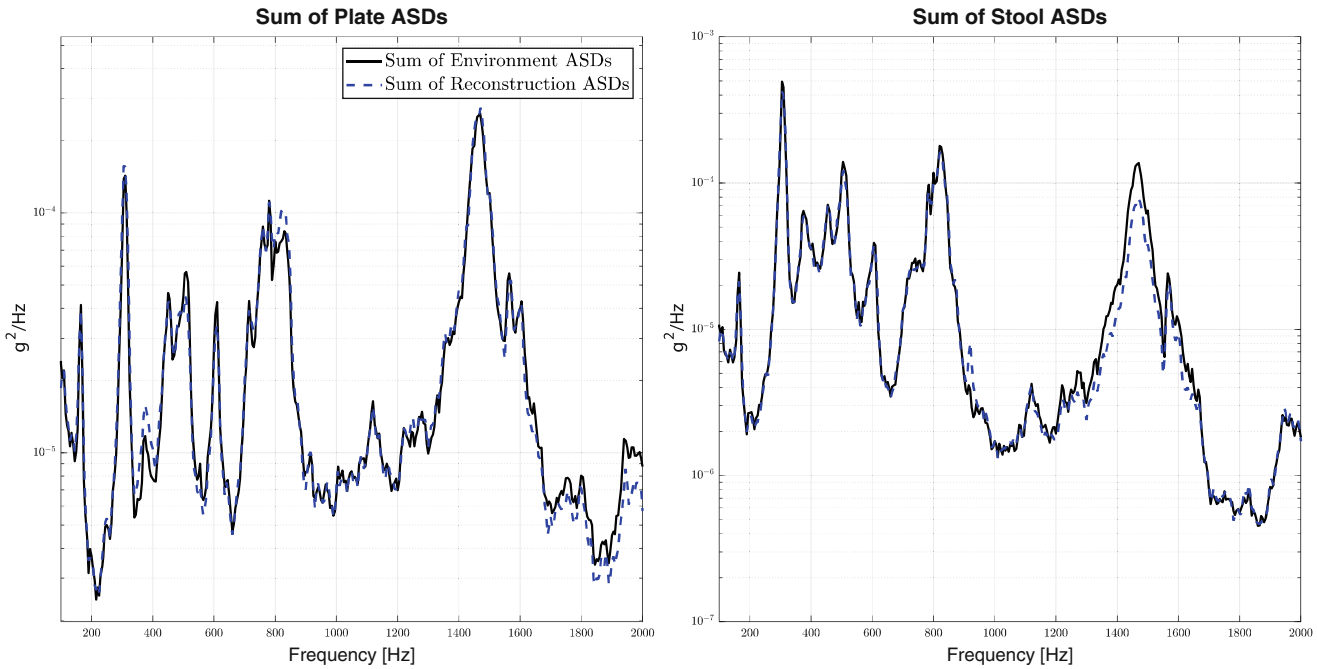

Fig. 12.10 MIMO test results for Setup 1 with condition number threshold = 0

Table 12.3 Summary of reconstruction results for Setup 1 (includes shaker in the spin direction) and Setup 2 (no shaker in the spin direction)

		Condition number threshold	
		0	0.1
Setup 1	Plate error (dB)	4.2	5.2
	Stool error (dB)	4.1	6.5
Setup 2	Plate error (dB)	–	7.5
	Stool error (dB)	–	9.9

A summary of reconstruction results for the two setups is given in Table 12.3. From these results, we conclude that the condition number threshold is a useful tool that can help tests be performed when shaker voltage limits are exceeded. It should be implemented carefully, though, as it can result in undertesting. It is best to select a set of shaker locations that can run without a condition number threshold or with a very small threshold, such as those in Setup 1, as such a test retains all the information in the FRF matrix, yielding the most accurate reconstruction. A well-conditioned setup seems to be one that minimizes shaker fighting and directly excites the structure in every direction it seeks to control. For a well-conditioned setup, there does not seem to be a good reason to implement a condition number threshold on the FRF matrix. However, for other structures or shakers, it may be necessary to implement a threshold even when the shakers are optimally placed.

12.7 Lower Bound of Shaker Dynamic Range

In reference [5], difficulty was encountered in reconstructing an environment at frequencies near a shaker mode as well as a fixed base mode of the DUT; similarly, in [8], it was found that the highest reconstruction error occurred at modes of the fixture-DUT system. A possible explanation for poor control at DUT and shaker armature modes is insufficient shaker dynamic range. Since the DUT response is amplified at a natural frequency, the voltage input must generally be reduced at these frequencies to avoid over-testing. If the shaker has insufficient dynamic range, the minimum signal at these frequencies (i.e., due to electrical noise) may be too large to limit the response at the resonance, resulting in over-testing.

The shaker armature, stinger, and DUT system can be represented by the dynamic model in Fig. 12.11. The first axial armature natural frequency can be estimated by plotting the FRF from force F to the displacement of the DUT $X2$. By modeling the stinger as a spring with stiffness EA/L, we can predict what length of stinger is required to move this armature mode out of the testing bandwidth. With an initial stinger length of 0.3 meters, the first axial armature mode was predicted to occur around 1270 Hz. When the stinger was shortened to 0.05 meters, the first axial armature mode was predicted to occur around 3110 Hz, which is far greater than the upper limit of the testing bandwidth at 2000 Hz. A set of stingers was cut to 0.05 m, and MIMO tests were performed using both sets of stingers in Setup 1.

One way to check if insufficient notching is occurring in a shaker is to compare the predicted and measured voltage auto spectra for a test, where the predicted voltage auto spectra are calculated in the pretest according to Eq. (12.11). The shakers used in this study were found to have enough dynamic range to control armature modes, so the Sigma Clip parameter was lowered to 0.8 for the radial and spin shakers to simulate a scenario in which the shaker dynamic range was insufficient. As seen in Fig. 12.12, when longer stingers were used, the shaker could not notch its voltage sufficiently from 1200 to 1400 Hz, where the armature mode was predicted to occur. When the stinger is shortened, this phenomenon is not observed. As seen in Fig. 12.13, there is significant overshoot from 1200 to 1400 Hz in the long stinger tests but not in the short stinger tests. Shortening stingers can therefore move a shaker armature mode out of a testing bandwidth, improving control when shakers have insufficient dynamic range.

It is worth emphasizing that using shorter stingers only moves the first axial armature mode to a different natural frequency. As seen in Table 12.4, the reconstruction error increased in the 100-4000 Hz testing bandwidth when using shorter stingers. The control seems to worsen at the armature mode when the shortened stinger is used, so stingers should be shortened if the armature mode cannot be controlled and if shortening the stingers can remove the armature mode from the testing bandwidth.

12.8 Conclusion

This work explored several of the issues that can make environment reconstruction and especially IMMAT testing challenging as compared to traditional single-axis testing. These include selecting shaker locations, selecting control accelerometers, and staying within a shaker's dynamic range. This work demonstrated that a MIMO simulation can be extremely useful as a

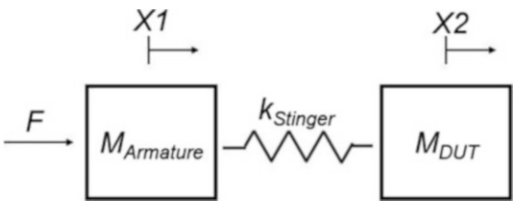

Fig. 12.11 Dynamic model of armature-stinger-DUT system

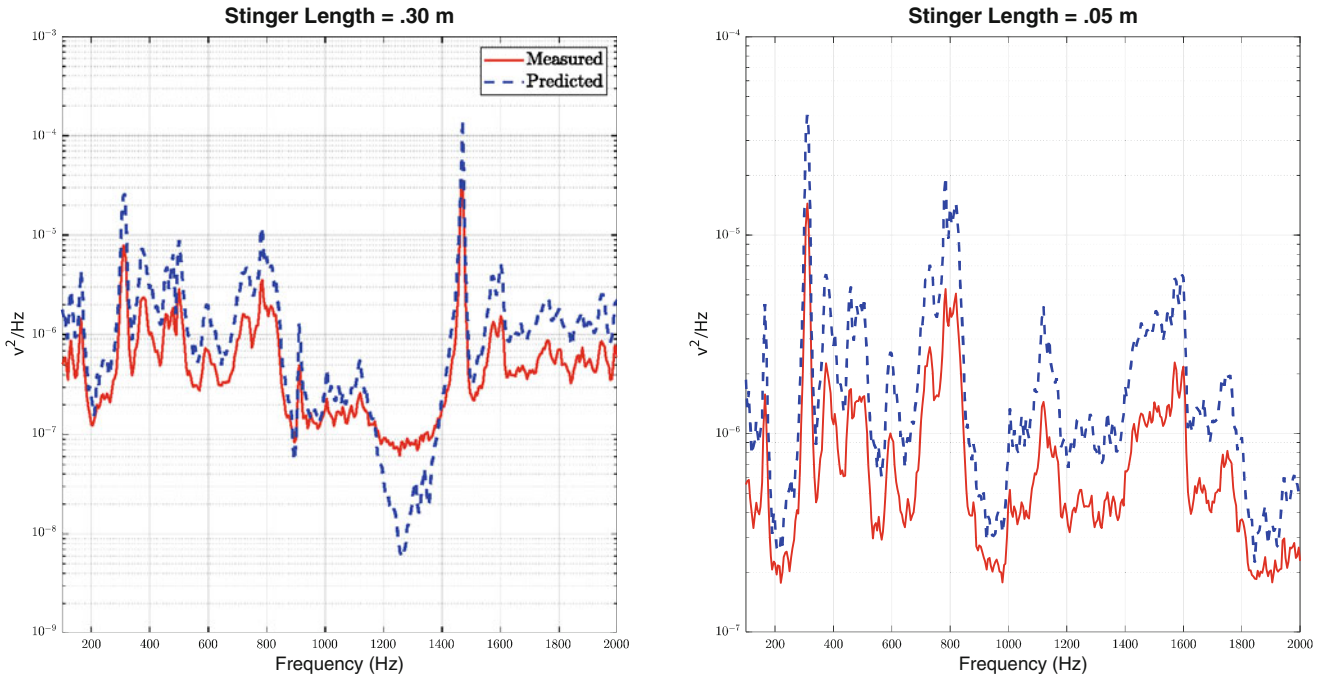

Fig. 12.12 LDS shaker predicted and measured voltage ASD for MIMO tests with long and short stingers

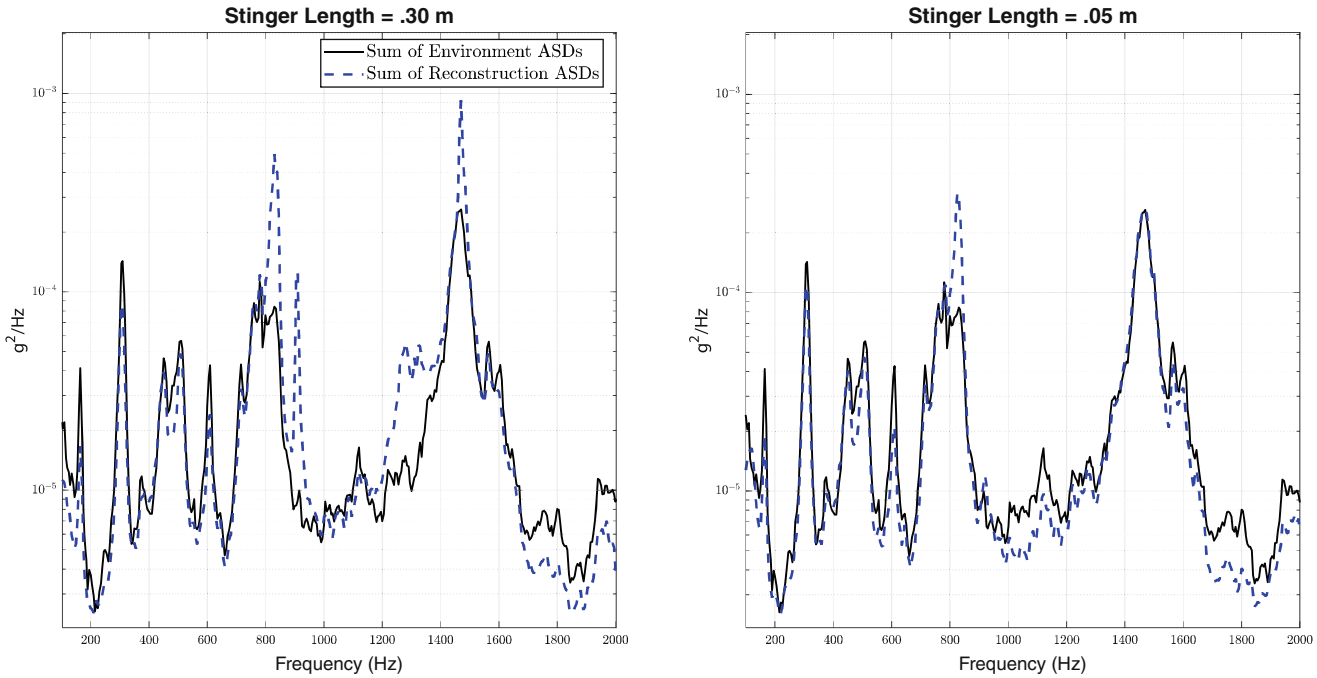

Fig. 12.13 Sum of plate ASDs for MIMO tests with long and short stingers\vspace*{-15pt}

Table 12.4 Summary of MIMO test results using short and long stingers (Setup 1)

Stinger length (m)	0.05		0.3	
Frequency bandwidth (Hz)	100-2000	100-4000	100-2000	100-4000
Plate error (dB)	6.1	12.7	7.2	8.5
Stool error (dB)	6.5	12.9	8.7	10.3

tool to predict the performance before performing a physical test, and can be used to help in selecting shaker locations using the iterative selection method introduced in [18]. It also can be used to predict shaker RMS voltages using a simple dynamic model of the shaker-stinger-DUT system. The lowest reconstruction error was found to occur when all available environment data was controlled to. Implementing a condition number threshold on the FRF matrix was found to reduce the required voltage input to each shaker, allowing tests to run that otherwise could not. Using shortened stingers in an IMMAT test was found to raise shaker armature modes, which are uncontrollable without sufficient dynamic range, out of a testing bandwidth, improving reconstruction results. IMMAT testing is certainly complex, but its accuracy can be greatly improved through small changes and simple modeling.

Future work could focus on modifying an environment specification to be more easily matchable in the lab, on modeling shaker dynamics in more detail, or perhaps on increasing the fidelity of the simulation to improve reconstruction in MIMO tests while reducing time wasted. Ultimately, it should focus on developing procedures to optimize the IMMAT testing process so it can be performed quickly on any part and with minimal prior knowledge of the dynamics of the part.

Acknowledgments The authors gratefully acknowledge the Department of Energy's Kansas City National Security Campus, operated by Honeywell Federal Manufacturing & Technologies LLC, for funding this work under contract number DE-NA0002839.

A.1 Appendix

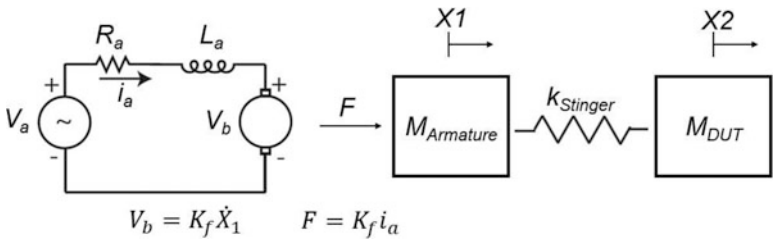

Fig. 12.14 Shaker dynamic model implemented in MIMO simulation

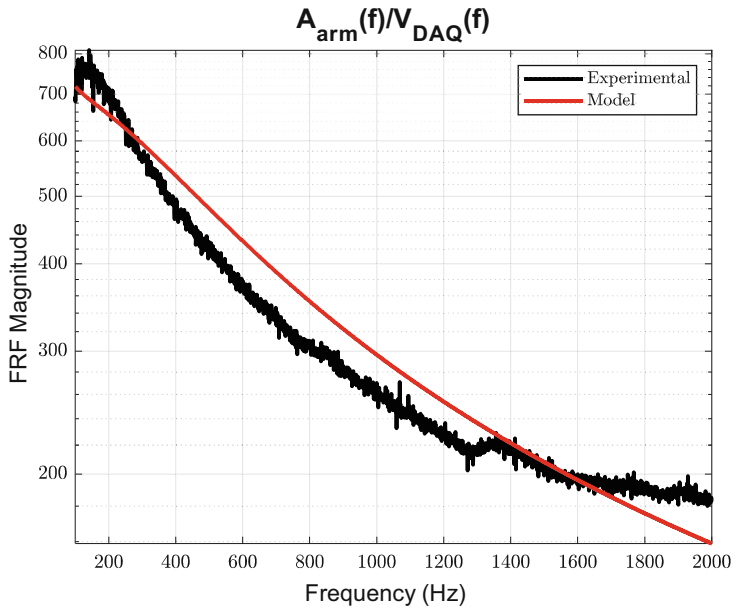

Fig. 12.15 Calibration plot for MS shakers

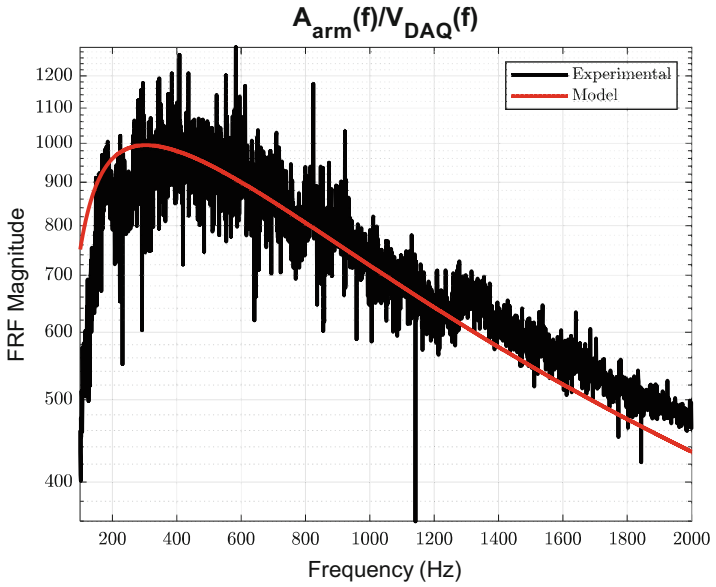

Fig. 12.16 Calibration plot for LDS shaker

Table 12.5 Parameter values for MS and LDS shakers

Parameter name	Value for MS shakers	Value for LDS shaker
Resistance (Ω)	0.4	1.5
Armature mass (kg)	0.09	0.10
Inductance (mH)	0.13	0.25
Back emf constant (V/m/s)	2.4	10
Armature stiffness (N/m)	2630	2630

References

1. National Aeronautics and Space Administration. Force Limited Vibration Testing, NASA-HDBK-7004B, 2003. [Online]. Available: http://standards.nasa.gov
2. Marchand, P., Singhal, R., O'Grady, M.: Force limited vibration using the apparent mass method. In: Shock & Vibration, Aircraft/Aerospace, Energy Harvesting, Acoustics & Optics, Volume 9, pp. 53–66, Cham (2016). https://doi.org/10.1007/978-3-319-30087-0_6
3. Reyes, J.M., Avitabile, P.: Force Customization to Neutralize Fixture-Test Article Dynamic Interaction, presented at the International Modal Analysis Conference 36, Orlando, FL, 2018
4. Van Fossen, T., Napolitano, K.: An acceleration-based approach to force limiting a random vibration test. In: Special Topics in Structural Dynamics & Experimental Techniques, Volume 5, pp. 315–325, Cham (2021)
5. Paripovic, J., Mayes, R.L.: Reproducing a component field environment on a six degree-of-freedom shaker. In: Linderholt, A., Allen, M., D'Ambrogio, W. (eds.) Dynamic Substructures, Volume 4, pp. 73–78. Springer International Publishing, Cham (2021). https://doi.org/10.1007/978-3-030-47630-4_6
6. Daborn, P.M., Roberts, C., Ewins, D.J., Ind, P.R.: Next-generation random vibration tests. **8**, 397–410 (2014). https://doi.org/10.1007/978-3-319-04774-4_37
7. Tuman, M.J., Allen, M.S., DeLima, W.J., Dodgen, E., Hower, J.: Balancing impedance and controllability in response reconstruction. In: Walber, C., Stefanski, M., Harvie, J. (eds.) Sensors and Instrumentation, Aircraft/Aerospace and Dynamic Environments Testing, Volume 7, pp. 133–143. Springer International Publishing, Cham (2023). https://doi.org/10.1007/978-3-031-05415-0_12
8. Rohe, D.P., Schultz, R.A., Schoenherr, T.F., Skousen, T.J., Jones, R.J.: Comparison of multi-axis testing of the BARC structure with varying boundary conditions. In: Sensors and Instrumentation, Aircraft/Aerospace, Energy Harvesting & Dynamic Environments Testing, Volume 7, pp. 179–193, Cham (2020)
9. Jankowski, K., Sedillo, H., Takeshita, A., Barba, J., Bouma, A., Abdelkefi, A.: Impacts of test fixture connections of the BARC structure on its dynamical responses. In: Sensors and Instrumentation, Aircraft/Aerospace, Energy Harvesting & Dynamic Environments Testing, Volume 7, pp. 175–177, Cham (2022). https://doi.org/10.1007/978-3-030-75988-9_13
10. Schultz, R., Avitabile, P.: Application of an Automatic Constraint Shape Selection Algorithm for Input Estimation, p. 11
11. Schultz, R., Nelson, G.: Techniques for modifying MIMO random vibration specifications. In: Sensors and Instrumentation, Aircraft/Aerospace and Dynamic Environments Testing, Volume 7, pp. 71–83, Cham (2023). https://doi.org/10.1007/978-3-031-05415-0_7

12. Pacini, B.R., Kuether, R.J., Roettgen, D.R.: Shaker-structure interaction modeling and analysis for nonlinear force appropriation testing. Mech. Syst. Signal Process. **162**, 108000 (2022). https://doi.org/10.1016/j.ymssp.2021.108000
13. Beale, C., Schultz, R., Smith, C., Walsh, T.: Degree of Freedom Selection Approaches for MIMO Vibration Test Design. In: Special Topics in Structural Dynamics & Experimental Techniques, Volume 5, pp. 81–90, Cham (2023). https://doi.org/10.1007/978-3-031-05405-1_10
14. Dumont, M., Cook, A., Kinsley, N.: Acceleration measurement optimization: mounting considerations and sensor mass effect. In: Topics in Modal Analysis & Testing, Volume 10, pp. 61–71, Cham (2016). https://doi.org/10.1007/978-3-319-30249-2_4
15. Tuman, M.J., Schumann, C.A., Allen, M.S., Delima, W.J., Dodgen, E.: Investigation of transmission simulator-based response reconstruction accuracy. In: Sensors and Instrumentation, Aircraft/Aerospace, Energy Harvesting & Dynamic Environments Testing, Volume 7, pp. 65–76, Cham (2022). https://doi.org/10.1007/978-3-030-75988-9_4
16. Schumann, C., Allen, M.S., Tuman, M., DeLima, W., Dodgen, E.: Transmission simulator based MIMO response reconstruction. Exp. Tech. (2021). https://doi.org/10.1007/s40799-021-00454-4
17. Schumann, C.A., Allen, M.S., DeLima, W.J., Dodgen, E.: Transmission simulator based MIMO response reconstruction for vehicle subcomponents. In: Special Topics in Structural Dynamics & Experimental Techniques, Volume 5, pp. 189–195, Cham (2021). https://doi.org/10.1007/978-3-030-47709-7_18
18. Rohe, D.P., Nelson, G.D., Schultz, R.A.: Strategies for Shaker placement for impedance-matched multi-axis testing. In: Sensors and Instrumentation, Aircraft/Aerospace, Energy Harvesting & Dynamic Environments Testing, Volume 7, pp. 195–212, Cham (2020). https://doi.org/10.1007/978-3-030-12676-6_18
19. Allen, M.S., Rixen, D., Van Der Seijs, M., Tiso, P., Abrahamsson, T., Mayes, R.L.: Substructuring in engineering dynamics: emerging numerical and experimental techniques. In: CISM International Centre for Mechanical Sciences. Springer (2019) [Online]. Available: https://doi.org/10.1007/978-3-030-25532-9
20. Mayes, R., Ankers, L., Daborn, P., Moulder, T., Ind, P.: Optimization of shaker locations for multiple shaker environmental testing. Exp. Tech. **44**(3), 283–297 (2020). https://doi.org/10.1007/s40799-019-00347-7
21. Kihm, F., Delaux, D.: Vibration fatigue and simulation of damage on shaker table tests: the influence of clipping the random drive signal. Procedia Eng. **66**, 549–564 (2013). https://doi.org/10.1016/j.proeng.2013.12.107

Chapter 13
A MIMO Time Waveform Replication Control Implementation

Ryan Schultz and Steven Carter

Abstract The importance of user-accessible multiple-input/multiple-output (MIMO) control methods has been highlighted in recent years. Several user-created control laws have been integrated into Rattlesnake, an open-source MIMO vibration controller developed at Sandia National Laboratories. Much of the effort to date has focused on stationary random vibration control. However, there are many field environments which are not well captured by stationary random vibration testing, for example shock, sine, or arbitrary waveform environments. This work details a time waveform replication technique that uses frequency domain deconvolution, including a theoretical overview and implementation details. Example usage is demonstrated using a simple structural dynamics system and complicated control waveforms at multiple degrees of freedom.

Keywords MIMO · Vibration testing · Control · Time waveform replication

13.1 Introduction

Sandia National Laboratories has been investigating and using multiple-input/multiple-output (MIMO) vibration testing for many years; however, much of that experience has focused on stationary, random vibration environments [1, 2]. Mature MIMO random vibration control methods exist in the literature, and some have been integrated into Sandia's in-house, open-source vibration control software, Rattlesnake [3]. However, there are many service environments that are not well represented as stationary, random vibration environments. For example, shock environments, sine sweep environments, or complex transient environments are typical in many aerospace and other industrial applications. As such, recent efforts have focused on understanding and implementing MIMO transient control capabilities with the goal of implementing them in Rattlesnake and performing vibration tests for complicated, multi-axis, or multi-input environments.

Time waveform replication (TWR) is a vibration control technique useful for these kinds of non-stationary signals or even arbitrary waveforms which may include combinations of shocks, sines, random vibrations, or any other time-varying content. In TWR control, the objective is to match a control signal time history, whereas the objective of random vibration control is to match a control power spectral density (PSD). Like random vibration control, the system output/input relationship is used in an inverse solution to estimate required inputs to best match some desired output. In TWR, the desired output is a linear spectrum representation of a control signal. Extending to multiple inputs and multiple outputs, MIMO TWR again uses an inverse solution of the system output/input relationships but now estimates a set of input linear spectra which best match linear spectra from a set of control signals. The control signals can be unique at each output sensor or degree of freedom (DOF) on the system, and similarly the estimated inputs at each input DOF can be unique. In this way, complicated, multi-axis motion can be replicated using MIMO TWR.

R. Schultz (✉) · S. Carter
Sandia National Laboratories, Albuquerque, NM, USA
e-mail: rschult@sandia.gov

J. Harvie (ed.), *Dynamic Environments Testing, Volume 7*, Conference Proceedings of the Society for Experimental Mechanics Series, https://doi.org/10.1007/978-3-031-34930-0_13

TWR can be implemented in the time domain via impulse response function representations of the system output/input relationships; however, it is more conveniently implemented in the frequency domain using the familiar FRF matrix system representation [4, 5]. Among other reasons, the frequency domain implementation is used because source estimation in the time domain (i.e., time domain deconvolution) is often computationally burdensome. Frequency domain TWR is sometimes called frequency domain deconvolution because it is effectively deconvolving the output and impulse response to estimate the system inputs. However, in practice, it simply involves multiplications of the inverse of the FRF matrix and the Fourier transform of the control signals, the output linear spectra. The inverse Fourier transform is then used to convert the estimated input signal linear spectra to the time domain. These input signals could then be used as shaker drives in a MIMO vibration test.

In many cases, the environment of interest is long duration, well in excess of the frame length for typical frequency resolution. It is often not convenient or possible to estimate an FRF matrix or linear spectra with small enough frequency resolution to cover a record that is many seconds or even minutes long. Instead, the TWR method presented here divides the long-duration signals into shorter-duration segments or frames. These shorter-duration frames can then be used, one at a time, in MIMO TWR control to determine the input signals needed for each frame. Then, these frames are added together to form the long-duration input signals needed for a TWR test. The process used to add the frames together is called constant-overlap-add (COLA). This process adds together overlapping, windowed frames of data [6–9]. The frame-to-frame overlap and window is chosen to provide a smooth transition of the signals between frames and preserve the signal amplitudes across frame boundaries.

This chapter provides an overview of MIMO TWR concepts, theory, and example usage. Section 13.2 provides a high-level, step-by-step view of the MIMO TWR process being utilized at Sandia and implemented into the Rattlesnake control software. Section 13.3 shows some of the theory behind MIMO TWR control. Section 13.4 demonstrates MIMO TWR usage on a simple multiple degree-of-freedom (MDOF) system. Two versions of that system are presented to demonstrate how MIMO TWR can provide nearly perfect control if the test setup is good, and how it may not perfectly control if the test setup is not ideal. To compare results, both time and frequency domain metrics are presented as it is often not sufficiently informative to simply compare control (desired) and achieved output signals.

13.2 Time Waveform Replication Process

Time waveform replication using frequency domain deconvolution can be summarized in a few steps:

1. Measure the system FRFs.
2. Break up the control signals into sequential, overlapping frames which span the total duration.
3. Zero-pad the frame of control signals.
4. For each frame, convert the control signals to the frequency domain with the Fourier transform.
5. Solve the frequency-domain deconvolution problem to estimate the inputs to best match each frame's control linear spectra given the system FRFs.
6. Convert the input linear spectra to time histories with the inverse Fourier transform.
7. Use the COLA process to add the input signals for all frames together to give input signals which span the entire duration.

While this is a straightforward process, there are several details in the implementation and usage which can be critical to TWR control performance. For example, the system FRFs must be properly estimated and at sufficient frequency resolution to capture important features. The FRFs and impulse responses should be carefully inspected to understand factors such as conditioning and singular value distribution, high- and low-frequency FRF accuracy, and impulse response causality. Additionally, the control signals should be filtered to fit well within the frequency range of interest (i.e., where the FRFs are nicely estimated) and the signals should be high-pass filtered to avoid very low frequency content which will be difficult to match due to the windowing and zero-padding needed for each frame. The frame length should be determined based on signal frequency content, signal duration, and FRF frequency resolution. Interpolation may be needed to get the FRF frequency resolution to align with the needed frame length. Prior to taking the Fourier transform in Step 4 above, the frame must be zero padded to avoid the convolution wrap-around error that may occur [9]. An additional improvement can be made if the signals are partially extended beyond the frame and smoothly tapered toward zero in the zero-padded sections. Another important consideration is the sample rate of the control signals and the test. The sample rate must be sufficiently high to resolve the waveforms, and typically this should be higher than just twice the maximum frequency of interest. Resampling may be needed to increase the sample rate prior to a TWR test. There are other factors which may need to be considered such as noise on the control signals and regularization in the inverse solution.

13.3 Theory

This section provides a brief overview of frequency-domain MIMO TWR theory. For a linear system with inputs x and outputs y, the output/input relationships for the j-th input and i-th output can be represented in the time domain as a convolution of the input and impulse response:

$$y_i(t) = h_{y_i x_j}(t) * x_j(t) \tag{13.1}$$

where $h_{y_i x_j}(t)$ is the impulse response matrix for that input-output pair at time t and the symbol $*$ denotes the convolution operator.

The system output/input relationship can also be represented in the frequency domain for a set of inputs and outputs as

$$Y(\omega) = H_{yx}(\omega) X(\omega) \tag{13.2}$$

where $X(\omega)$ is a vector of the input linear spectra, $Y(\omega)$ is a vector of the output linear spectra, and $H_{yx}(\omega)$ is the system frequency response function (FRF) matrix at a frequency ω. Multiplication in the frequency domain is more convenient than convolution in the time domain, so frequency domain analysis is used here. Although this is no longer applying convolution directly in the time domain, zero-padding the input time history is still necessary to avoid circular convolution wrap around error.

Determining inputs to best match some control response signals can be achieved in the frequency domain by

$$X(\omega) = H_{yx}^{+}(\omega) Y(\omega) \tag{13.3}$$

where $H_{yx}^{+}(\omega)$ is the pseudo-inverse of the FRF matrix.

A Fourier transform converts the time domain signals to frequency domain linear spectra. Similarly, an inverse Fourier transform converts the frequency domain linear spectra to time domain signals. This can be done for an entire time record or for segments (frames) of the record. For long-duration TWR testing, the entire record is split into sequential, overlapping frames that can be added together to recreate the entire record as

$$x(t) = \sum_{i=0}^{n} w(t) x_i(t) \tag{13.4}$$

where the signal for a given frame is $x_i(t)$, n is the number of frames, and the entire signal is $x(t)$. $w(t)$ is a window function which smoothly tapers each frame's signal to zero. The window shape and the overlap frame-to-frame are chosen to ensure a constant amplitude over the entire record (i.e., the summation of overlapped windows is equal to one over the entire record). More details on COLA can be found in [8].

13.4 Model-Based Example

To provide an example of how this TWR process works, a model-based example is provided. Here, a simple dynamic system is first subjected to some non-stationary loads to produce a set of control signals. Next, the TWR control methodology is used to derive new inputs which can best match those control signals and then those inputs are applied to the system to predict the response. The results are compared using plots of the control and predicted waveforms, the time response assurance criteria (TRAC), running root mean square (RMS) response, and the time-evolving PSD via spectrograms.

13.4.1 Model Description

The example free-free, multi-DOF model is shown in Fig. 13.1. The model is composed of six point masses connected with linear springs and has motion in one direction only. Each mass is 1 kg. The spring stiffness between DOF 1-2, 2-3, 4-5, and 5-6 is 5×10^5 N/m and the spring stiffness between DOF 1-4, 2-5, and 3-6 is 1×10^6 N/m. There are three outputs on DOFs 1, 2, and 3 and two inputs on DOFs 4 and 6. Modes are computed from the model mass and stiffness matrices. There are five

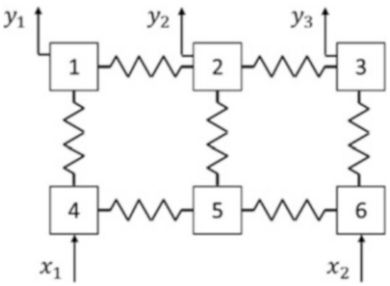

Fig. 13.1 MDOF model with three outputs and two inputs

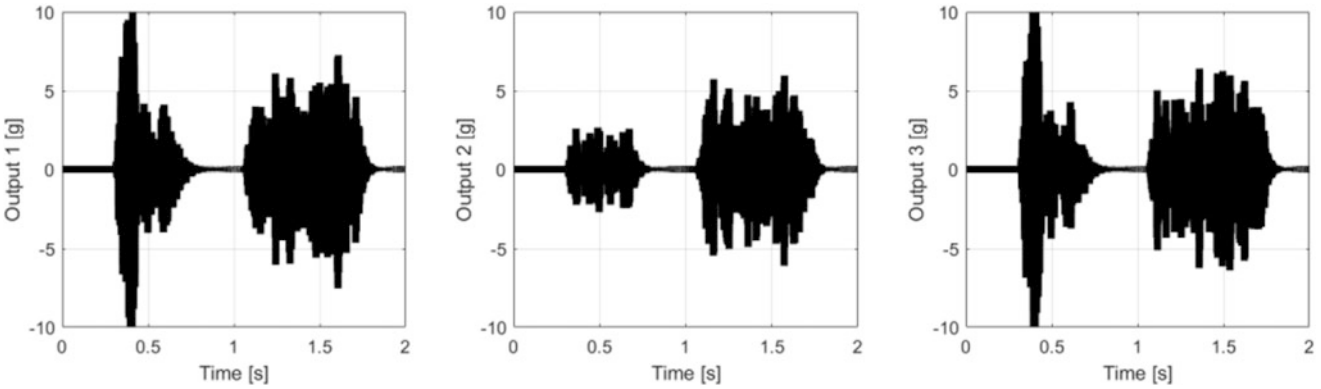

Fig. 13.2 Control time histories at the three output DOFs

elastic modes that range between 112 and 297 Hz in addition to one rigid body mode. All six modes are used to synthesize the acceleration/force frequency response functions (FRFs) between the three outputs and two inputs, evaluated in 1 Hz steps up to 4096 Hz.

13.4.2 Example Transient Inputs and System Response

Two different, non-stationary force inputs are created to excite the system and the acceleration response is measured at the three outputs. The input signals are composed of two band-limited burst random events which start and end at different times in a two-second record with an 8192 Hz sample rate (twice the max FRF frequency). The first burst random event has frequency content between 50 and 200 Hz and the second has frequency content between 200 and 500 Hz. Band-limiting is accomplished by applying a finite impulse response filter to pure random noise.

Modal time integration is used to simulate the system's response to these two inputs. To minimize error due to the time integration process, time integration is performed at 16x the nominal sample rate (131,072 Hz). The resulting acceleration responses at the three output DOFs are the control signals that will be used in time waveform replication. If the time waveform replication process is successful, the original input signals should be recovered. Figure 13.2 shows the acceleration response signals for the three output DOFs and Fig. 13.3 shows the time histories for the two input DOFs.

13.4.3 TWR Control Results

The control signals are fed into the time waveform replication algorithm along with the system FRF matrix pseudo-inverse to compute the estimated input signals needed to best match the output at each time. The pseudo-inverse of the FRF matrix is computed using a singular value decomposition at each frequency line. In this case, no regularization was utilized though that is typically necessary to minimize the effects of noise on the estimated inputs.

In this example, the environment duration is long, in excess of the block length determined by the FRF matrix frequency resolution (i.e., $T = 1/df$). Thus, the entire record is broken up into five overlapping frames. Each frame is 0.5 seconds long and is overlapped with the adjacent frames by 0.125 seconds. The amount of overlap frame-to-frame could be changed with

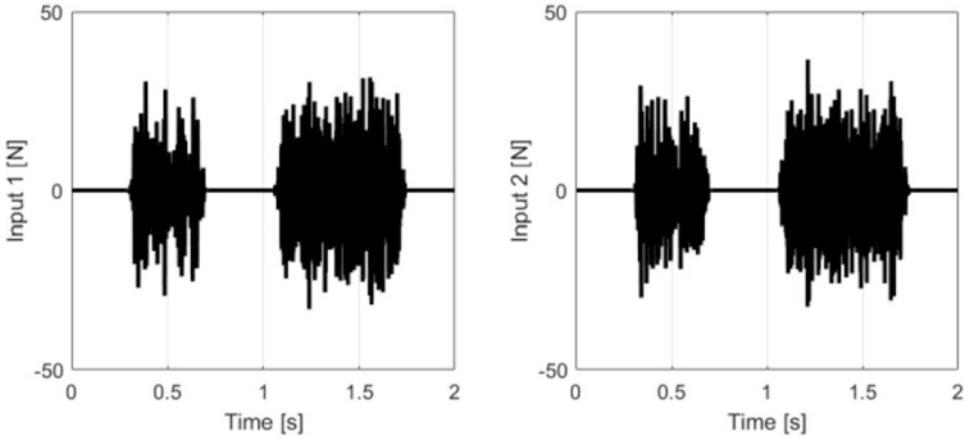

Fig. 13.3 Input time histories at the two input DOFs

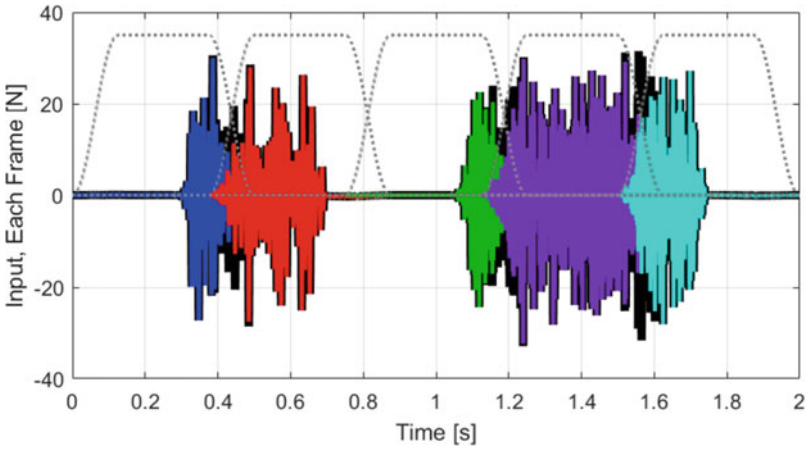

Fig. 13.4 Estimated input time histories for each of five overlapping frames which sum to the total input signal

negligible effect on the results. Figure 13.4 shows the five overlapping frames (in blue, red, green, purple, cyan) and how the estimated input signal (in black) is composed of a summation of estimates for each frame. The Tukey window which was used to taper each set of signals to zero at the ends of the frames is shown by the gray dotted lines (window amplitude is scaled to be visible in this plot).

Next, the estimated input signals are applied to the model. Again, modal time integration is used with the same oversampling as in the original simulation. The resulting response can then be compared with the original, control responses to assess how well time waveform replication could control this MDOF system.

Time History Comparisons

Time histories can be compared by simply plotting the control specification and predicted signals for each DOF, along with the error signal, $e(t) = y_{\text{predicted}}(t) - y_{\text{control}}(t)$, as shown in Fig. 13.5. In this case, the true inputs are known so the same comparison can be done for the input time histories as well, Fig. 13.6. Here, both the inputs and outputs match the original (specification) time histories very well, with only minor errors. The error signal is near zero for all DOFs over the entire record. Computing a running root mean square (RMS) can provide a simple view of the DOF energy versus time as shown in Fig. 13.7. This shows how each DOF's energy is accurately replicated by TWR control. A time response assurance criterion (TRAC) provides a scalar metric of the overall match of a pair of time histories (i.e., specification versus prediction for a given DOF) [10]. Here, the TRAC for each of the output DOFs is 1.0 and the TRAC for each of the input DOFs is 0.99, indicating a near perfect match of the time histories. Note that the TRAC will be sensitive to any phase shift or frequency errors, so this metric should be used with caution or at least in conjunction with other metrics.

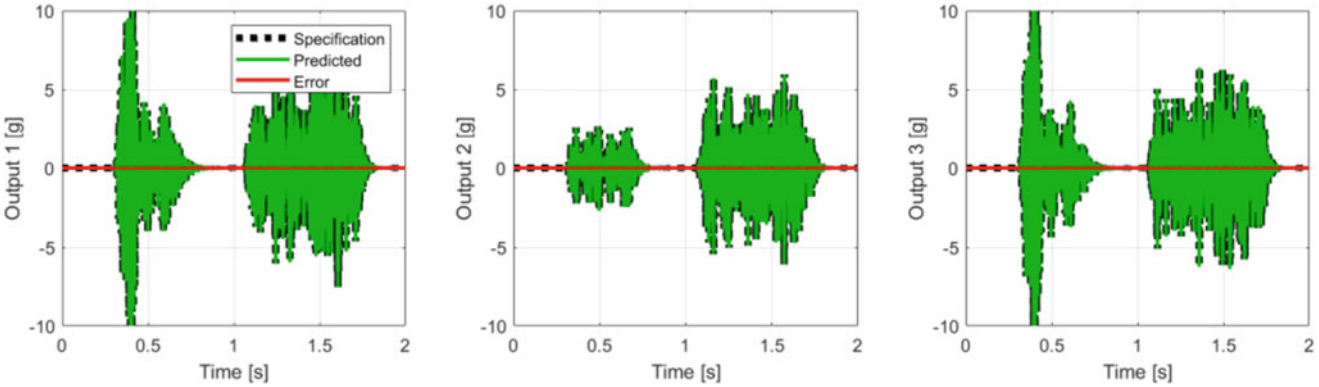

Fig. 13.5 Output time histories comparing the original (specified) versus predicted

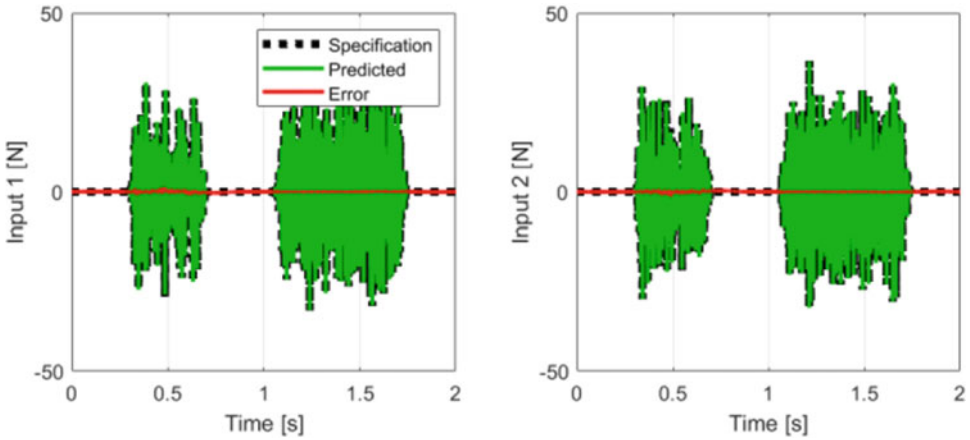

Fig. 13.6 Input time histories comparing the original (specified) versus predicted

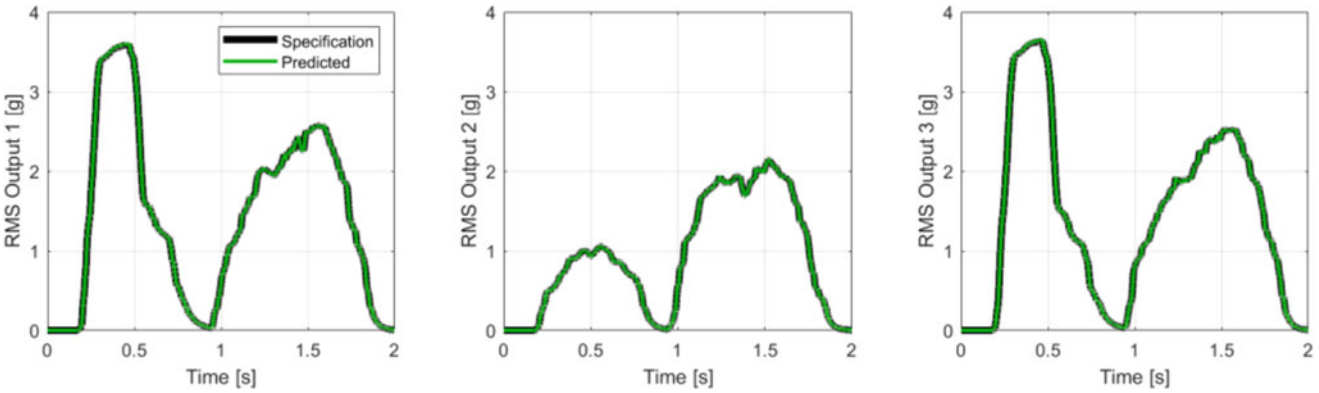

Fig. 13.7 Running RMS of the output time histories comparing the original (specified) versus predicted

Moreover, it is important to note that comparisons in the time domain can, in general, be misleading and may be of little use to the practitioner. This is because they are essentially showing the errors at every frequency line for every moment in time. As such, errors that are limited to a specific frequency band (while the remaining frequency lines are considered accurate) could lead to significant amplitude or phase errors in the time domain. While it is important to understand this time domain error, it is unlikely that the practitioner would notice that it is due to a specific frequency band, limiting the actionable information in the comparison.

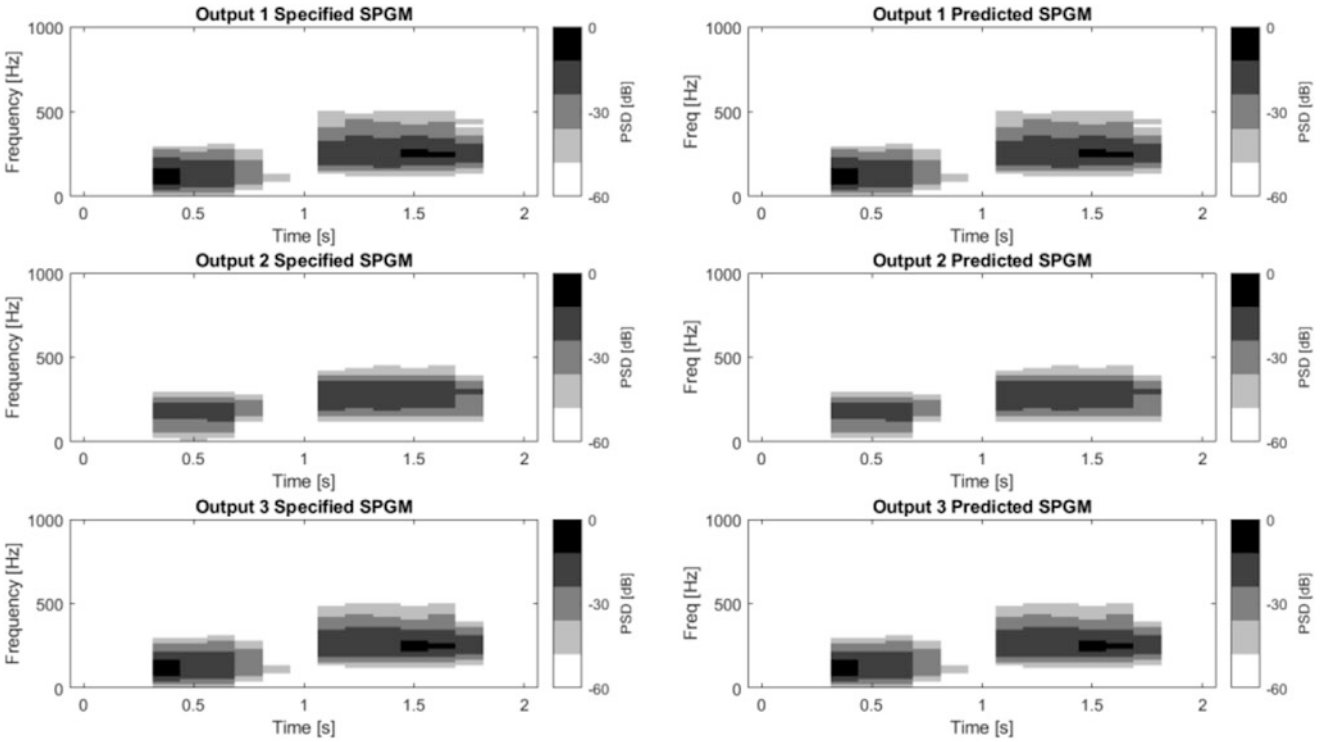

Fig. 13.8 Spectrograms to compare the original outputs (left) and predicted outputs (right)

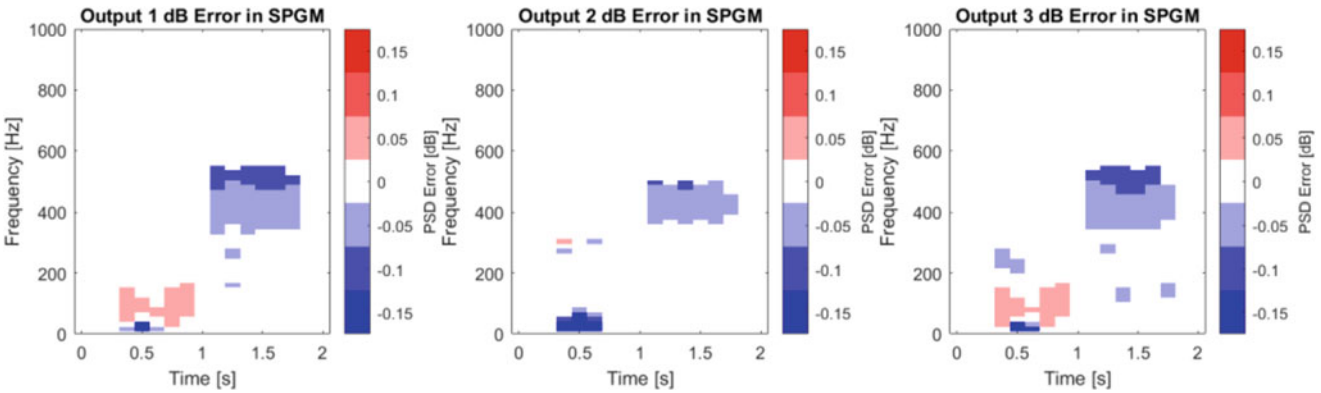

Fig. 13.9 dB error in the spectrograms for each of the three output DOFs

Spectrogram Comparisons

In addition to the time history comparisons shown above, it is informative to compare TWR results in terms of time-evolving frequency content. This can be done by computing a spectrogram, which is the signal power spectral density (PSD) as a function of both time and frequency. Figure 13.8 shows the control and predicted response spectrograms for each of the three output DOFs. Note that the Z-axis (i.e., color) is set to show the dominant frequency content. Qualitatively, the spectrograms match very closely, indicating good control at each DOF. To quantify the spectrogram comparison, an error spectrogram can be computed by taking the ratio of the predicted and specified spectrograms and converting to decibels (dB). In this way, a single plot can show the TWR performance in terms of under- or over-test for both time and frequency. Figure 13.9 shows this dB error spectrogram for each output DOF. As the TWR control worked well, the errors are low for all times and frequencies. To show some error in these plots, the limits of the plot are just $+/-$ 0.15 dB.

Table 13.1 Mode frequencies of the original and modified systems

Mode #	Original system mode frequency [Hz]	Modified system mode frequency [Hz]
1	0.2	0.2
2	113	106
3	195	185
4	225	216
5	252	249
6	298	281

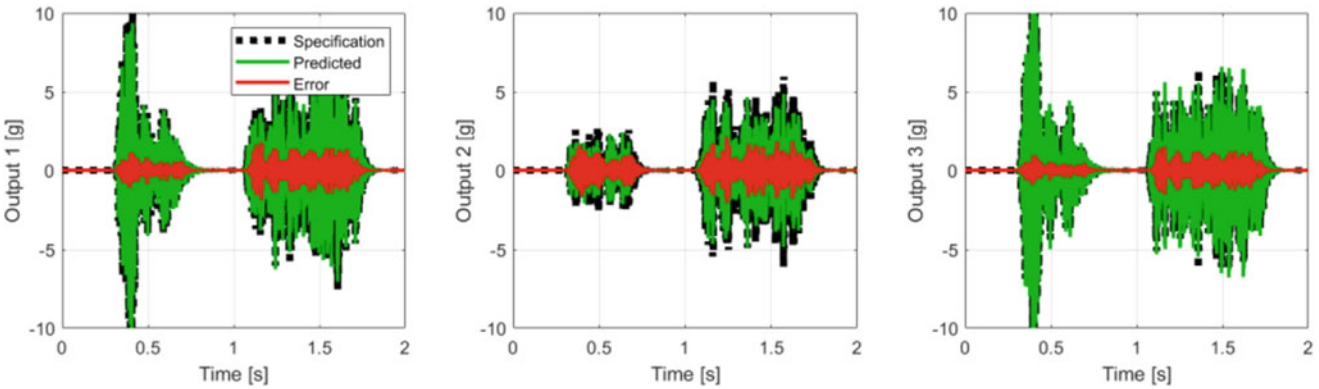

Fig. 13.10 Output time histories comparing the original (specified) versus predicted for the modified system

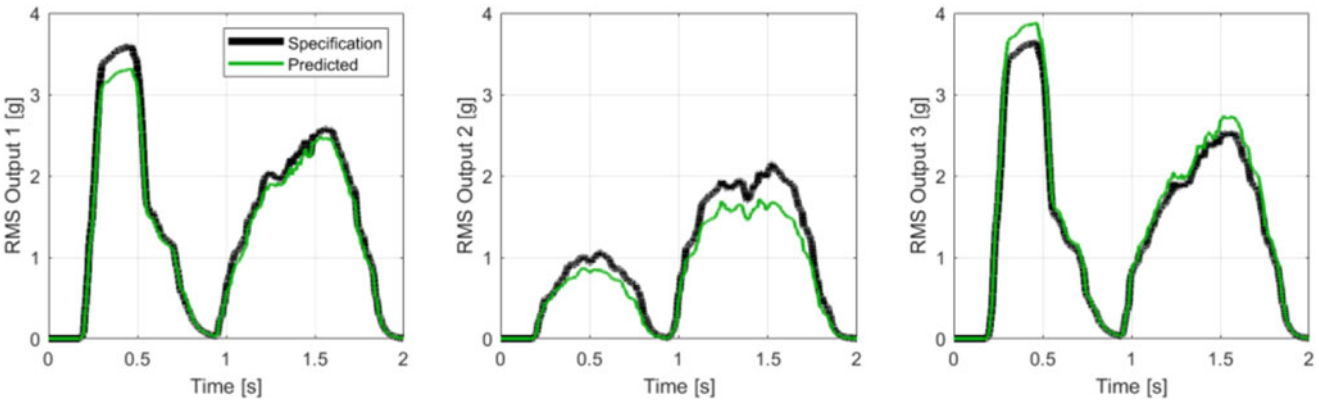

Fig. 13.11 Running RMS of the output time histories comparing the original (specified) versus predicted for the modified system

13.4.4 Modified System Results

To better show how these metrics look when results are not perfect, a modified system is created by slightly changing the spring stiffness between the masses. This mimics what could be seen in actual tests, where the specification is derived from a unit in the field and then applied to a TWR test of a different unit in the laboratory test. This change in stiffness results in a slight change in mode frequencies as shown in Table 13.1. TWR is then applied using the FRFs from this new system, along with the control waveforms from the original system. The change in system dynamics makes it more difficult to perfectly match the control response as can be seen in the comparison plots in the following sections.

Time History Comparisons

As seen in Figs. 13.10 and 13.11, the modified system cannot perfectly match the specified response. There is some error in the time histories of each DOF, and the running RMS shows an under-test for DOF 1 and 2 and a slight over-test for DOF 3. The TRAC metric also reflects the error with values of 0.96, 0.89, and 0.97 for DOF 1, 2, and 3, respectively.

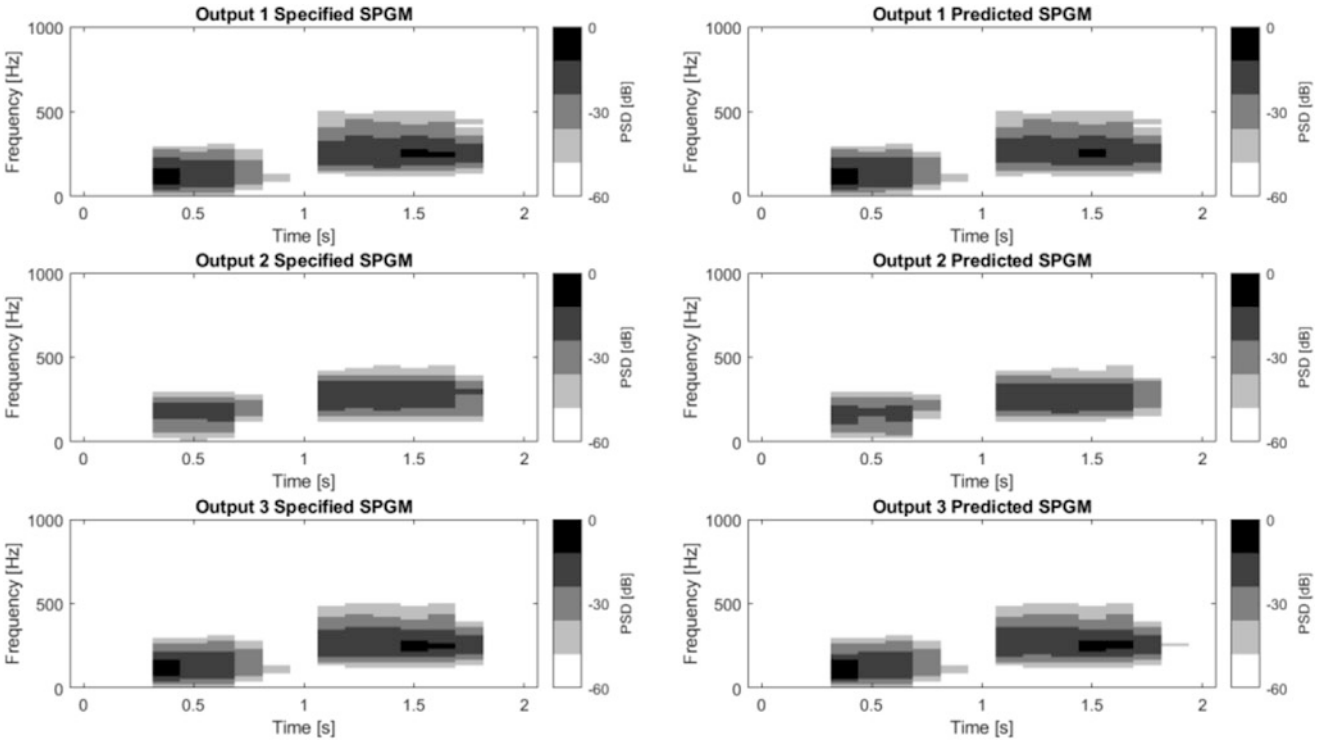

Fig. 13.12 Spectrograms to compare the original outputs (left) and predicted outputs (right) for the modified system

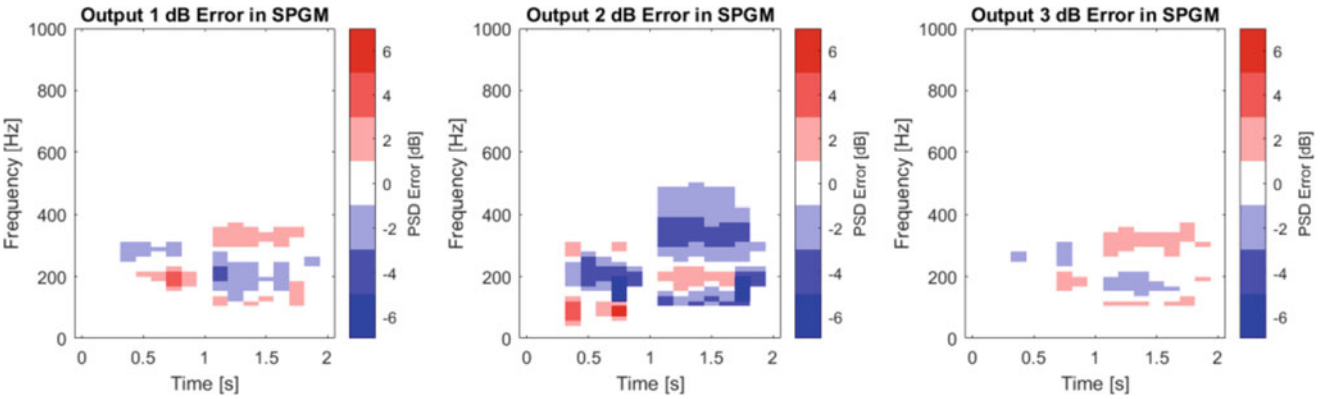

Fig. 13.13 dB error in the spectrograms for each of the three output DOFs for the modified system

Spectrogram Comparisons

The specified and predicted spectrograms in Fig. 13.12 indicate that the general distribution of energy versus time and frequency is achieved, with approximately the right frequency content occurring at the right time. However, there is some difference in the PSD levels. This can be seen more closely in the dB error spectrograms in Fig. 13.13 where there are indications of a slight over-test (indicated in red) or slight under-test (indicated in blue) for some points in time for certain frequency ranges. For example, DOF 2 shows a general under-test between 250 and 500 Hz in the 1 to 2 second time range. This means that DOF 2 is not being excited properly during the second burst random excitation.

13.5 Conclusion

MIMO vibration testing can accurately mimic complicated, multi-axis service environment response. Strong research and development efforts in recent years indicate that the industry understands this and is moving toward MIMO vibration testing. To help enable research in MIMO control, Sandia National Laboratories has developed an open-source MIMO vibration control software called Rattlesnake. To increase the capabilities of Rattlesnake, Sandia researchers are investigating TWR control methods. This chapter presents a frequency domain deconvolution approach to MIMO TWR which will soon be integrated into Rattlesnake and utilized in multi-axis transient vibration testing. Demonstration of this MIMO TWR control method on an example dynamic system shows that near perfect control is possible when the problem is well posed. To demonstrate how control suffers when the problem is poorly posed, the example system was modified and then used in MIMO TWR predictions. Due to the time-varying, broadband content in these kinds of tests, there is likely no one metric that is best, so various comparison metrics were used to assess results, including running RMS, spectrograms, and the TRAC.

References

1. Smallwood, D.O.: Multiple shaker random control with cross coupling. In: Proceedings of the Institute of Environmental Sciences (1978)
2. Smallwood, D.O., Paez, T.L.: A frequency domain method for the generation of partially coherent normal stationary time domain signals. Shock. Vib. **1**(1) (1991)
3. Rohe, D.P., Schultz, R., Hunter, N.: Rattlesnake: An open-source multi-axis and combined environments vibration controller. In: Proceedings of IMAC-XL, the 40th International Modal Analysis Conference, Orlando, FL (2022)
4. Musella, U., Zanellati, L., Grottoli, M., Celiberti, F., Peeters, B., Marulo, F., Guillaume, P.: Driving a motion platform with vibration control software for multi-axis environmental testing: challenges and solutions. In: Proceedings of IMAC XXXVI, the 36th International Modal Analysis Conference (2018)
5. Paulter Jr., N.G.: A causal regularizing deconvolution filter for optimal waveform reconstruction. IEEE Trans. Instrum. Meas. **43**(5) (1994)
6. Smith III, J.O.: Spectral Audio Signal Processing, Standford University, [Online]. Available: https://ccrma.stanford.edu/~jos/sasp/. [Accessed 2018].
7. Trethewey, M.W.: Window and overlap processing effects on power estimates from spectra. Mech. Syst. Signal Process. **14**(2), 267–278 (2000)
8. Schultz, R., Nelson, G.D.: Input signal synthesis for open-loop multiple-input/multiple-output testing. In: Proceedings of IMAC XXXVII, the 37th International Modal Analysis Conference (2019)
9. Press, W.H., Teukolsky, S.A., Vetterling, W.T., Flannery, B.P.: Numerical Recipes in C: The Art of Scientific Computing, 2nd edn, Cambridge (1992)
10. Pingle, R., Avitabile, P.: Prediction of full field dynamic stress/strain from limited sets of measured data. In: Proceedings of IMAC-XXVIII, the 28th International Modal Analysis Conference, Jacksonville, FL (2010)

Chapter 14
Demonstration of Output Weighting in MIMO Control

Ryan Schultz

Abstract Multiple-input/multiple-output (MIMO) vibration control often relies on a least-squares solution utilizing a matrix pseudo-inverse. While this is simple and effective for many cases, it lacks flexibility in assigning preference to specific control channels or degrees of freedom (DOFs). For example, the user may have some DOFs where accuracy is very important and other DOFs where accuracy is less important. This chapter shows a method for assigning weighting to control channels in the MIMO vibration control process. These weights can be constant or frequency-dependent functions depending on the application. An algorithm is presented for automatically selecting DOF weights based on a frequency-dependent data quality metric to ensure the control solution is only using the best, linear data. An example problem is presented to demonstrate the effectiveness of the weighted solution.

Keywords MIMO · Random vibration · Vibration testing · Weighted least squares

14.1 Introduction

In a typical multiple-input/multiple-output (MIMO) random vibration test, a controller determines inputs to match specified outputs as closely as possible. This is often accomplished using a direct inverse solution of the test system frequency response function (FRF) matrix, which relates the test system inputs and outputs. While this direct inverse solution is often sufficiently accurate, it lacks flexibility in terms of tailoring the inputs and outputs as the direct inverse solution is a least-squares regression and there are no settings or user-controllable parameters.

An ideal test would be perfectly accurate at all output locations or degrees of freedom (DOFs). However, it is often not possible to obtain perfect control accuracy at all output DOFs due to test setup constraints or mismatches between the specification response and the test system dynamics. In those cases, the test engineer is limited to either controlling to all available output DOFs or removing poorly performing DOFs. Neither of these choices are desirable as controlling to poorly performing DOFs or not having enough DOFs may introduce errors which affect the accuracy across the test system. Instead, it would be best to apply weighting to the output DOFs to best utilize both good and bad DOFs in the control solution.

This chapter presents a straightforward method for introducing output DOF weighting in the MIMO control solution by scaling up or down entries of the specification cross-power spectral density (CPSD) and FRF matrices which correspond to output DOFs. Scaling up entries makes the output DOF more important and scaling down entries makes the output DOF less important. This simple scaling works because the direct inverse solution in MIMO control is effectively a least-squares solution across all output DOFs. Scaling up entries for a DOF makes its contribution to the total error larger while scaling down entries for a DOF makes its contribution to the total error smaller. Higher weighted DOFs will therefore be more

R. Schultz (✉)
Sandia National Laboratories, Albuquerque, NM, USA
e-mail: rschult@sandia.gov

J. Harvie (ed.), *Dynamic Environments Testing, Volume 7*, Conference Proceedings of the Society for Experimental Mechanics Series, https://doi.org/10.1007/978-3-031-34930-0_14

accurately matched than lower weighted DOFs because the least-squares solution will determine inputs which better match the high-weight DOFs than the low-weight DOFs.

As MIMO random vibration control is evaluated frequency line by frequency line, the DOF weighting can be made frequency dependent. Choosing weights for each DOF as a function of frequency can be manually specified or automated. Here, an automatic weight selection method is presented which chooses weights based on linearity of each output DOF to the inputs, which effectively ensures that the highest quality (most linear) responses are emphasized in the control solution. This helps MIMO control by not allowing poor responding or nonlinear responding DOFs to contaminate the control solution. This is just one possible weight selection method – many others are possible and could be implemented in a similar way in this DOF weighting framework.

This weighting technique is not novel or unique as there are examples in various mathematics papers, texts, and even websites, for example [1–3]. However, there is not much in the MIMO vibration literature regarding weighted solutions. As such, the purpose of this chapter is to show, in a clear and simple way, how flexibility can be added to MIMO control solutions by using weighting of the output DOFs. This chapter is organized as follows. Section 2 presents the MIMO control and weighted least-squares theory. Section 3 provides step-by-step implementation details for weighted MIMO control. Section 4 discusses automatic weight selection methods. Section 5 shows results of a model-based demonstration of weighted MIMO control, where a structural dynamics model is used to compare standard and weighted MIMO control and demonstrate how automatic DOF weighting can help suppress errors in the control solution.

14.2 Theory

A multiple-input, multiple-output linear system can be represented in the frequency domain as

$$Y = H_{yx} X \tag{14.1}$$

where X are the inputs, Y are the outputs, and H_{yx} is the FRF matrix which relates the inputs to the outputs. Note that Eq. 14.1 is evaluated at each frequency line of interest. For ease of notation, the frequency dependence has been omitted in this and all subsequent equations. In MIMO random vibration, the inputs and outputs are typically represented as CPSD matrices and Eq. 14.1 becomes

$$S_{yy} = H_{yx} S_{xx} H_{yx}^{H} \tag{14.2}$$

where S_{xx} is the input CPSD matrix, S_{yy} is the output CPSD matrix, and H_{yx} is the same FRF matrix from above [4–6]. The superscript $\blacksquare^{H}$ denotes a conjugate transpose.

In MIMO random vibration control, the direct inverse, open-loop solution determines inputs to best match some desired or specified response, $S_{yy,\,spec}$, by multiplying Eq. 14.2 by the pseudo-inverse of the FRF matrix, H_{yx}^{+}:

$$S_{xx} = H_{yx}^{+} S_{yy,spec} H_{yx}^{+H} \ . \tag{14.3}$$

These inputs would then be applied to the test article to run the MIMO random vibration test. It should be noted that this pseudo-inverse results in a least-squares solution where the inputs are determined to minimize the squared error in the outputs. As such, outputs with large responses or high errors have relatively large influence on the results. Outputs from this test can be predicted using the FRF matrix using Eq. 14.2. This simple CPSD representation of the linear system and control solution is used in this work to derive inputs and predict responses.

Weighting of output DOFs can be accomplished in the MIMO random vibration control solution (i.e., Eq. 14.3) by applying a diagonal matrix W to both the FRF matrix and the specification CPSD matrix as [1, 2]:

$$\hat{H}_{yx} = W H_{yx}, \tag{14.4}$$

$$\hat{S}_{yy,spec} = W S_{yyx} W, \tag{14.5}$$

where the "hat" on the FRF and CPSD indicate the weighted versions of the matrices. Then, the control solution is evaluated using the weighted CPSD and FRF matrices:

$$S_{xx} = \hat{H}_{yx}^{+} \hat{S}_{yy,spec} \hat{H}_{yx}^{+H} \ . \tag{14.6}$$

By expanding this, we get:

$$S_{xx} = \left(W H_{yx}\right)^{+} \left(W S_{yy,spec} W\right) \left(W H_{yx}\right)^{+H} \ . \tag{14.7}$$

The weights apply to the rows of the FRF matrix, which correspond to the output DOFs. Weights apply to both the rows and columns of the output CPSD matrix as that matrix has output DOFs on both the rows and columns. Note that the values in the weight matrix can be any positive real number, and the relative weight between DOFs is only determined by the ratio of weights of those DOFs, not the overall level of the weights. For example, with three DOFs, the weights [10, 2, 1] and [100, 20, 10] would have the same effects.

Scaling up or down the values in the specification CPSD and FRF matrices associated with output DOFs changes the relative contributions of errors in the least-squares solution. For example, if DOF 1 is weighted by 100 and DOF 2 is weighted by 1, the error in DOF 1 becomes much larger in the least-squares solution compared with DOF 2, so inputs estimated with Eq. 14.6 will be biased to minimize error on DOF 1. As these expressions are evaluated frequency line by frequency line, the weight matrix could be frequency dependent to emphasize or ignore different DOFs at different frequencies in the test bandwidth.

14.3 Implementation Details

Implementing weighted MIMO control for random vibration is straightforward and outlined in the steps below.

1. Choose weights for each output DOF and form the weight matrix.
2. Perform a system identification test and form the FRF matrix.
3. Apply the weight matrix to the FRF and specification CPSD matrices.
4. Estimate the input CPSD matrix which best matches the weighted specification CPSD matrix.
5. Predict response with the estimated inputs and verify the quality of the results.
6. Adjust weights if the effects of the weights are not achieved in the predictions.
7. Run the test with the estimated inputs.

This weighted MIMO control solution fits nicely into typical MIMO control methods and can be easily implemented into existing controller workflows. One thing to note is that because weights are applied to both the specification CPSD matrix and the FRF matrix, no scaling is needed to "undo" the effects of the weights on the input CPSD.

Determining weight values which provide the desired effects, for example emphasizing or ignoring specific DOFs, may not be straightforward, so some iteration on choosing weights and predicting results is recommended. In the course of this work, it was found that a 100× ratio in weights was effective in emphasizing or ignoring DOFs.

An optional step is to normalize the specification CPSD and FRF matrices to unity auto-power spectral density (APSD) levels prior to applying weights. This forces the specification amplitudes to be the same, unity, for all DOFs at all frequency lines. This avoids any biasing due to relative response amplitudes and ensures that the chosen weights are implemented as desired.

14.4 Automatic Weight Selection Methods

In some cases, it may be useful for DOF weights to be determined automatically on a frequency-by-frequency basis. For example, weights could be determined based on response amplitude, linearity, or data quality. As MIMO random vibration control (at least as described above) is based on linear system theory, utilizing output DOFs which have good linear response to inputs is critical.

If the linearity between outputs and inputs is poor, the estimated inputs and resulting responses may be poor as well. As such, it is desirable to not utilize DOFs with poor linearity. However, there may be cases where DOFs cannot be simply removed from the control set due to having limited control DOFs or wanting to utilize as much specification data as possible. A weighted MIMO solution can allow DOFs with marginal or poor linearity to still be used in the control solution but be de-emphasized by using smaller weights.

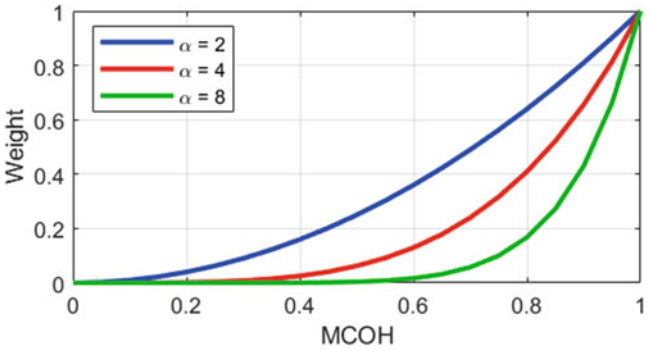

Fig. 14.1 Weight vs MCOH using different α values

Linearity between an output and multiple inputs can be quantified with the multiple coherence, which takes values between zero and one, with zero indicating no linear relationship and one indicating a strong linear relationship. Multiple coherence is a function of frequency and output DOF, so it can be leveraged to create a set of weights as

$$W_i = MCOH_i^{\alpha}, \tag{14.8}$$

where W_i is the weight for the i-th DOF which has multiple coherence $MCOH_i$. The factor α is used to exaggerate the difference between high and low multiple coherence. In this work, an α of 8 was used and provided good results, allowing DOFs with multiple coherence near one to have weights near one but DOFs with lower multiple coherence to have very small weights. Fig. 14.1 demonstrates how α affects the MCOH to weight relationship.

One can envision a similar method applied to signal-to-noise ratios or some other data quality metric as a way to de-emphasize poorly responding DOFs. Similarly, weighting could be determined based on DOF response accuracy, where the weight is determined by the predicted response accuracy using an unweighted solution. DOFs with good accuracy could be assigned large weights and DOFs with poor accuracy could be assigned smaller weights. This may help account for location-specific errors (e.g. remove effects of one inaccurate gauge or gauges on a component that cannot be properly excited). Different weighting approaches could also be combined by simply multiplying them together, for example, the total weight could be a product of multiple coherence weights and control accuracy weights. In short, there are many ways to create weights that would improve MIMO control solutions and result in the best balance between data quality, available specification data, and control accuracy.

14.5 Demonstration of Weighted MIMO Control

To demonstrate how weighted MIMO control works, a model-based example is created. This example system is first subjected to one set of inputs which represent loads in a field or service environment. The response from this field configuration becomes our MIMO specification. Next, inputs are moved to different locations to represent a laboratory (lab) test configuration. This input DOF change is utilized to demonstrate a common challenge in MIMO testing where the true load paths are unknown or not available in the lab test, and this mismatch of input DOFs creates a non-trivial control solution. The lab system FRFs are used to predict the inputs and responses of a lab test and these responses are compared with the specification to assess test accuracy. Weights are then applied to demonstrate how output DOF weighting can be used to affect test results.

14.5.1 Example System

The example system is shown in Fig. 14.2 below. A finite element model of this system was used to compute the modes, and then those modes were used in modal transient simulations to get acceleration response due to force inputs. Two configurations are shown, the field configuration and the lab configuration. The system is the same in each configuration but the input locations and directions change. In the field configuration, uncorrelated force inputs are applied in the X, Y,

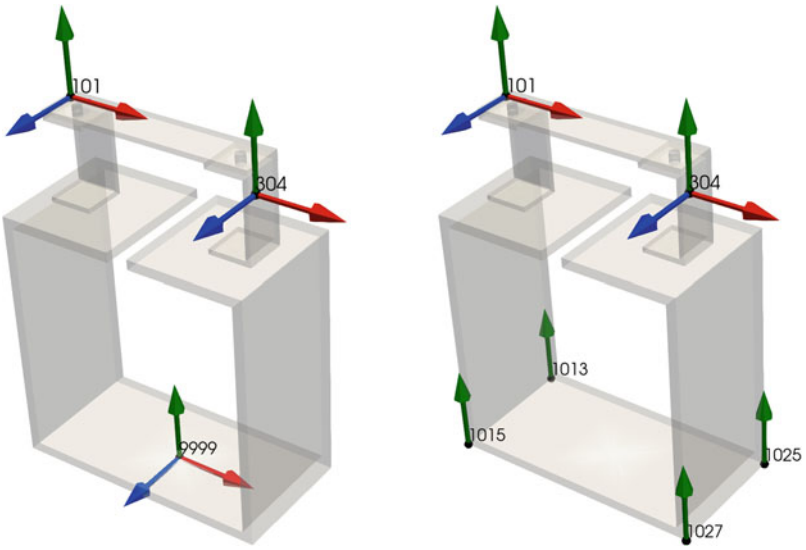

Fig. 14.2 Example system with outputs (labeled 101, 304) and inputs for both field (left, labeled 9999) and lab (right, labeled 1013, 1015, 1025, 1027). Directions indicated by arrow color with red = X, green = Y, blue = Z

and Z directions. Response time histories at the output DOFs (two locations labeled 101 and 304, three directions each) are processed into the specification CPSD matrix. FRFs for the lab configuration are determined using the responses at the output DOFs due to uncorrelated force inputs at four locations in the Y direction at the bottom corners of the system. Noise can be added to the time histories to simulate some data contamination effects.

14.5.2 Weighted MIMO, Constant Weights

First, an example with constant weights is provided. Here the Y-direction DOFs ($101Y+$ and $304Y+$) have high weights (1.0) and the X- and Z-direction DOFs ($101X+$, $101Z+$, $304X+$, and $304Z+$) have low weights (0.01). The weights are constant for all frequency lines. Figure 14.3 shows the APSD response predictions compared with the specification APSD using unweighted (standard MIMO) and weighted MIMO control solutions. Figure 14.4 shows the APSD response in terms of decibel (dB) error with respect to the specification APSD. Figure 14.5 shows the RMS of the dB errors to provide a single error value for each DOF. These results clearly show how applying weights causes the Y DOFs to have nearly perfect control, though at the expense of accuracy at the X and Z DOFs. Intuitively, changing the relative weights, either higher or lower, changes the balance of accuracy between the DOFs (Fig. 14.6).

14.5.3 Weighted MIMO, Automatically Chosen Weights

To demonstrate how weights can be automatically determined using multiple coherence, first the FRF data needed to be contaminated with noise to cause the coherence to drop. This is akin to what may happen to low-responding channels in a system, where the response is near the noise floor of the sensor. Here the 101 X, Y, and Z DOFs had low noise and 304 X, Y, and Z DOFs had high noise. The multiple coherence computed from this noisy data shows how the noise affects the linear relationship (Fig. 14.7). Next, the multiple coherence is converted to weights for each DOF at each frequency line using an α of 8. Figure 14.7 shows how the weights are just an exaggeration of the multiple coherence, and how low multiple coherence results in very low weights as desired.

Using the multiple coherence-determined weights is effective in improving control to the 101 DOFs where FRF linearity is good as shown in Figs. 14.8, 14.9, and 14.10. Accuracy at the 304 DOFs is not as good but still reasonable. This demonstrates how using a weighted approach is preferable to simply removing the 304 DOFs entirely for two reasons. First, if the 304 DOFs were removed entirely, the problem would go from over-determined to under-determined, which would require a completely different solution method which has its own challenges. Second, by still including the 304 DOFs, some response

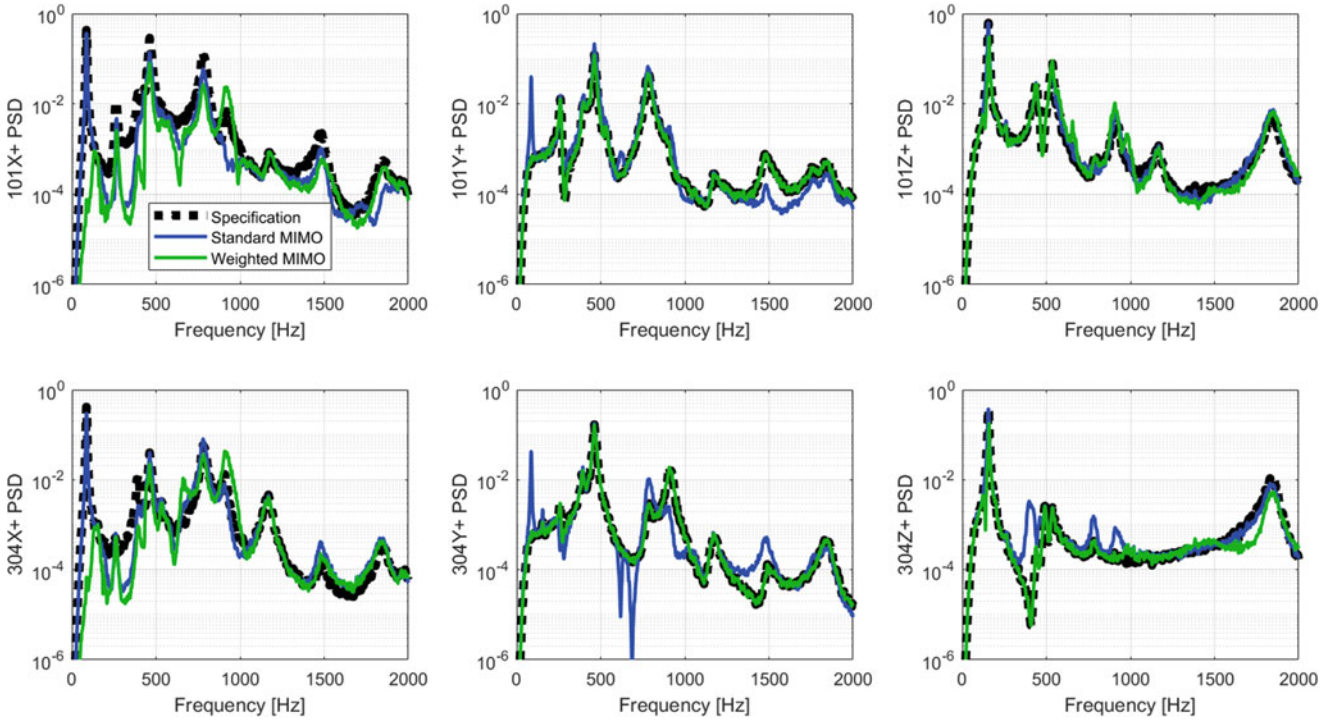

Fig. 14.3 APSDs for each of the six output DOFs comparing the field response (specification, black dotted line) and MIMO test predictions using unweighted (standard, blue line) and weighted (green line) MIMO solutions

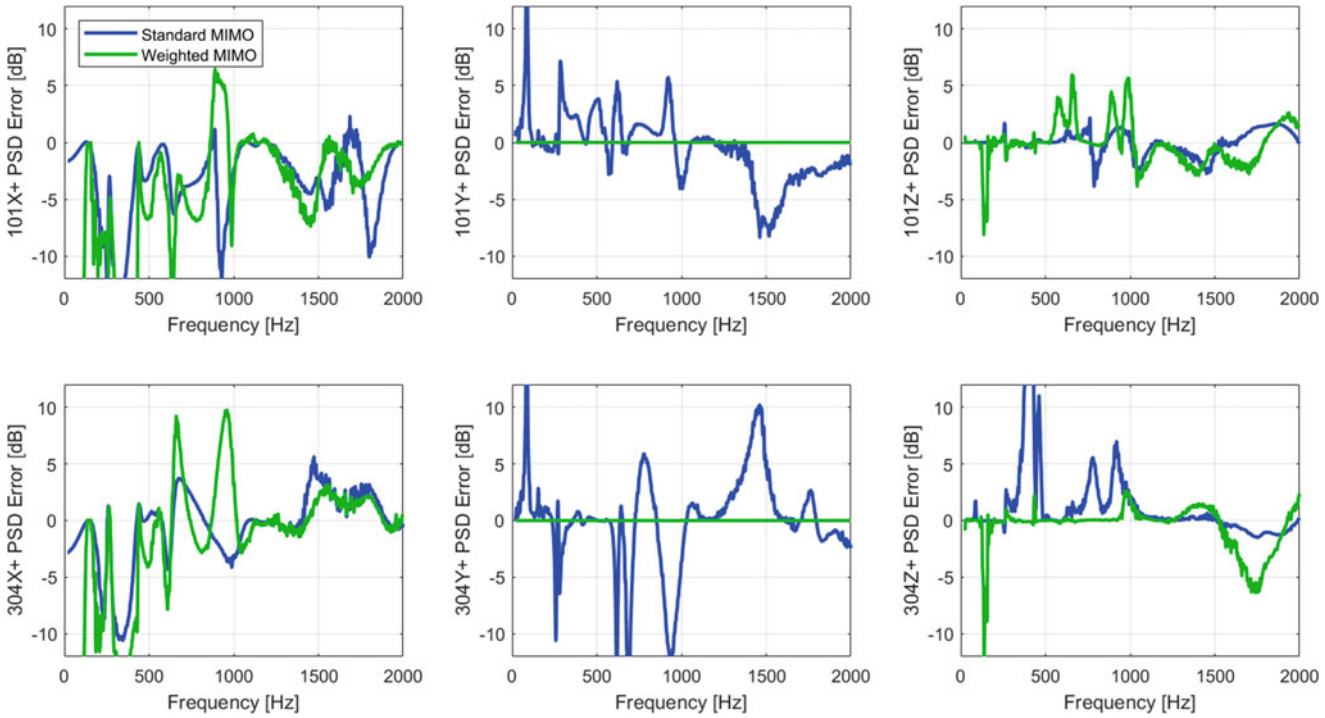

Fig. 14.4 dB error in APSDs with respect to the field response comparing unweighted (standard, blue line) and weighted (green line) MIMO solutions

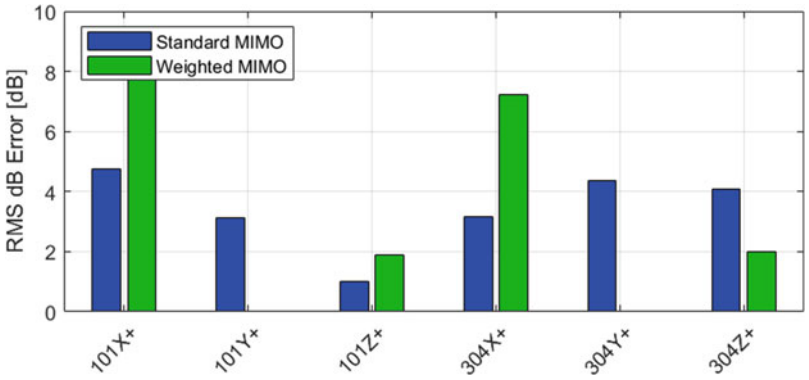

Fig. 14.5 RMS of the dB error comparing unweighted (standard, blue) and weighted (green) MIMO solutions

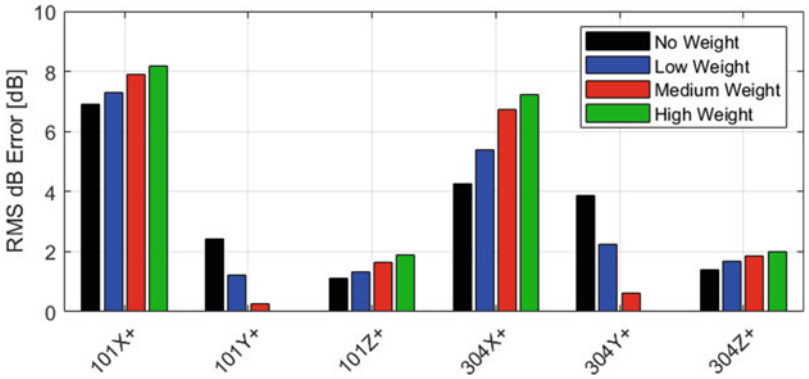

Fig. 14.6 RMS of the dB error for different amounts of weighting between the *Y* and *X*, *Z* DOFs

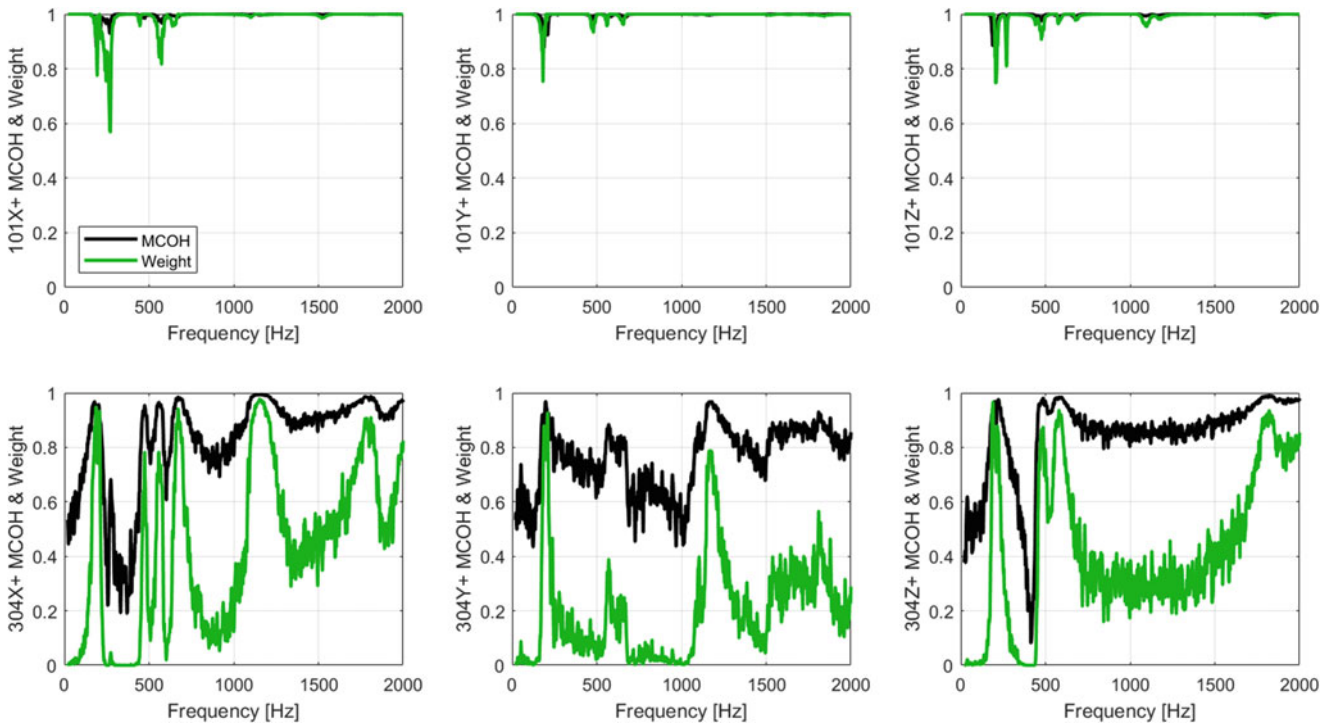

Fig. 14.7 Multiple coherence (black) and weights derived from the multiple coherence (green) at each of the six output DOFs

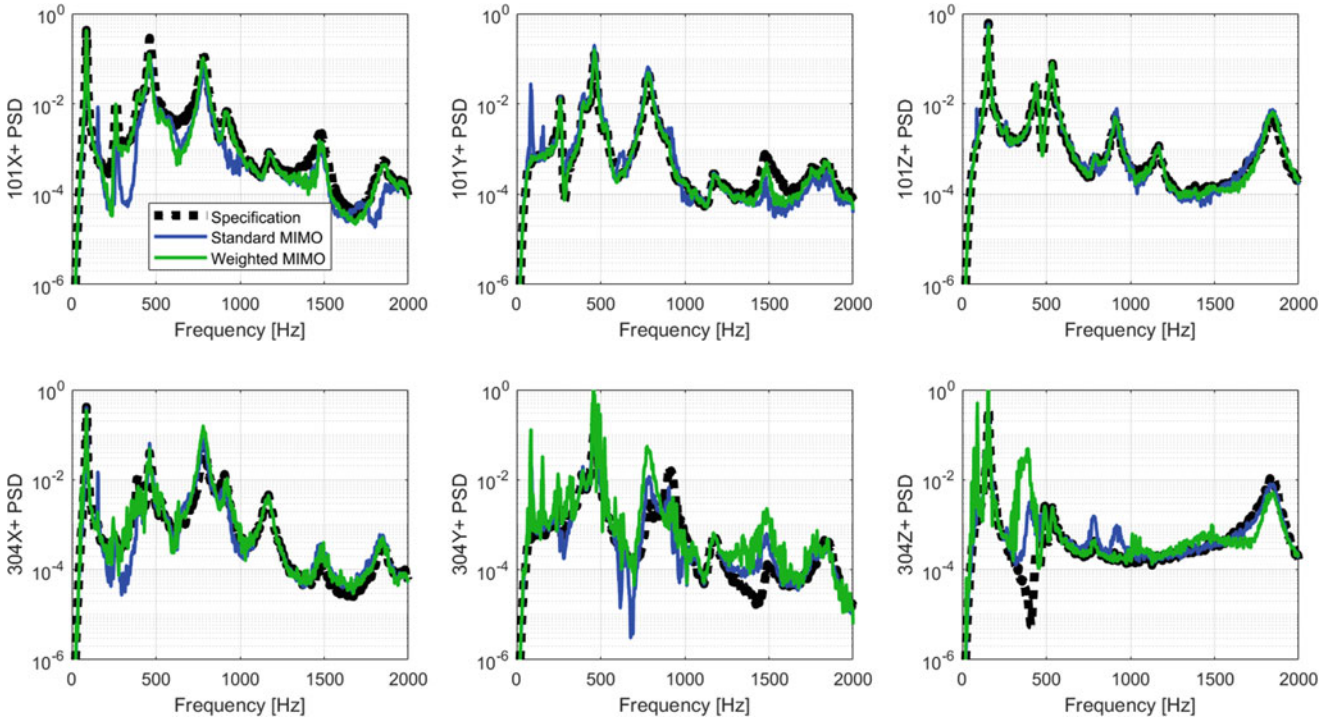

Fig. 14.8 APSDs for each of the six output DOFs comparing the field response (specification, black dotted line) and MIMO test predictions using unweighted (standard, blue line) and weighted (green line) MIMO solutions. Weighted solution utilizes weights automatically determined based on multiple coherence

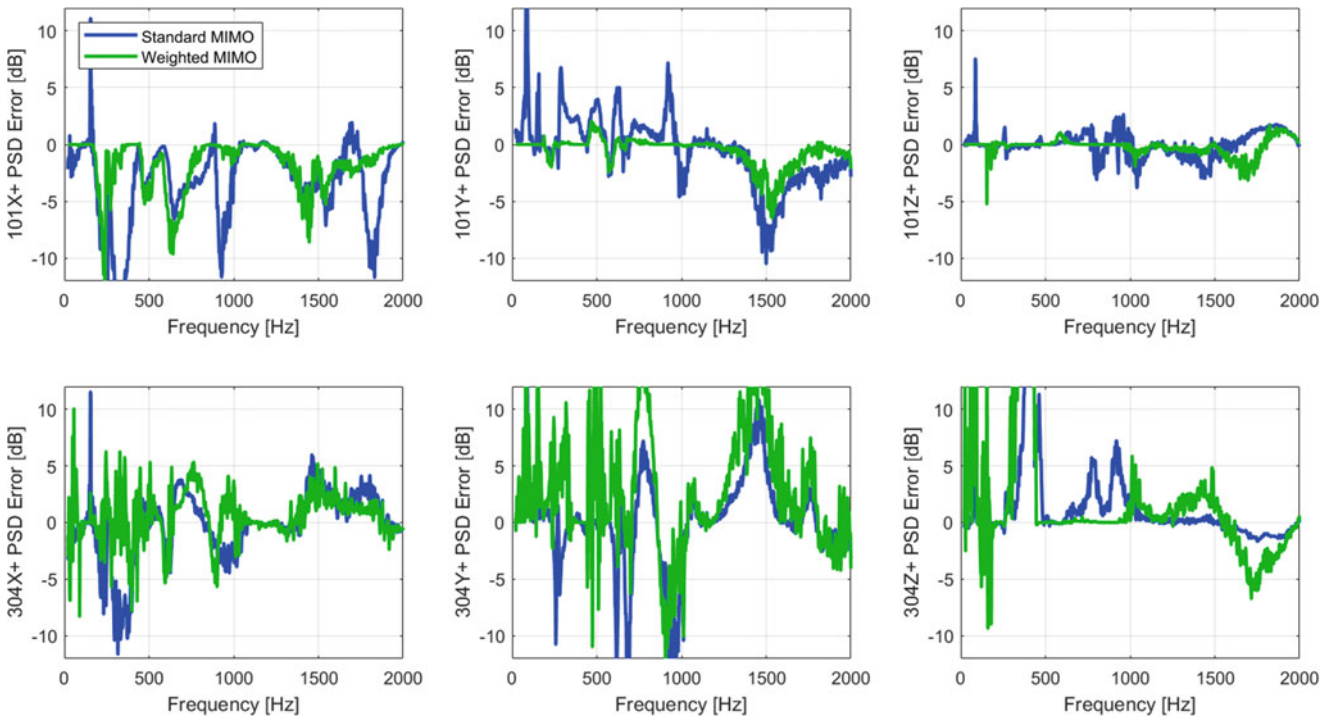

Fig. 14.9 dB error in APSDs with respect to the field response comparing unweighted (standard, blue line) and weighted (green line) MIMO solutions. Weighted solution utilizes weights automatically determined based on multiple coherence

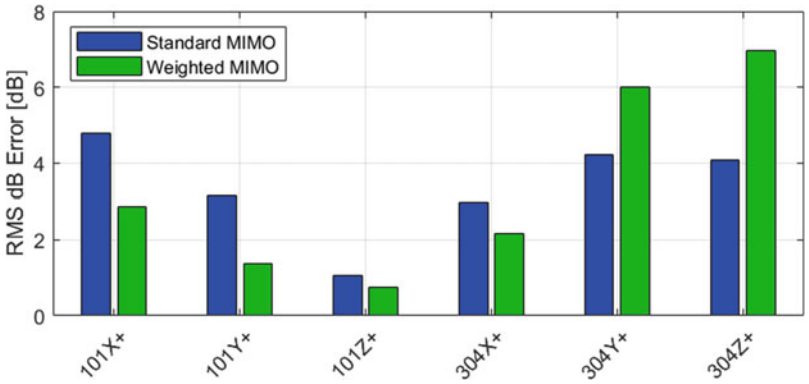

Fig. 14.10 RMS of the dB error comparing unweighted (standard, blue) and weighted (green) MIMO solutions. Weighted solution utilizes weights automatically determined based on multiple coherence

accuracy can be maintained at that location. If it were completely removed from the solution, the response could become very inaccurate at that location.

14.6 Conclusions

Flexibility is useful in MIMO control solutions to enable the test engineer to achieve desired results or make the best use of available data. Weighted MIMO control is one tool that can provide additional flexibility. By simply scaling the output DOF terms in the specification CPSD and FRF matrices, the least-squares solution utilized in MIMO control can be biased to increase or decrease the accuracy of solutions at specific DOFs. Further, because the MIMO control solution is evaluated at each frequency line, frequency-dependent weights can be utilized. Here, a method for automatically determining DOF weights is presented. This approach deweights DOFs with poor linearity, which would otherwise be detrimental to the solution. Many other possible weight selection methods are possible and could be explored in future work. Overall, weighted MIMO control is practical and effective, as demonstrated in a simple model-based example.

References

1. Chatterjee, S., Hadi, A.S.: Regression Analysis by Example, 4th edn. Wiley-Interscience (2006)
2. Vaghefi, R.: "Weighted Linear Regression," Towards Data Science, 3 Feb 2021. [Online]. Available: https://towardsdatascience.com/weighted-linear-regression-2ef23b12a6d7. Accessed 1 Sept 2022
3. Brunton, S.L., Kutz, J.N.: Data-Driven Science and Engineering: Machine Learning, Dynamic Systems, and Control. Cambridge University Press (2019)
4. D'Elia, G., Musella, U., Mucchi, E., Guillaume, P., Peeters, B.: Analyses of drives power reduction techniques for multi-axis random vibration control tests. Mech. Syst. Signal Process. **135** (2020)
5. Daborn, P.M.: Smarter Dynamic Testing of Critical Structures. PhD Thesis, University of Bristol (2014)
6. Schultz, R., Avitabile, P.: Shape-constrained input estimation for efficient multi-shaker vibration testing. Exp. Tech. **44**, 409–423 (August 2020)

Chapter 15
Shaker Capability Estimation Through Experimental Dynamic Substructuring

Peter Fickenwirth, John Schultze, Dustin Harvey, and Michael Todd

Abstract Electrodynamic shaker systems are a staple in shock and vibration environments testing, yet the specific performance limits of these systems are not well characterized. Manufacturer ratings give a general idea of a system's capability, but the details of their performance remain uncharacterized, often leaving test engineers using their best judgment to determine if a test is feasible. This work applies dynamic substructuring to better predict shaker capability throughout the system's full range. By modeling a shaker system, insight is gained into the potential performance, but the difficulty remains that the dynamics of the system will change depending on how the test configuration is defined. If no analytical model of the article exists, it is challenging to make evaluations of the new coupled system's behavior. An experimental model of the test article is developed through modal impact testing, without the need of a shaker. This experimental model is then coupled to a 4-DOF lumped-parameter electromechanical shaker model through dynamic substructuring. The coupled system can then be used for shaker capability estimation for a specific test configuration. By utilizing a modal test and substructuring to estimate performance, no time is lost with the article on the shaker determining if a test specification is achievable. Beyond time savings, the modal model could be coupled to multiple shaker models to determine the best machine for a given test.

Keywords Dynamic substructuring · Environments testing · Modal testing

15.1 Introduction

Historically, equipment for vibration testing of assemblies has been selected based on past tests, engineering judgment, and simple calculations using Newton's second law of physics. However, the electrodynamic shaker systems used to perform these tests have complicated dynamics, and there are many variables to consider when predicting a system's capability. The device under test (DUT) and its various orientations being tested, the fixturing required for testing, the shaker and amplifier used, and even the software used to control the system all influence the dynamics of the shaker. These dynamics in turn affect its capability to achieve the specified mechanical outputs. A more detailed understanding of these systems can be achieved through modeling of the shaker itself. Updating the model with experimentally collected data further ensures an accurate characterization of its performance. However, more information is needed still, as the setup of the test on the shaker may strongly influence the dynamics of the now coupled system. Modal testing can relatively quickly characterize the dynamics of a device under test, which can then be coupled to the shaker model through dynamic substructuring to achieve a full understanding of the coupled system.

P. Fickenwirth (✉) · J. Schultze · D. Harvey
Los Alamos National Laboratory, Test Engineering Group, Los Alamos, NM, USA
e-mail: pfickenwirth@lanl.gov

M. Todd
University of California, San Diego, Department of Structural Engineering, Los Alamos National Laboratory, Los Alamos, NM, USA

J. Harvie (ed.), *Dynamic Environments Testing, Volume 7*, Conference Proceedings of the Society for Experimental Mechanics Series, https://doi.org/10.1007/978-3-031-34930-0_15

15.2 Background

15.2.1 Shaker Modeling

Many modeling approaches have been taken to capture the dynamics of electrodynamic shaker systems. All of these models seek to characterize the fundamental modes of a shaker system. These are the isolation mode, where the shaker entirely moves together on its isolation mounts, the suspension mode, where the armature moves in opposition to the body, and the coil mode, where the armature table and coil move in opposition to one another [1]. Figure 15.1 shows a diagram of a typical electrodynamic shaker.

Most modeling approaches use a lumped parameter model with anywhere from 2 mechanical degrees of freedom (DoFs) up to 6, all with one additional electrical degree of freedom. Both Schultz [2] and Mayes et al. [3] used 4-DOFs, modeling the shaker body, armature, and a mass on the end of a stinger. Many others modeled the voice coil of the shaker and armature table as two separate degrees of freedom, such as Ricci and Peeters [4], as well as Manzato et al. [5], in their work on virtual shaker testing. Other approaches sought to make an impedance model, with Smallwood using a two-port network model to represent the shaker as an impedance matrix [6], and Tiwari et al. utilizing a 4-DOF lumped parameter model but using the impedance analogy to develop an equivalent electrical model [7]. Some models ignore the motion of the body and, therefore, the isolation mode, as some shakers are rigidly attached to the ground, or to a mass so large that the natural frequency of the isolation mode is too low to practically characterize [8, 9]. Models that utilized more degrees of freedom attempted to characterize some of the out-of-axis motion of the shaker table, with Hoffait et al. modeling the table with rotational degrees of freedom [10].

15.2.2 Experimental Dynamic Substructuring

Dynamic substructuring is the set of techniques used to break down a large, complex dynamic system into substructures for higher fidelity modeling and analysis, while still preserving the overall dynamics of the system. These techniques are commonly applied to finite element analysis models to save time by modeling substructures separately and reassembling the results later. In experimental analysis, substructuring is used to test substructures separately, characterize local dynamics, and then assess their contributions to system-level dynamics. One of the most powerful applications of dynamic substructuring is the ability to combine analytical and experimental analyses of substructures into a full model together [11].

Dynamic substructuring can be represented and applied in many domains, but for this work, the focus is on the frequency domain. Specifically, the Lagrange-multiplier frequency-based-substructuring method (LM-FBS) is used, as described by de

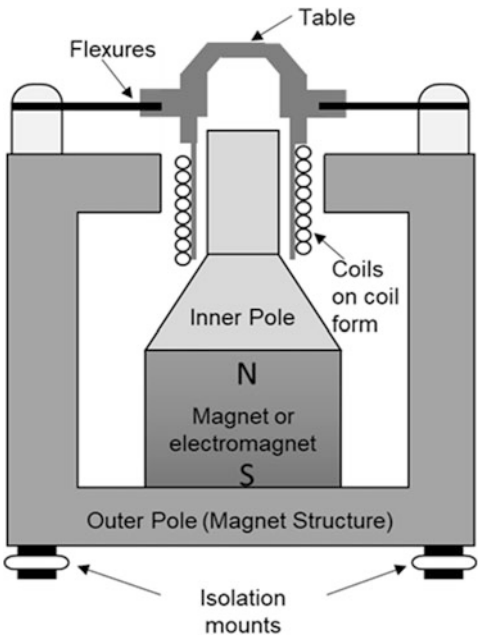

Fig. 15.1 Diagram of an electrodynamic shaker

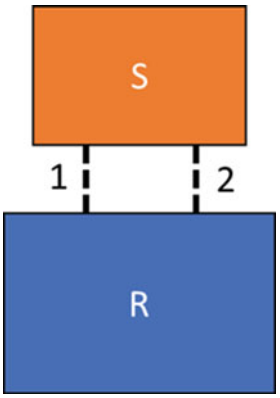

Fig. 15.2 Example of two substructures, *S* and *R*, coupled together at two locations, 1 and 2

Klerk et al. [12], who showed that this method of frequency-based substructuring is equivalent to the classical FBS developed by Jetmundsen [13], but in a simpler form. Consider two substructures, S and R, to be coupled together at two locations, 1 and 2, as shown in Fig. 15.2.

Two interface conditions must be satisfied to assemble the substructures together and understand their coupled dynamics: compatibility and equilibrium. The compatibility condition requires that the responses at the degrees of freedom on either side of the interface between the two substructures must be equal. The equilibrium condition requires that the sum of the internal forces, the forces imparted by the substructures on one another at the interface, must be zero when assembled. A signed Boolean mapping matrix, **B**, is defined by how the substructures are coupled. The matrix can be defined as two submatrices, one for each substructure, that is then concatenated.

$$\mathbf{B}^{\mathrm{S}} = \begin{matrix} \\ 1 \\ 2 \end{matrix} \overset{\begin{matrix} \mathrm{S}_i & \mathrm{S}_{b1} & \mathrm{S}_{b2} \end{matrix}}{\begin{bmatrix} 0 & \mathrm{I} & 0 \\ 0 & 0 & \mathrm{I} \end{bmatrix}}, \mathbf{B}^{\mathrm{R}} = \overset{\begin{matrix} \mathrm{R}_i & \mathrm{R}_{b1} & \mathrm{R}_{b2} \end{matrix}}{\begin{bmatrix} 0 & -\mathrm{I} & 0 \\ 0 & 0 & -\mathrm{I} \end{bmatrix}} \tag{15.1}$$

$$\mathbf{B} = \left[\mathbf{B}^{\mathrm{S}}, \mathbf{B}^{\mathrm{R}}\right] \tag{15.2}$$

The columns of **B** are the degrees of freedom of the substructures with S_{i} and R_i being the internal degrees of freedom of each substructure, S_{b1} and R_{b1} the degrees of freedom on interface 1, and S_{b2} and R_{b2} the degrees of freedom on interface 2. The non-zero elements indicate which DOFs are at connections. The rows are the interfaces where those DOFs are connected. The compatibility condition can then be written using this matrix as

$$\mathbf{Bu} = \mathbf{0} \tag{15.3}$$

Where **u** is the vector of all responses at the interfaces. The LM-FBS method utilizes a dual assembly approach, which introduces interface forces **g**, that automatically satisfy the equilibrium condition.

$$\mathbf{g} = -\mathbf{B}^{\mathrm{T}}\boldsymbol{\lambda} \tag{15.4}$$

This definition for the interface forces can then be substituted into the dynamic equilibrium equation.

$$\mathbf{u} = \mathbf{Y}\left(\mathbf{f} - \mathbf{B}^{\mathrm{T}}\boldsymbol{\lambda}\right) \tag{15.5}$$

Where **Y** is the frequency response matrices of the two substructures assembled blockwise diagonally. Substituting this definition of **u** into the compatibility condition in Eq. 15.3 and then simplifying, $\boldsymbol{\lambda}$ can be determined.

$$\boldsymbol{\lambda} = \left(\mathbf{BYB}^{\mathrm{T}}\right)^{-1}\mathbf{BYf} \tag{15.6}$$

This definition of $\boldsymbol{\lambda}$ can be substituted into the dynamic equilibrium Eq. 15.5 and simplified again.

$$\mathbf{u} = \left(\mathbf{Y} - \mathbf{YB}^{\mathbf{T}}\left(\mathbf{BYB}^{\mathbf{T}}\right)^{-1}\mathbf{BY}\right)\mathbf{f} \tag{15.7}$$

Equation 15.5 defines the dynamic equilibrium of the fully coupled system. The new coupled FRF matrix $\mathbf{Y}_{\text{dual}}$ can then be defined.

$$\mathbf{Y}_{\mathbf{coupled,dual}} = \mathbf{Y} - \mathbf{YB}^{\mathbf{T}}\left(\mathbf{BYB}^{\mathbf{T}}\right)^{-1}\mathbf{BY} \tag{15.8}$$

Equation 15.6 is the formula for LM-FBS and defines the FRF matrix of the fully coupled system. $\mathbf{Y}_{\text{dual}}$ is defined for all the local DOFs on all the substructures and, therefore, contains redundant information at the DOFs that have been coupled. To utilize the LM-FBS formula, driving point FRFs are required for every DOF coupled together, as well as at any other DOFs of interest.

15.3 Shaker Model Development

A 4-DOF lumped parameter electromechanical model for the shakers was chosen. This model was chosen because it captures the dynamics of the three main modes of a shaker system but is simple enough to develop by hand and computationally easy to implement. This 4-DOF model appeared multiple times in the literature and proved to capture the dominant dynamics of most shaker systems. The model consists of three mechanical DOFs, the body of the shaker, the armature table, and the armature coil. These are elastically connected to one another with springs and dampers. The fourth DOF is the charge in the electrical component of the system. The circuit consists of a source EMF, an inductor, and a resistor. The two models are connected by the force imparted on the mechanical system, which is proportional to the current, and the corresponding back EMF on the electrical system, which is proportional to the relative velocity of the body and coil. A diagram of the model is shown in Fig. 15.3.

The model consists of 12 parameters. The mechanical side contains three masses, M_b, M_t, and M_c, three stiffnesses, k_b, k_t, and k_c, and three dampings, c_b, c_t, and c_c. The electrical model contains the resistance of the coil, R, and the inductance, I. Lastly, the two systems are coupled together by the coupling factors, which are replaced with a single constant K. These

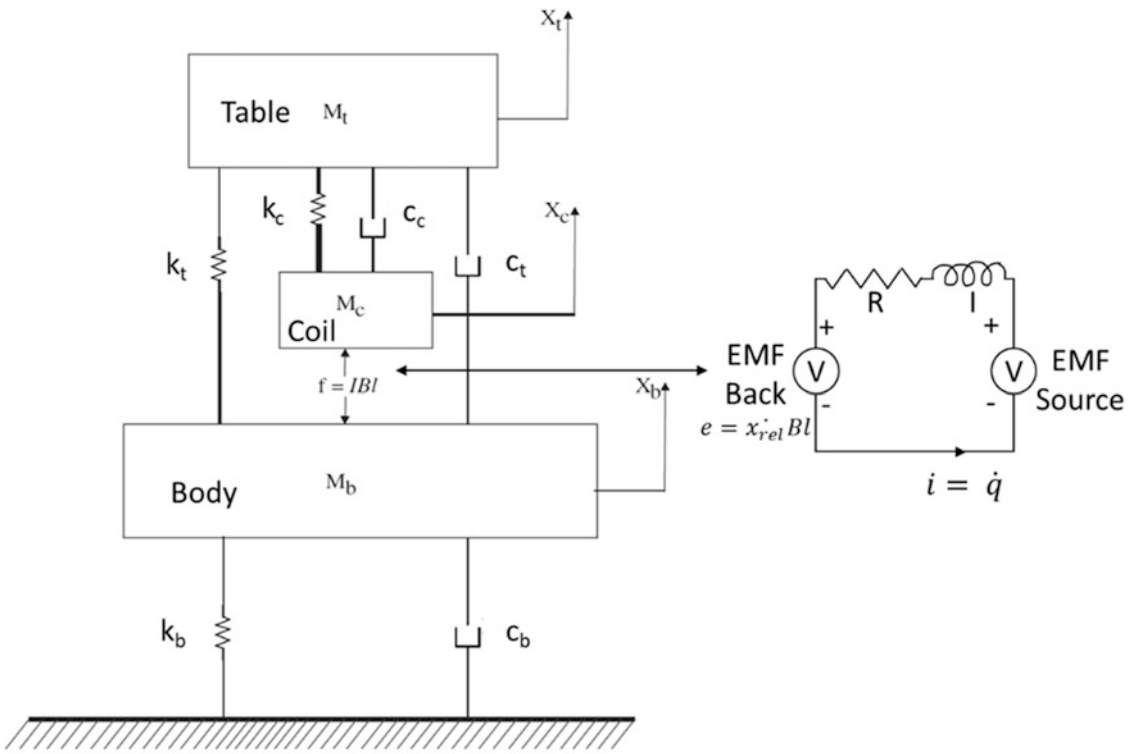

Fig. 15.3 Shaker electromechanical model diagram

factors are only equal if SI units are used. Of these 12 parameters, 5 were determined from the specification sheet provided by the shaker manufacturer and measurements made on the system. The shaker's body mass and armature mass, the sum of both the table and coil, and the flexure stiffness, *kt*, were available. The resistance of the coil was measurable directly on the shaker input terminal. The remaining parameters must be estimated through measurements on the system itself.

The end-use of this model is ultimately FBS, which couples together the frequency response functions (FRFs) of two different substructures to determine their coupled dynamics. Therefore, the FRFs of interest for this model must be calculated from it. First the equations of motion of the system were assembled based on the model. The displacements of the body, table, and coil are the mechanical DOFs and charge is chosen as the electrical DOF, so that the time-derivatives of the DOFs remain consistent.

$$\begin{bmatrix} M_b & 0 & 0 & 0 \\ 0 & M_t & 0 & 0 \\ 0 & 0 & M_c & 0 \\ 0 & 0 & 0 & L \end{bmatrix} \begin{Bmatrix} \ddot{x}_b \\ \ddot{x}_t \\ \ddot{x}_c \\ \ddot{q} \end{Bmatrix} + \begin{bmatrix} c_b + c_t & -c_t & 0 & K \\ -c_t & c_t + c_c & -c_c & 0 \\ 0 & -c_c & c_c & -K \\ -K & 0 & K & R \end{bmatrix} \begin{Bmatrix} \dot{x}_b \\ \dot{x}_t \\ \dot{x}_c \\ \dot{q} \end{Bmatrix} + \begin{bmatrix} k_b + k_t & -k_t & 0 & 0 \\ -k_t & k_t + k_c & -k_c & 0 \\ 0 & -k_c & k_c & 0 \\ 0 & 0 & 0 & 0 \end{bmatrix} \begin{Bmatrix} x_b \\ x_t \\ x_c \\ q \end{Bmatrix} = \begin{Bmatrix} f_b \\ f_t \\ f_c \\ E \end{Bmatrix} \tag{15.9}$$

If the matrices are then denoted **M**, **C**, and **K** respectively, the vector of response DOFs is denoted **x**, and the vector of input forces **f**, the system can efficiently be written in a familiar form.

$$\boldsymbol{M}\ddot{\boldsymbol{x}} + \boldsymbol{C}\dot{\boldsymbol{x}} + \boldsymbol{K}\boldsymbol{x} = \boldsymbol{f} \tag{15.10}$$

From Eq. 15.9 and its restatement as Eq. 15.10, the FRFs of the system can be easily calculated using the direct frequency response method.

$$\boldsymbol{H} = \left(-\omega^2 \boldsymbol{M} + j\omega \boldsymbol{C} + \boldsymbol{K}\right)^{-1} \tag{15.11}$$

Where *H* is the frequency response function matrix of the full system. H is calculated on a frequency line basis, with ω being the frequency, in radians, at that line. The result is 4×4×n matrix, where n is the number of frequency lines calculated. There are no input forces on the mechanical degrees of freedom, so only the fourth column of FRFs is needed, which are the responses to an electrical input, *E*. The impedance of the shaker is calculated from the electrical DOF, while the acceleration-voltage FRF is derived from the table DOF. The acceleration-current FRF is the product of the acceleration-voltage FRF and the impedance.

The three FRFs of interest are affected by each of the parameters in the model. A parameter sensitivity study was performed to understand how changes in these parameters manifest in the FRFs. A baseline value was chosen for each of the parameters and held constant throughout. Then, one parameter at a time was subjected to an upward and downward perturbation. After completing the perturbations for each of the parameters, the effects on the FRFs were assembled into Table 15.1, as well as the expected source for that parameter value. While the effects on all three FRFs were viewed, the effects in Table 15.1 focus on the shaker's impedance.

Table 15.1 Model parameter sensitivities

Parameter	Source	Effect on impedance
M_b – Shaker body mass	Spec sheet	Shifts frequency of isolation mode
M_t – Table mass	Spec sheet, estimate$M_t + M_c = M_{\text{armature}}$	Shifts frequency of isolation mode and suspension mode
M_c – Coil mass	Spec sheet, estimate$M_t + M_c = M_{\text{armature}}$	Shifts frequency of isolation mode and coil mode
C_b – Isolation mount damping	Estimate	Shifts amplitude of isolation mode
C_t – Flexure damping	Estimate	Shifts amplitude of suspension mode
C_c – Coil damping	Estimate	Shifts amplitude of suspension mode and coil mode
K_b – Isolation mount stiffness	Estimate	Shifts frequency of isolation mode
K_t – Flexure stiffness	Spec sheet	Shifts frequency of suspension mode
K_c – Coil stiffness	Estimate	Shifts frequency of suspension mode, slightly coil mode
R – Coil resistance	Measure	Shifts overall amplitude slightly, significantly shifts coil mode amplitude
L – Coil inductance	Estimate	Shifts coil mode frequency

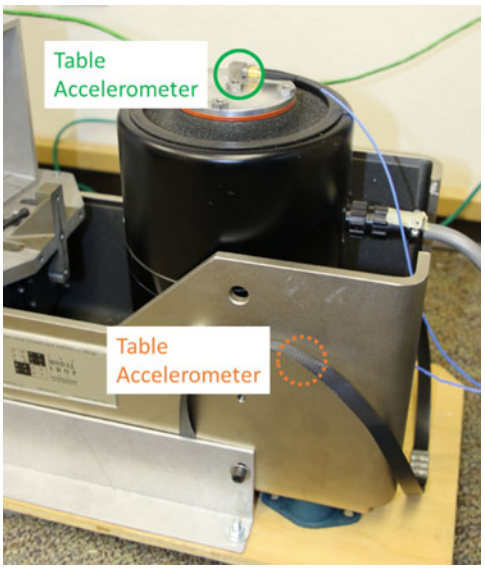

Fig. 15.4 Small shaker model validation test setup

15.4 Shaker Model Validation and Updating

The model developed must be validated using data from the shaker itself. This is especially important, as only 5 of the 12 parameters are known. To capture the behavior of the shaker, a test was set up to measure the three FRFs of interest. The shaker characterized was a Modal Shop (TMS) K2075E dual-purpose 75lbf shaker. Two triaxial accelerometers were placed on the shaker, with one on the armature table and one on the body of the shaker, as shown in Fig. 15.4. The accelerometer on the body is located on the black body of the shaker but obscured by the slip table housing. The amplifier's built-in current monitor was used to measure the current supplied, and a voltage probe was attached to the amplifier output terminal to measure the voltage input supplied. In addition to the voltage from the amplifier, the drive voltage from the data acquisition unit (DAQ) was measured. This setup captures nearly all the degrees of freedom in the model, but the armature coil is inaccessible for direct measurement.

The test profile used was a flat 1 g RMS power spectral density (PSD) from 1 Hz to 6500 Hz with a 1 Hz frequency spacing to characterize the full range of the shaker's dynamics. The frequency limits were based on the limitations of the equipment used, the expected dynamics of the system, and the controllability of the profile. The test was controlled using the Siemens LMS Testlab 2021.1 software's Random Vibration control module. The test was run both open loop and closed loop to observe any effects of the controller on the FRFs. For the closed loop control, the test was controlled on the Z-axis of the table accelerometer. The data was collected in the time-domain using a sample rate of 25.6 kHz.

The results from the characterization test closely matched the shape of the expected curves from the literature. The three FRFs were calculated from the time data collected using a two second Hanning window with a 50% overlap. Figure 15.5 shows the results of the test with the model results. The shaker impedance, which is the measured voltage over the measured current across the frequency range, is shown in the real-imaginary form, while the other two FRFs are displayed in magnitude-phase form. Very little difference was seen between the open and closed loop controls, with less than 5% difference in magnitude for all three FRFs. The closed loop results are displayed in the figure. Two modes, the suspension and coil modes, are clearly visible on the plots, but the isolation mode is not. It is possible that either the mode is out of the range of interest or does not have sufficient amplitude to be viewed. In either case, this indicates that the model may be successful without including the body degree of freedom.

The data collected in the characterization test was then used for updating the model. First, the model was updated by hand to get an approximate fit of the data and provide a starting point for an optimization that would determine the final fit of the model. Using the results of the parameter sensitivity study, model parameters were chosen by trial and error and evaluated compared to the data. Table 15.2 shows the values chosen for the hand-fit of the model. An imaginary component was added to the inductance, as Mayes et al. [3] found their amplifier exhibited a fixed phase difference between the current and voltage. This phase difference results in a real component of the impedance increases proportional with frequency. Making the inductance complex compensates for this, it is not indicative of the physical phenomenon occurring.

The hand-fit model was then used as the initial state for the optimization to make the final model fit. MATLAB's *fmincon* algorithm was used for the optimization. *fmincon* is a gradient-based nonlinear constrained optimization algorithm. The

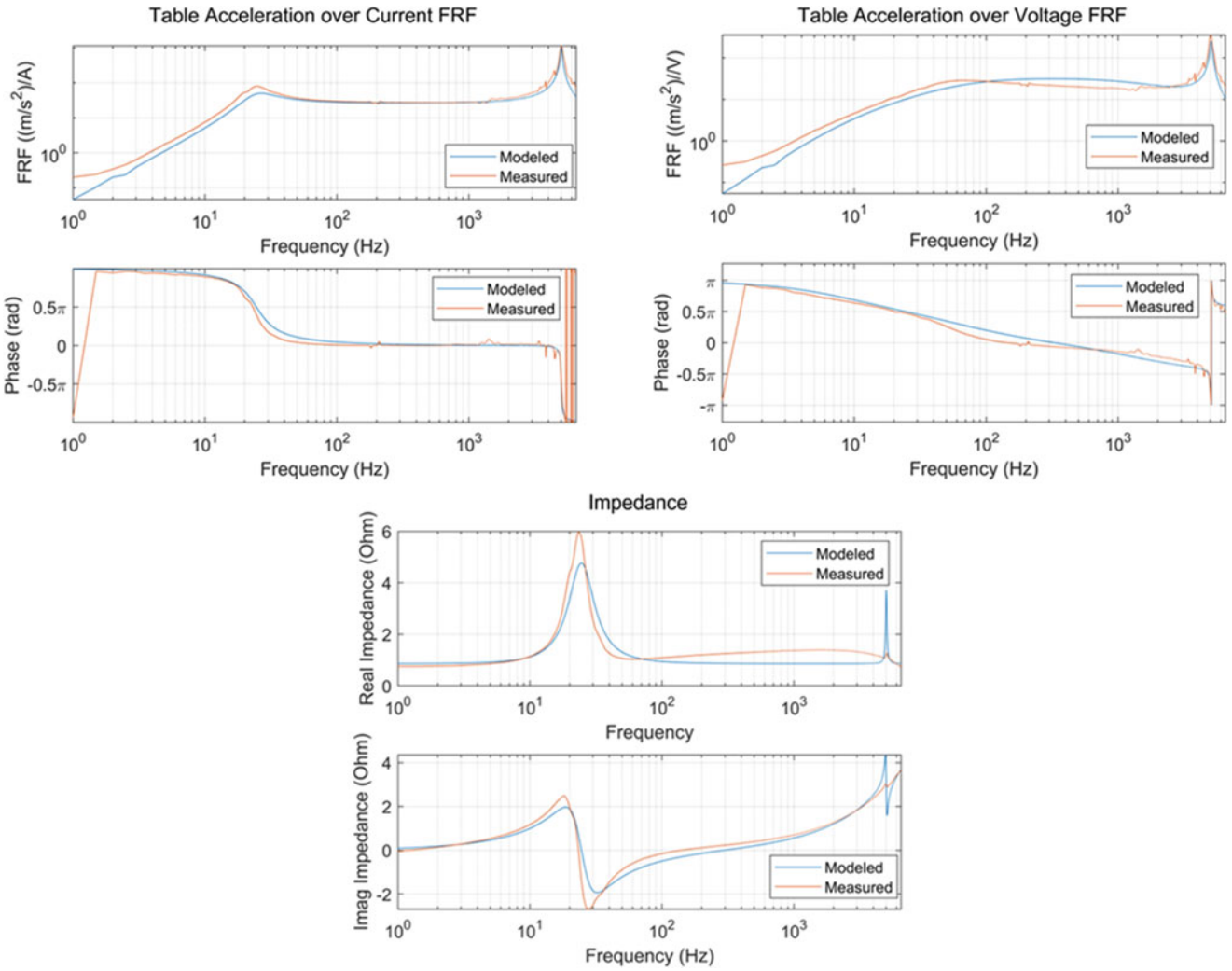

Fig. 15.5 Comparison of the updated model FRFs to the measured FRFs of the shaker

Table 15.2 Chosen model parameters

Parameter	Hand fit value	Updated value	Units
Body mass	15.55	15.55 (fixed)	kg
Table mass	0.40	0.40 (fixed)	kg
Coil mass	0.05	0.05 (fixed)	kg
Body damping	100	0.00451	N/(m/s)
Flexure damping	20	37.8	N/(m/s)
Coil damping	40	39.7	N/(m/s)
Body stiffness	10,000	3.34e3	N/m
Flexure stiffness	10,500	10,500 (fixed)	N/m
Coil stiffness	4.50e7	4.72e7	N/m
Resistance	0.86	0.86 (fixed)	Ω
Real (inductance)	0.00012	9.46E-05	H
Imag (inductance)	2.00E-05	5.22E-14	H
Coupling coefficient	12	13.2	–

objective function used was a weighted sum of the root mean square errors of the real and imaginary parts of each FRF across all frequency lines.

$$e_{\text{FRF}} = \sqrt{\frac{\sum_{n=1}^{N} \sum \left(\text{real}\left(h_{n,\text{model}}\right) - real\left(h_{n,\text{measured}}\right)\right)^2}{N}} + \sqrt{\frac{\sum_{n=1}^{N} \sum \left(\text{imag}\left(h_{n,\text{model}}\right) - real\left(h_{n,\text{measured}}\right)\right)^2}{N}} \tag{15.12}$$

$$e_{\text{model}} = a_1 e_{\text{Impedance}} + a_2 e_{\text{Accel-Voltage}} + a_3 e_{\text{Accel-Current}} \tag{15.13}$$

In these equations, h_n is the value of the FRF at the nth frequency line, N is the total number of frequency lines, and a_i is the weight assigned to the RMS error of that FRF. Weights were assigned to compensate for the varying magnitudes of the FRFs investigated, otherwise the acceleration-current FRF dominates the error. The five model parameters that could be determined from the specification sheet of the shaker and measurements (body mass, table mass, coil mass, flexure stiffness, and resistance) were held fixed while the remaining seven parameters were allowed to vary. The only constraint used was that parameters must be nonnegative. Table 15.2 also shows the parameter values determined from the optimization, and Fig. 15.5 compares the calculated FRFs from these parameters to the measured data. Most of the model parameters were not drastically changed; however, the damping and stiffness related to the body degree of freedom did. This is likely because the isolation mode is not clearly seen in the measured data and had little impact on the value of the objective function. The imaginary portion of the inductance approached zero, indicating the phase difference was likely not seen in the equipment used.

15.5 BARC Base Modal Testing

A generic DUT was needed for assessing the effectiveness of using experimental dynamic substructuring for shaker capability estimation. The base of the Box Assembly and Removable Component (BARC) was chosen as the DUT. The BARC is a common challenge testbed used within the dynamic environments testing community. The base of the BARC, i.e., without the removable component, was used because it does not contain any bolted joints, which are dynamically complex and difficult to characterize.

A multi-reference impact test (MRIT) was performed to develop a modal model of the BARC base. The test was performed with the BARC suspended from a modal test stand using fishing wire to approximate a free-free boundary condition. A combination of uniaxial and triaxial accelerometers were used, totaling 12 sensors and 24 reference channels. The extensive instrumentation was chosen for possible future applications of a virtual point transformation to aid the results of the FBS, where the motion in 6-DOFs at virtual connection points is estimated by making measurements around each point [14]. A PCB 086C02 modal impact hammer was used for excitation. All data were collected using a Siemens LMS SCADAS Mobile DAQ and Siemens Simcenter Testlab software. A bandwidth of 8192 Hz with 16,384 spectral lines was used, resulting in a two second acquisition window. The structure is very lightly damped and continued to resonate after the acquisition window ended, causing low-frequency leakage, so a 30% exponential decay window was applied to the data collected. A 5% force-exponential window was used on the input. Five averages were collected for each FRF. Figure 15.6 shows the test setup.

A driving point measurement is needed at each of the connection points for substructure coupling. In addition, each point of interest anywhere else on the structure also requires a driving point. These points could be potential control points that must be evaluated for estimating shaker capability. The results of the driving point measurements are a 24 × 24 × 16384 FRF matrix that was used for modal parameter estimation.

Modal parameter estimation was performed using the orthogonal polyreference, or OPoly, tool in the third-party MATLAB toolbox, IMAT 7.9.0, developed by ATA Engineering. First, the full range of interest, from 1 Hz up to 6500 Hz, was attempted for modal parameter estimation. However, the parameter estimation algorithm struggled with fitting such a large frequency range. This difficulty is likely because the test conducted did not well characterize the rigid body modes which occurred between 0 Hz and 10 Hz. Additionally, the input spectrum achieved by the hammer begins to roll off significantly after 6000 Hz. Instead, a shorter range was fit, from 50 Hz to 1960 Hz, which spanned from the first elastic mode up to the eleventh.

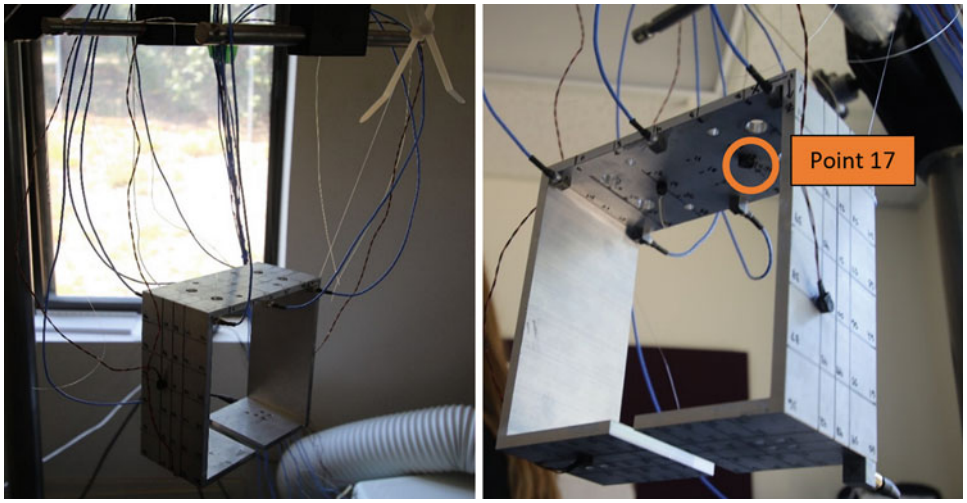

Fig. 15.6 Modal impact test setup

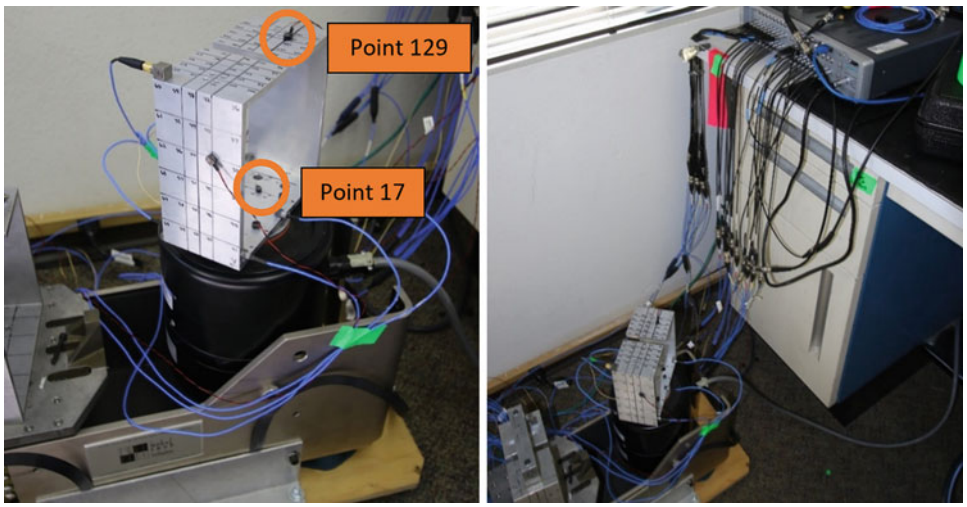

Fig. 15.7 Setup of the substructure coupling validation test

15.6 Substructuring Analysis and Results

The experimental model of the BARC base was analytically coupled to the analytical model of the small shaker using Eq. 15.8. The synthesized FRFs of the BARC base are the data used for the substructure coupling analysis, because they are analytically derived from the estimated modal parameters and are less noisy. The inversion in the LM-FBS coupling equation causes the formula to be susceptible to noise in the FRFs used. Similarly, the FRFs calculated from the model of the shaker are used. Points 17 and 19, located on the base between the mounting holes, were chosen as the analytical coupling points on the BARC base and were coupled with the table DOF of the shaker model. This creates two interface conditions. Using Eq. 15.8, the coupled FRF matrix is then calculated on a frequency line basis. The frequency range of the modal parameter estimation, 50 Hz to 1960 Hz, with a 1 Hz spacing was used.

The substructuring analysis must be experimentally validated, so a random vibration test of the BARC base attached to the shaker was conducted. This test utilized the same instrumentation setup on the BARC base as in the modal test, but also measured the current and voltage supplied by the amplifier to the shaker. The test was again run using the Random Vibration control module of Siemens Simcenter Testlab. The test was conducted from 10 Hz to 6000 Hz with a 2 Hz frequency resolution. A sample rate of 25.6 kHz was used. Figure 15.7 shows a setup of the test. Similar to the test analysis performed for the shaker model validation, the impedance, acceleration over voltage, and acceleration over current FRFs were calculated from the time history data collected and can be found in Fig. 15.8.

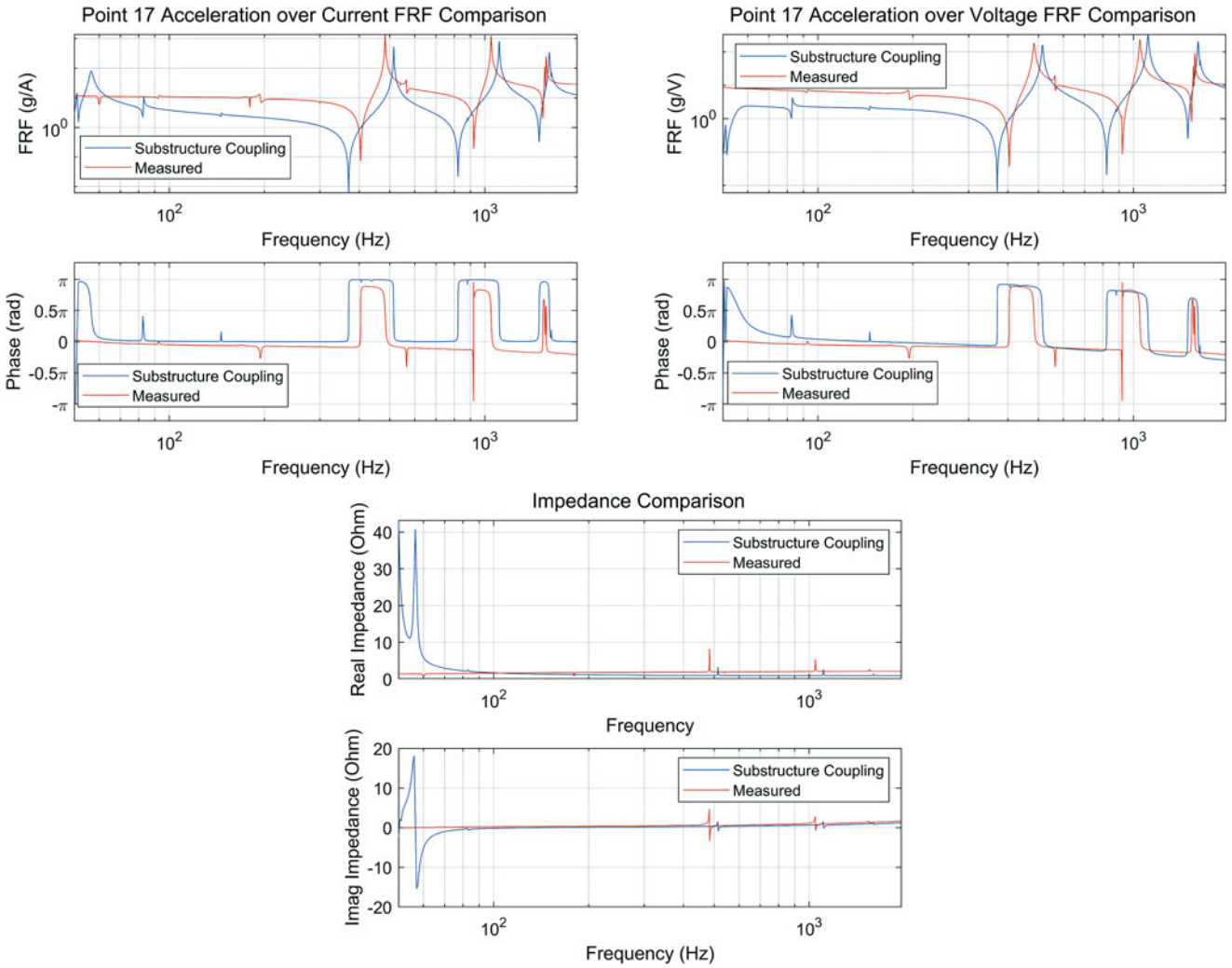

Fig. 15.8 FRFs at Point 17 estimated from substructure coupling compared to measured FRFs at Point 17

The results of the coupling shown in Figs. 15.8 and 15.9 are compared to the validation test results. The results of the substructuring analysis are not perfect but indicate that the method could be used for predicting shaker capability, with some improvement. The modeled impedance matches the amplitude of the measured impedance but sees large erroneous peaks at the low frequency. Points 17 and 129, both uniaxial accelerometers measuring in the vertical direction, were used for comparisons. Point 17 was a coupling point between the modal model of the BARC base and shaker model, while point 129 is located on top of the BARC base. In both cases, the model has the same overall shape as the measured FRFs for both points, though the resonant frequencies are generally underestimated in the lower frequency range (50 Hz to 300 Hz) and overestimated in the upper frequency range (300 Hz to 1960 Hz). These upper frequency range resonances are also overestimated in the impedance. The overall magnitude of the acceleration FRFs also appears to be too low.

15.7 Conclusions

The results of this work show promise that shaker capability could be estimated for individual test setups following this same process of modeling the shaker, experimentally characterizing the DUT, and potentially even fixturing, and then, coupling all the components together with dynamic substructuring. Once the FRFs of the system are calculated, they can be inverted and used as filters to determine the electrical input spectra required to achieve an acceleration PSD test specification. The

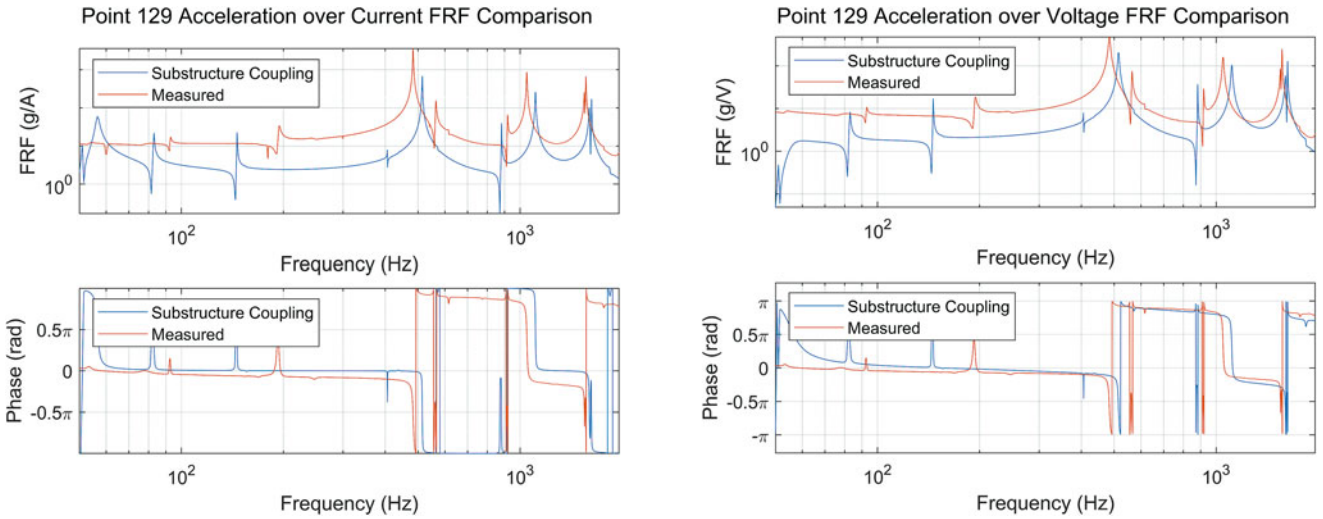

Fig. 15.9 FRFs at Point 129 estimated from substructure coupling compared to measured FRFs at Point 129

shaker model adequately captured the shaker's dynamics, and the modal parameter estimation was successful in the limited range that was fit. Based on the FRFs calculated from the measured data on the shaker, it may be possible to remove the body degree of freedom, as the isolation mode was not clearly visible. This may also improve the efficiency of the optimization used to update the model by reducing the solution space.

The results of the substructuring analysis could see significant improvement. A very simple method of experimental dynamic substructuring was used, and the coupling points chosen, while in the middle of the shaker-BARC interface, were not at all co-located with the physical connection points. More advanced techniques for substructuring, such as using a virtual point transformation to couple at the physical connection points and with more degrees of freedom, could improve results. In addition, the narrow dynamic range fit for the modal model did not include the shaker's armature resonance, which often introduces the most difficulties to testing. Capturing a wider range would better describe the capabilities of the shaker at all operating ranges, and significantly improve the usefulness of this method. A better fit of the lower range may also improve the results of the substructuring, as the rigid body motion of the BARC base was not captured.

Acknowledgments This work was funded by the Delivery Environments program at Los Alamos National Laboratory, under the Office of Engineering and Technology Maturation.

References

1. Lang, G.F., Snyder, D.: Understanding the physics of electrodynamic shaker performance. Sound Vib. **35**(10), 24–33 (2001)
2. Schultz, R.: Calibration of Shaker Electro-mechanical Models. In: Proceedings of the 38th IMAC (2020)
3. Mayes, R. L., Ankers, L., Daborn, P. M., Moulder, T., Ind, P.: Optimization of shaker locations for multiple shaker environmental testing. In: Proceedings of IMAC XXXVII, the 37th International Modal Analysis Conference (2019)
4. Ricci, S., Peeters, B., Fetter, R., Boland, D., Debille, J.: Virtual Shaker Testing for Predicting and Improving Vibration Test Performance. In: Proceedings of the IMAC-XXVII (2009)
5. Manzato, S., Bucciarelli, F., Arras, M., Coppotelli, G., Peeters, B., Carrella, A.: Validation of a Virtual Shaker Testing approach for improving environmental testing performance. In: Proceedings of ISMA 2014 - International Conference on Noise and Vibration Engineering (2014)
6. Smallwood, D. O.: Characterizing Electrodynamic Shakers. In: Annual Technical Meeting and Exposition of the Institute of Environmental Sciences (1997)
7. Tiwari, N., Puri, A., Saraswat, A.: Lumped parameter modelling and methodology for extraction of model parameters for an electrodynamic shaker. J. Low Freq. Noise Vib. Active Control. **36**(2), 99–115 (2017)
8. McConnell, K.: Vibration exciters. In: Vibration Testing: Theory and Practice, pp. 363–440. John Wiley & Sons (1995)
9. Varoto, P.S., De Oliveira, L.P.R.: Interaction between a vibration exciter and the structure under test. Sound Vib. (October 2002)
10. Hoffait, S., Marin, F., Simon, D., Peeters, B., Golinval, J.C.: Measured-based shaker model to virtually simulate vibration sine test. Case Stud. Mech. Syst. Signal Process. **4**, 1–7 (2016)
11. de Klerk, D., Rixen, D.J., Voormeeren, S.N.: General framework for dynamic substructuring: history, review, and classification of techniques. AIAA J. **6**(5), 1169–1181 (2008)

12. de Klerk, D., Rixen, D.J., de Jong, J.: The Frequency Based Substructuring (FBS) Method reformulated according to the Dual Domain Composition Method. In: Proceedings of the XXIV International Modal Analysis Conference, January (2006)
13. Jetmundsen, B.: On Frequency Domain Methodologies for Structural Modification and Subsystem Synthesis, Ph.D. thesis. Rensselaer Polytechnic Institute, Troy (1986)
14. van der Seijs, M. V., van den Bosch, D. D., Rixen, D. J., de Klerk, D.: An improved methodology for the virtual point transformation of measured frequency response functions in dynamic substructuring. In: 4th ECCOMAS Thematic Conference on Computational Methods in Structural Dynamics and Earthquake Engineering, pp. 4334–4347 (2013)